5-30-2014

The Effects of Active Flow Control on High-Speed Jet Flow Physics and Noise

Zachary P. Berger
Syracuse University

Abstract

The work to be presented focuses on the noise generation of a fully turbulent, compressible jet flow within a large scale anechoic chamber. The investigations are aimed at understanding the complex nature of the jet flow field in an effort to reduce the far-field noise through active flow control and novel reduced-order modeling. The flow field of a highly subsonic, axisymmetric jet with a nozzle diameter of two inches (50.8 *mm*), is probed through the implementation of two-component particle image velocimetry (PIV) in the streamwise plane, along the jet's centerline. These measurements are coupled with simultaneously sampled near and far-field pressure measurements, in an effort to understand the relationship between the complex flow field in the near region of the jet and large pressure fluctuation in the far-field, responsible for the noise. In order to reduce these large pressure fluctuations in the acoustic field, it is imperative to first understand the interaction of structures in the flow field and evaluate how this relates to the propagation of acoustic signatures to the far-field.

We seek to establish a low-dimensional representation of the nonlinear, turbulent flow field through the implementation of reduced-order modeling in the form of proper orthogonal decomposition. In the first set of experiments conducted, active flow control is employed in the form of synthetic jet actuation at the nozzle lip, based on previous investigations. The effects of the flow control are observed using large-window PIV and far-field pressure measurements. The results suggest that an $\mathcal{O}(\varepsilon)$ input elicits an $\mathcal{O}(1)$ response, with both open and closed-loop flow control. While no noise reductions are seen in the far-field as compared to the uncontrolled jet, control authority over the jet is observed. The flow control greatly enhances mixing, thus reducing the length of the potential core and causing shear layer expansion. The second set of experiments involves the implementation of a time-resolved PIV system to effectively capture the temporal evolution of the flow physics in the streamwise plane. Low-dimensional velocity modes are directly correlated to low-dimensional acoustic modes in the far-field, using the observable inferred decomposition. Preliminary findings suggest that a small subset of low-dimensional velocity modes greatly contribute to the far-field acoustics. The spatiotemporal nature of these

"loud" modes are investigated in the context of potential noise-producing events. It has been found that for the Mach 0.6 uncontrolled jet, focusing on the region near the collapse of the potential core, modes 6 and 14 appear to be the loud modes, contributing significantly to the far-field noise. Further exploration of mode 6 reveals a unique interaction of structures at very specific instances in time. Thus, it is concluded that from a low-dimensional viewpoint, we have identified the deterministic spatial structures in the velocity that most highly contributes to the noise in the far-field. It is possible from this analysis to begin to identify noise-producing events and examine these interactions in both time and space. Lastly, loud modes are identified for the controlled jet (using time-resolved PIV), however initial findings imply that the control greatly increases the complexity of the problem. Despite this fact, it is found that there may be similarities in the spatial structure of the loud modes for two different closed-loop control cases. In any case, through the use of active flow control and reduced-order modeling, preliminary steps have been taken to understand the sources of jet noise with respect to the flow physics, in an overall effort to efficiently achieve far-field noise reductions for practical applications.

THE EFFECTS OF ACTIVE FLOW CONTROL ON HIGH-SPEED JET FLOW PHYSICS AND NOISE

by
Zachary P. Berger
B.S. Syracuse University, May 2009
M.S. Syracuse University, May 2011

SUBMITTED IN PARTIAL FULFILLMENT OF THE
REQUIREMENTS FOR THE DEGREE OF
DOCTOR OF PHILOSOPHY
IN
MECHANICAL AND AEROSPACE ENGINEERING
AT
SYRACUSE UNIVERSITY
SYRACUSE, NEW YORK, U.S.A.

May 2014

Acknowledgements

First and foremost, I would like to thank my family and friends for their continued love and support throughout my studies, I could not have done it without you. In particular I would like to thank my parents and my sisters for always being there for me no matter what the circumstances.

I would like to thank my advisor, colleague, mentor and academic father, Mark Glauser, for taking me into his group as a young undergraduate researcher. Being a part of the group through my PhD, Mark has taught me to be a confident, free-thinker with an intellectual curiosity that I could have never imagined. I would also like to thank Gina-Lee Glauser for making me feel like a part of the family and for the many insightful discussions about my career.

I would like to thank Jacques Lewalle, for teaching me to think about problems in a different way, always providing new insights, and for being a mentor throughout my time at Syracuse University. I'd also like to thank Bernd Noack, for many insightful discussions both in Syracuse and Poitiers - and hopefully many more to come.

I'd like to thank the entire L.C. Smith college of engineering staff for their support and help over the many years: Linda Lowe, Debbie Brown, Kim Drumm-Underwood, Kathy Madigan, Colleen Patterson, Dick Chave, Bill Dossert, John Banas, Pat Shanahan, Neil Jasper and Kathleen Joyce. I am so happy, proud and lucky to have been a part of your family.

I would like to thank all of the Skytop research group at Syracuse University, both past and present, for being my peers, mentors, friends and helping to make me the person I am today. Thanks to Guannan Wang, Ryan Wallace, Marlyn Andino, Jakub Walczak, Matt Berry, Andy Magstadt, Pingqing Kan, Zhe Bai, Alexis Zelenyak and John-Michael Velarde.

I'd also like to acknowledge the former jet group researchers for laying the groundwork for my studies: Charles Tinney, Jeremy Pinier and Andre Hall. In particular, thanks to Charles and Jeremy for always supporting me by attending all of my presentations at conferences and providing me with wonderful feedback and new insights.

Thanks to the physics machine shop, Charlie Brown and Lou Buda, for their willingness to help out with all of our projects, no matter how challenging or time consuming.

I would like to thank Spectral Energies, LLC. for loaning us the time-resolved PIV system to run our experiments. Thanks to Sivaram Gogineni, Stan Kostka, and Naibo Jiang for helping us perform the experiments and many insightful discussions during their visits.

I'd also like to thank Christina Simmons for always being there for me during the toughest of times. The countless late night phone calls and random catch-up sessions, whether good or bad, always got me through the day and kept me sane.

A special thanks to Kerwin Low for being my mentor and teaching me everything from how to run the facility, to how to give presentations, to how to be inquisitive and many other life lessons. A special thanks goes to Patrick Shea for also being my mentor throughout my studies, and being there for me to help run experiments, analyze data, and discuss every project, big and small.

I would not be where I am today without the support of my friend, colleague, mentor, roommate, partner-in-crime, and everything in between, Chris Ruscher. I can't thank Chris enough for everything he has done for me over the many years we have spent together at Syracuse, from undergrad all the way to PhD. I will never forget all of the guidance, collaboration, insightful discussions and simply being there for me whenever I needed it most. Here's to a lifetime of collaboration and friendship - cheers Dr. Ruscher, we did it!

I'd like to thank my funding sources: the L.C. Smith College of Engineering, Barry Kiel and the Air Force Office of Scientific Research, Spectral Energies, LLC. and the Syracuse University Center for Advanced Systems and Engineering (CASE).

Lastly, I would like to thank my dissertation committee for their support and time during the defense process: Drs. John Dannenhoffer III, Melissa Green, Benjamin Akih-Kumgeh and Makan Fardad.

Contents

List of Figures

List of Tables

Nomenclature

$a_n(t)$	n^{th} time-dependent POD coefficient
A	area
$B_{ij}(\theta,\theta')$	two-point correlation tensor for pressure
c_0	speed of sound
C_p	isentropic pressure ratio
$C(t,t')$	two-time cross-correlation tensor
C_{kn}^{pu}	linear mapping transformation matrix
C_μ	coefficient of momentum
D	jet diameter
D_{nn}	azimuthal spectrum of near-field pressure
f	frequency
G_{nn}	single-sided power-spectral density
$I(\vec{x})$	sound intensity
K	total turbulent kinetic energy
K_p	feedback controller gain
L	characteristic length scale
m	azimuthal mode number
M	Mach number
p_{ij}	stress tensor
P	barometric pressure
P_0	total pressure
P_s	static pressure
Q	number of synthetic jet actuators
r	radial jet direction
R	ideal gas constant
R_{ij}	two-point cross-correlation tensor
R_{nn}	azimuthal cross-covariance
Re	Reynolds number
S_{nn}	two-sided power-spectral density

St	Strouhal number
t	time
T	time period
T_0	temperature
T_{ij}	Lighthill stress tensor
u	fluctuating streamwise velocity component
U	mean streamwise velocity component
$\tilde{u}$	instantaneous streamwise velocity component
V	volume
x	streamwise jet direction
$y(t)$	actuation input signal
δ_{ij}	Kronecker delta function
γ	heat capacity ratio for air
λ^n	n^{th} mode POD eigenvalue
Λ^n	n^{th} mode POD eigenvalue overall contribution to TKE
μ	viscosity
Ω_o	Helmholtz resonance frequency
$\varphi(\theta)$	spatial eigenfunctions of the acoustics
$\phi^n(\vec{x})$	n^{th} POD mode spatial eigenfunction of velocity
Φ_{ij}	cross-spectral tensor
ρ	density of air
σ	standard deviation
τ	time lag
τ_{ij}	viscous stress tensor
θ	azimuthal angle centered on jet centerline

To my family,
And in memory of Dr. Hiroshi Higuchi . . .

Chapter 1

Introduction

In the field of engineering, innovation, discovery, and novel problem-solving have served as pillars for hundreds of years and continue to be at the forefront of today's advances in technology and the solving of fundamental problems. In the field of fluid dynamics, understanding turbulent flows remains to be a challenging task. In fact, according to Holmes *et al.* (1998) [110], "Turbulence in the last great unsolved problem of classical physics." The non-linearity of the Navier-Stokes equations, which govern turbulent flows, makes this problem particularly difficult to fully interpret. One of the most widely studied turbulence-related problems is that of jet noise. Over the past fifty years, the jet noise problem has been extensively examined and continues to be a growing concern around the world.

Research interests into the jet noise problem are two-fold, focusing on both the commercial and military industries. For the commercial applications, noise pollution and increasing amounts of air traffic over highly residential areas during takeoff and landing are the main concerns. According to a report released in 2013 by the Federal Aviation Administration (FAA) [1], "As the fleet grows, the number of general aviation hours flown is projected to increase an average of 1.5 percent a year through 2033." This means that jet noise from commercial aircraft will continue to have a great impact on the communities

close to airports.

From the military perspective, tactical maneuvers that a military aircraft might have to undergo during a mission remains a high priority. In addition, the hearing loss experienced by flight deck crews on aircraft carriers also motivates an increased interest in the jet noise problem. The jet noise generated during takeoff is transmitted not only to the flight deck but also radiates throughout the gallery and to various other decks. The Naval Safety Center reports that, "In 2004, the Veterans Administration (VA) spent $108 million in disability payments to 15,800 former Navy personnel for hearing loss [2]." In addition, the Navy considers any sound above 84 decibels (dB) as hazardous. The following figure shows a few typical noise sources on the decibel spectrum.

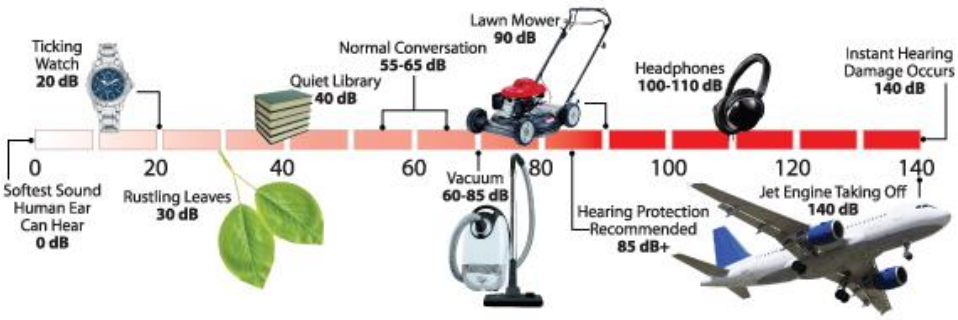

Figure 1.1: Typical sound levels in decibels (dB) provided by the Hearing, Speech & Deafness Center [3]

Figure 1.1 shows that a jet engine during takeoff can be as loud as 140 dB, where instant hearing damage occurs. This further motivates the ever-increasing interest in the jet noise problem. Both military and commercial sectors are looking into regulations which would reduce jet noise. In fact, according to Viswanathan & Pilon [239], "The International Civil Aviation Organization (ICAO) is considering more stringent noise regulations for commercial aircraft, which would be quieter by approximately 6-9 EPNdB (effective perceived noise, in decibels)...initial implementation date of around 2017. The pending

noise rules have spurred a flurry of technical activities aimed at both gaining better insights into noise source mechanisms and developing low-noise designs." The turbulence community continues to be at the forefront of these studies, focusing on noise source identification and far-field acoustic noise suppression.

The complexity of the jet noise problem is not only evident in the non-linearity governing the turbulence, but also in the need to control such flow physics in the context of aeroacoustic noise reduction. Research over the past fifty years has focused extensively on understanding the turbulence, thereby leading to ideas regarding control. Since the jet flow is both highly non-linear as well as high-dimensional, the community seeks to simplify the dynamics. This is mainly examined through a low-dimensional representation of the flow, extracting the coherent structures of the jet. By having a low-dimensional description of the flow, one can then begin to think about control strategies, based on the simplified dynamics of the jet. Examining the flow physics in this manner can be useful in studying the highly turbulent flow field exhibited by the jet; however, caution should be taken to make sure key information pertaining to the noise is not lost. In this spirit, if a low-dimensional representation of the flow field is established, while retaining the relevant flow physics, effective and practical control design is possible.

In recent years, many researchers have attempted to characterize the near region of the jet, specifically the velocity field and hydrodynamic pressure, in an effort to relate these quantities to the far-field acoustics. At NASA Langley's Jet Noise Laboratory, Seiner (1998) [204] emphasized a "rational approach" to jet noise reduction involving the coupling of low-dimensional modeling with velocity measurements to understand the flow and thereby effectively implement control. Moreover, Seiner emphasized the need for both numerical and experimental methodologies to tackle the jet noise problem.

Facing the jet noise problem using low-dimensional tools coupled with velocity field measurements has been an area of interest in the community for some time, especially in

the spirit of Seiner's earlier work. Specifically at Syracuse University's Skytop Turbulence Laboratory, much work has been done over the past ten years to relate near and far-field quantities through novel mathematical approaches and data acquisition tools. A fundamental understanding of the relationship between the velocity field, hydrodynamic pressure near the jet's exit, and the far-field acoustics, has been extensively studied.

Moreover, low-dimensional characteristics of the flow field are obtained to design an effective and feasible controller to reduce the noise in the far-field. One common mathematical tool that is implemented in this spirit is the proper orthogonal decomposition (POD). This is a tool which has been used to identify the most energetic structures in the velocity field in order to develop low-dimensional models [90, 148, 182, 227]. In addition, cross-correlations between the near and far-field pressure have been computed to gain insight into the relationship between the hydrodynamic and acoustic fields [91–93, 228, 230]. These cross-correlations also provide the time lag information associated with large scale events of the jet flow. Additional work has been done with spatial Fourier decompositions to determine low-order modal information of the near-field pressure [90–93, 182, 227, 228, 230]. In addition, spectral approaches coupled with linear stochastic estimation (LSE) have been used to develop a low-dimensional, time-resolved velocity field using the near-field pressure measurements [228, 230]. These results were then extended to estimate the acoustic field using Lighthill's analogy [227, 230]. Most recently, flow control has been implemented at the nozzle lip, achieving a slight reduction in far-field noise [148, 149]. The motivation for the control strategies was driven heavily by near-field/far-field pressure correlations [93–95].

The current investigation is an extension of the previously mentioned studies both within the Syracuse University group, as well as the rest of the community. The majority of the efforts are focused on examining the flow physics of a subsonic jet at Mach 0.6, both in the uncontrolled and controlled cases. In order to observe the effects of the control on

the flow physics, the velocity field has been probed and measurements have been simultaneously sampled with near and far-field pressure. Low-dimensional tools are implemented in the spirit of the above discussions in an ultimate effort to develop novel and feasible flow control strategies. The end goal is of course to reduce far-field jet noise and this task is quite daunting when one considers the scale and complexity of the problem. Even so, recent advances in data acquisition, control approaches, computational horsepower, and support from the community as a whole, have fostered a favorable environment for controlling jet noise. The focus of this work will hone in on incorporating novel reduced-order models of the flow physics with active control strategies in an overall effort to integrate closed-loop flow control onto a real system for significant jet noise reduction.

1.1 Turbulence Research

The field of turbulent flows encompasses a rich history dating back nearly 150 years to Osborne Reynolds, who first experimentally investigated the laminar to turbulent transition in pipe flows in 1883 [188, 189]. These studies spawned the dimensionless Reynolds number, quantifying the ratio of inertial to viscous forces. In addition, Reynolds' proposition to decompose the flow into its mean and fluctuating quantities, known as Reynolds decomposition, became the basis of much of the work done in the turbulence community today [190]. The framework for turbulence research relies on statistical mathematics as well as a fundamental understanding of fluid flows, examined primarily through experimental studies. Much of the early work in the turbulence field to follow that of Reynolds, was taken on by researchers including Prandtl (1925) [186], Taylor (1935) [222] and von Karman (1937-1938) [240, 241, 243] to name a few. Moving forward through the 1940s and 1950s, turbulence research began to focus on spectral and correlation-based approaches in the context of analyzing flow structures of various time and length scales. The velocity field was measured using newly developed experimental techniques such as hot-wire anemometry. Some of the pioneers in turbulence at this time included Batchelor (1948,1953) [25, 26], Corrsin (1949) [53], Heisenberg (1948) [103], von Karman (1948) [242], Kolmogorov (1941) [122, 123], Landau & Lifshitz (1959) [128], Townsend (1947) [232] and Yaglom (1948) [256]. In particular, the work of Kolmogorov laid much of the ground work for modern turbulence, still used today.

As both technology and experimental equipment began to improve, the mathematical and fundamental concepts governing turbulence began to be applied to more difficult problems and complex flow phenomena. From a computational standpoint, this technological surge allowed for the development of a field known as computational fluid dynamics (CFD). This branch of study fostered the development of closure models, aimed at solving a class of problems through the Navier-Stokes equations. This effort was led primarily by

Harlow *et al.* [96–101] and inspired the development of advanced numerical approaches. These include Large Eddy Simulation (LES) studied by Deardorff (1970) [58], Reynolds Averaged Navier-Stokes (RANS), and Direct Numerical Simulation (DNS), studied by Orszag & Patterson (1972) [172]. These techniques have been used extensively in field since their inception and more details on this can be found in the work of Gatski (1996) [77].

To complement the computational analyses described above, experimental techniques to probe the velocity field had also been improving. Many of these experiments were qualitative at first and so any form of flow visualization, such as smoke and dye, were acceptable. Once quantitative measurements were desired, the community moved to hot-wire anemometry, a technique which measures a single component of the velocity field and is temporally resolved, seen in the works by Comte-Bellot (1976) [52], Ewing *et al* (1995) [67], Bruun (1995) [40], Wyngaard (1968) [255], Klewicki & Falco (1990) [121] and Zhu & Antonia (1996) [259].

As time went on, the need for non-intrusive velocity measurements was desired and so optically-based measurements were developed to probe the flow field without interrupting the physics. These laser-based diagnostic tools included Laser Doppler Anemometry (LDA), sometimes known as Laser Doppler Velocimetry (LDV), and Particle Image Velocimetry (PIV). LDA and PIV were developed to obtain velocity measurements which are capable of obtaining multiple velocity components simultaneously. LDA, first introduced by Yeh & Cummins (1964) [257], uses the doppler shift principle to obtain a small volume of information in a flow field. If three lasers of different wavelengths are used, the result is a three component velocity measurement at a single point and is time resolved. This is comparable to a hot-wire measurement except that since it is optically based, it is not intrusive to the flow field. LDA measurements in turbulent flows can be seen in the works of Buchhave *et al.* (1979) [41], George & Lumley (1973) [78], Lau *et al.* (1979) [129],

Adrian & Yao (1986) [6], Durst *et al.* (1995) [66] and Romano *et al.* (1999) [192].

The PIV is another optically-based measurement technique, developed in the late 1970s by Barker & Fourney [24], Dudderar & Simpkins [63], Grousson & Mallick [88], and further developed by Meynart [154–159], Pickering & Halliwell [180] and Adrian [5] in the early 1980s. The PIV technique uses a camera to capture images of the flow-field. This is done by means of seeding the flow with particles and illuminating these particles with a laser sheet. The camera captures image pairs and since the distance a particle has traveled between the two images can be calculated, and the time between images can also be calculated, a velocity vector field is then established. This technique measures two-dimensional planes of flow with up to three velocity components. Standard PIV systems are capable of sampling rates of $\mathcal{O}(Hz)$. Improvements to the lasers and cameras have allowed for the development of higher sampling rates on the order of 10-20 kHz. These high sampling rate systems, known as time-resolved PIV (TRPIV) systems, allow one to fully capture the time evolution of high Reynolds number flows, such as that of the jet flow. A few researchers who have used TRPIV to analyze high speed jet flows include, Wernet (2007) [252], Murray *et al.* (2012) [166], and Low *et al.* (2013) [149].

1.1.1 Coherent Structures

Ever since scientists have been able to observe fluid flow using flow visualization, the curiosity for how these structures convect, dissipate, and interact has always been an area of great interest. Turbulence is based upon the cascading of energy across various time and length scales, which depend on the particular flow field of interest. Early pioneers in the field became interested in the idea of extracting and understanding the different types of flow structures which make up a turbulent flow field. A prominent contribution to many turbulent flows are coherent structures. Hussain (1983) [113] describes a coherent structure as, "...a connected, large-scale turbulent fluid mass with a phase-correlated vorticity

over its spatial extent. That is, underlying the three-dimensional random vorticity fluctuations characterizing turbulence, there is an organized component of the vorticity which is phase correlated (i.e. coherent) over the extent of the structure." Coherent structures can also be described as the structures in the flow field which are characterized by regularly occurring, organized features that undergo some characteristic temporal life cycle [79]. Coherent structures are not necessarily categorized as large or small scale events, but rather are deterministic structures which can take on any size at various frequencies [136].

Coherent structures have been studied extensively for the past fifty years by various researchers in the field. The first extensive studies of coherent structures related to turbulent flow fields were those of Crow and Champagne (1971) [55], Winant and Browand (1974) [254], and Brown and Roshko (1974) [39]. Crow and Champagne were the first to study the effects of Reynolds number on the jet flow, and to analyze the structure of the jet's preferred mode. Moreover, they were able to observe coherent structures in the jet at various Reynolds numbers in both water and air, using flow visualization techniques. The other researchers mentioned, focused more on how mixing layers are dominated by the larger scale coherent structures in the flow. They were the first among many to observe and study how vortices pair during the streamwise convection of a turbulent flow, once again with the aid of flow visualization. Coherent structures were further studied in this regard by those such as, Townsend (1956) [233], Cantwell (1981) [44], Hasan & Hussain (1982) [102], Hussain (1983) [113], Fiedler (1988,1998) [73, 74] and Tam & Chen (1994) [218], among many others. A flow visualization of an axisymmetric, circular jet from the work of Fiedler can be found in Figure 1.2 to follow.

A great deal of work regarding coherent structures in turbulent flows was fueled by Lumley in the mid 1960's. Lumley [150] proposed a way of identifying coherent structures through a method known as the proper orthogonal decomposition (POD). This concept, which has been used extensively in the mathematics community for quite some time

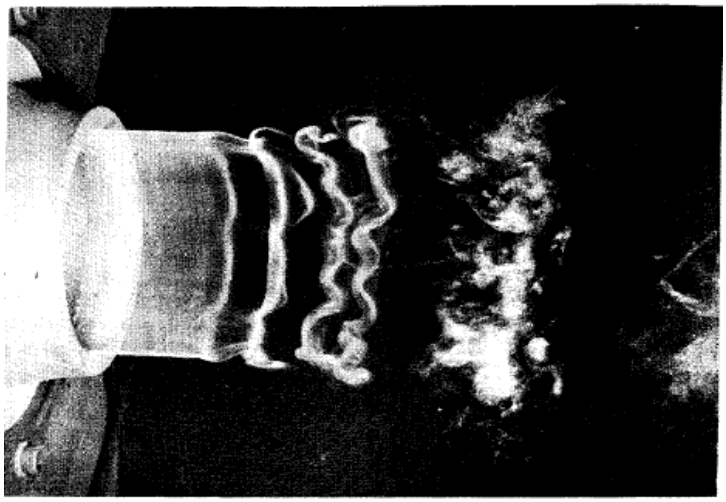

Figure 1.2: Axial instability of a vortex: smoke photograph of periodically excited ring-vortices in laminar-turbulent transition regime of a circular jet (axisymmetric shear layer) [73]

(sometimes referred to as principal component analysis, or PCA), had never been applied to turbulent flows, up to this point. The POD serves as a low-dimensional representation of a given flow field by means of a decomposition, which maximizes the mean squared turbulent kinetic energy. This methodology serves as a way to objectively determine the existence of coherent structures.

The first experiments in turbulence which implemented the POD techniques, specifically for a free shear flow, were performed by Glauser *et al.* in 1987 [79, 81–83]. In these studies, the focus was the mixing layer of a turbulent jet. An array of hot-wires was used to probe the velocity field in the radial direction of the jet, three diameters downstream of the nozzle lip. Through the use of POD and cross-spectral analysis of the velocity measurements, Glauser *et al.* found that the large scale events account for about 40& of the overall energy in the flow field. Moreover, approximately 25% and 15% of the total energy accounts for the 2^{nd} and 3^{rd} order structures, respectively. This meant that the original instantaneous flow field (in terms of streamwise velocity) could be nearly reconstructed using

only the first few POD modes. Glauser *et al.* then added an azimuthally varying hot-wire array to obtain azimuthal structures in the flow [79]. From this analysis, they found that "ring-like" or "donut-like" structures seen in the first POD mode characterized the axisymmetric mode, near the potential core. In addition, they found that higher order modes (4, 5, and 6 for example), were seen as "passive contributors" to the slow region of the mixing layer.

They ultimately developed a model describing the life cycle of coherent structures [80]. According to Glauser *et al.*, this life-cycle can be grouped into four main stages: first, is the initial onset which is caused by mean flow instability; next, is the interaction of vortex rings, characterized by a "leap-frogging" of the two vortex rings, where the faster moving ring upstream bursts through the downstream ring; this leads to a vortex instability and breakup, leading to the eventual cascade of energy. This process can be seen in Figure 1.3 to follow.

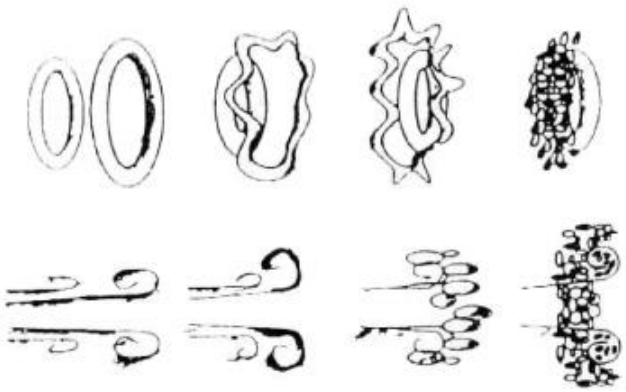

Figure 1.3: Glauser's four stage process for large scale structure interactions [79]

These results were later extended by Citriniti & George in 2000 [45]. Similar measurements were conducted but for a larger area of the flow. For these experiments, a polar array of 138 hot-wires was used in the same downstream location. The configuration can be seen

with flow visualization in Figure 1.4.

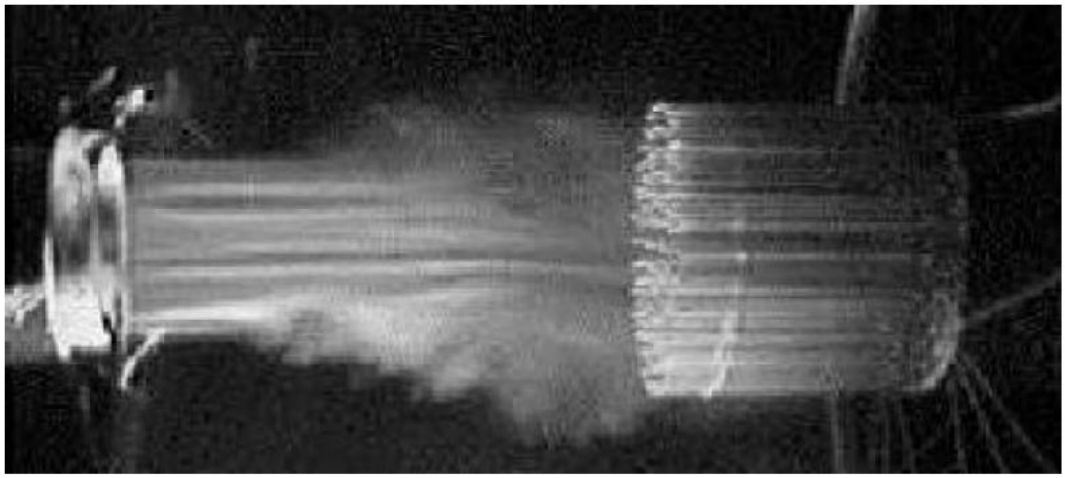

Figure 1.4: Smoke visualization of axisymmetric jet into hot-wire array, Citriniti & George (2000) [45]

Citriniti & George also concluded that the flow field could be rebuilt with a small number of the first few azimuthal modes, namely 0, 3, 4, 5 and 6. Moreover, they again found the "volcano-like" events around the potential core, as mentioned by Glauser *et al.* One last finding of Citriniti & George were streamwise vortex pairs amongst the original azimuthal vortex pairs, previously investigated. The interaction of the coherent structures with the rest of the mixing layer is depicted in Figure 1.5. For more information, the reader is referred to Citriniti & George (2000) [45].

1.2 The Axisymmetric Jet

From the study of coherent structures, the focus is now turned to the axisymmetric jet, which has been extensively studied in recent years due to its fundamental nature. An axisymmetric jet is characterized by a bulk fluid, having a constant momentum flux, which is expelled and interacts with some ambient medium. In the case of the axisymmetric jet,

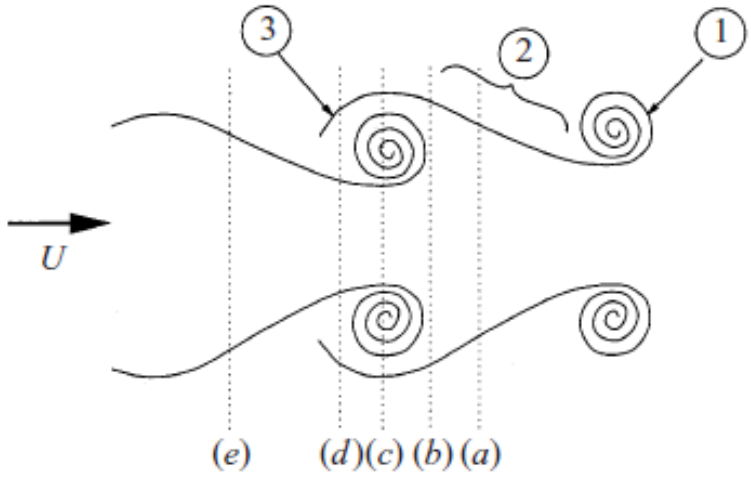

Figure 1.5: Coherent structure interaction with (1) the azimuthally coherent ring, (2) the braid region and (3) the streamwise component of the large-scale motion, Citriniti & George (2000) [45]

the bulk fluid is characterized by an irrotational velocity field, known as potential flow. This potential flow moves through a nozzle into the ambient medium; and in the case of the axisymmetric jet, the nozzle is circular. The differences in velocity between the potential flow and the ambient medium cause an instability known as the Kelvin-Helmholtz instability. This forms a velocity shear and is often referred to as the shear layer. As the ambient medium interacts with the potential flow, the ambient fluid is entrained by the bulk flow causing rotation of the fluid. As a result, vorticity is developed in the shear layer. These vortices grow and roll up to form large-scale structures that continue to propagate downstream. This is represented schematically by Moore (1977) [162] in Figure 1.6.

The interaction of vortices in the jet's shear layer, which results in vortex pairing and the establishment of large-scale structures is elaborated upon by Moore [162] and further explained by Ffowcs Williams & Kempton (1978) [72].

The jet is often characterized by various non-dimensional quantities, the most common being the dimensionless velocity, or Mach number. The Mach number is defined in

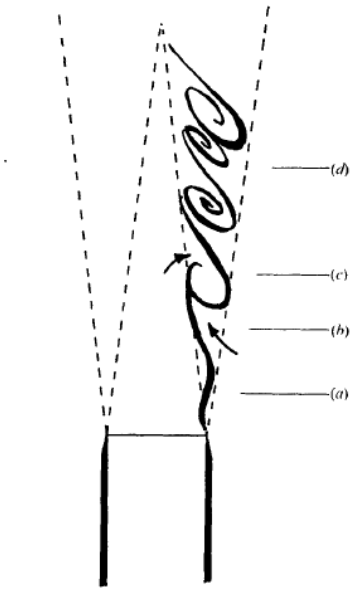

Figure 1.6: Schematic of jet shear layer as described by Moore (1977) [162]: (a) Shear layer oscillates (b) Air becomes entrained (c) Vortices form (d) Vortices form pairs and so increase axial spacing

equation 1.1:

$$M = \frac{U}{c_0} \tag{1.1}$$

where U is the free-stream velocity and c_0 is the speed of sound, defined as:

$$c_0 = \sqrt{\gamma R T_0} \tag{1.2}$$

In equation 1.2, γ is the heat capacity ratio of air, R is the ideal gas constant and T_0 is the temperature of the medium. For air at sea level, the speed of sound is 340 m/s. Therefore, for the majority of the experiments presented, the Mach number is 0.6, corresponding to a free-stream bulk velocity of 204 m/s in the potential flow region. This irrotational region of an axisymmetric jet is often refereed to as the potential core. The frequency of shear layer instabilities and that of the large-scale structures are quite different and therefore these

quantities are also non-dimensionalized by a characteristic length scale and free-stream bulk velocity. The Strouhal number (St), is a non-dimensional frequency defined in the following way:

$$St = \frac{fL}{U} \tag{1.3}$$

where f is the frequency, L is the characteristic length scale, and U is the characteristic velocity. The shear layer instability *St* number is typically on the order of 0.013 [201]. The frequency of the large scale structures throughout the evolution of the potential core are known as the jet column mode instability. The *St* number of these instabilities is on the order of 0.3. There is also an azimuthal mode instability seen throughout the development of the potential core. Due to the convection of the jet flow and interaction of the shear layers, the bulk flow of the jet can only sustain itself for so long. At this point the shear layers expand so much that the potential core, or bulk flow of the jet, collapses. The collapse of the potential core involves the interaction of vortices at several different scales, in both time and space. Another schematic showing the development of the axisymmetric jet is shown in Figure 1.7 from the work of Yule *et al.* (1978) [258].

The entrainment and roll-up of vortices results in a transitional flow regime as well as a turbulent flow regime. The diagram shown in Figure 1.7 is generated based on the experiments and flow visualizations of Lau & Fisher (1975) [130], Crow & Champagne (1971) [55] and Moore (1977) [162]. Additional flow visualizations of shear layers were carried out by Brown & Roshko (1974) [39] and Winant & Browand (1974) [254]. Figure 1.7 depicts a representation of the axisymmetric jet from a two-dimensional viewpoint. It is important to keep in mind that this flow field is highly three-dimensional. Yule *et al.* go on to develop a qualitative description of the axisymmetric jet based on experiments conducted. This can be seen in Figure 1.8. The jet structure has been investigated extensively in this spirit by Lau *et al.* (1972) [131], Lau (1979) [129] and Tam (1998) [217], among

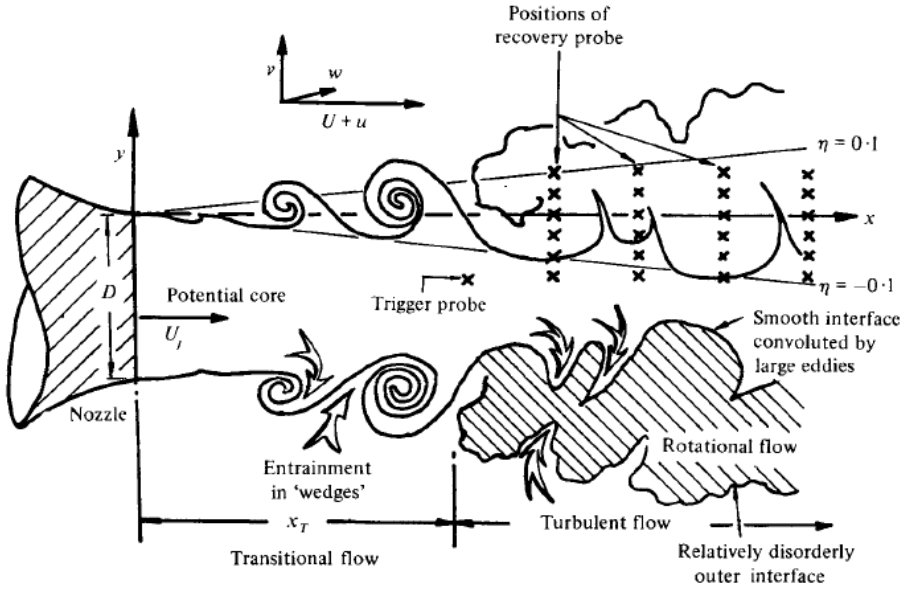

Figure 1.7: Notation for round free jet as described by Yule *et al.* (1978) [258]

others.

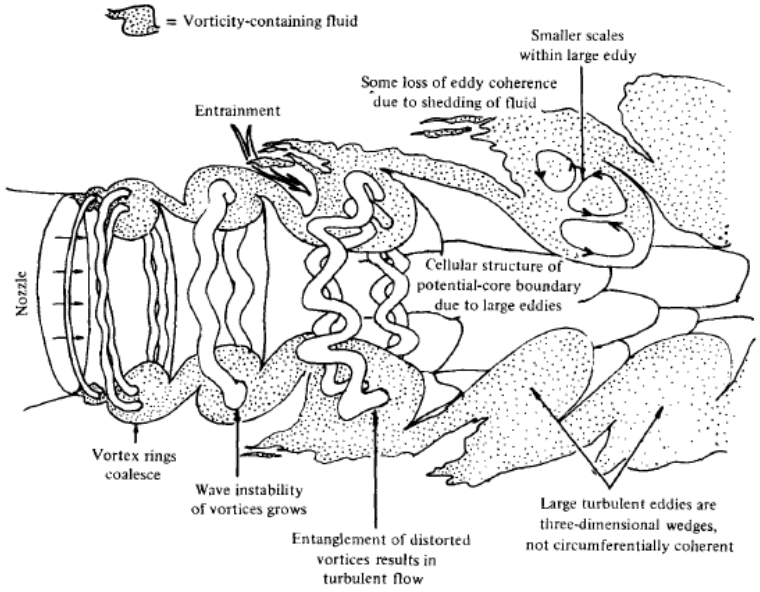

Figure 1.8: Physical structures of transitional jet as described by Yule *et al.* (1978) [258]

As seen in Figure 1.8, the natural instability of the shear layer creates a "street of vortex-ring-like vorticity concentrations" [258]. The vortex rings then coalesce and thus the instability wave then grows with the entrainment process, creating the large scale structures. The vortex pairing, coalescing, breakdown, and other high strain events are believed to be the primary sources of far-field noise. More specifically, the entrainment of the ambient fluid leads to large pressure fluctuations in the near-field of the jet resulting in large acoustic signatures seen in the far-field [227]. Moreover, it has been shown that the largest sources of noise are a result of the interaction of coherent structures at the collapse of the potential core [90, 204]. The large-scale structures in this region of the jet experience growth followed by a sudden decay, believed to be responsible for the magnitude of the propagated sound [72]. The expansion of the shear layer for an axisymmetric jet has been shown to be approximately $0.07x$, where x is the downstream location in the streamwise direction (see Tennekes & Lumley (1972) [224]). Experimental studies typically estimate a shear layer expansion closer to $0.1x$, giving a potential core collapse of approximately six diameters for the jet to be investigated in the current work [113].

In addition, by studying the far-field pressure spectra, it has been proposed by Tam & Chen (1994) [218] and Tam & Auriault (1999) [220], that the jet exhibits a two-noise source model responsible for directivity effects. According to this model, fine-scale turbulence is propagated to the larger polar angles with respect to the jet axis, while large turbulence structures convect towards the shallower polar angles, closer to the jet axis. This is shown in the schematic diagram provided by Tam *et al.* (2008) [221], shown in Figure 1.9.

The large-scale structures observed in Figure 1.9 are sometimes referred to as F-spectrum and these structures tend to have low frequencies. Conversely, the fine-scale turbulence of higher frequency is refereed to G-spectrum, as discussed by Mollo-Christensen (1964) [161], Tam & Chen (1994) [218] and Nance & Ahuja (2009) [170]. The concept of jet noise directivity in the context of aeroacoustic propagation will be addressed in subsequent

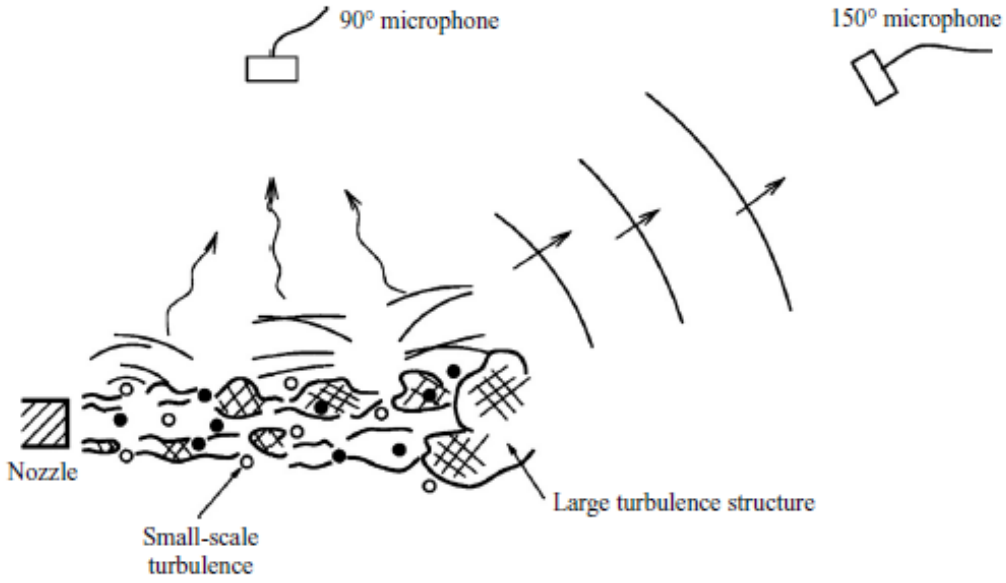

Figure 1.9: Schematic diagram of the sources of jet noise radiating to the side line and the downstream directions, Tam *et al.* (2008) [221]

sections.

1.3 Aeroacoustics and the Acoustic Analogy

The theory of modern day aeroacoustics began with early advances in aerospace technology, related to propeller noise of early aircrafts in the 1930s and 1940s [59, 89, 109, 225]. This led to a series of experiments on this topic and eventually led to in-depth exploration of acoustics by Lighthill in the early 1950s [139, 140]. At this time, Lighthill presented the acoustic analogy, a theoretical formulation aimed to form a relationship between the equations of fluid motion and the wave equation for a uniform acoustic medium at rest. This analogy has become the basis for various jet noise studies ranging from experimental to numerical and theoretical investigations. The basis of the analogy is governed by a fluctuating fluid flow in a medium without resonance or solid boundaries. Lighthill makes

several assumptions to establish the acoustic analogy, many of which simplify the overall problem but sacrifice complete accuracy for noise prediction. This was the first analogy of its type in that it estimated the far-field noise generated by a source without using approximations from the Navier-Stokes equations. There has been a certain amount of criticism of the analogy over the years due to the fact that there are some limitations, such as the speed of sound and mean density which are assumed to be constant [174]. Obviously this is not always the case, however, it does indeed cover a wide class of problems. The analogy is unable to accurately predict the convection of sound taking into account the effects of refraction through the shear layer. Work has been done in this spirit to account for the refraction effects [217]. Since the acoustic analogy was first introduced into the field, many researchers have continued to study it, including Phillips (1960) [178], Ffowcs Williams (1963) [68], Csanady (1966) [56], Ffowcs Williams & Hawkings (1969) [71], Ffowcs Williams & Hall (1970) [70], Lilley (1974) [141], Howe (1975) [112], Goldstein (1976) [85], Dowling (1978) [62], Mohring (1978) [160] and Durbin (1983) [64, 65]. In the meantime, a number of experiments have been conducted to account for the nonlinear wave operator, taking into account the effects of solid boundaries and mean flow refraction [8]. Further descriptions of the developments in the field of aeroacoustics can be found in the works of Ffowcs Williams (1977) [69], Goldstein (1984) [86], and Tam (1998) [217].

With the background provided, a brief overview of Lighthill's acoustic analogy is presented for reference. The mathematical formulation of the analogy under the assumptions is quite rigorous and thus it is the grouping of the terms that is more significant. Once again the analogy seeks to establish a relationship between the equations of fluid motion and the wave equation for a uniform acoustic medium at rest. The analogy is exact and does not rely on approximations from the Navier-Stokes equations. The governing equation for the analogy is:

$$\frac{\partial^2 \rho'}{\partial t^2} - c_0^2 \nabla^2 \rho' = \frac{\partial^2 T_{ij}}{\partial x_i \partial x_j} \tag{1.4}$$

such that $\rho' = (\rho - \rho_0)$, where ρ is the fluid density, c_0 is the speed of the sound and therefore,

$$T_{ij} = \rho' u_i u_j + p_{ij} - c_0^2 \rho' \delta_{ij} \tag{1.5}$$

which is known as Lighthill's turbulence stress tensor. In this equation u_i is the fluctuating fluid velocity in the x_i direction. Then the stress tensor, p_{ij} is defined in the following way:

$$p_{ij} = (p - p_0)\delta_{ij} - \tau_{ij} \tag{1.6}$$

where the viscous stress tensor, τ_{ij}, can be expressed by:

$$\tau_{ij} = \mu \left(\frac{\partial u_i}{\partial x_j} + \frac{\partial u_j}{\partial x_i} - \frac{2}{3} \delta_{ij} \frac{\partial u_k}{\partial x_k} \right) \tag{1.7}$$

In equation 1.7, μ is the coefficient of viscosity and δ_{ij} is the Kronecker delta function:

$$\delta_{ij} = \begin{cases} 1 & \text{if } i = j \\ 0 & \text{if } i \neq j \end{cases} \tag{1.8}$$

Lighthill then performed some additional scaling analyses to determine that the turbulent stress tensor can be simplified if the Mach number is low enough, and if the jet is considered mildly heated. Rearranging the stress tensor to a more suitable form gives:

$$T_{ij} = \rho' u_i u_j + ((p - p_0) - c_0^2(\rho - \rho_0))\delta_{ij} - \tau_{ij} \tag{1.9}$$

In equation 1.9, the viscous term, τ_{ij} can be neglected since viscous effects are negligi-

ble at a large enough distance from the source. In addition, the second term in the equation (known as the entropy term) can also be neglected, for a moderately heated isothermal flow. Therefore we are left with the following equation, indicating the main source of noise is due to the fluctuating Reynolds stresses in the flow.

$$T_{ij} \approx \rho_0 u_i u_j \tag{1.10}$$

Another important concept which is then brought about by the acoustic analogy is the further decomposition of the Reynolds stress term. Ribner (1964) [191] proposed that the Reynolds stress could be decomposed into "shear-noise" and "self-noise". This concept has been studied ever since and is summarized in the work of Ukeiley *et al.* (2007) [234]. According to Ribner, a Reynolds decomposition is performed on the source terms to separate the mean and fluctuating components of the velocity:

$$u_i(\vec{x},t) = \tilde{u}_i(\vec{x},t) - U_i(\vec{x}) \tag{1.11}$$

With three components of velocity and three spatial dimensions, there are a total of thirty-six terms that can be reduced to only nine [191, 234]. The shear-noise or fast pressure terms occur as a result of the turbulence interacting with the mean flow. The dominant shear noise terms in this case comes from the axial velocity component:

$$U_1 U_1' \langle u_1 u_1' \rangle \quad U_1 U_1' \langle u_2 u_2' \rangle \quad U_1 U_1' \langle u_3 u_3' \rangle \tag{1.12}$$

The self-noise or slow pressure terms therefore occur as a result of the turbulence interacting with itself. Therefore, there are nine self-noise terms, shown in the following equation:

$$\begin{array}{ccc} \langle u_1^2 u_1'^2 \rangle & \langle u_2^2 u_2'^2 \rangle & \langle u_3^2 u_3'^2 \rangle \\ \langle u_1^2 u_2'^2 \rangle & \langle u_1^2 u_3'^2 \rangle & \langle u_2^2 u_3'^2 \rangle \\ \langle u_1 u_2' u_1 u_2' \rangle & \langle u_1 u_3' u_1 u_3' \rangle & \langle u_2 u_3' u_2 u_3' \rangle \end{array} \tag{1.13}$$

In the above terms, the prime ($'$) represents spatially and temporally dependent velocity terms. Ukeiley *et al.* [234] and Ribner [191] discuss the contributions of each term in greater detail. In addition, since the entropy term can not be neglected for a hot jet, the analysis requires an additional term and this can be found in the work of Hall (2007) [90].

The final result from this analogy is that the density in the far-field can be estimated as a function of the near-field source terms. The density is given by the following volume integral,

$$\rho - \rho_0 \approx \frac{1}{4\pi c_0^2} \frac{x_i x_j}{x^3} \int_{\mathscr{V}} \frac{1}{c_0^2} \frac{\partial^2}{\partial t^2} T_{ij} \left(y, t - \frac{|x-y|}{c_0} \right) dV(y) \tag{1.14}$$

The above equation is also commonly rearranged and expressed in terms of pressure:

$$p'(x,t) \approx \frac{1}{4\pi} \int_{\mathscr{V}} \frac{1}{c_0^2} \frac{\partial^2 T_{ij}}{\partial x_i x_j} \left(y, t - \frac{|x-y|}{c_0} \right) \frac{dy}{|x-y|} \tag{1.15}$$

In the equation for pressure, x and y are the locations of the observer and the source respectively, V is the volume of the fluid and $t - \frac{|x-y|}{c_0}$ is the retarded time.

1.3.1 Directivity

As previously mentioned in § 1.2, the aeroacoustic propagation of noise sources from the jet exhibit a distinct directivity effect. More specifically, the fine-scale turbulence in the shear layer is being transported downstream by the mean flow. The sound that radiates

from these small scales must traverse the shear layer, therefore undergoing refraction due to velocity and density gradients in the shear layer [221]. Furthermore, the large scale structures tend to propagate in all directions, with the sound focused towards the shallow polar angles. Regardless, the acoustic waves tend to bend away from the jet flow direction by means of refraction. This causes a "cone of silence" about the centerline of the jet. Complementary to the cone of silence is the "cone of coherent noise" which accounts for the large scale coherent noise seen from approximately 15° to 45° with respect to the jet centerline. The combination of these directivity patterns leads to a heart shape, outlining the acoustic propagation. This is commonly known as the heart of jet noise [15] and can be seen in Figure 1.10.

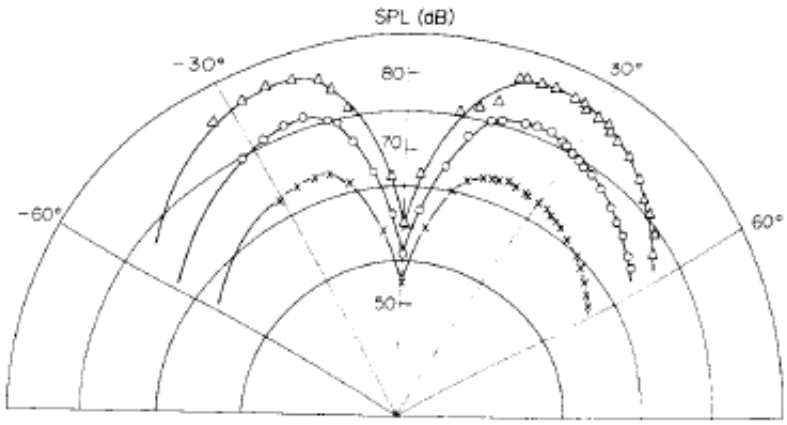

Figure 1.10: Directivity patterns for 3/4-inch jet: 6% filtered signals, center frequency 3000 Hz, Morris *et al.* (1973) [164]

The effects of refraction on the directivity of the noise produced by the jet have been extensively studied by Mollo-Christensen *et al.* (1964) [161], Ribner (1964) [191], Atvars *et al.* (1965) [15], Morris *et al.* (1973) [164], Tam & Auriault (1998,1999) [219, 220] and Tam *et al.* (2008) [221].

1.4 Previous Work at Syracuse University

The framework for the experiments and results to be presented are motivated by the earlier work conducted within Syracuse University's Skytop anechoic chamber and jet facility. This facility was modified in 2001 to accommodate fundamental jet noise studies. A full description of the modifications made to the facility for these experimental studies can be found in the work of Tinney *et al.* (2004) [229].

1.4.1 Spectral Stochastic Estimation

The first set of experiments considered were performed by Tinney *et al.* (2005,2006,2008) [226, 228, 230]. These experiments focused on an axisymmetric Mach 0.85 cold jet with a two-inch (50.8 mm) nozzle diameter. The goal of the study was to develop a low-dimensional approximation of the jet flow field using the POD technique. The flow field was probed with simultaneous near-field velocity and pressure measurements. In addition, the far-field noise was also simultaneously sampled. For near-field velocity measurements, standard (4 Hz) PIV was used in the stereoscopic configuration to capture all three instantaneous velocity components in the $r-\theta$ plane. Various discrete streamwise locations (x/D = 3 to 8 in 0.25 diameter increments) were sampled. For near-field pressure, an azimuthal array of fifteen pressure sensors was placed 0.875 diameters downstream of the nozzle exit and 0.875 diameters from the centerline in the radial direction. This configuration can be seen in Figure 1.11.

Far-field acoustic measurements were taken using a boom array of six microphones located seventy-five diameters downstream of the nozzle exit. Measurements were taken from 15° - 90° (in increments of 15°) with respect to the centerline of the jet axis. Tinney *et al.* performed a scalar decomposition of the streamwise velocity component, revealing a peak in azimuthal mode 5, consistent with results of Glauser *et al.* In addition, it was shown that there is a shift in the dominant azimuthal mode as the jet evolves downstream

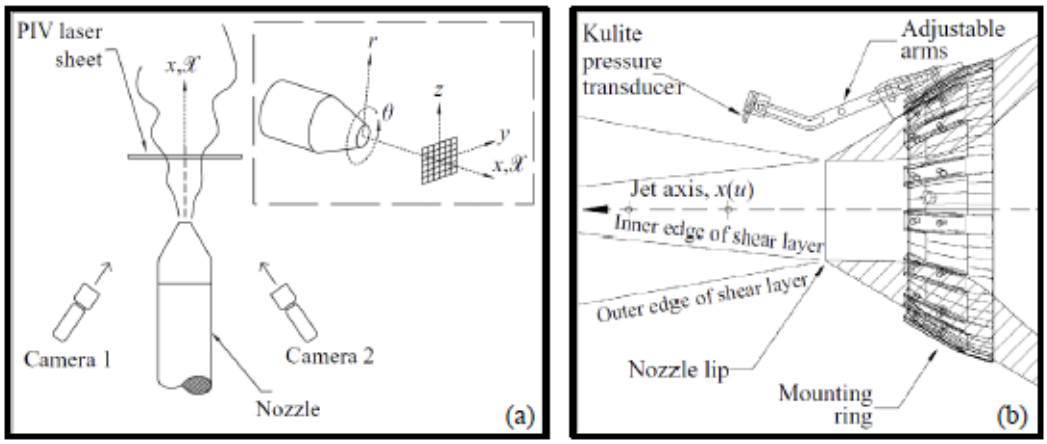

Figure 1.11: Experimental Setup at Syracuse University anechoic chamber, Tinney *et al.* (2005) [227]

[228].

Since the PIV system had a sampling rate of 4 Hz, Tinney *et al.* could not resolve the time scales of the flow field directly. Therefore, estimation techniques were developed to explore the dynamic characteristics of the flow field. The idea was to obtain an estimate of the acoustic source field and thereby predict the far-field noise using an estimate of the turbulent kinetic energy. Tinney *et al.* used the Modified Complementary Technique which utilizes the simultaneous time-resolved hydrodynamic pressure measurements coupled with the statistically independent PIV measurements to produce a low-dimensional time-resolved estimate of the flow field.

Tinney *et al.* then used a concept known as linear stochastic estimation (LSE) to estimate the Lighthill source field. The LSE (first proposed by Adrian (1977) [4]) develops a time-resolved estimate of an under-sampled experimental quantity, in this case the velocity field acquired with PIV, using a simultaneously sampled time-resolved measurement, in this case the near-field pressure. Tinney *et al.* performed these calculations in spectral space using the sLSE. Then the estimated velocity field was used to predict the Lighthill source field. The results from these experiments can be found in Figure 1.12. Further

results can be found in the works of Tinney *et al.* [228, 230].

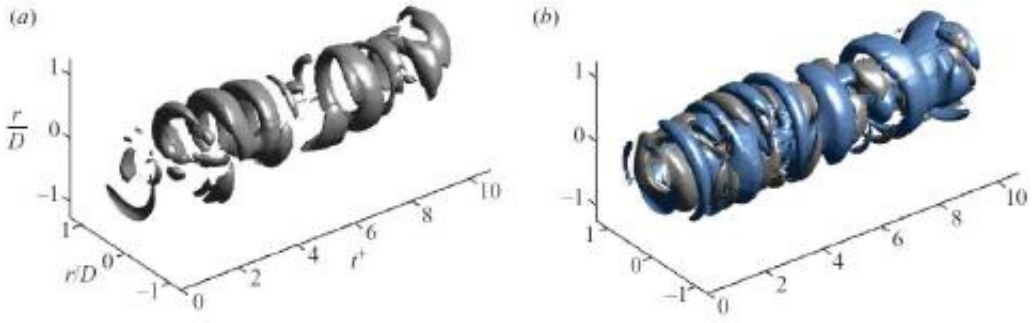

Figure 1.12: (a) Q surface of the vorticity field at x/D = 3.0 using n = 1+2 and m = 0+1 and (b) corresponding source field, Tinney *et al.* [230]

1.4.2 Dual-Time Particle Image Velocimetry

The work of Tinney *et al.* was extended by Pinier (2007) [183], who further investigated the dominant Fourier modes in the near-field hydrodynamic region, in an effort to determine which low-order Fourier modes have the strongest correlation with the far-field. The idea was to develop a low-order dynamical system (LODS) using a dual-time PIV (DT-PIV) experimental setup. The far-field microphone configuration used in this case was the same as that of Tinney *et al.* and can be found in Figure 1.13.

In the first part of the investigation, Pinier used an azimuthal array of fifteen pressure sensors placed radially, 10 *mm* outside of the expanding shear layer. This array was traversed from x/D = 1 to 11, in 18 discrete steps. In order to find the dominant sound sources in the near-field, cross-correlations between the fluctuating near-field pressure and the far-field acoustics were computed. It was determined from this analysis that the dominant sound sources are located between 6 and 10 diameters downstream of the nozzle exit. This

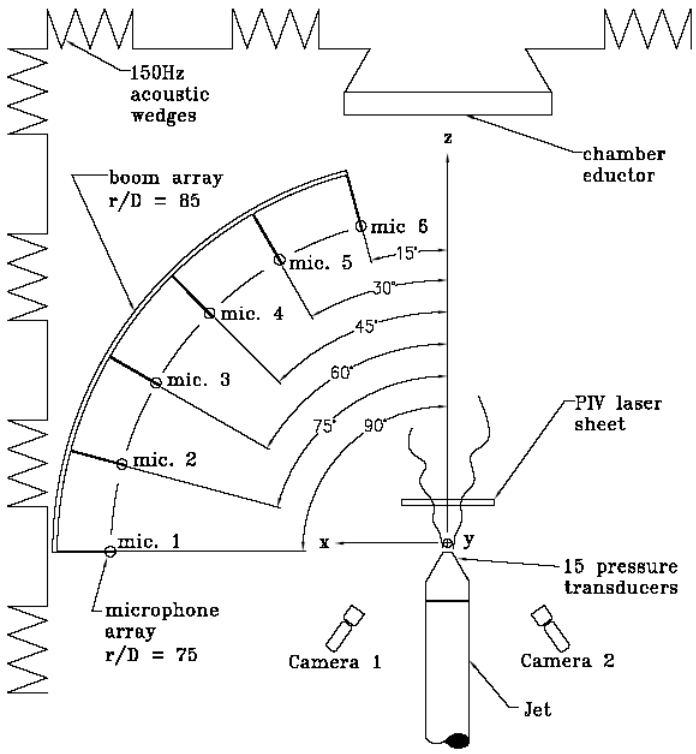

Figure 1.13: Experimental setup (top-view), Pinier (2007) [183]

is the region just beyond the collapse of the potential core, and these results can be seen in Figure 1.14.

Correlating the near-field pressure array at x/D = 7 with each of the six far-field microphones, the relative lag time decreases from 11 ms at the 90° microphone to 9.5 ms at the 15° microphone. Moreover, the correlation strength increases by approximately 10% moving from the 90° microphone to the 15° microphone, as shown in Figure 1.15.

The azimuthal near-field pressure array allows for the opportunity to compute a spatial Fourier decomposition of the data. From this analysis, Pinier showed that the unfiltered pressure could be almost completely rebuilt with a low-dimensional approximation using only the first two azimuthal Fourier modes. In addition, modes 0 and 1 are of equal strength

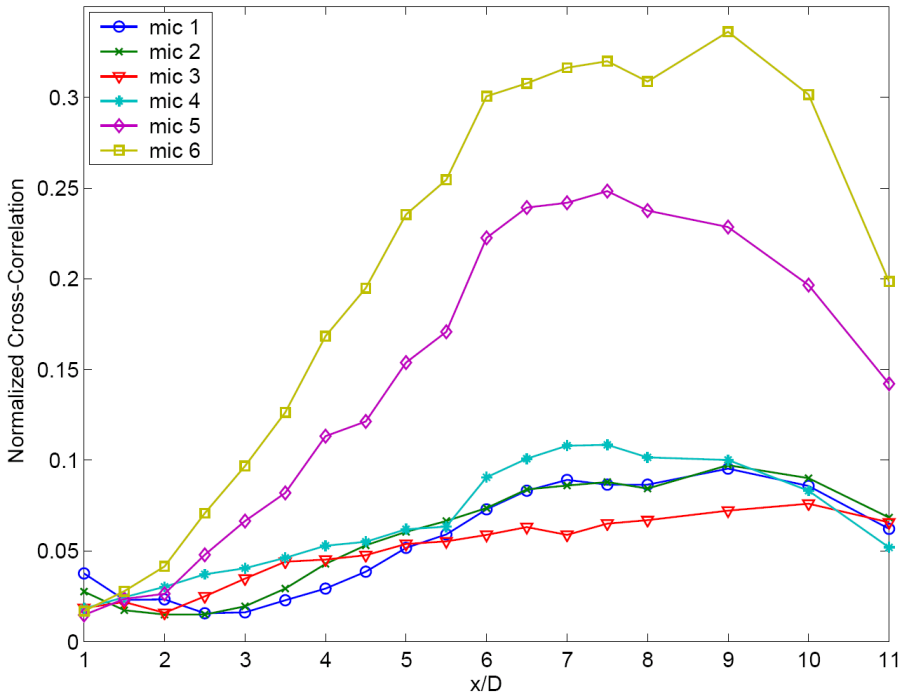

Figure 1.14: Maximum normalized cross-correlations between the near-field and far-field pressure as a function of downstream position, Pinier (2007) [182]

in terms of the pressure, and the rebuilt near-field pressure signal can be seen in Figure 1.16. From this analysis, Pinier also observed that modes 0 and 1 remain dominant at all downstream locations sampled (see Figure 1.17).

Perhaps one of the most significant results of this work is the cross-correlation between the first two near-field pressure Fourier modes and the far-field acoustics. Despite the fact that modes 0 and 1 are of equal strength, Fourier mode 0 has a much stronger correlation with the far-field than that of mode 1. In fact, none of the other higher order Fourier modes show a strong correlation with the far-field, only mode 0. This result served as the basis for many future investigations and showed that Fourier mode 0 of the near-field pressure has the strongest correlation with the far-field acoustics. Since Fourier mode 1 strongly represents the near-field pressure but is weakly correlated with the far-field, the idea is to use this mode

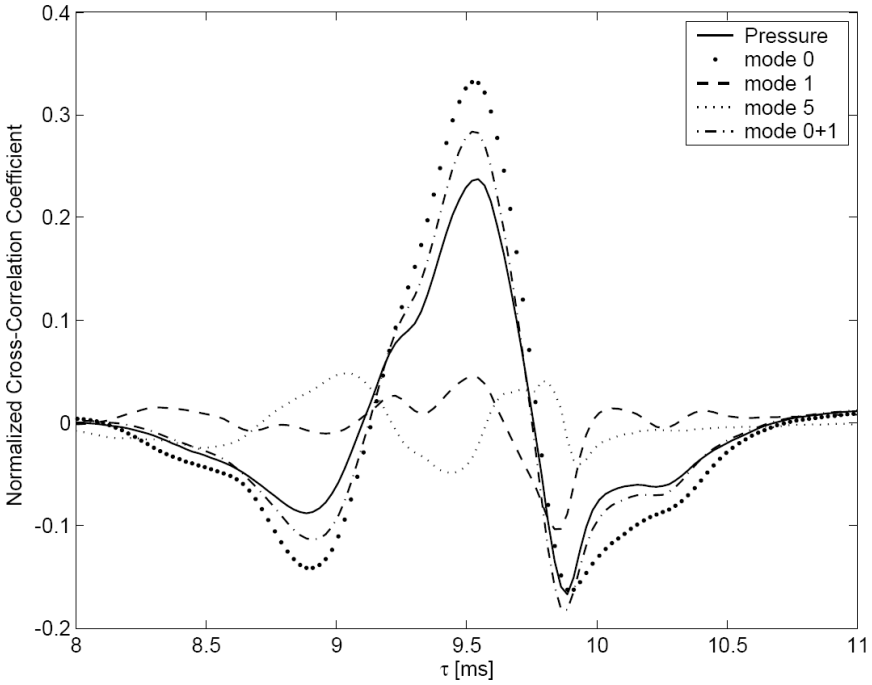

Figure 1.15: Comparison of the normalized cross-correlation between the far-field sound at $\phi = 30^\circ$ and the mode-filtered near-field pressure at $\theta = 96^\circ$, x/D = 8, Pinier (2007) [182]

to decrease the Fourier mode 0 correlation in the far-field, thereby potentially reducing the noise. This concept will be further explored in subsequent sections, but remains one of the most significant contributions from this analysis thus far.

The second portion of Pinier's studies involved training a dynamical system for the jet using the acceleration field. These measurements were directly obtained using two stereoscopic PIV systems. By measuring the velocity field in the same measurement plane with a known time delay, the acceleration was calculated directly. This became known as a dual-time PIV setup, consisting of four cameras and two lasers, as seen in the setup in Figure 1.18.

From the acceleration field, Pinier developed a low-order dynamical system representation of the jet. A movie was created based on the LODS and a single snapshot can be seen

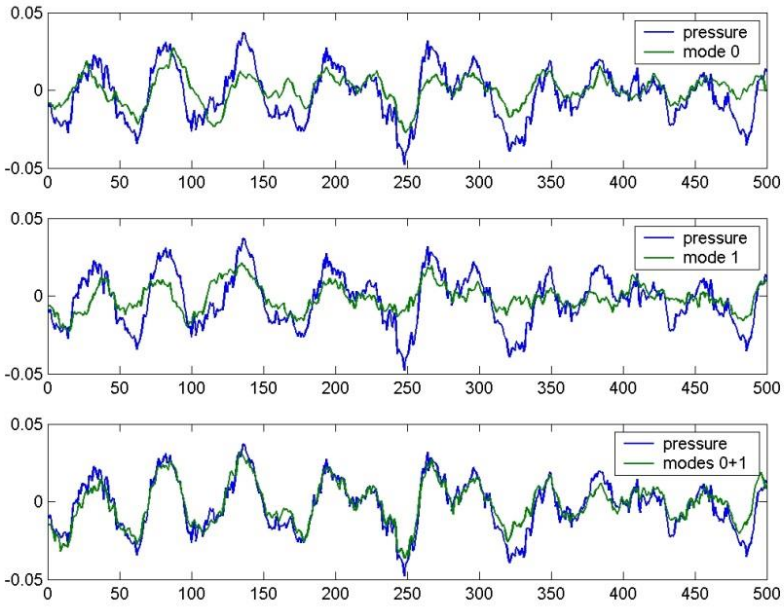

Figure 1.16: Time series of the near-field pressure compared to (top) the mode 0 part of the pressure only, (middle) the mode 1 part of the pressure only and (bottom) the sum of modes 0 and 1, Pinier (2007) [182]

in Figure 1.19. This shows a 30 POD mode reconstruction of the axial fluctuating velocity at eight diameters downstream.

1.4.3 The Heated Jet

With the goal of investigating jet flow fields closer to real world applications, Andre Hall [90–92] investigated the differences between a heated and cold jet flow, at Mach 0.6. During the facility modification, a heating unit was installed in order to perform measurements with operating temperatures as high as $1000^{\circ}F$. The studies in this case focused on how large temperature differences in the core jet flow affect the far-field noise. Two different Mach 0.6 experiments were carried out for comparison, having a temperature ratio of 0.93

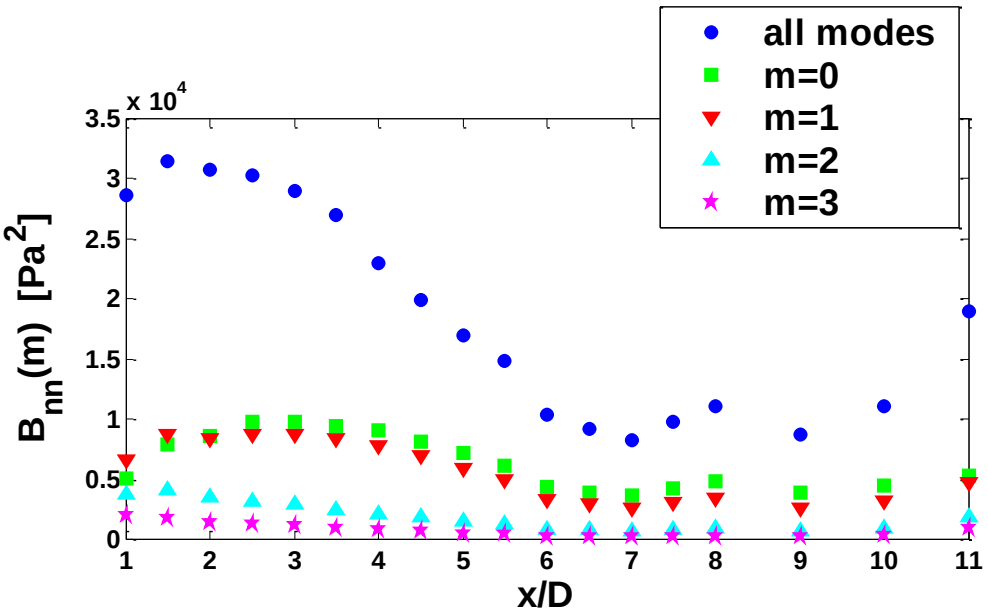

Figure 1.17: Comparison of the level of energy in azimuthal Fourier modes 0 to 3 as a function of downstream position, Pinier (2007) [182]

(cold) and 1.7 (heated). Once again in all of these experiments, the near-field pressure and velocity were sampled simultaneously with far-field acoustics. Similar to past experiments, PIV measurements were taken in the $r-\theta$ plane at various streamwise locations. Hall determined from these experiments that the heated jet has a shorter potential core length and larger shear layer thickness as compared to the cold jet. In addition, the hot jet seems to organize the low-dimensional spatial structures. The POD modes resemble azimuthal Fourier modes for the heated jet as seen in Figure 1.20. From this analysis, Hall found the column mode to be the dominant Fourier mode in the hot jet whereas the helical mode was dominant in the cold jet.

Moreover, the hot jet radiated higher levels of acoustic pressure fluctuations in the far-field, especially seen at the shallow polar angles with respect to the centerline of the jet. In all cases, the hot jet causes a low frequency increase and high frequency decrease in the far-field acoustic levels. The far-field sound pressure levels for the heated and cold jet can

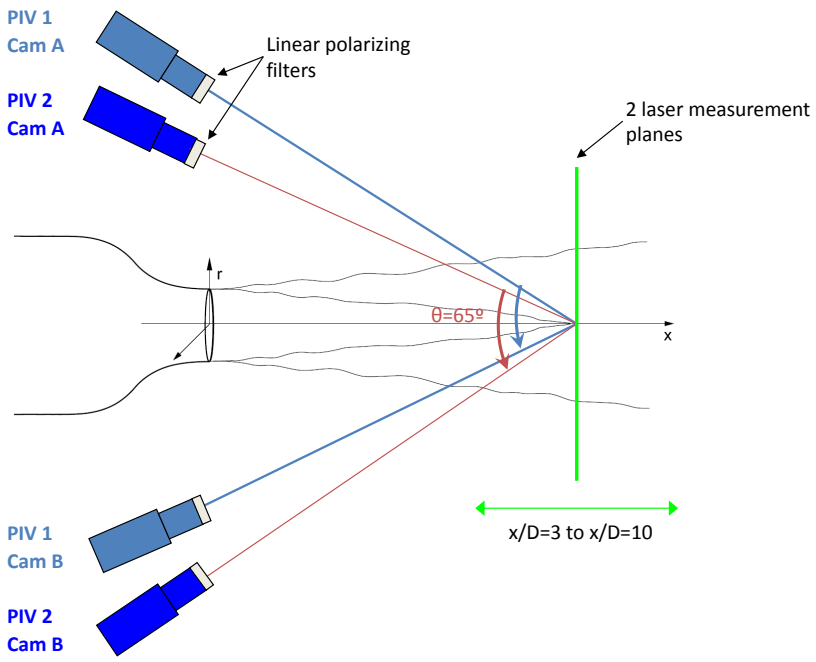

Figure 1.18: Top view of the Dual-Time PIV experimental setup, Pinier (2007) [182]

be found in Figure 1.21.

1.4.4 Active Flow Control

Most recently, Kerwin Low explored the first active flow control experiments for jet noise at Syracuse University [144–147, 149]. Low performed a number of experiments using an actuation system driven by piezoelectric disks operating as synthetic jet actuators. A series of open and closed-loop experiments were performed, aimed at reducing the far-field noise. Cross-correlations were computed between the near-field pressure and far-field acoustics and compared for the different control cases with respect to the uncontrolled jet. Low found that all of the open-loop cases only made the jet louder at every microphone. However, using a simple proportional closed-loop control scheme, a modest reduction of approximately 1.22 dB was seen at the far-field microphone at 15°. In this case, the Fourier-

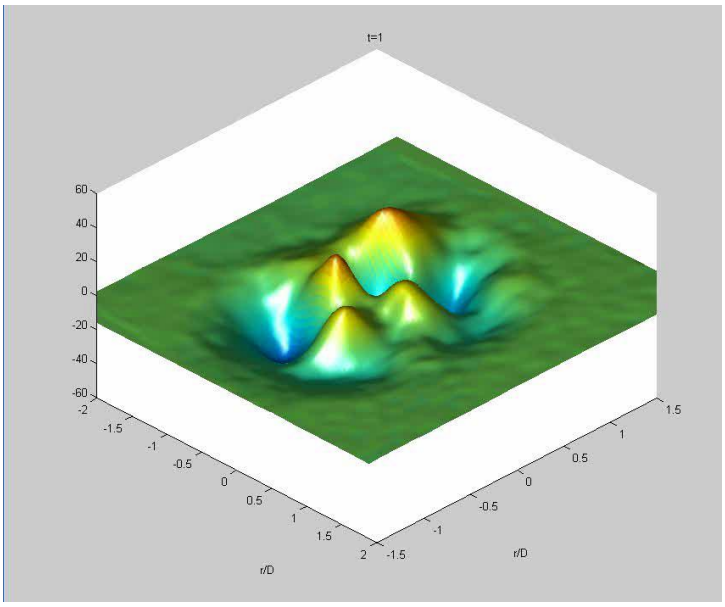

Figure 1.19: 30 POD mode quadratic model of axial fluctuating velocity at x/D = 8, Pinier (2007) [182]

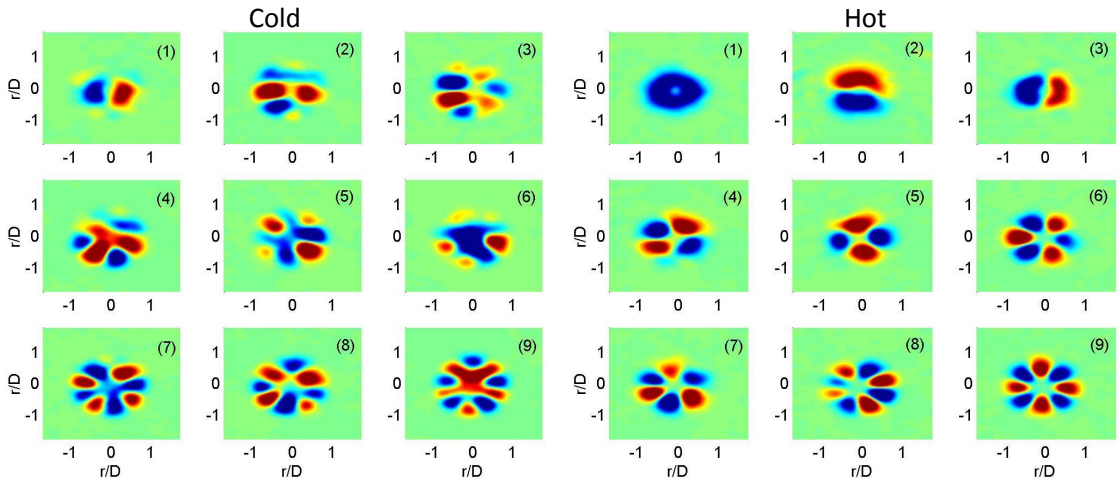

Figure 1.20: POD modes for the hot and cold jet at x/D = 4.5, Hall (2008) [90]

filtered mode 1 of the near-field pressure (at x/D = 6) was fed back to physically force azimuthal Fourier mode 0 at the nozzle lip. For this forcing mode, all actuators operated

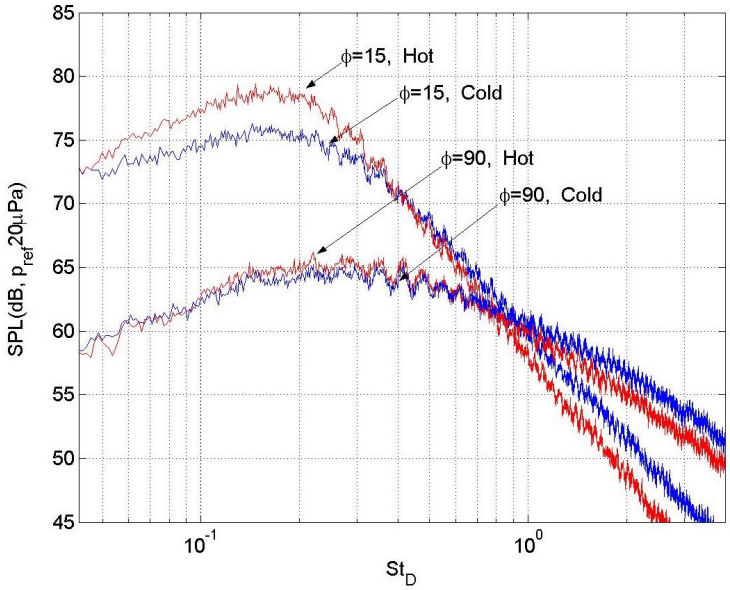

Figure 1.21: Far-field sound pressure levels for the hot and cold jet, microphones at 15° and 90°, Hall (2008) [90]

in phase to appeal to the column mode of the jet. The directivity plot for the overall sound pressure levels can be seen in Figure 1.22, where the black curve represents the baseline, uncontrolled jet and the blue curve represents the closed-loop control case.

It is worthwhile to point out at this point that the uncertainty of the overall sound pressure level is approximately ± 1 dB, with a repeatability of ± 0.2 dB, based on the measurements, verified by Laurendeau *et al.* (2008) [134]. Despite the fact that the reduction in noise seen at the 15° microphone was only slightly above the uncertainty, the trend is moving in the right direction, suggesting more advanced control schemes are worth exploring. In addition, Low *et al.* (2010) [146] has shown that for a range of open-loop tests, all results were louder than the uncontrolled jet, suggesting closed-loop control is a more viable solution.

After this series of tests were conducted, Low *et al.* then worked to implement time-resolved PIV measurements into the experiments to analyze the time-evolution of the jet

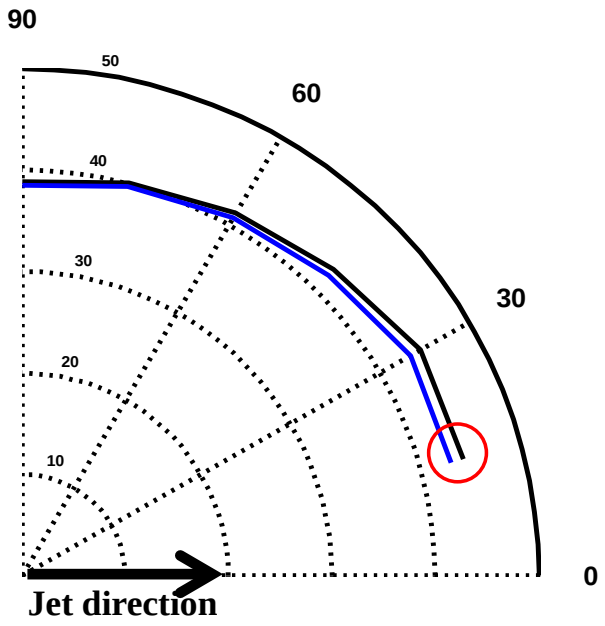

Figure 1.22: Directivity Plot for Overall Sound Pressure Level, Low (2012) [148]

flow field directly. A 10 kHz PIV system was utilized in the streamwise plane of the jet. Two-component measurements were collected due to the hardware limitations of only have one camera, however now the velocity field would be time-resolved. Through the simultaneous sampling of near and far-field pressure as well as time-resolved PIV, Low *et al.* found that for a specific PIV window location and Mach number, a "loud" mode existed in the flow field. This mode was obtained by a direct cross-correlation between the POD modes of the velocity field and the far-field acoustic pressure. This "loud" mode is characterized by a low-dimensional velocity mode having a correlation level of equal strength to the far-field as that of the near-field. Therefore this mode would seem to have a strong contribution to the far-field acoustics. It was found that mode 6 was the "loud" mode for Mach 0.6 at x/D = 5–6.5, and modes 6 and 14 were found to be the "loud" modes for Mach 0.6 at x/D = 6–7.5 [149]. These results can be seen in Figure 1.23.

The results presented from the work of Tinney [226–230], Pinier [182, 184, 185], Hall

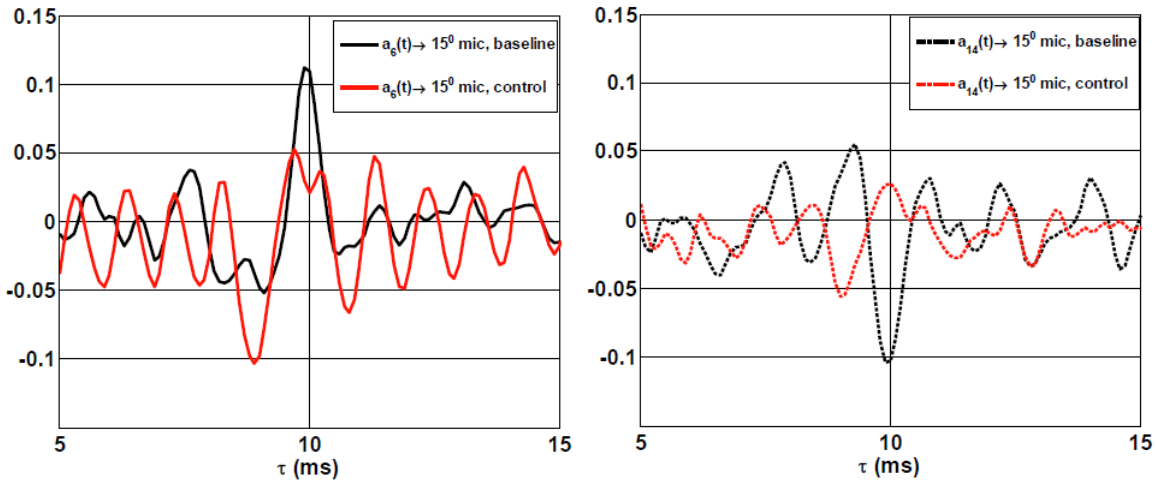

Figure 1.23: Correlations levels of POD modes 6 and 14 with microphone 15° for the baseline and open-loop jet, Low (2013) [149]

[90–92] and Low [146, 148, 149], lay the foundation for the jet noise studies within the Syracuse University laboratory. Justification for analyses and control methodologies in the current investigation will be presented in the context of these previous findings (see § 1.5 for more information).

1.5 Current Experimental Investigation

The complexity of the jet noise problem is governed by the nonlinear turbulence present in a fully three-dimensional flow field, as observed in § 1.2 & § 1.3. In order to fully understand the noise generating mechanisms in the jet, it is imperative to examine the full three-dimensional flow field. In terms of probing the flow field, the previous investigations within the Skytop research group have focused primarily on three-component velocity field measurements in the $r-\theta$ plane using standard PIV techniques (see § 1.4). Despite the fact that these measurements are not time-resolved, simultaneous pressure measurements allow estimations of the time-resolved field to be computed, using all three velocity components.

The three component velocity measurements in the $r-\theta$ plane provide useful information about the velocity field, but still only consist of two-dimensional slices of the jet. The current investigation complements these measurements by looking at the streamwise plane of the jet along the centerline. The centerline is chosen since the axisymmetric jet is azimuthally invariant in the mean sense. The measurements in the streamwise plane provide two-component velocity fields that are *time-resolved*. The two-component measurements taken are a result of hardware limitations, having one camera for the TRPIV experiments. Despite this limitation, the time-resolution of the measurements allows for the direct evaluation of the temporal evolution of the jet, without the use of estimation techniques. In addition, a three camera *standard* PIV setup is used to capture a large window of the jet, again with two-component measurements in the streamwise plane of the jet along the centerline.

The state of the art $10\,kHz$ TRPIV and large window PIV (LWPIV) setups provide complementary data sets to the previous $r-\theta$ data sets collected. With the LWPIV, the effects of the control can clearly be observed, in a statistical sense, with respect to the large scale dominant flow structures. In addition, the TRPIV enables direct comparisons of the flow field with the far-field acoustics in the context of the controlled jet. It is understood that the jet noise problem is not only nonlinear but also fully three-dimensional, however the experiments performed will provide new insight into the flow physics responsible for the noise with respect to a slice of the jet. The current hardware limitations, particularly with respect to the TRPIV, allow for a two-component, time-resolved view of a slice of the jet. Despite not having information of the entire three-dimensional flow field, much insight about how the flow physics are related to the noise, in the context of control, can be still be gained.

Chapter 2

Experimental Jet Facility

The experiments to be discussed were conducted in the Syracuse University large scale anechoic chamber and high-speed jet facility on the Skytop campus. The large scale anechoic chamber was constructed under the direction of Dosanjh during the 1970's. The anechoic chamber was built to perform various aeroacoustics studies, including the effects of several differet nozzle configurations on noise suppression in supersonic heated jets. The details of these studies can be found in the works of Dosanjh *et al.* (1974,1975) [60, 61] and Ahuja (1976) [7]. Additional research in the anechoic chamber was conducted by Sheplak & Spina (1994) [211], focusing on high speed impinging jets. The recent jet noise studies began in the early 2000s under the direction of Glauser. The description of the facility, with respect to designing the high-speed jet experiments, is laid out in greater detail by Tinney *et al.* (2004) [229].

2.1 The Anechoic Chamber

The anechoic chamber, as described by Ahuja *et al.* [7], is constructed from twelve inch thick reinforced, single poured concrete. The inner dimensions of the chamber itself are 30 x 24 x 18 ft (12,960 ft^3). The chamber is acoustically treated from floor to ceiling

with fiberglass wedges having a cutoff frequency of 150 Hz. The free space dimensions of the chamber are 26 x 20 x 14 ft (7,280 ft^3). Several modifications have been made to the chamber in recent years and the latest configuration can be seen in Figure 2.1.

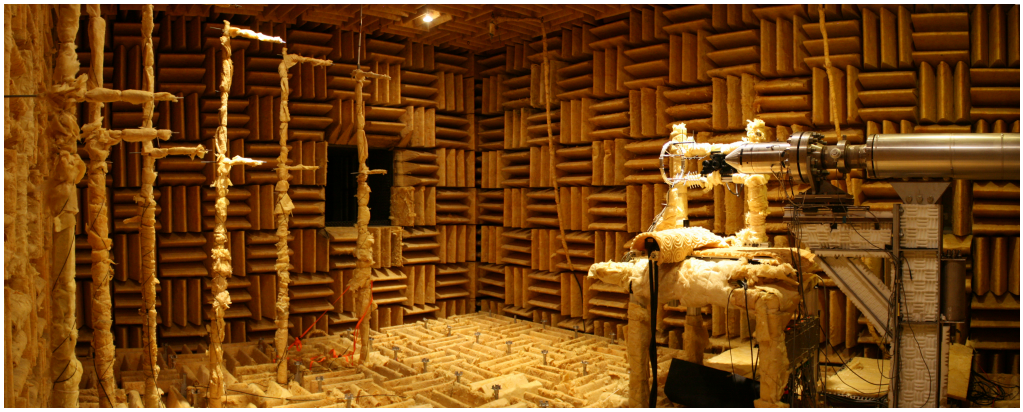

Figure 2.1: Syracuse University anechoic chamber and high-speed jet facility

2.1.1 High-Speed Jet

The jet rig previously shown was installed by Tinney *et al.* [227, 229] and is constructed from three mated stainless steel sections, intended to withstand high temperatures for heated jet experiments. The rig contains a ceramic flow straightener capable of withstanding high temperatures (up to $2600^{\circ}F$). The jet rig sits on a rail system allowing for material expansion during heated jet experiments. The nozzle profile follows a matched 5^{th} order polynomial with a 3:1 contraction ratio and a diameter at the exit of 50.8 mm (two inches). The jet can be seen in Figure 2.2 and further information can be found in Tinney *et al.* [229].

2.1.2 Compressed Air and Controller

The air being supplied to the jet is generated via a 100 horsepower, two-stage Joy compressor which discharges compressed air to five tanks having a volumetric capacity of 1100 ft^3.

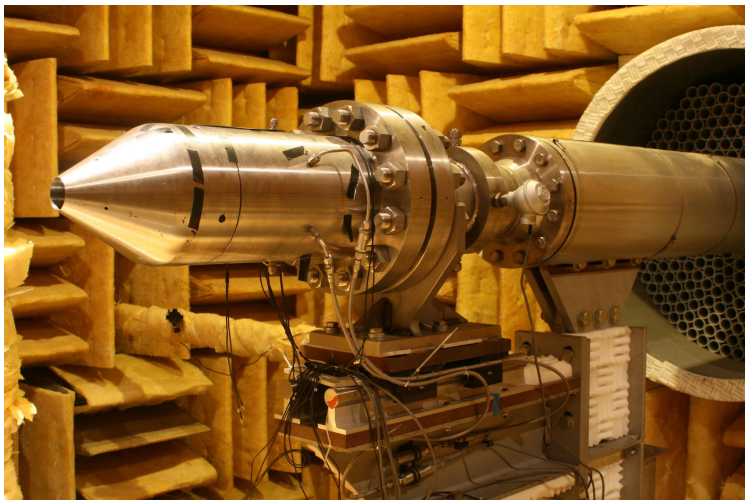

Figure 2.2: High-speed jet rig within Syracuse University anechoic chamber

The tanks are rated to 500 psig, with a discharge rate of 4.5 ft^3/s, which allow for operational Mach numbers between 0.3 and 1.2. A pneumatically actuated *Fisher* valve operated by a 100 psi *Kaiser* compressor is throttled to control the discharged air, in order to achieve the desired Mach number at the jet exit. The Mach number setting is based on the isentropic pressure relationship whereby sensors in the pipe (upstream of the contraction) and chamber measure static pressure and absolute pressure, respectively. The static pressure is used to calculate the Mach number, based on a calibration with the total pressure. Tinney *et al.* [229] found a linear relationship between the total and static pressure, using these calibrations.

Using the static pressure in the nozzle, the total pressure sensor in the chamber and the barometric pressure sensor in the plenum chamber, the Mach is set using the isentropic relationship as follows:

$$C_p = \frac{P_o}{P_s} \tag{2.1}$$

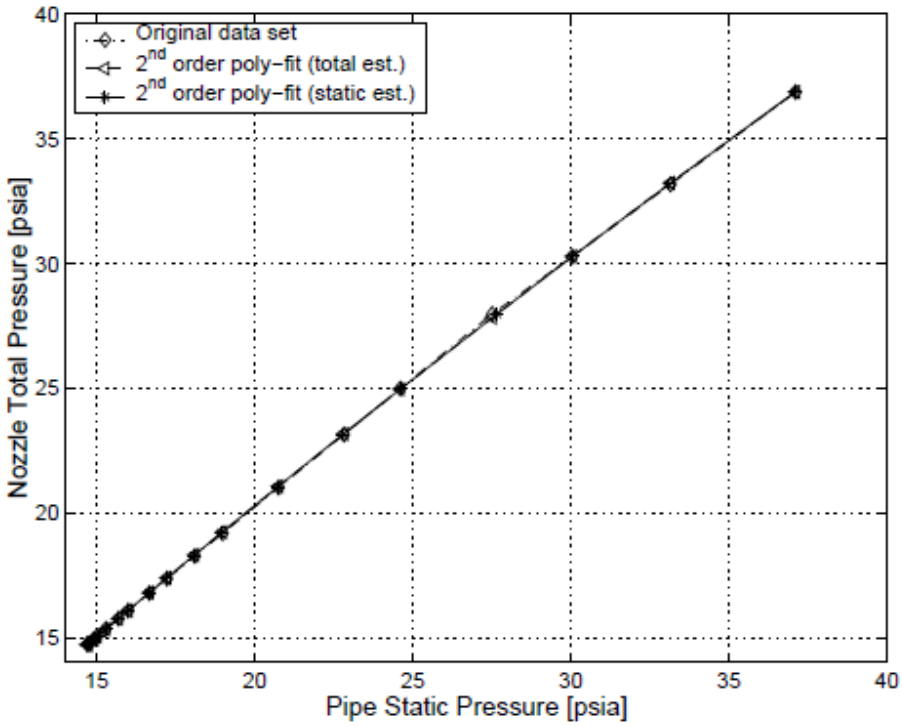

Figure 2.3: Relationship between nozzle total pressure and nozzle static pressure, Tinney *et al.* (2004) [229]

$$M = \left[\frac{2}{\gamma - 1} \left(\left(\frac{C_p P_s}{P}^{\frac{\gamma-1}{\gamma}} \right) - 1 \right) \right]^{1/2} \tag{2.2}$$

where M is the Mach number, P_o is the total pressure, P_s is the static pressure, and P is barometric pressure. The Mach number is then maintained using an Allen Bradley, Pro-Logix Control (PLC) system, which implements a PID (proportional-integral-derivative) feedback control loop. The *PLC* throttles the *Fisher* valve to maintain the desired Mach number at the jet exit. The uncertainty of the pressure sensor within the nozzle is less than 0.5% at Mach 0.6 [148]. As previously mentioned, the pressurized tanks are rated to 500 psi, but are normally charged to 400 psi as an added factor of safety. With recent maintenance performed on the compressor, the tanks charge in under two hours, as compared to the two to three hours as quoted by Low (2012) [148]. At Mach 0.6, the jet can operate for

approximately thirty continuous minutes.

In order to keep the entrained flow around the jet structure organized, a co-flow is provided via a Make-Up Air (MUA) unit on top of the anechoic chamber building. In addition, an exhaust fan operates on the opposite wall of the jet to pull the air out of the chamber. This push-pull system is important for maintaining a constant pressure in the chamber during experiments, as well as drawing the hot air out of the chamber during heated jet experiments. The exhaust fan has a discharge rate of 166.7 ft^3/s, while the equalizing MUA unit supplies air at a rate ranging from 116.7 ft^3/s – 233.3 ft^3/s. Moreover, for the heated jet experiments, the facility also houses a 470 kW *Chromalox* electric circulation heater which can produce temperatures up to 1000°F at the nozzle exit. More details on the anechoic chamber and jet facility can be found in the work of Tinney *et al.* [227].

2.2 Experimental Equipment

The instrumentation used for the experiments comprises of data acquisition systems, near and far-field pressure sensors and two different PIV systems. During each set of PIV experiments, both near and far-field pressure are simultaneously sampled. The orientation of the near-field array of pressure transducers is slightly modified for each of the experiments conducted.

2.2.1 Data Acquisition

For all data acquisition, three *National Instruments* PXI systems are used in conjunction with *LabView* software. In order to collect near and far-field pressure measurements, a series of PXI cards are used. For near-field pressure, a set of three 8-channel PXI-4472 analog to digital (A/D) cards capture the DC signals. Each channel is capable of a dedicated 100 kHz sampling rate with no cross-talk between channels. These cards have built-in

analog low-pass filters automatically set to half of the sampling frequency to avoid aliasing of the signals, and are 24-bit resolution. An additional series of AC cards are used to collect the far-field pressure data from the microphones.

A separate dedicated *PXI/SCXI* system is used to collect the near-field pressure and perform real-time calculations to be used for closed-loop control. Using *Labview's* real-time capabilities, Fourier transforms are performed on the azimuthal array of near-field pressure sensors and used for feedback in the control schemes. In all cases, the trigger signal from the PIV is split and sampled by each system to ensure pressure and velocity measurements can be properly aligned during post-processing.

While the *PXI* system samples all of the data, it is also responsible for powering the far-field microphones as well as the actuated control system. For control, the output signal is sent from the *PXI* to the actuators via a *PXI* 6733 analog to digital output module. The signal is first sent through an *AA Labs* amplifier (20X amplification). Further details on the actuation system will be discussed in the next chapter.

2.2.2 Near-field *Kulite* Pressure Transducers

In order to measure the near-field pressure in the hydrodynamic region of the jet, a series of high temperature miniature pressure transducers are used. These *Kulite* XCE-093-5G series transducers are robust and their small size and fast response makes them ideal for the measurements of interest. The sensors can operate between $-65^{\circ}F$ and $525^{\circ}F$, with a gage pressure range of 5 psi and a sensitivity of 20 mV/psi. The *Kulites* are 0.095 inches in diameter and are powered by *Endevco 136* three-channel signal conditioners. These power supplies output a 10 volt DC excitation with a differential-voltage amplification.

For the various experiments conducted, the *Kulites* are arranged in a combination of linear and azimuthal arrays, supported by a pressure ring. The pressure ring contains arms which hold the sensors and is configured for an azimuthal arrangement of five, nine or

fifteen sensors. In addition, each of the arms can house up to six sensors in the streamwise direction for a linear array. In both configurations, the sensors are placed approximately 1 *cm* outside of the expanding shear layer to measure the hydrodynamic pressure. For each of the experiments conducted, a different *Kulite* configuration was used and can be seen in Figure 2.4. A new pressure ring was manufactured following the 2011 TRPIV experiments, in order to make the arms more rigid.

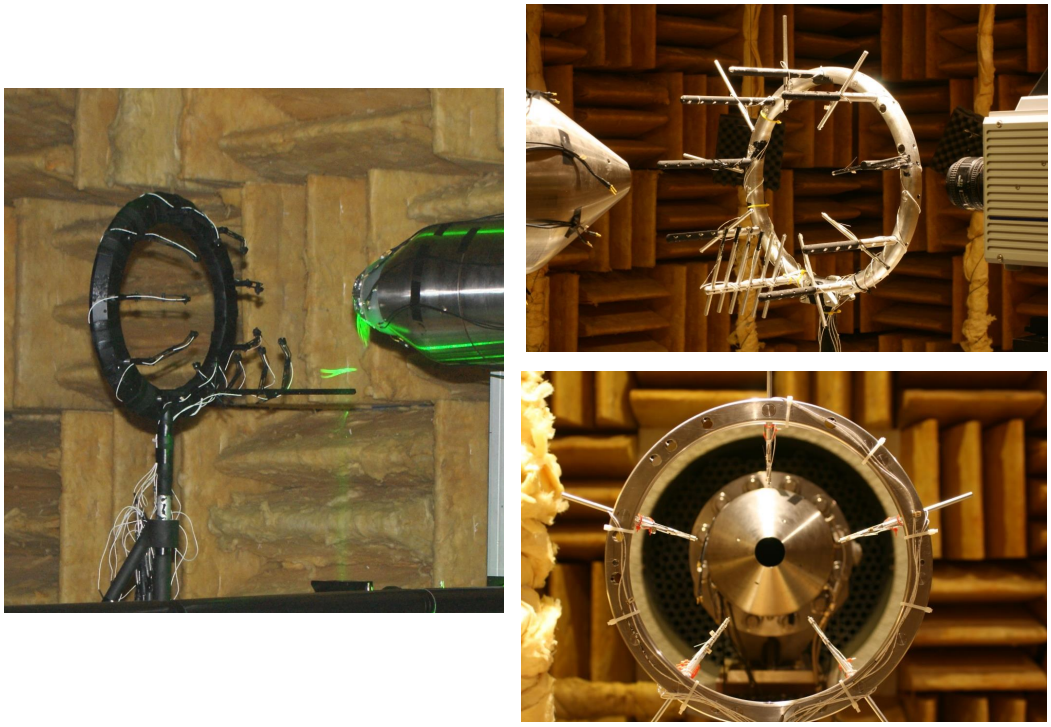

Figure 2.4: Near-field pressure ring for the 2011 TRPIV experiments (left), 2013 TRPIV experiments (top right), 2013 LWPIV experiments (bottom right)

Regardless of the *Kulite* configuration, each of the experiments contains an azimuthal array located at $x/D = 6$. These sensors are used for feedback to the closed-loop controller. The reasoning for this particular location for feedback to the controller relies on the fact that the potential core of the jet collapses at approximately 6D, leading to the largest sources of far-field noise production.

2.2.3 Far-field G.R.A.S. Microphones

For far-field acoustic measurements, a series of 1/4 inch pre-polarized free-field condenser microphones are used. These microphones are manufactured by *G.R.A.S.* sound and vibration, and they are Type *40BE*. This particular class of microphone exhibits a flat response in the frequency domain of ± 1 dB for 10 Hz to 40 kHz, ± 2 dB for 4 Hz to 80 kHz and ± 3 dB for 4 Hz to 100 kHz. These microphones operate as capacitors which ultimately convert acoustic energy to electric energy. In addition, a permanent voltage is supplied across the capacitor, such that an external power supply is not needed. Free-field microphones, such as the ones used in these experiments, are ideal for measurements being conducted in an atmosphere with no reflections, such as the anechoic chamber. The dynamic range of these *G.R.A.S.* microphones is 166 dB with a thermal noise floor of 30 dB. The reference pressure is 20 μPa and the sensitivity is 4 mV/Pa. Each microphone is powered through the *PXI* and utilizes a *G.R.A.S.* Type *26CB* preamplifier. For each set of experiments conducted, the microphone sensitivities are calibrated using a *G.R.A.S. Type 42AB* Pistonphone source, to account for environmental and hardware drift. The calibrator outputs a constant 1 kHz sine wave at 114 dB.

There are a total of twelve microphones arranged in an arc configuration with respect to the jet. There are two arrays each comprised of six microphones. The first array of microphones is oriented in the horizontal plane of the jet and the second array is offset by 15° out of plane with respect to the jet. For each array, the microphones are spaced evenly from 15° to 90° with respect to the jet axis, in increments of 15°. All microphones are located 75D downstream of the nozzle lip to ensure true far-field measurements. The microphone configuration can be seen in Figure 2.5 and the top view with respect to the jet can be seen in Figure 1.13.

As seen in Figure 2.5, additional acoustic treatment has been placed behind each microphone in order to mitigate low frequency acoustic reflections from the walls of the chamber.

Figure 2.5: Microphone array within the Syracuse University anechoic chamber

The first set of TRPIV experiments conducted (2011) contained six microphones in plane with the jet. For the LWPIV and later TRPIV experiments (2013), the additional six out of plane microphones were added. The additional microphones provide a three-dimensional acoustic observance field, which will be a crucial aspect of noise source identification techniques. Moreover, the added plane of microphones doubles the amount of observers used in reduced-order modeling schemes to be discussed.

2.2.4 Particle Image Velocimetry Systems

Both LWPIV and TRPIV are used in separate experiments to obtain two-component velocity measurements in the streamwise plane of the jet. The LWPIV experiments were conducted to observe the effects of the open and closed-loop flow control, having a large view of the overall flow field. Two sets of TRPIV experiments were conducted, to observe

the time-dependent nature of the uncontrolled jet at different Mach numbers, to observe the effects of open-loop forcing (2011), and to study the effects of open-loop and real-time closed-loop flow control (2013).

Dantec Dynamics Flow Manager software and *LaVision's DaVis* software are used to process the LWPIV and TRPIV data sets, respectively. The PIV snapshots are processed using single-image, dual-frame cross-correlation techniques. Adaptive correlations are used with decreasing interrogation areas such that the final window size is 32×32 pixels with a *50%* overlap. A single level, two-component calibration target is used to compute a scale factor relating the pixels to the physical distance between particles. The uncertainty associated with the PIV measurements can be found in Appendix A.

Large-Window PIV Experimental Setup

For the LWPIV measurements, a (15 Hz) *Dantec Dynamics* PIV system is used. The system consists of three 12-bit, 1 megapixel *HiSense* cameras and a *New Wave Gemini* Neodym-YAG (Nd:YAG) laser with a peak output of 200 mJ/pulse. Measurements are taken along the centerline of the jet. The three cameras are placed side by side with a slight overlap in order to obtain a larger interrogation region of approximately three to nine diameters in the streamwise direction. The experimental setup can be found in Figure 2.6.

As shown in Figure 2.4, the *Kulite* configuration for this set of experiments encompasses two azimuthal arrays, each containing five evenly spaced sensors at 6D and 8D downstream from the nozzle lip. These locations are chosen to sample the hydrodynamic pressure near the collapse of the potential core, and immediately after. The sensors located at 6D are used in the closed-loop control feedback loop.

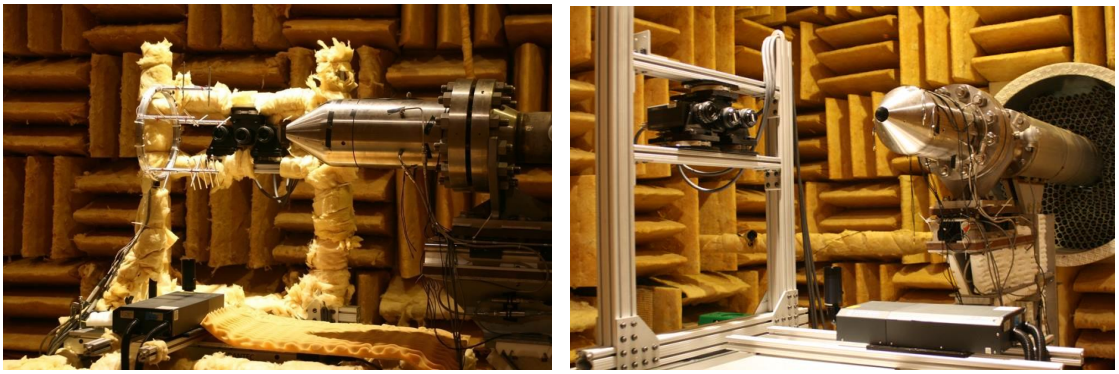

Figure 2.6: 2013 Large-Window PIV experimental setup

Time-Resolved PIV Experimental Setup

For the TRPIV measurements, a 10 kHz system is provided by *Spectral Energies, LLC.*. The system includes a *Photron* FASTCAM CCD camera and a *Quantronix Hawk-Duo* series high energy, diode-pumped Nd:YAG laser ($\lambda = 532nm$) with a peak output of 12 mJ (4 mJ per pulse). Since the laser and chiller/power supply are significantly larger than a standard PIV system, the chiller/power supply is placed outside of the chamber (see Figure 2.7). This unit is approximately 19 x 20 x 28 inches in size and weighs about 204 lbs. The cables are therefore connected to the rest of the system via a small access hole between the anechoic chamber and the adjoining control room. The laser is stationed on a table in the chamber next to the jet rig (see Figure 2.7). In order to reach the measurement plane of interest, the laser beam was redirected using a series of optical mirrors placed on the jet rig's primary measurement table. The laser sheet optics and camera system are therefore mounted on a traverse system such that several downstream locations may be obtained and re-calibration between tests is not needed. As the camera and laser are traversed, the near-field pressure ring remains stationary. The configuration for the 2011 TRPIV experiments is shown in Figure 2.8.

In this set of experiments, the near-field pressure ring is placed at 6D downstream of

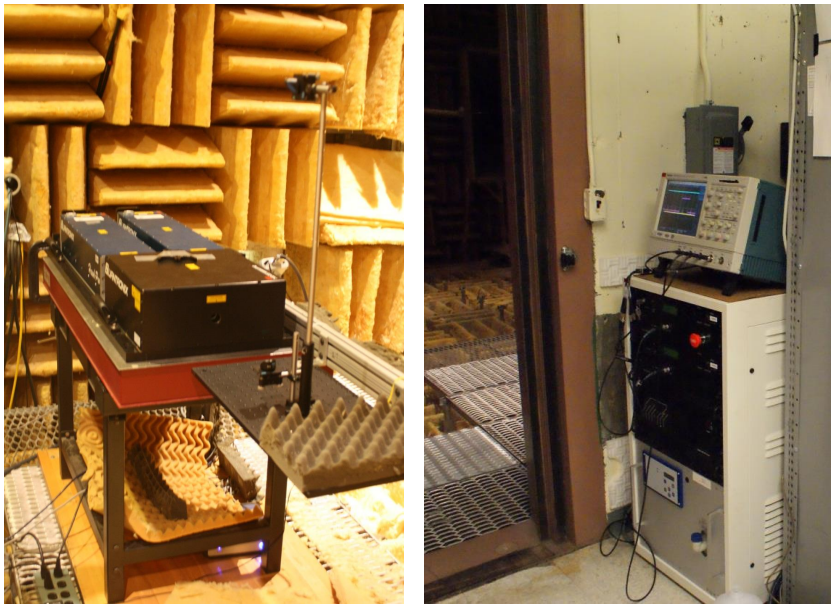

Figure 2.7: 2011 Time-Resolved PIV laser and chiller

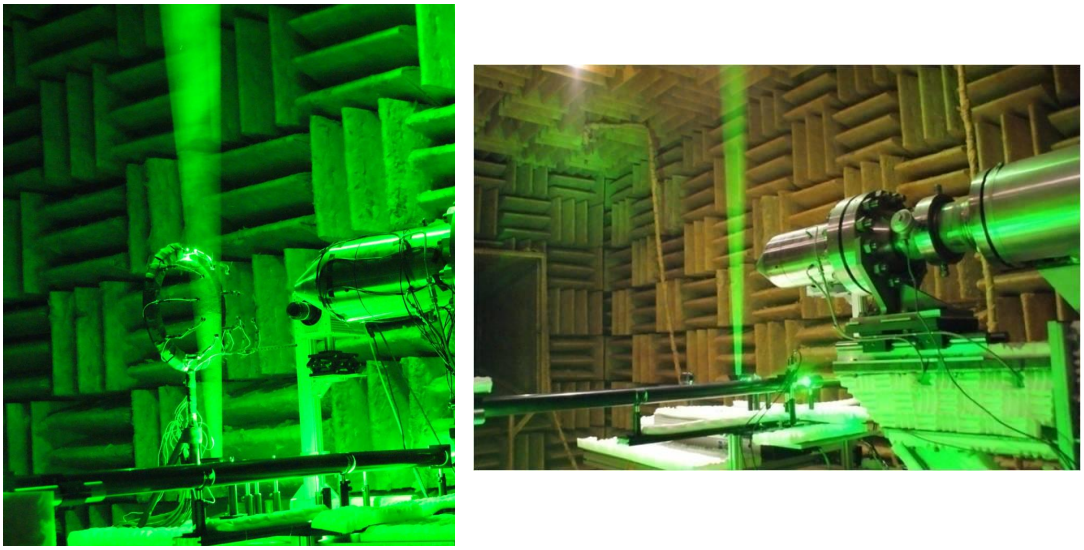

Figure 2.8: 2011 Time-Resolved PIV experimental setup

the nozzle exit. There are two arrays, one azimuthal containing nine sensors, and one linear containing five sensors. The sensors in the linear array are positioned from x/D = 4-8, with

a 1D spacing. The sensor at 6D is also part of the azimuthal array, accounting for thirteen total sensors (see Figure 2.4). The setup for the 2013 TRPIV experiments (see Figure 2.9) is the same as that of the 2011 experiments with the exception of the orientation of the linear *Kulite* array. Since the pressure ring was changed, the configuration of the linear array in the 2013 experiments has sensors positioned from x/D = 4-6.5, with a 0.5D spacing. Once again the sensor at 6D is also part of the azimuthal array and therefore there a total of fourteen sensors.

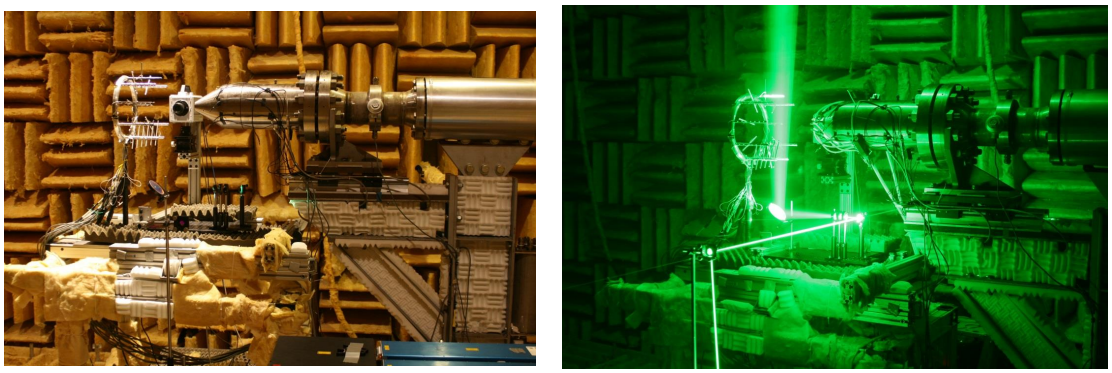

Figure 2.9: 2013 Time-Resolved PIV experimental setup

The newer pressure ring has its advantages and disadvantages related to the experimental setup. The new pressure ring is more rigid and therefore the placement of sensors is more precise. However, due to the new design of the *Kulite* arms, it is not possible to take PIV measurements beyond 6D, as with the 2011 experiments. Despite this drawback, all other downstream locations are still obtained in the 2013 experiments.

Flow Seeding

In order to seed the flow field, both the bulk flow of the jet as well as the co-flow must be seeded so as to ensure uniform particle distribution. For the bulk jet flow, a *PIVTEC*-twelve Laskin nozzle is used in order to overcome the back pressure experienced in the jet

piping ($\sim 10bar$). The Laskin nozzle aerosolizes extra virgin olive oil using compressed air drawn from the small *Kaiser* compressor. The particle size of the aerosolized olive oil is $\mathcal{O}(1\ \mu\text{m})$, which has been shown by Melling (1997) [51] to be the optimal size for laser-based measurements. The pressure of the Laskin nozzle was adjusted based on the Mach number of the jet to ensure a sufficient amount of seeding. In order to seed the co-flow, a commercial *'show fogger'* is used to fill the plenum chamber. This provides a uniform distribution of particles throughout the entrainment region of the jet, and was again adjusted based on the Mach number of the jet. These seeding units are seen in Figure 2.10.

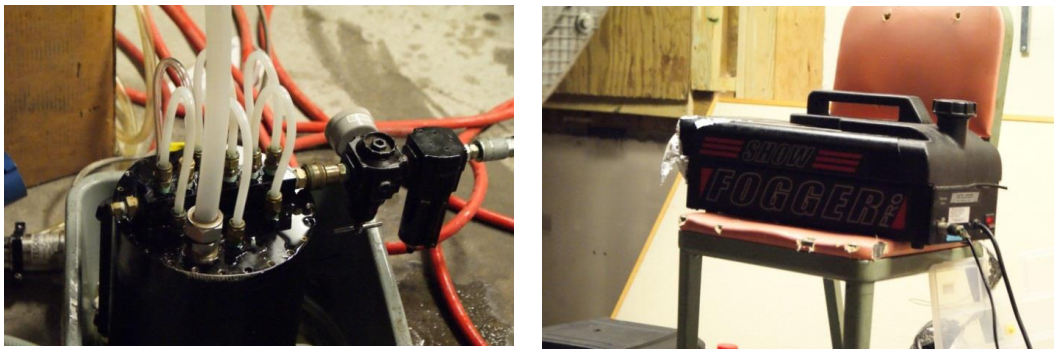

Figure 2.10: Laskin nozzle (left) and 'show fogger' (right) used for PIV seeding

2.3 Data Processing

Due to the large amount of pressure and velocity data acquired for all of the experiments conducted, it would be quite difficult to process, manage and organize the results with conventional methods. To assist with the data processing and management, a code has been developed by Christopher Ruscher at Syracuse University (2014) [194]. This code, known as *Orange High Speed Data (HSD)*, is operated using *Matlab* controlled with a graphical user interface (GUI). This GUI is shown in Figure 2.11 for reference. This code has been used extensively to format, process, organize, and analyze the data, to be presented.

Specifically, *Orange HSD* has been used to perform much of the POD and create the movies associated with the time-resolved data sets. The code solves the POD problem such that the large data sets acquired here may be processed efficiently. A cautionary note to the reader is that while *Orange HSD* is a very powerful processing tool, the analysis and interpretation of the results are left to the user. For more details regarding the inner workings of the code, please refer to the work of Ruscher [194].

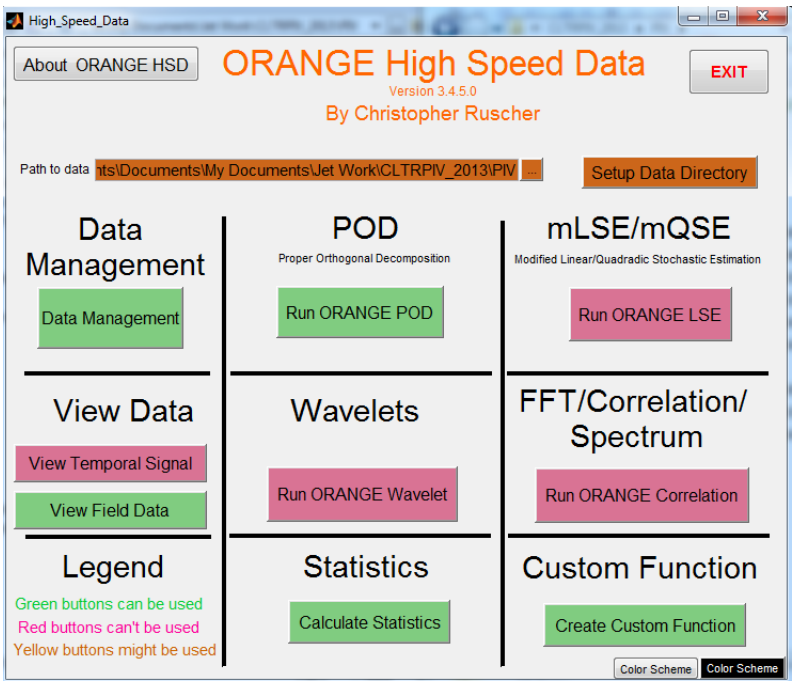

Figure 2.11: GUI for the *Orange HSD* processing tool, Ruscher (2014) [194]

Chapter 3

Flow Control Strategies

The manipulation of a fluid flow for practical applications is an integral aspect of improving a system based on design parameters and performance, in the fluid mechanics community and beyond. Flow control involves altering a flow field based on specific control objectives, such as system performance. Flow control has been explored extensively in the context of free and bounded shear flows, airfoils, and three-dimensional bluff bodies, to name a few examples. In addition, flow control has been at the forefront of jet noise studies since the first jet engines.

Over the past ten years at Syracuse University, many experiments have been conducted to demonstrate the effectiveness of flow control at both a fundamental as well as applicable level. Ausseur *et al.* (2004-2006) [17–20], Ausseur & Pinier (2005) [16] and Pinier *et al.* (2007) [183] were able to reattach the separated flow over a *NACA 4412* airfoil using closed-loop flow control. Later, Andino *et al.* (2008,2011) [10, 11, 13], Wallace *et al.* (2008-2012) [237, 244–249], Andino & Glauser (2010) [12], Shea *et al.* (2012) [210] and Shea & Glauser (2012,2013) [208, 209] showed a reduction in the flow separation over a non-conformal three-dimensional turret. More recently, Wang *et al.* (2013) [251] minimized the load fluctuations on an airfoil section used for wind turbine applications. In all of these cases open and closed-loop control is implemented with blowing and/or suction

at the surface of the body. The concept of flow control has been recently applied for jet noise reduction by Low *et al.* (2013) [149], using synthetic jet actuators.

There are two main types of flow control, passive and active flow control, each having their advantages and disadvantages depending on the system of interest and desired control objectives. In addition, there are two types of active flow control, open-loop and closed-loop flow control. All forms of flow control have been applied to the jet noise problem over the past sixty years. The control objectives for the jet noise problem have included enhancing mixing, thrust vectoring, and far-field noise reduction, which is the focus of the current investigation.

3.1 Passive Flow Control

Passive flow control is a form of flow control in which a system is altered geometrically in order to change the overall performance based on some sort of control objective. Since passive control is characterized by geometric modifications, it has served as an attractive form of flow control, as it does not require any energy input to the system.

Looking specifically at jet noise reduction, passive control has been studied since the development of jet engines, where the initial focus was aimed at improving propulsive efficiency. As engines within commercial aircrafts continued to grow, the design was shifted to high bypass ratio engines, with two goals in mind. First, this design aims to improve fuel economy, a growing concern in the industry. The second goal is to have the engine generate a large amount of thrust with reduced exit velocities. This is achieved by increasing the inlet air and fan area, through a bypass (secondary air stream), in order to maximize the mass intake while minimizing the primary stream of air. The reduction in exit velocity will greatly reduce the noise since sound intensity, $I(\vec{x})$, is proportional to the 8^{th} power of velocity. This is shown from a similarity analysis for the emitted sound as proposed by Lighthill's analogy [127, 139]. The sound intensity equation is as follows,

$$I(\vec{x}) = \rho_0 \frac{U^8}{c_0^2} \left(\frac{L}{x} \right)^2 \tag{3.1}$$

where c_0 is the speed of sound, L is the characteristic length and x is the distance from source to observer. Therefore, even a small reduction in exhaust velocity results in a significant reduction in sound intensity. The trade off with the high bypass ratio is that the engines need to be larger and therefore heavier, causing increased drag and loading on the aircraft. For this reason, additional strategies must be explored.

Another method for passive control on commercial aircrafts for jet noise reduction is the concept of chevrons. Chevrons are triangular-shaped serrations arranged azimuthally around the nozzle exit to induce counter-rotating streamwise vorticity. This process shortens the potential core by enhancing the mixing process. Moreover, chevrons also reduce the large pressure fluctuations leading to the far-field noise (Bargsten (2011) [23]). The chevrons themselves can have different lengths and angles with respect to the jet exit, depending on the size of the nozzle, Mach number of interest and various other parameters. Studies have shown that chevrons provide the best trade off in terms of thrust loss versus noise reduction [23]. Some of these designs from NASA can be seen in Figure 3.1.

The NASA research team conducted tests showing that the asymmetrical engine nozzle chevron design on a *General Electric (GE)* engine helped to reduce noise both inside and outside of the aircraft [22]. An image of this engine with the chevrons can be seen in Figure 3.2.

Many aeroacoustic researchers in the community have studied the benefits of chevrons, especially within the last ten years including, Bridges & Brown (2004) [36], Brown & Bridges (2003,2006) [37, 38], Mengle (2005) [152], Callender *et al.* (2005) [43], Mengle *et al.* (2006) [153], Tinney *et al.* (2006) [226] and Alkislar *et al.* (2007) [9]. It has been shown by these researchers that chevrons reduce the far-field noise only in the low frequency band, and increase the noise in the high frequency band. In addition, since

Figure 3.1: NASA noise suppression nozzles from the Advanced Subsonic Technology Program, (2011) [23]

chevrons are a permanent geometrical modification to the nozzle, they cannot be turned off during cruise, for example, when they are not needed. For these reasons, a different form of flow control which can be turned on and off for efficiency purposes, and reduces noise across the entire frequency band, is desired within the community. In order to address these issues, the focus is shifted to active flow control.

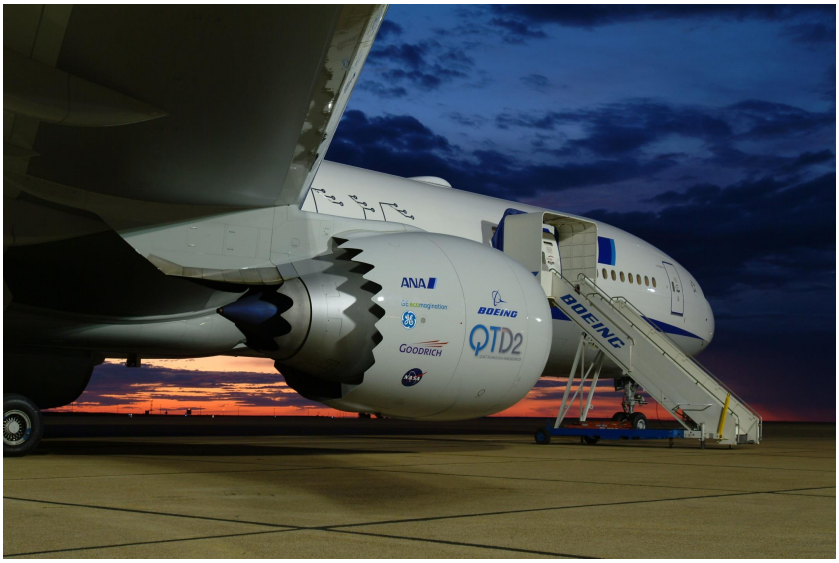

Figure 3.2: NASA chevron design on GE engine for noise reduction, Banke (2009) [22]

3.2 Active Flow Control

Active flow control is characterized by an energy input into the system to alter the flow properties. Active flow control can be more desirable than passive methods in some applications where a permanent geometry change is not wanted or needed. For open-loop control, some energy input often in the form of actuation, is provided to the system without any knowledge of the flow physics. In some cases, the complexity of the flow field warrants a control scheme that gains intelligence from the system for the control objective, and this is known as closed-loop control. Each strategy has its own advantages and disadvantages based on the problem at hand.

3.2.1 Open-Loop Flow Control

While passive methods for flow control applied to jet noise have been extensively studied over the years, open-loop control has also been an area of interest since the first jet engines. Open-loop control is an attractive flow control option due to its robustness and

ability to be turned on and off for different applications. The first recorded experiment regarding open-loop flow control for jet noise reduction is that of Kurbjun (1958) [126]. In these experiments, water was injected into the exhaust of an after-burning jet engine (see Figure 3.3).

Figure 3.3: Fluidic injection experiments by Kurbjun (1958) [126], taken from Henderson (2009) [104]

Kurbjun found a reduction in the far-field noise at the low frequencies and a 6 dB reduction in the overall sound pressure level at the peak jet noise direction. Following this work, Lilley (1961) developed a similar fluidic injection strategy for jet noise reduction [142]. The work of Kurbjun and Lilley inspired much of the recent open-loop flow control work involving fluidic injection. This body of work is highlighted by Henderson (2009) in "Fifty years of fluidic injection for jet noise reduction" [108].

The next big advancement in fluidic injection for jet noise reduction after Kurbjun and Lilley, has been observed within the last ten or so years. The development of simple fluidic injection designs led to microjets, characterized by azimuthally distributed injection of fluid into the bulk jet flow. The use of microjets, with water as the injection fluid, was

pioneered by those such as Krothapalli *et al.* (2003) [125], Norum (2004) [171] and Greska *et al.* (2005) [87]. Water injection reduces the jet velocity through momentum transfer and modification of the turbulence. It has been shown to be more effective at reducing the noise in cold jets [104].

Many researchers also began to use air as the working fluid in microjet actuation. In this configuration, the microjets are arranged and pulsed so as to mimic the counter-rotating streamwise vorticity produced by chevrons. In addition, researchers also began to combine chevrons with fluid injection. This strategy became known as fluidic chevrons, or is sometimes referred to as "fluidevrons". Fluidic chevrons for jet noise reduction have been studied by Araleri *et al.* (2003) [14], Henderson *et al.* (2005,2006) [105, 106], Laurendeau *et al.* (2005,2006,2008) [132–134], Alkislar *et al.* (2007) [9], Petitjean *et al.* (2007) [177], Henderson & Norum (2008) [107], Papamoschou *et al.* (2009) [175] and Maury *et al.* (2011) [151]. In general, this technique shows reductions in the low frequency noise.

Alkislar *et al.* (2007) in particular, studied the differences between microjets and chevrons with respect to streamwise vorticity and the effects on the noise in a Mach 0.9 jet. Looking at the axial vortex displacement in Figure 3.4, the chevrons seem to cause more disorganization in the streamwise vortices.

This is also seen in the spatial evolution of the velocity field as shown in Figure 3.5. The microjets and chevrons produce counter-rotating vortices as expected, and those produced by the microjets are more compact with larger spacing between pairs, as compared to the chevrons.

Alkislar *et al.* also looked at the effect of the different open-loop control strategies on the far-field noise (see Figure 3.6). Both the microjets and the chevrons show a noticeable reduction in the sound pressure level (SPL) at the lower frequencies. The chevrons show a better improvement below St = 0.5, however the microjets exhibit a more broadband reduction. The chevrons make the jet substantially louder above St = 1.0, while the microjets

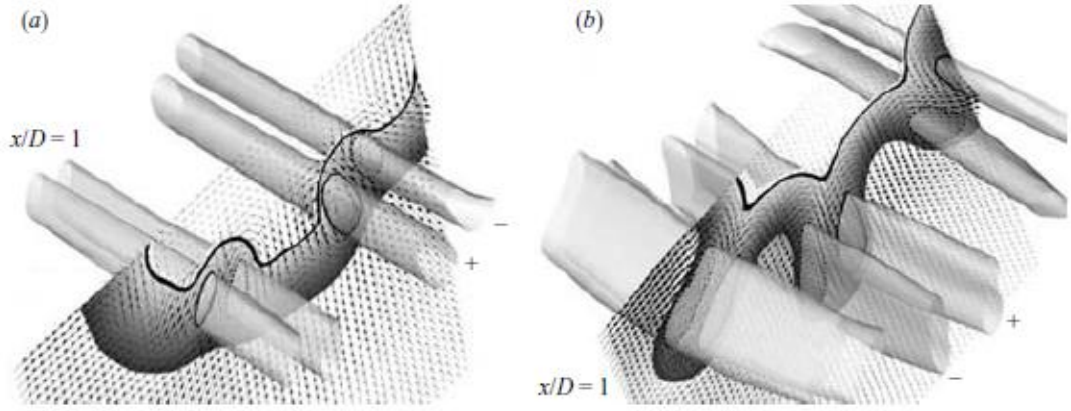

Figure 3.4: Axial vortex displacement for (a) microjets and (b) chevrons, Alkislar *et al.* (2007) [9]

have a lower SPL out to St = 3.0.

The work of Laurendeau *et al.* (2005,2008) [133, 134] also compared microjets to chevrons, showing that chevrons shorten the potential core length by enhancing mixing, while microjets tend to reduce the mixing which extends the potential core length. In these experiments, Laurendeau *et al.* used sixteen microjets to form eighteen equidistantly spaced fluidic chevrons (as seen in Figure 3.7). These results show approximately a 2 dB reduction in the SPL at 90°, using the fluidic chevrons. Reductions of this sort are also seen at shallow polar angles with respect to the jet axis. This reduction is fairly broadband out to approximately St = 5.0, where the control then increases the SPL in the far-field.

Similar studies were conducted by Henderson & Norum (2008) [107], looking specifically at fluidic chevrons with various flow conditions. They found that with a specific injection configuration, the dominant shock noise could be significantly reduced. Several nozzle pressure ratios (NPR), observation angles and mass flow rates were investigated and the effectiveness of the fluid chevrons can be seen in Figure 3.8.

More recently, the concepts of fluid injection and fluidic inserts for supersonic jet noise applications have been explored by researchers such as Kastner *et al.* (2012) [120], Morris

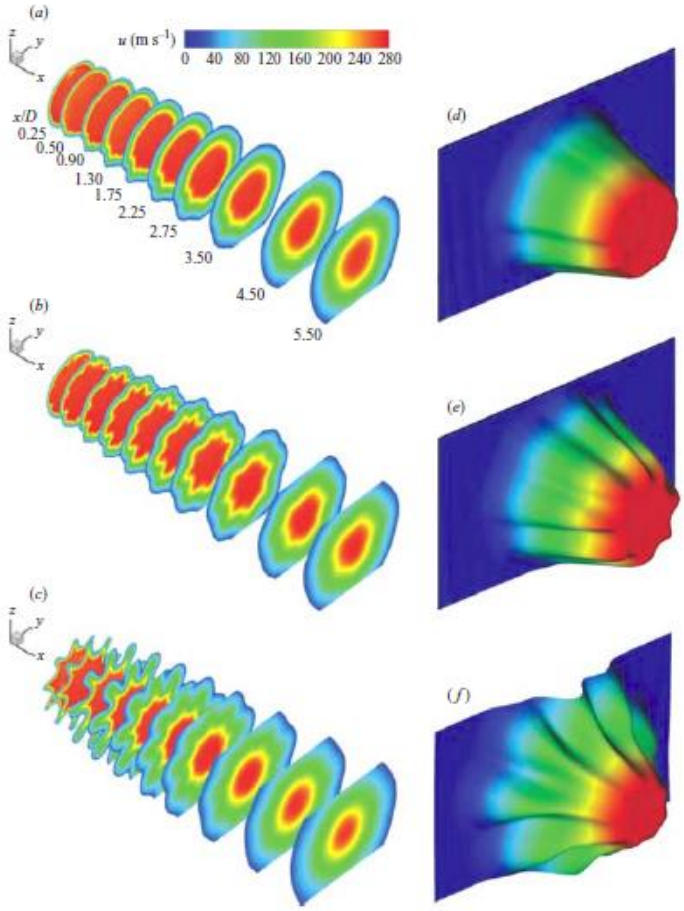

Figure 3.5: The three-dimensional spatial evolution of the jets (a) base (b) microjet (c) chevron and the velocity profiles at x/d = 2: (d) base (e) microjet (f) chevron, Alkislar *et al.* (2007) [9]

et al. (2013) [163], Cuppoletti *et al.* (2014) [57] and Pilon *et al.* (2014) [181]. Much of this work is inspired by the corrugated seal inserts on the *F404-400* engines designed by Seiner *et al.* (2005) [205]. The work of Kastner *et al.* [120] shows a noticeable reduction in the overall sound pressure level across all microphone locations using Fluidically Enhanced Chevrons (FEC) and Baseline Fluidic Injection (BFI). Both methods show a significant improvement over chevrons alone, as seen in Figure 3.9.

Morris *et al.* [163] investigated the differences between hard-wall corrugations and fluidic inserts as compared to the uncontrolled jet. Examining the directivity of the overall

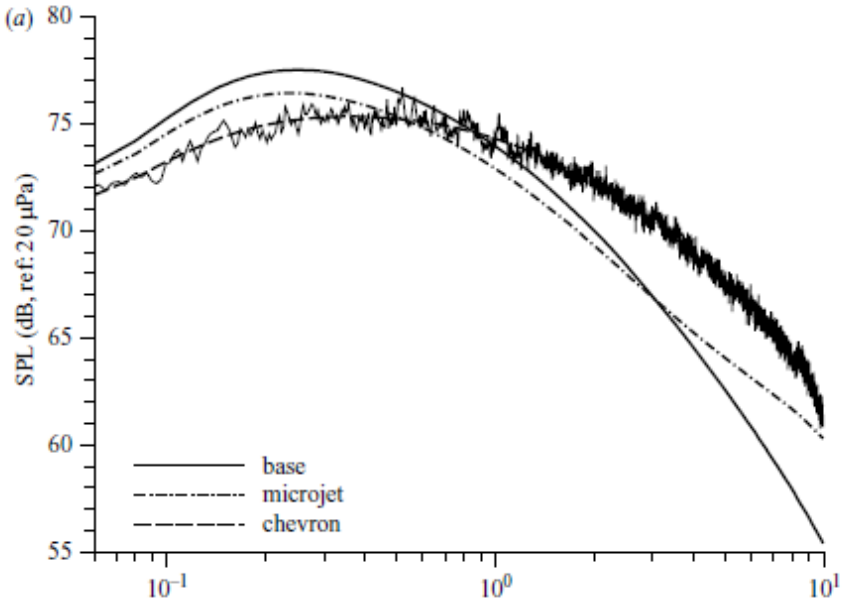

Figure 3.6: The SPL spectra at nozzle inlet angle of 90°, Alkislar *et al.* (2007) [9]

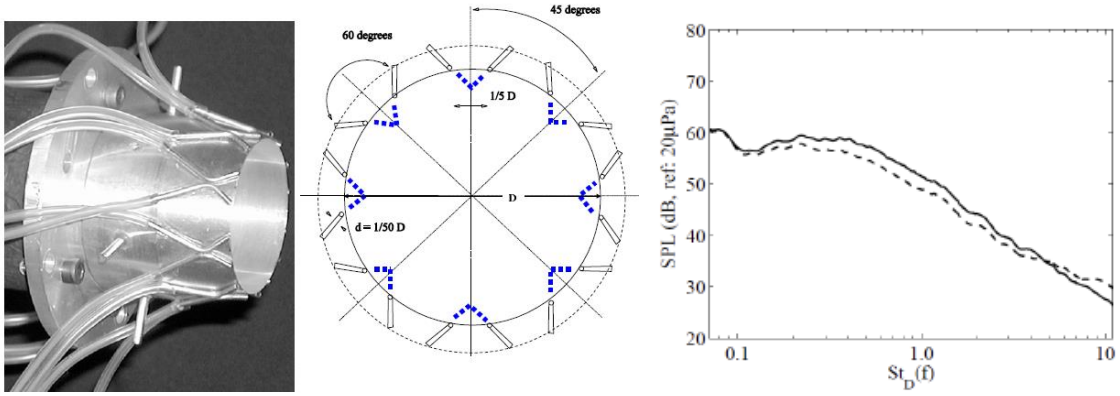

Figure 3.7: Fluidic chevron configuration: control (- -) vs. no control (–), Laurendeau *et al.* (2005,2008) [133, 134]

sound pressure levels, the two different control methods exhibit similar trends, both reducing the noise as compared to the uncontrolled jet (see Figure 3.10). Following up on this work, Pilon *et al.* [181] showed reductions in the SPL across most of the frequency band,

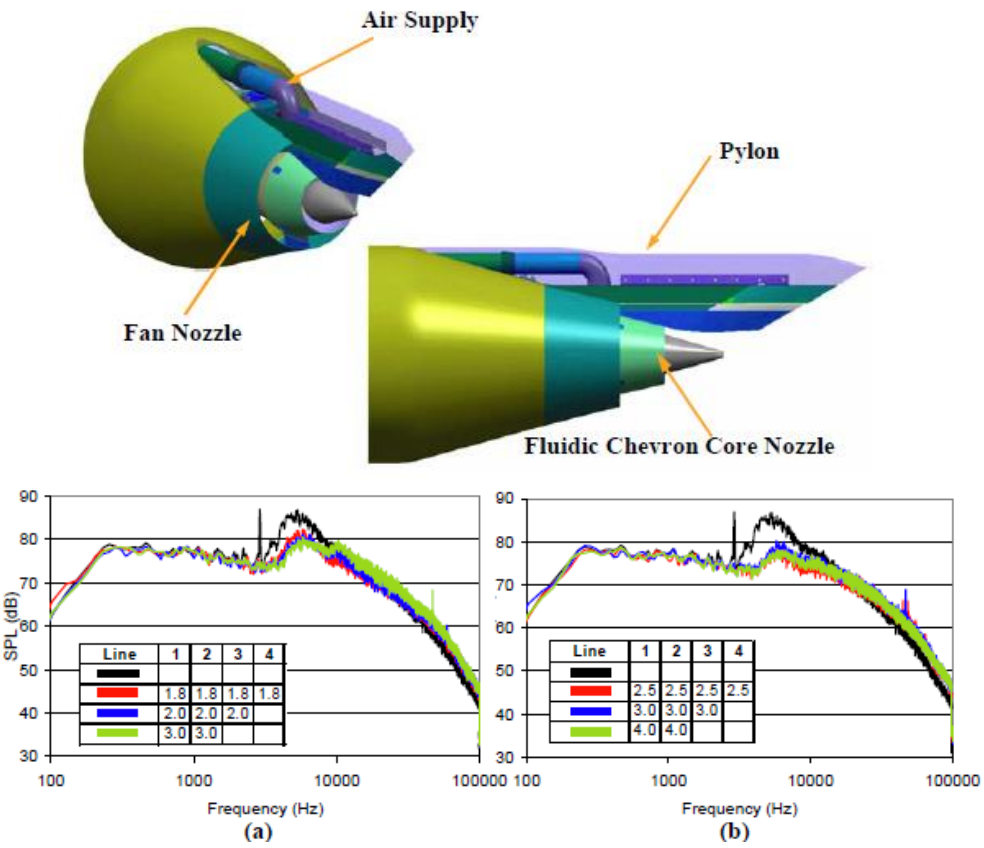

Figure 3.8: SPL for the fluidic chevron experiments with NPR = 2.18, observation angle = 61°, and injection mass flow rate of (a) 0.7% and (b) 1.2% of the core flow, Henderson & Norum (2008) [107]

at several polar angles, using deflected seal inserts (seen in Figure 3.11). It was shown that the broadband shock associated noise is decreased by approximately 8 dB, with the penalty of an increased overall peak frequency.

The mass injection actuation systems have proven to be effective however the downside lies in the additional fluid and tubing needed in a real system. The microjets and fluidic chevrons have nonetheless provided the community with some valuable insight into control strategies for jet noise reduction. Recent advances in the form of fluidic inserts and corrugated seals show much promise in reducing jet noise on a real system.

Another type of flow control used for jet noise studies involves plasma actuators primar-

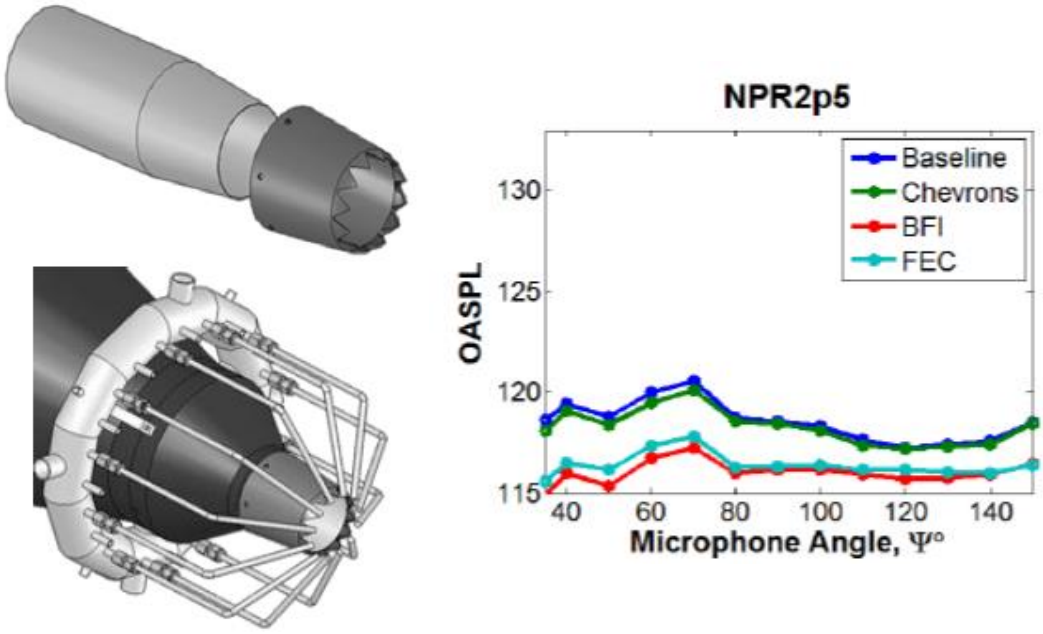

Figure 3.9: Overall sound pressure levels for the baseline, chevron, FEC and BFI configurations, Kastner *et al.* (2012) [120]

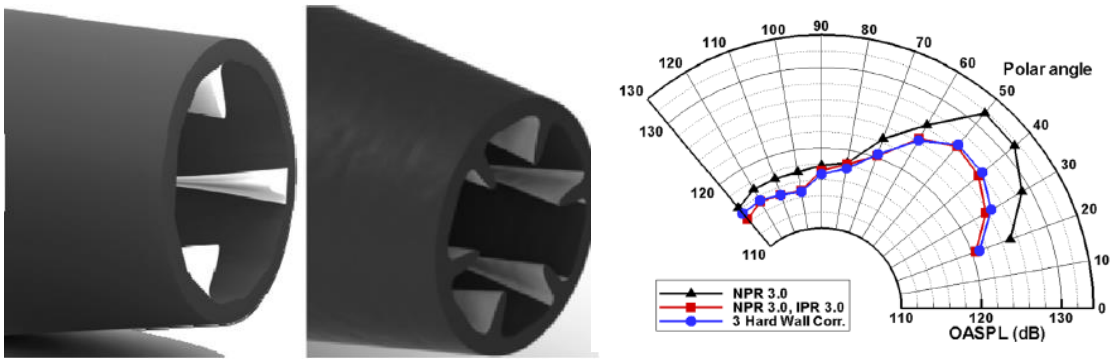

Figure 3.10: Overall sound pressure level directivity for baseline (black), fluidic inserts (red) and hard-wall corrugations (blue), Morris *et al.* (2013) [163]

ily studied by Samimy *et al.* (2004-2007,2010,2011) [196–201], Fischer & Samimy (2010) [75] and Gaitonde & Samimy (2010) [76]. These localized arc filament plasma actuators (LAFPA) have been used to excite various instabilities in the shear layer via a thermally driven process. These devices allow for high voltage actuation to excite frequencies as

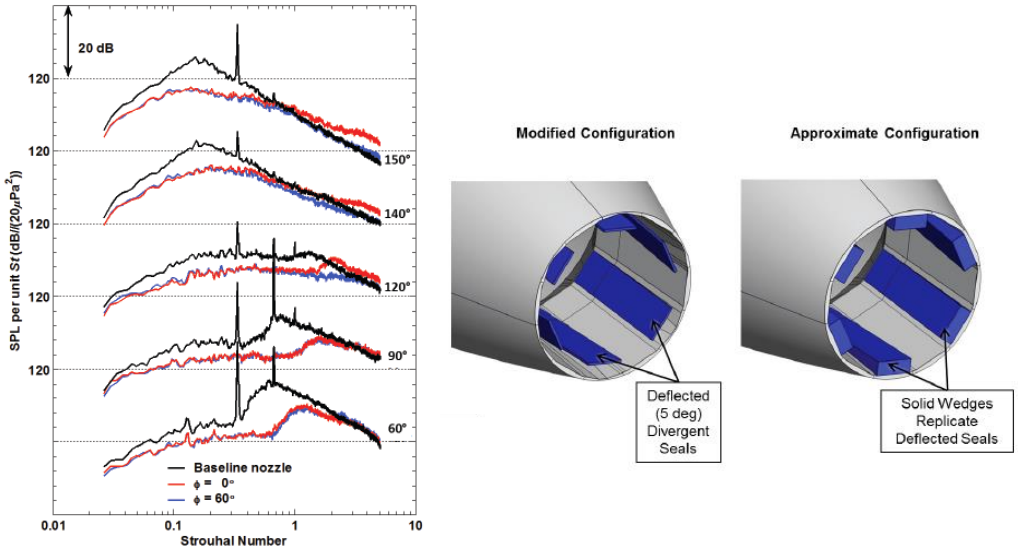

Figure 3.11: Far field acoustic power spectral densities for the baseline and Gen1B 3DS10 nozzle from cold jets with NPR = 3.3, M_j = 1.43, TTR = 1, scaled R/D = 100, Pilon *et al.* (2014) [181]

high as 200 kHz at up to 10 kV. Samimy *et al.* (2007) [201] used eight LAFPA's arranged azimuthally around the jet's periphery to excite various instabilities. This was done for a Mach 0.9 jet by exciting various azimuthal and mixed azimuthal modes (m = 0, 1, $\pm$1, 2, $\pm$2, 3 and $\pm$4). The LAFPA are driven over a range of actuator Strouhal numbers, scaling with the jet's preferred instability as well as the shear layer instability. A noise increase of $\mathcal{O}$(3 dB) was seen when actuating near the jet's preferred mode (St = 0.36), however a slight reduction in noise, $\mathcal{O}$(1 dB), was seen at the 30° microphone, when actuating closer to shear layer instabilities (St = 1.07). Similar reductions are seen at the 90° microphone for much higher frequency actuation (St = 3.0 - 3.5). The LAFPA system and results for the St = 1.07 forcing can be seen in Figure 3.12. Although promising results are seen with this type of actuation, the high-voltage power required to operate the LAFPAs is somewhat unrealistic for practical applications at this time.

The last type of actuation used for open-loop flow control is synthetic jet actuation,

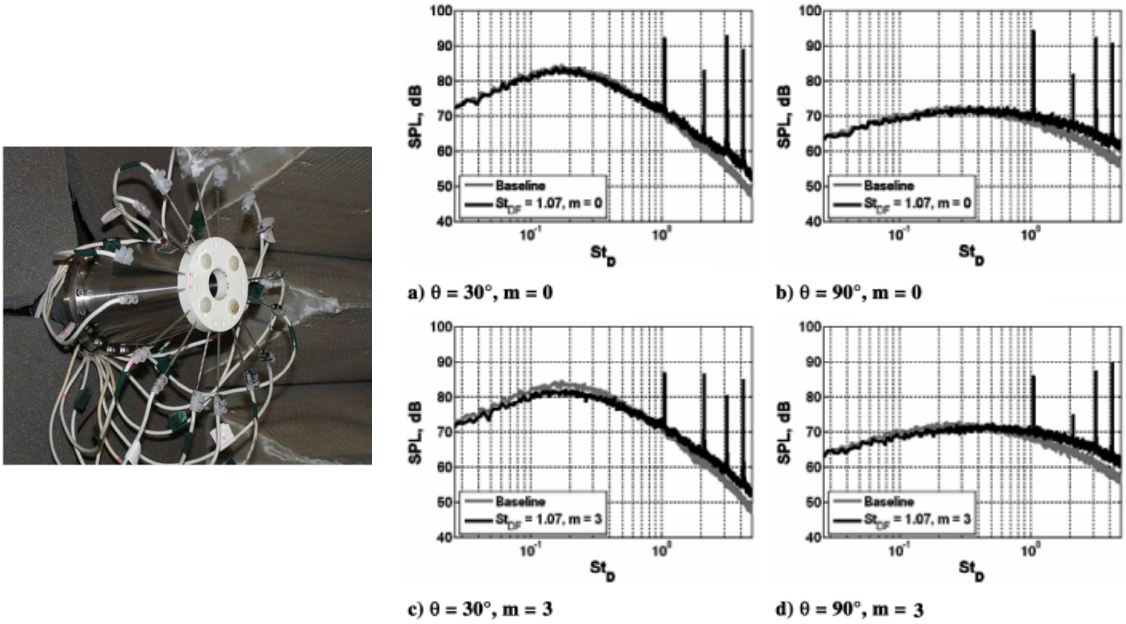

Figure 3.12: LAFPA system, Samimy (2014) [195] and far-field acoustic power spectra at 30° and 90° for shear layer excitation (St = 1.07) with two different azimuthal modes (m = 0 and 3), Samimy *et al.* (2007) [201]

which is the focus of the current investigation. These actuators will be discussed in detail in § 3.3.

3.2.2 Closed-Loop Flow Control

Closed-loop control is a type of active flow control that fuses the actuation system with intelligence from the overall system. In order to do so, sensors are used to feed back information to the actuators in real time. Therefore as the dynamics of the flow change in real time, the actuation also changes to achieve the desired control objective(s). There has been a significant amount of closed-loop control research conducted at Syracuse University related to three dimensional turrets (Wallace *et al.* (2008,2010-2012) [245–249], Vaithinathan *et al.* (2010,2012) [236, 237] and Andino *et al.* (2011) [13]), wind turbine

airfoil sections (Wang *et al.* (2013) [251]) and jet noise reduction (Low *et al.* (2013) [149]).

In addition to the work conducted by Low *et al.* (2013) [149], Sinha *et al.* (2010,2011) [212, 213] explored closed-loop control for jet noise applications using LAFPA technology discussed in the previous section. They have explored a model free extremum seeking feedback controller for their experiments. Sinha *et al.* developed two different feedback control algorithms which modified existing extremum seeking techniques [212]. The modified Nelder-Mead algorithm (mNMA) and modified Kiefer-Wolfwowitz algorithm (mKWA) are used as a simplex based optimization process and more details can be found in Sinha *et al.* [212]. From the experiments conducted, Sinha *et al.* found that the mean square pressure of the irrotational near-field is related to the Reynolds stresses in the mixing layer by a weighting function. In particular, this weighting function is inversely proportional to the wavenumber to the 4^{th} power, showing the near-field pressure acts as a low pass filter of the velocity field.

Aside from the experiments conducted by Sinha *et al.*, closed-loop control for jet noise applications has not been extensively studied by the community. The experiments conducted in the current investigation, involving closed-loop control using synthetic jet actuators, will be discussed in § 3.3.

3.3 Synthetic Jet Actuators

For the actuation system used at Syracuse University, synthetic jet actuators are implemented for both open and closed-loop flow control strategies. A synthetic jet is a flow phenomenon which involves the unsteady suction and blowing of some fluid within a jet's cavity volume through a slot at the exit. The attractive property of synthetic jets is that they only rely on the working fluid of the cavity volume and therefore they are zero-net mass flux, as described by Glezer & Amitay (2002) [84]. The unsteady suction and blowing results in the oscillatory motion of a surface which can be done through acoustically exciting

a cavity, electromagnetically driving a piston, or piezoelectrically driving a membrane. The last strategy is the method used for the Syracuse University experiments.

The oscillatory motion of the piezoelectrically driven membrane creates an oscillatory pressure deficit across the exit slot, resulting in a time-periodic generation of discrete vortices. The result is a miniature jet emitted from the exit slot with a top-hat type velocity profile across the span of the slot. The vortical structures generated by the actuators can be seen in Figure 3.13. One of the most appealing aspects of the synthetic jet actuators is that they do not require any external tubing or working fluid supply. Moreover the synthetic jets have a fairly broadband frequency response making them more attractive than valves, which typically rely on steady blowing or suction. Additionally, these actuators are incredibly inexpensive which makes them ideal for fundamental studies. Moreover, synthetic jets can be scaled up and down for various flow applications as shown by Coe *et al.* (1994,1995) [46, 47] and Muller *et al.* (2001) [165]. The one major downside to the actuators is that they are relatively unreliable, having a high failure rate when operated for long durations or under extreme conditions (i.e. ingesting large amounts of olive oil during PIV experiments). Figure 3.14 shows a schematic of a synthetic jet as well as the evolution of a synthetic jet's flow impinging on a wall (Krishnan & Mohseni (2010) [124]).

As mentioned, the current investigation uses zero-net mass flux piezoelectrically driven synthetic jets, modeled after the designs of Smith & Glezer (1997,1998) [215, 216], Crook *et al.* (1999) [54], and Glezer & Amitay (2002) [84]. Each synthetic jet consists of a piezoelectrically drive membrane, or diaphragm, which is coated with a ceramic composite (brass in this case) that deforms when a voltage is applied to it. This voltage is applied with an oscillatory sinusoidal signal, causing the diaphragm to displace and ultimately leading to unsteady blowing and suction through the exit. One of these piezoelectric disks can be seen in Figure 3.15.

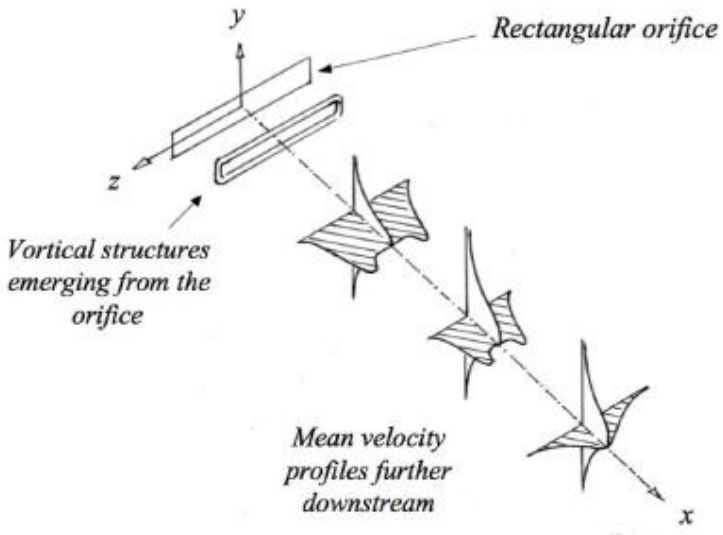

Figure 3.13: Illustration of vortical structures generated by synthetic jet actuators [148]

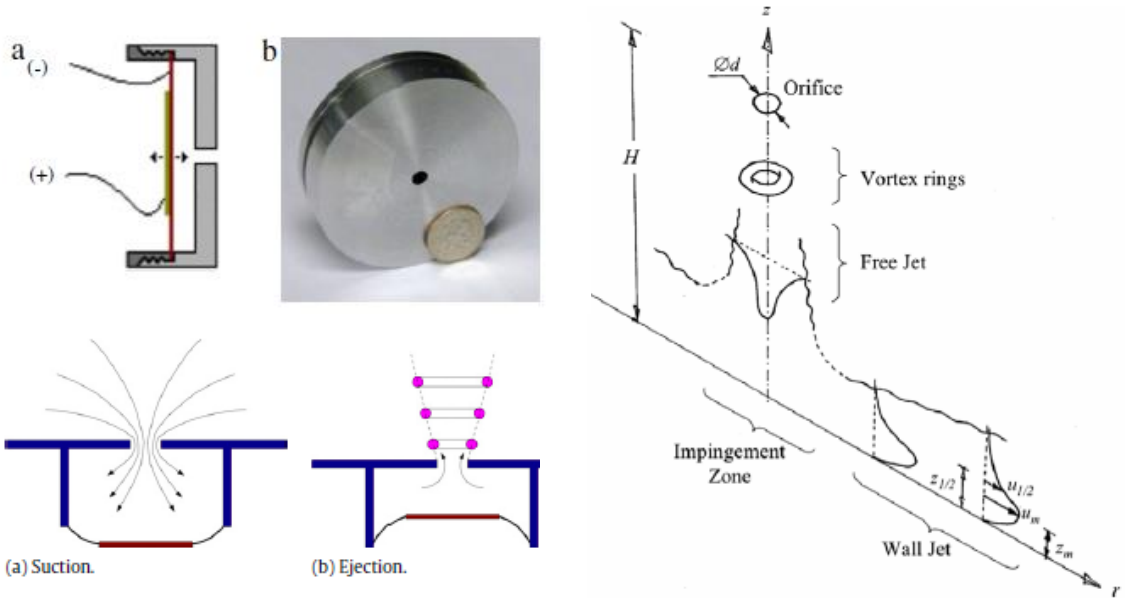

Figure 3.14: Schematic of a synthetic jet actuator and evolution of flow impinging on a wall, Krishnan & Mohseni (2010) [124]

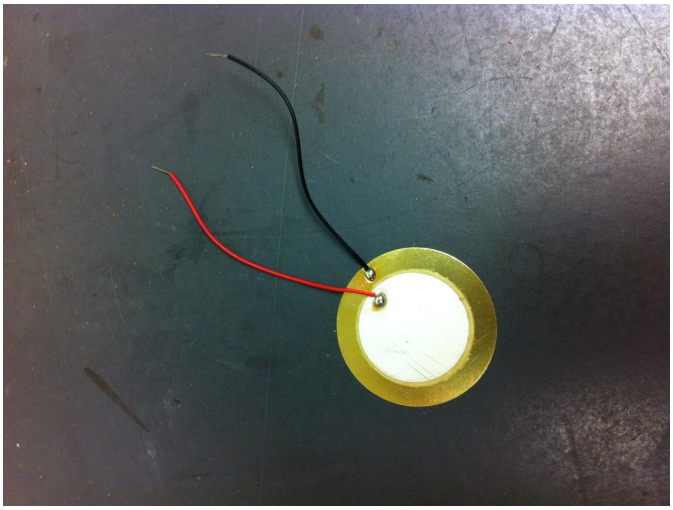

Figure 3.15: Piezoelectric synthetic jet actuator used in Syracuse University active flow control experiments

3.3.1 Syracuse University Actuation Glove

For open and closed-loop flow control experiments, an actuation glove has been designed and optimized for shear layer excitation. This actuation glove fits securely on the end of the nozzle so as to provide azimuthally uniform, unsteady velocity fluctuations. The actuation glove contains eight individual synthetic jet actuators, azimuthally distributed around the jet nozzle exit (see Figure 3.16). The piezoelectric disks are manufactured by *Omega Piezo* (OPT-BD-27T-2.6A1) and the glove itself was manufactured using rapid prototyping in the form of stereolithography (SLA). Figure 3.16 shows the actuation glove on a test stand as well as placed on the jet nozzle for experimental testing. Based on hotwire measurements at the exit slots, velocities on the order of 30-60 m/s are achieved. These velocities are sufficient enough to disturb the developing shear layer. The individual slots are located 0.6 *mm* from the nozzle lip and account for the entire circumference of the jet exit.

The actuation glove was first designed by Pinier *et al.* [182], based on the concept of Helmholtz resonance. The design has since been modified in order to ensure uniform forcing across all of the actuators. The dimensions of the Helmholtz resonator were opti-

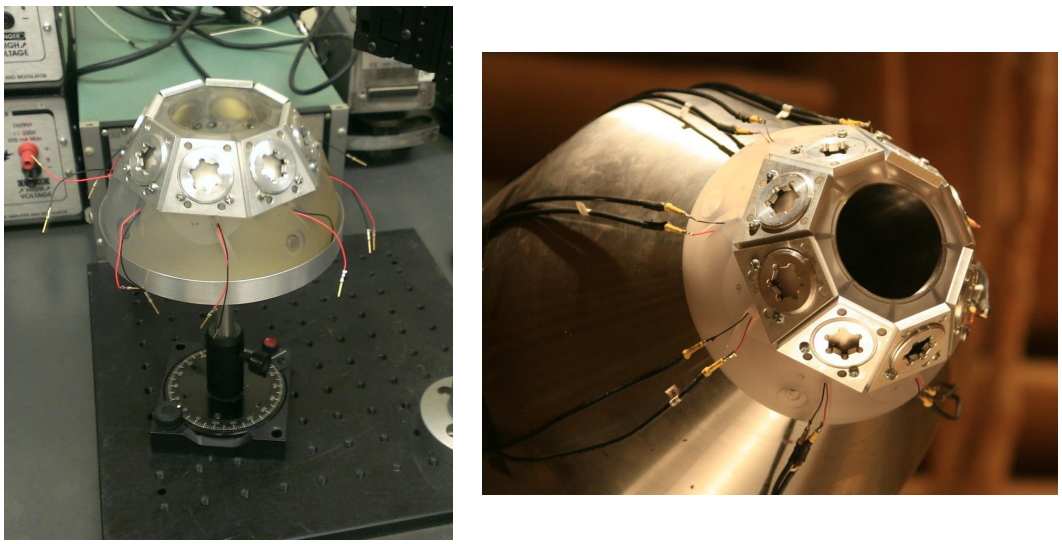

Figure 3.16: Actuation glove on a test stand (left) and placed on the jet nozzle (right)

mized based on a parametric study to match the resonance frequency of the cavity with the piezoelectric disk, based on the characteristic length, as seen in the following equation.

$$\Omega_o \propto \sqrt{\frac{c_0^2 A}{LV}} \tag{3.2}$$

In equation 3.2, A is the slot area, L is the neck length, V is the volume and c_0 is the speed of sound. An exploded view of the 3^{rd} generation actuation glove can be seen in Figure 3.17. Each piezoelectric disk is held in its own actuation pod via an *O-ring* and threaded plug. The full actuation glove is then attached to the jet nozzle with a set of screws to ensure it is secured during experiments.

The unique design of the actuation glove also allows each actuator to be controlled independently in order to force spatially azimuthal modes such as modes 0, 1, $\pm$1, $\pm$2, and $\pm$4 (see Low (2012) [148]). Moreover, the glove is designed such that the actuators inject flow to the main jet at a 45° angle.

Figure 3.17: Exploded view of the 3^{rd} generation actuation glove

3.3.2 Open and Closed-Loop Control Schemes

Active flow control is applied to the Mach 0.6 jet at Syracuse University using the actuation glove described, in both open and closed-loop configurations. The implementation of the different control strategies used in the current investigation are inspired by previous studies within the group [90, 94, 148, 182, 227]. Control application is restricted to the Mach 0.6 jet due to the control authority of the actuation system. Two non-dimensional quantities related to the actuation are defined, the synthetic jet Strouhal number (St_{sj}) and the coefficient of momentum (C_μ). The synthetic jet Strouhal number is defined as:

$$St_{sj} = \frac{f_{sj} D}{U_j} \tag{3.3}$$

where f_{sj} is the synthetic jet actuation frequency, D is the nozzle exit diameter and U_j is the velocity of the main jet. In all experimental results presented, St_{sj} is either 0.25 or 0.30,

which is the preferred operating range of the synthetic jets for optimal performance. The coefficient of momentum for this particular experimental setup, as defined by Low (2012) [148], is:

$$C_\mu = Q\frac{U_{sj}^2 A_{sj}}{U_j^2 A_j} \tag{3.4}$$

where Q is the total number of actuators, U_{sj} is the synthetic jet velocity, A_{sj} is the area of the synthetic jet slot and A_j is the area of the nozzle exit. For the control experiments, C_μ is calculated to be approximately 0.0016. Extensive studies varying both St_{sj} and C_μ were conducted by Low (2012) [148].

Two types of physical forcing using the actuation glove are implemented in the current schemes. These will be denoted as Fourier-azimuthal forcing modes, appealing to the axisymmetric nature of the jet. The first forcing mode is a Fourier-azimuthal mode 0, in which all actuators are driven in phase to mimic a column mode type forcing (Figure 3.18). The second forcing mode is a Fourier-azimuthal mode 1, in which the top 4 and bottom 4 actuators are driven 180° out of phases to mimic a "flapping-mode" type forcing (Figure 3.18). Since the jet is axisymmetric, Fourier-azimuthal mode 1 could have been implemented using any orientation of a set of 4 actuators, however the top/bottom configuration is chosen due to the orientation of the PIV window. Since the PIV plane is in the streamwise direction, the orientation of the mode 1 forcing can be observed. Other forcing modes have been implemented and these results can be found in the work of Low (2012) [148]. Fourier-azimuthal forcing modes 0 and 1 are used in both the open and closed-loop control cases in the current investigation.

For open-loop forcing, Fourier-azimuthal modes 0 and 1 are driven with the following signal:

$$y(t) = K_p sin(2\pi f_{sj} t) \tag{3.5}$$

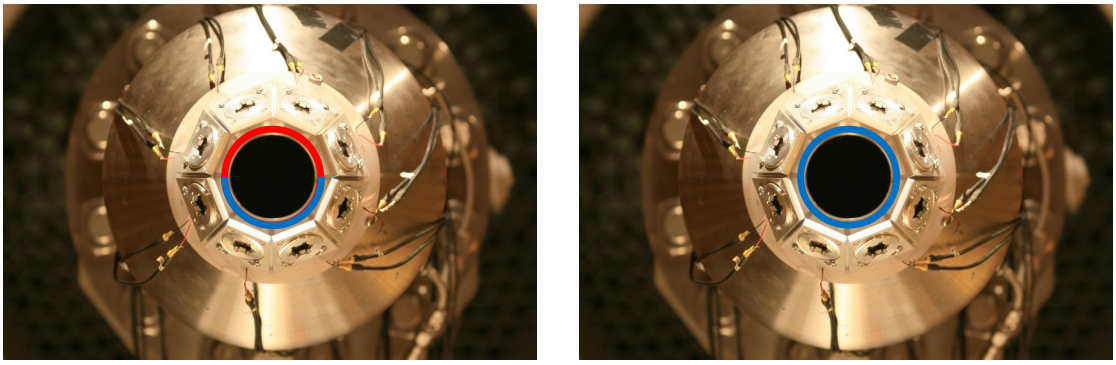

Figure 3.18: Fourier-azimuthal forcing mode 1 (left) and mode 0 (right)

where K_p is the control gain and f_{sj} is the synthetic jet actuator frequency. For the closed-loop control cases, some additional explanation is needed.

Recall from § 1.4.2, that Fourier-filtered modes 0 and 1 of the near-field pressure are of equal strength and nearly rebuild the unfiltered pressure signal. Moreover, Fourier-filtered pressure mode 0 exhibits a strong correlation with the far-field acoustics, while mode 1 (and all other modes) exhibit a weak, nearly non-existent, correlation with the far-field acoustics. Therefore, the idea is to somehow use Fourier-filtered pressure modes in conjunction with Fourier-azimuthal forcing modes (with closed-loop control) to exploit some of these features in an effort to reduce the far-field noise.

In order to use these low-dimensional pressure modes in a real time control scheme, a spatial Fourier modal decomposition is computed on the near-field pressure, using the azimuthal pressure array 6D downstream. The pressure field acts as a low pass filter of the velocity field and exhibits low-dimensional characteristics [148, 182, 227]. Moreover at 6D, near the collapse of the potential core, the majority of the energy is in the first two modes [182]. In order to extract the low-dimensional pressure modes, the azimuthal spectrum of the near-field pressure array is computed:

$$D_{nn}(f) = \frac{1}{2\pi}\int_0^{2\pi} R_{nn}(\Delta\theta, \tau = 0)e^{-2i\pi m\Delta\theta}d\Delta\theta \tag{3.6}$$

where $\Delta\theta$ is the azimuthal separation between the sensors, and the azimuthal cross covariance $R_{nn}(\Delta\theta, \tau = 0)$ is given as:

$$R_{nn}(\Delta\theta, \tau) = \overline{p_n(\theta, t)p_n(\theta + \Delta\theta, t + \tau)} \tag{3.7}$$

Since the azimuthal near-field pressure array in the LWPIV experiments only contains five sensors, only the first three azimuthal modes (0, 1 and 2) are extracted to avoid spatial aliasing. Taking the inverse Fourier transform of the mode-filtered pressure, the low-dimensional pressure in terms of time is obtained:

$$\tilde{p}(\theta, t) = \int_{-\infty}^{\infty} \hat{p}(m, t)e^{im\theta}d\theta \tag{3.8}$$

These Fourier-filtered pressure modes are computed in real time and fed back to the actuators, as shown by the schematic in Figure 3.19. The signal that drives the actuators in the closed-loop control cases can be seen in equation 3.9:

$$y(t) = K_p P_m(t) sin(2\pi f_{sj} t) \tag{3.9}$$

where K_p is the controller gain, f_{sj} is the synthetic jet actuator frequency and $P_m(t)$ is the Fourier-filtered pressure mode, used as an amplitude modulation in the control loop. Since Fourier-filtered pressure modes 0 and 1 are significant contributors to the unfiltered pressure signal, these are the only modes used in the current investigation.

Given what is already known about the relationship between the Fourier-filtered pressure modes and the far-field acoustics, one control approach, implemented by Low (2012) [148], fed back Fourier-filtered pressure mode 1 to force Fourier-azimuthal mode 0, in order to diminish the correlation of the strong Fourier mode. This strategy is also used in the

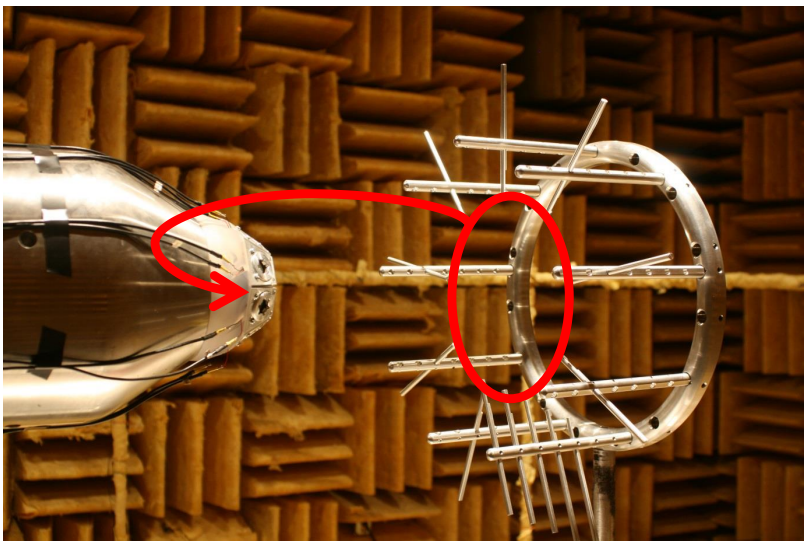

Figure 3.19: Closed-loop flow control feedback schematic

current investigation along with another approach in the same spirit. Just as Fourier-filtered mode 1 of the pressure can be used to diminish the strong pressure mode, Fourier-filtered mode 0 of the pressure can be used to amplify the weak pressure mode. This is done by feeding back Fourier-filtered pressure mode 0 to drive Fourier-azimuthal forcing mode 1. The idea in both cases is to use knowledge of how the near and far-field pressure are related to reduce far-field noise through active flow control. Using Fourier modes 0 and 1 for feedback and actuation, there are two more closed-loop control combinations and all four scenarios are seen in Figure 3.20.

Fourier-filtered Pressure Mode	Fourier-azimuthal Forcing Mode	Objective	Abbreviated Representation
Mode 0	Mode 1	Amplify weak pressure mode	M0 → M1
Mode 0	Mode 0	Amplify strong pressure mode	M0 → M0
Mode 1	Mode 0	Diminish strong pressure mode	M1 → M0
Mode 1	Mode 1	Diminish weak pressure mode	M1 → M1

Figure 3.20: Different closed-loop control schemes and associated objectives

The other two control scenarios ($M0 \rightarrow M0$ and $M1 \rightarrow M1$) are not discussed in this investigation since both cases make the jet substantially louder than the other cases. In particular, case $M0 \rightarrow M0$ amplifies the strong pressure mode, while case $M1 \rightarrow M1$ diminishes the weak pressure mode; thus increasing the far-field noise in both cases. Therefore, the closed-loop control cases for the current investigation will focus on $M0 \rightarrow M1$ and $M1 \rightarrow M0$. Combining this with the open-loop cases, the four control cases studied are shown in Figure 3.21. While the open-loop cases do not drawn on any intelligence from the system, they can be compared to the closed-loop cases in the context of the change in flow physics and the overall relation to the far-field noise.

Control Case	Fourier-filtered Pressure Mode	Fourier-azimuthal Forcing Mode
Open-Loop Control 1 (OLC1)	\	Mode 1
Open-Loop Control 2 (OLC2)	\	Mode 0
Closed-Loop Control 1 (CLC1)	Mode 0	Mode 1
Closed-Loop Control 2 (CLC2)	Mode 1	Mode 0

Figure 3.21: Open and closed-loop control cases for the current set of experiments

Throughout the course of the analyses and discussions, the control cases are referred to using the abbreviations (*i.e. OLC1*), for simplicity. All four control cases are implemented with both the LWPIV and TRPIV. Near and far-field pressure are simultaneously sampled with PIV, while the active flow control is operating. Therefore the effects of the control can be observed and compared to uncontrolled (baseline) jet flow.

Chapter 4

Reduced-Order Modeling

In general, turbulent flows are characterized by a high level of complexity which is driven by the inherent nonlinearities of the governing equations. Turbulent flows encompass a large range of the length and time scales, evolving in three-dimensional space as well as in time. In working to interpret these complex flow physics, a technique which reduces the complexity of the problem is employed. Reduced-order modeling (ROM) provides a methodology for decomposing a quantity into its fundamental building blocks. Depending on the ultimate goal of the model, the decomposition can be truncated to include only contributions of interest. This methodology of developing a low-dimensional representation of a given quantity is especially useful in the context of real time closed-loop flow control. ROM can be implemented to extract the most important features of the flow to achieve the particular control objective of interest, and begin to interpret the flow physics from a high level.

With respect to the jet noise problem specifically, increasingly large data sets and complex flow physics warrant the implementation of ROM. The ROM allows for the extraction of large scale, dominant flow structures, with respect to the turbulent kinetic energy. The current investigation seeks to find a relationship between the velocity field and the far-field acoustics through the use of ROM. In order to achieve this, a low-dimensional

representation of the velocity field is computed based on turbulent kinetic energy. If the noise-producing events in the flow field can be identified, one can imagine using this information in a closed-loop control scheme to reduce the far-field noise. The following section discusses one such ROM technique, known as the proper orthogonal decomposition.

4.1 Proper Orthogonal Decomposition

Proper orthogonal decomposition (POD) is a mathematical technique which takes a group of variables and uses an orthogonal set of basis functions to form a set of linearly uncorrelated variables. Therefore POD is a form of singular value decomposition (SVD) and has been used in the mathematics community since the 19^{th} century. POD goes by many names depending on the field of interest, however its most common alternative name is principal component analysis (PCA), as the linearly uncorrelated variables are known as principal components. PCA was developed by Pearson in 1901 [176], and its popularity grew in other fields developing names such as the Hotelling transform (1933) [111] in quality control, the Karhunen-Loève transform (KLT) (1945) [119, 143] in signal processing, and POD (1967) [150] in turbulence. The POD soon became a strong analysis tool in many other fields including but not limited to, image processing, data compression, optimal control and signal analysis. The classical form of the POD [150] and a modification of the approach appealing to data with a large amount of grid points [214], are presented as the current formulations of interest.

4.1.1 Classical POD

As previously discussed, POD has been implemented in several fields over the last hundred years, however the idea was first introduced into the field of turbulence by Lumley in 1967 [150]. At the time, many researchers were studying large scale coherent structures present

in turbulent flow fields (see § 1.1.1). This prompted a desire to develop a quantitative representation of the large scale motion and thus POD was implemented. Since the POD is an energy based decomposition, in the context of turbulent flows, it is ideal for identifying the differences in large and small scale structures.

The POD starts by taking a random set of realizations and obtaining a basis that best describes the signal in an averaged mean squared sense. In the case of the jet, the random realizations are instantaneous snapshots of fluctuating velocity, obtained either experimentally (PIV) or computationally (LES, RANS, etc.). The goal is to determine a function having the largest mean squared projection on the velocity field. From this, the entire flow field is decomposed into spatial eigenfunctions and time dependent expansion coefficients. The spatially resolved eigenfunctions are thought of as the deterministic building blocks of the flow while the expansion coefficients provide the time record of the structures, thereby forming the entire spatial and temporal field. One important feature of the POD is that the orthogonal transformation ensures that the first principal component has the largest variance. In the context of turbulence, the extracted structures, known as *modes*, are ordered in terms of the contributions to the overall turbulent kinetic energy. Therefore the first mode contains the largest amount of energy and the subsequent modes proceed in descending order with respect to energy.

The formulation of the classical POD begins with scalar fields, being complex valued functions defined on an interval, as stated by Berkooz *et al.* (1993) [33]. Since the problem of interest involves a fluid flow with a finite amount of turbulent kinetic energy, the scalar fields are restricted to square integrable functions defined in the following way:

$$\int_{-\infty}^{\infty} |f(x)|^2 dx < \infty \tag{4.1}$$

The function defined in equation 4.1 then forms an inner product as follows:

$$(f,g) = \int_{\mathscr{D}} f(x)g^*(x)dx \tag{4.2}$$

In equation 4.2, $f(x)$ and $g(x)$ are square integrable functions as defined in equation 4.1, and the $(^*)$ represents the complex conjugate. Therefore, the norm of these functions in the Hilbert space is defined as,

$$\|f\| = (f,f)^{1/2} \tag{4.3}$$

Equations 4.1 - 4.3 provide the necessary background to form the POD. Starting with an ensemble of realizations, $u(\vec{x},t)$, we seek to identify which single deterministic function, $\phi(\vec{x})$, is most similar in an average mean squared sense, to that ensemble. In this particular case, the realizations are instantaneous snapshots of velocity and the deterministic functions are the building blocks or basis functions of the flow field. This leads to a constrained optimization problem defined by:

$$\begin{cases} max_{\psi} \frac{\langle |(u,\psi)|^2 \rangle}{(\psi,\psi)} = \frac{\langle |(u,\phi)|^2 \rangle}{(\phi,\phi)} \\ (\phi,\phi)^2 = 1 \end{cases} \tag{4.4}$$

where $\langle \bullet \rangle$ denotes an averaging operation and $|\bullet|$ denotes the absolute value. This implies that the spatial eigenfunctions are orthogonal and from calculus of variations, in order for equation 4.4 to hold, $\phi(\vec{x})$ must be an eigenfunction of the two-point correlation tensor [150]. A schematic of the fundamental decomposition can be seen in the work of Low (2012) [148]. The problem subsequently reduces to the solution of the Fredholm integral eigenvalue problem:

$$\int_{\mathscr{D}} R_{ij}(\vec{x},\vec{x}')\phi_j^n(\vec{x}')d\vec{x}' = \lambda\phi_i(\vec{x}) \tag{4.5}$$

In equation 4.5, λ are the eigenvalues, $\phi_i(\vec{x})$ are the eigenfunctions and R_{ij} is the ker-

nel. Therefore, R_{ij} is defined as the ensemble-averaged two-point, spatial cross-correlation tensor, whereby the correlations are obtained from the fluctuating velocity components, as seen in equation 4.6.

$$R_{ij}(\vec{x},\vec{x}') = \langle u_i(\vec{x},t)u_j(\vec{x}',t)\rangle \tag{4.6}$$

From equation 4.6, $u_i(\vec{x},t)$ is the fluctuating velocity obtained from a Reynolds decomposition of the instantaneous velocity, $\tilde{u}_i(\vec{x},t)$:

$$u_i(\vec{x},t) = \tilde{u}_i(\vec{x},t) - U_i(\vec{x}) \tag{4.7}$$

where $U_i(\vec{x})$ is the ensemble-averaged mean velocity field.

In the case of the formulation of the POD for the jet problem, the kernel R_{ij} is symmetric and thus the integral eigenvalue problem can be solved using Hilbert-Schmidt theory (eigenfunction expansion), since the domain $\mathscr{D}$ is bounded [79, 150]. In Hilbert-Schmidt theory, the kernel of an integral, as in equation 4.5, is investigated by means of its eigenfunctions to solve the integral [150]. The solutions are bounded with a finite dimensional inner product space as previously discussed. The Hilbert-Schmidt theory therefore ensures an orthonormal basis, which can be represented as a diagonal matrix of eigenvalues with real entries. Therefore the solution to the integral eigenvalue problem gives a set of empirical eigenfunctions, $\phi^{(n)}(\vec{x})$ with a corresponding real and distinct eigenvalue, $\lambda^{(n)}$. Therefore, equation 4.5 can be represented as:

$$\int_{\mathscr{D}} R_{ij}(\vec{x},\vec{x}')\phi_j^{(n)}(\vec{x}')d\vec{x}' = \lambda^{(n)}\phi_i^{(n)}(\vec{x}), \quad (n = 1,2,3\ldots) \tag{4.8}$$

In defining the POD, there are some important properties that will be crucial for the analysis. First, as previously stated, the discrete set of empirical eigenfunctions $\phi^{(n)}(\vec{x})$ are orthonormal:

$$\int_{\mathscr{D}} \phi_i^{(p)}(\vec{x})\phi_i^{(q)}(\vec{x}')d\vec{x}' = \delta_{pq} \tag{4.9}$$

where δ_{pq} is the Kronecker delta function. Moreover, the eigenvalues are arranged in terms of descending energy such that,

$$\lambda^{(1)} \geq \lambda^{(2)} \geq \lambda^{(3)} \cdots > 0 \tag{4.10}$$

In addition, as shown by Glauser (1987) [79], the kernel can be decomposed into the following convergent series:

$$R_{ij}(\vec{x},\vec{x}') = \sum_{n=1}^{\infty} \lambda^{(n)} \phi_i^{(n)}(\vec{x})\phi_j^{(n)}(\vec{x}') \tag{4.11}$$

Once the empirical eigenfunctions are obtained by solving the integral eigenvalue problem, the time-dependent expansion coefficients, $a_n(t)$, are obtained by projecting the original realizations onto the basis functions as follows:

$$a_n(t) = \int_{\mathscr{D}} u_i(\vec{x},t)\phi_i^{(n)}(\vec{x})d\vec{x} \tag{4.12}$$

These coefficients are uncorrelated because of the diagonal representation of the two-point correlation tensor [150]:

$$\langle a_n, a_m \rangle = \lambda^{(n)} \delta_{nm} \tag{4.13}$$

With the spatial eigenfunctions, $\phi_i^{(n)}(\vec{x})$, and corresponding time-dependent expansion coefficients, $a_n(t)$, defined, the original random field can be reconstructed via a summation of the two quantities as shown in the following equation,

$$u_i(\vec{x},t) = \sum_{n=1}^{N} a_n(t)\phi_i^{(n)}(\vec{x}) \tag{4.14}$$

The distribution of turbulent kinetic energy amongst the time-dependent modes $a_n(t)$ can be represented with its corresponding eigenvalue $\lambda^{(n)}$. The total turbulent kinetic energy is then represented by a summation over all of the eigenvalues as shown in the following equation.

$$\int_{\mathscr{D}} \langle u_i(\vec{x},t) u_i(\vec{x},t) \rangle d\vec{x} = \sum_{n=1}^{\infty} \lambda^{(n)} \tag{4.15}$$

Therefore, from equation 4.13, the square of each time-dependent expansion coefficient is equal to the energy of that particular mode.

In the context of designing low-dimensional models for understanding the flow physics and developing control algorithms, the convergence rate of the modes is an important aspect of the POD. Knowing the rate of convergence gives an idea of how the energy is distributed throughout the modes and thus this becomes crucial when making truncations of the data. Many times the goal of the truncation is to retain as much energy as possible with as few modes as possible. In order to do so, one can examine the contribution of energy to each individual eigenvalue, $\lambda^{(n)}$ (mode), defined as:

$$\Lambda^{(n)} = \frac{\lambda^{(n)}}{K} \times 100 \tag{4.16}$$

where K is the total turbulent kinetic energy of the system and is defined in equation 4.17.

$$K = \sum_{n=1}^{N_{POD}} \lambda^{(n)} \tag{4.17}$$

4.1.2 POD for the Axisymmetric Jet in r-θ

The POD can be reformulated for the axisymmetric jet in the r-θ plane as shown by Glauser (1987) [79] and Tinney *et al.* (2008) [228, 230]. If the field of interest is either homoge-

neous, periodic or stationary in one direction, the POD can be formulated using a set of harmonic eigenfunctions in that direction. Therefore for the axisymmetric jet, in the r-θ plane, the flow is stationary in time and periodic in the azimuthal direction. Thus, the POD reduces to a spatial Fourier decomposition in the azimuthal direction, leading to a reformulation of the kernel R_{ij}. Since the jet is stationary in time in the azimuthal direction (in the r-θ plane), the Fourier transform is implemented [79, 228, 230] to obtain:

$$\Phi_{ij}(r,r',\Delta\theta,z_0,f) = \int\int R_{ij}(r,r',\Delta\theta,z_0,\tau)e^{-i(2\pi f\tau+m\Delta\theta)}d\tau d\theta \tag{4.18}$$

In equation 4.18, Φ_{ij} is the cross-spectral tensor, r is the radial separation in the inhomogeneous direction and $\Delta\theta$ is the azimuthal separation. Moreover, z_0 is the streamwise location, f is the frequency and τ is the time difference.

The kernel, R_{ij}, in this case is defined as [227],

$$R_{ij} = \langle u(r,\theta_0,z_0,t)u(r',\theta',z_0,t)\rangle \tag{4.19}$$

The cross-spectral tensor, Φ_{ij}, is then decomposed in the periodic direction, corresponding to the cosine transform of the kernel.

$$\Phi_{ij}(r,r',\Delta\theta,z_0,f) = \sum_{m=0}^{\infty} A_{ij}(r,r',m,z_0,f)\cos(m\theta) \tag{4.20}$$

Then, the complex coefficients, A_{ij}, of the series are defined for $m = 0$ as:

$$A_{ij}(r,r',0,z_0,f) = \frac{1}{\pi}\int_0^{\pi} \Phi_{ij}(r,r',\Delta\theta,z_0,f)d\theta \tag{4.21}$$

Therefore, in general, equation 4.21 becomes:

$$A_{ij}(r,r',m,z_0,f) = \frac{2}{\pi}\int_0^{\pi} \Phi_{ij}(r,r',\Delta\theta,z_0,f)\cos(m\theta)d\theta \tag{4.22}$$

The integral eigenvalue problem is then formed by a decomposition in the inhomogeneous direction using A_{ij}. The resulting integral eigenvalue problem is defined as [228, 230]:

$$\int_{\mathscr{D}} A_{ij}(r,r',m,z_0,f)\phi_j^{(n)}(r',m,z_0,f)r'dr' = \lambda^{(n)}(m,z_0,f)\phi_i^{(n)}(r,m,z_0,f) \tag{4.23}$$

4.1.3 Snapshot POD

As computational and experimental spatial grids continue to grow with advances in computing capabilities and data acquisition systems, the classical POD becomes computationally cumbersome and expensive. Thus, Sirovich (1987) [214] proposed the snapshot POD to address this concern. This formulation is used when the number of spatial grid points (multiplied by the number of velocity components) is greater than the number of flow realizations, *i.e.* snapshots. Therefore the problem is reworked to become a temporal formulation instead of a spatial formulation. As such, the integral eigenvalue problem is analogous to that of the Fredholm integral eigenvalue problem in its classical form, however the variables now have a temporal dependence as opposed to the spatial dependence of the classical formulation. The integral eigenvalue problem is defined in equation 4.24.

$$\int_T C(t,t')a_n(t')dt' = \lambda^{(n)}a_n(t) \tag{4.24}$$

In equation 4.24, $a_n(t)$ is the temporal eigenfunction and the kernel $C(t,t')$ is now the *two-time* correlation tensor, defined by:

$$C(t,t') = \frac{1}{T}\int_{\mathscr{D}} \sum_{i=1}^{3} u_i(\vec{x},t)u_i(\vec{x},t')d\vec{x} \tag{4.25}$$

The snapshot POD yields similar properties to the classical formulation. The time-

dependent expansion coefficients are random and uncorrelated. Moreover the mean squared value corresponds to its associated eigenvalue as follows:

$$\langle a_m(t), a_n(t) \rangle = \lambda^{(m)} \delta_{mn} \tag{4.26}$$

The spatial eigenfunctions, $\phi_i^{(n)}(\vec{x})$, are therefore defined in the following way:

$$\phi_i^{(n)}(\vec{x}) = \frac{1}{T\lambda^n} \int_T a_n(t) u_i(\vec{x}, t) dt \tag{4.27}$$

Equation 4.27 can be represented by a summation as follows:

$$\phi_i^{(n)}(\vec{x}) = \sum_{k=1}^{T} a_n(t_k) u_i(\vec{x}, t_k) \tag{4.28}$$

With the spatial eigenfunctions and time-dependent expansion coefficients known, the original random flow field can be reconstructed with equation 4.14.

4.2 Stochastic Estimation Techniques & ROM

While linear stochastic estimation (LSE) is not a reduced-order model on its own, the mathematical framework of LSE has been combined with ROM to estimate properties in a flow field. Before addressing the technique known as observable inferred decomposition (OID), some background of LSE must first be established. LSE was first proposed by Adrian (1977) [4] as a way to estimate a given quantity using a conditional average. The main concept behind the LSE is that conditionally correlated data can be averaged from a field of vectors and can then be used to estimate the dynamic condition from an unconditional source at the same instant in time [231].

Following the initial work of Adrian, many researchers have used LSE to estimate the time-dependent velocity field from a set of time-dependent pressure measurements. The

success of the LSE relies on the level of correlation between the conditional and unconditional data, *i.e.* pressure and velocity. Cole *et al.* (1992) [50] performed LSE in the mixing layer of an axisymmetric jet. They were able to compute an estimate of the velocity field using a coarse array of hot wire anemometers.

Building on the work of Adrian [4] and Cole *et al.* [50], Ukeiley *et al.* (1993) [235] and Bonnet *et al.* (1994) [35] developed the complementary technique. This modified form of the LSE (mLSE) combines the LSE and the POD to obtain a time-dependent, low-dimensional description of the flow field. Ukeiley *et al.* [235] and Bonnet *et al.* [35] used the mLSE to estimate the low-dimensional velocity field in the mixing layer of a jet. Cole & Glauser (1998) [49] also showed much success in estimating the velocity field of a sudden expansion using LSE.

In addition, LSE has been used extensively in the turbulence community to estimate the velocity field using surface pressure as the unconditional source. This includes the work of Picard & Delville (2000) [179], Naguib *et al.* (2001) [169], Taylor & Glauser (2004) [223] and Murray & Ukeiley (2007) [167], to name a few. At Syracuse University, the mLSE techniques were also successfully applied to a NACA 4412 airfoil for control applications by Ausseur (2007) [21] and Pinier *et al.* (2007) [183].

Building on the mLSE approach, Tinney *et al.* (2006,2008) [230, 231] employed an additional modification whereby a spectral LSE (sLSE) was applied to the jet. The sLSE was developed to exploit the rich spectral content of the pressure field. Thus the sLSE is performed in the frequency domain, as opposed to the time domain with the conventional LSE approach.

A brief description of the mLSE technique is presented for clarification, in the context of the NACA 4412 airfoil data set [21, 183]. As previously stated, the low-dimensional time-dependent expansion coefficients of the velocity field are estimated from a series of pressure sensors, in this case located on the airfoil surface. Therefore for each POD mode,

the estimated coefficient can be represented by a series expansion of the discrete instantaneous surface pressure measurements [21]:

$$\tilde{a}_n(t) = A_{ni}p_i(t) + B_{nij}p_i(t)p_j(t) + C_{nijk}p_i(t)p_j(t)p_k(t) + \ldots \quad i,j,k \in [1,q] \tag{4.29}$$

In equation 4.29, $\tilde{a}_n(t)$ is the estimated expansion coefficient, where n is the POD mode number. Then $p_i(t)$ is the instantaneous surface pressure at streamwise position i on the airfoil surface. Therefore, q is the total number of pressure sensors and A, B and C are the estimation coefficients. Since the current focus is LSE, only the linear term in the equation is retained, giving a single-time, multi-point estimation as follows:

$$\tilde{a}_n(t) = A_{ni}p_i(t) \quad i \in [1,q] \tag{4.30}$$

In equation 4.30, A_{ni} are the time-dependent linear estimation coefficients which must be solved for. In order to do so, a least-squares problem is solved to minimize the mean square error between the estimated and original POD coefficients. The mean square error, $e_{\tilde{a}_n}$ is thus defined as:

$$e_{\tilde{a}_n} = \langle |\tilde{a}_n(t) - a_n(t)|^2 \rangle \tag{4.31}$$

Combining equations 4.30 and 4.31, and taking the derivative of equation 4.31 with respect to the linear estimation coefficient, the mean square error for each POD mode is minimized for each coefficient A_{nk}:

$$\frac{\partial e_{\tilde{a}_n}}{\partial A_{nk}} = 0 \quad \forall k \in [1,q], \forall n \leq N$$

$$\Leftrightarrow \frac{\partial \langle [A_{ni} p_i(t) - a_n(t)]^2 \rangle}{\partial A_{nk}} = 0$$

$$\Leftrightarrow \langle p_j(t) p_k(t) \rangle A_{nj} = \langle a_n(t) p_k(t) \rangle \tag{4.32}$$

Therefore, equation 4.32 is reformulated into matrix form as follows:

$$\begin{bmatrix} \langle p_1 p_1 \rangle & \cdots & \langle p_q p_1 \rangle \\ \vdots & \ddots & \vdots \\ \langle p_1 p_q \rangle & \cdots & \langle p_q p_q \rangle \end{bmatrix} \begin{bmatrix} A_{n1} \\ \vdots \\ A_{nq} \end{bmatrix} = \begin{bmatrix} \langle a_n p_1 \rangle \\ \vdots \\ \langle a_n p_q \rangle \end{bmatrix} \tag{4.33}$$

From equation 4.33, it can be seen that the pressure correlation matrix is symmetric and has dimension $q \times q$. The pressure-POD cross terms are averaged over the total number of ensembles. The linear estimation coefficients are then solved for and substituted into equation 4.30. Therefore, having the pressure measurements and solving for the linear estimation coefficients, the estimated instantaneous velocity field can be obtained from the estimated POD expansion coefficients and the spatial eigenfunctions (known *a priori*). The equation for the instantaneous estimated velocity field is shown as follows:

$$\tilde{u}(x,t) = \sum_{n=1}^{N} \tilde{a}_n(t) \phi^{(n)}(x) \tag{4.34}$$

Many extensions of the stochastic estimation techniques exist such as the modified and spectral approaches. In addition, the quadratic stochastic estimation (QSE) retains the first and second terms in equation 4.29 (see Murray & Ukeiley (2007) [167]). The stochastic estimation techniques have also been coupled with reduced-order modeling to find corre-

lations between two low-dimensional quantities, such as pressure and velocity. This was first explored by Taylor & Glauser (2004) [223], who correlated wall pressure with POD velocity modes. Later, Tinney *et al.* (2006,2008) [230, 231] extended this to correlating low-dimensional (Fourier) pressure modes and POD velocity modes. The analysis was performed in spectral space using the sLSE as previously mentioned. Moreover, the velocity was measured in the r-θ plane and thus the POD velocity modes reduced to Fourier modes. A relationship was found between the low-dimensional velocity and pressure fields using sLSE coupled with ROM, in the form of the POD. The work of Taylor & Glauser [223] and Tinney *et al.* [230] inspired further investigations in this area to be discussed in the next section.

4.3 Observable Inferred Decomposition

With the success of stochastic estimation techniques and the coupling of these methods with ROM, applications to the jet noise problem in the context of identifying noise producing events became prevalent. Tinney *et al.* [228, 230] were the first to correlate the low-dimensional pressure modes in the near-field with the low-dimensional velocity modes using POD and sLSE. This inspired an extension of the work to explore the low-dimensional relationship between the near-field velocity and the far-field pressure. Much work had already been done to relate the near and far-field pressure, but directly linking the near-field velocity with the acoustics had been a somewhat untapped resource. Drawing on the ideas of Tinney *et al.* [230], Jordan *et al.* (2007) [114] proposed a way to identify the "noisy" and "quiet" modes in a jet through a technique known as the most observable decomposition (MOD). This involved the same mathematical technique of Tinney *et al.* [230], however now the low-dimensional far-field acoustics were correlated with the low-dimensional velocity modes in the near-field.

This spawned the acoustically optimized ROM technique known as the observable in-

ferred decomposition (OID), first introduced by Jordan *et al.* [114] and Schlegel *et al.* (2009,2012) [202, 203]. Within a Galerkin framework, this approach uses the POD to optimally identify acoustically weighted flow features (source) as a function of an observable subspace constructed from a discrete set of linearly related "observables" (far-field microphones). The technique provides a linear mapping between the most energetic velocity modes and the most energetic features of the far-field acoustics. A schematic representation can be seen in Figure 4.1. In this representation, a cause and effect relationship is shown between the velocity and acoustic fields. In the schematic, u and v represent the velocity components, p and q are different microphone signals, a is the corresponding low-dimensional filtered mode (POD) and C is the linear mapping matrix which relates the two low-dimensional fields.

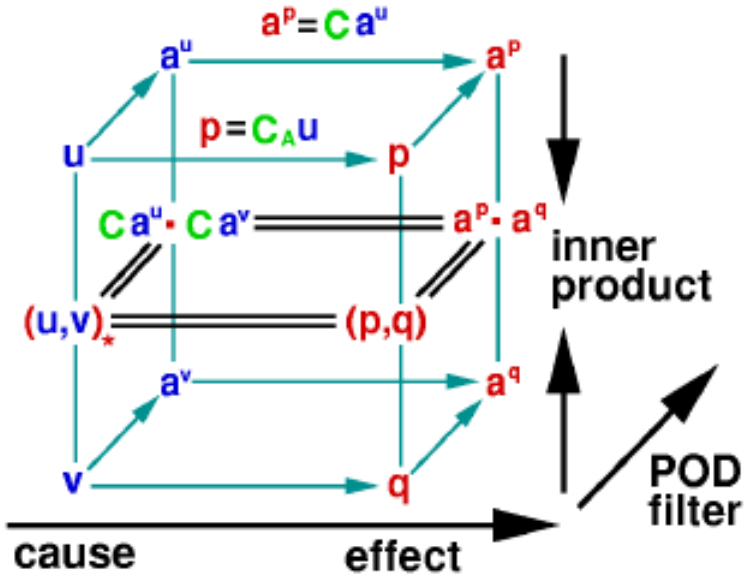

Figure 4.1: Commutative diagram of OID products, defined in the hydrodynamic state space, the space of the observable and the respective POD subspace representations, Jordan *et al.* (2007) [114]

The mathematical approach used in the current study is defined as follows. First the

low-dimensional approximations of both source (hydrodynamic attractor, *i.e.* flow-field) and observer (acoustics, *i.e.* far-field) are estimated via the POD method. The snapshot form of POD is used to obtain a low-order representation of the flow-field, and the classical form of POD is used to extract the modes of the acoustic field, since there are a discretized number of microphones. Depending on the experiment of interest presented herein, there will either be six or twelve OID modes, corresponding to the number of far-field microphones. The mathematical procedure for both the classical and snapshot methods are outlined in § 4.1. In order to clarify the technique in the context of identifying noise producing events, some general equations are redefined in this section. To begin, a low-order representation of the velocity field is established as follows:

$$u(\vec{x},t) = \sum_{n=1}^{N} a_n^u(t)\phi_i^{(n)}(\vec{x}) \tag{4.35}$$

In addition, a reduced-order Galerkin approximation of the fluctuating far-field acoustics is also obtained,

$$p(\theta,t) = \sum_{k=1}^{K} a_k^p(t)\varphi_i^{(k)}(\theta) \tag{4.36}$$

In equation 4.36, θ is the polar separation between the jet centerline axis and the observer (microphone). Then $a_k^p(t)$ is the time-dependent expansion coefficient of the acoustic field. As shown in § 4.1, the spatial eigenfunctions of the far-field acoustics, along with the corresponding eigenvalues $\lambda_p^{(n)}$ are obtained by solving the integral eigenvalue problem, as follows:

$$\int_T B_{ij}(\theta,\theta')\varphi_i^{(k)}(\theta)d\theta' = \lambda_p^{(k)}\varphi_j^{(k)}(\theta) \tag{4.37}$$

In equation 4.37, the two-point correlation tensor of the acoustics, $B_{ij}(\theta,\theta')$, is defined in the following way:

$$B_{ij}(\theta,\theta') = \langle p_i(\vec{\theta},t), p_i(\vec{\theta}',t)\rangle \tag{4.38}$$

Therefore the spatial eigenfunctions of the acoustics, $\varphi^{(k)}(\theta)$, can be thought of as the low-dimensional POD modes that most efficiently decompose the acoustic field. The time-dependent expansion coefficients are then obtained by projecting the far-field acoustic pressure back onto the spatial eigenfunctions, as shown in equation 4.39.

$$a_k^p(t) = \int_\Theta p_i(\theta,t)\varphi_i^{(k)}(\theta)d\theta \tag{4.39}$$

Equipped with a low-dimensional approximation of the most efficient features of both the velocity and acoustic fields (source and observer, respectively), a linear mapping between the instantaneous turbulent fluctuating velocity components and the acoustic far-field must be identified, based on the assumption of a linear relationship between the velocity and acoustic fields. Jordan *et al.* [114] justified this assumption in the context of shear and self-noise. In summary, the shear-noise (characterized as the fast-pressure term) is the dominant source with respect to the near-field pressure fluctuations in the hydrodynamic region. Moreover, the shear-noise is the most efficient at correlating with the far-field acoustics. The self-noise (slow-pressure term), is the quadratic terms and is much weaker in the correlations. Coiffet *et al.* (2006) [48] also explains that the noise producing mechanism is dominated by coherent structures in the region before the collapse of the potential core, which is a linear process. Therefore, the linear mapping between the time dependent expansion coefficients of the velocity and acoustic field is shown in the following equation:

$$\tilde{a}_k^p(t) = \sum_{n=1}^{N} C_{kn}^{pu} a_n^{(u)}(t-\tau) \tag{4.40}$$

In equation 4.40, τ is the lag time of acoustic propagation and C_{kn}^{pu} is the linear mapping transformation matrix. In order to solve for this linear mapping term, a least squares mini-

mization is performed, as with the LSE approach (see equation 4.30). Therefore, the mean square error between the estimate of far-field pressure modes and the actual measurement is minimized as follows:

$$\frac{1}{K}\sum_{k=1}^{K}(a_k^p - \tilde{a}_k^p)^2 \rightarrow min \tag{4.41}$$

This term is expanded with the incorporation of equation 4.40, and the derivative is taken and set to zero, as in equation 4.32. With some rearranging, the linear mapping between the time dependent expansion coefficients of the velocity and acoustic fields is communicated by:

$$C_{kn}^{pu} = \sum_{j=1}^{T} \frac{1}{T\lambda_p^{(k)}} a_k^p(t_j) a_n^u(t_j - \tau) \tag{4.42}$$

The linear mapping term, C_{kn}^{pu}, therefore represents the degree of linearity between the low-dimensional dynamics of the velocity and the acoustic fields (*i.e.* hydrodynamic attractor and observable, respectively), as stated by Jordan *et al.* [114]. Therefore, C_{kn}^{pu} breaks down the flow field and exposes features which are most correlated to the acoustic pressure fluctuations in the far-field. The POD modes that have the largest contribution to the corresponding OID mode, will be coined as "loud" modes in the flow field.

In order to obtain an estimation of the most observable velocity modes, $u_i^\star(\vec{x})$, as a function of this mapping, the transformation matrix is projected onto the truncated spatial velocity modes (see equation 4.43). A more in depth derivation and discussion of the plausibility of the OID method is addressed in Schlegel *et al.* [203].

$$u_i^\star(\vec{x}) = \sum_{k=1}^{S}\left(\sum_{n=1}^{N} C_{kn}^{pu}\phi_i^{(n)}\right) \tag{4.43}$$

Since the low-dimensional modes of the velocity and far-field acoustics are both time-resolved, the transformation matrix, C_{kn}^{pu}, can be calculated directly without having to use

spectral estimation techniques, as used in Tinney *et al.* [230]. The focus of the current investigation will be on the linear mapping matrix, C_{kn}^{pu}, in the context of identifying and extracting "loud" modes in the time-resolved flow field.

4.4 Low-Dimensional Modes

The results to be presented in the following chapters will discuss various types of low-dimensional temporal and spatial representations of various quantities, that are denoted as *modes*. It is important to delineate between the various modes in the analysis. For physical forcing of the actuation system, these will be denoted as azimuthal-Fourier forcing modes, described in § 3.3.2. For the low-dimensional representation of the near-field pressure, these will be referred to as azimuthal Fourier-filtered pressure modes, as outlined in § 3.3.2. The azimuthal-Fourier forcing modes and azimuthal Fourier-filtered pressure modes will be represented with an M followed by the respective mode number.

When addressing the low-dimensional velocity field, POD is performed to extract spatial eigenfunctions and time dependent expansion coefficients. The spatial eigenfunctions will be denoted as the spatial POD velocity modes, $\phi(\vec{x})$ (see equation 4.28) and the time dependent expansion coefficients will be referred to as temporal POD velocity modes, $a_n^u(t)$. Similarly, the temporal low-dimensional acoustic modes will be referred to as temporal POD acoustic modes, $a_k^p(t)$. Lastly, when referring to the linear mapping matrix, C_{kn}^{pu}, we will refer to these as OID modes, corresponding to a specific k and n as described in § 4.3.

Chapter 5

Large-Window Flow Field

In order to observe the effects of the open and closed-loop control on the flow field, a large-window PIV (LWPIV) setup is implemented to capture a sizeable interrogation region of the jet in the streamwise direction (approximately six jet diameters). The area of interest is the region around the collapse of the potential core ($\sim 6D$), and thus the LWPIV viewing region is centered at $6D$. As mentioned in § 2.2.4, three cameras are used to simultaneously sample the flow field from approximately $3.25D$ to $9D$ in the streamwise direction. The sampling rate of the cameras allow for data acquisition of $4\ Hz$ for each PIV window. The following chapter presents velocity field data, both in its raw form as well as with low-dimensional representations using the POD. In addition, near-field pressure spectra and far-field sound pressure levels are also presented with respect to the various flow control schemes.

5.1 LWPIV Microphone and Camera Setup

The configuration of the three camera setup and the twelve far-field microphones are seen in Figure 5.1. As previously mentioned in § 2.2.3, the additional acoustic treatment on each microphone (seen in Figure 5.1) is the result of an extensive study conducted in December

2012 to mitigate the low frequency reflections from the walls of the chamber. The far-field pressure spectra previously revealed low frequency oscillations, particularly seen at the 75° and 90° (in-plane) microphones.

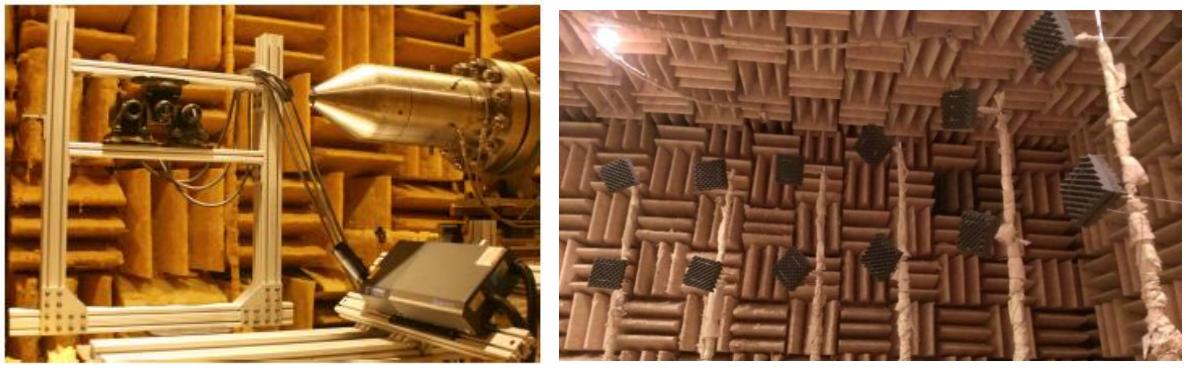

Figure 5.1: Large-window PIV camera configuration (left) and far-field microphone configuration (right)

Due to their position in the chamber, these particular microphones are close to the chamber walls. As a result of various facility modifications [250] and general wear and tear, the wedges on this particular wall have been slightly degraded, thus causing low frequency reflections of the acoustic waves to the sideline microphones. The study conducted has shown that the additional acoustic treatment mitigates the low frequency reflections from the walls. This can be seen in the far-field spectra at the 90° in-plane microphone (see Figure 5.2). The acoustic treatment was then placed on all far-field microphones to ensure low frequency reflections are minimized at all locations. Similar trends are seen for the microphone at 75° which will be seen in the presentation of all far-field spectra in subsequent sections.

For the flow field measurements, the three cameras are arranged with a slight overlap in the viewing field such that the images can be stitched together, to obtain a large interrogation region. The stitching of the individuals windows was done during post-processing using an algorithm developed by Shea *et al.* (2014) [207]. The stitching of the simultane-

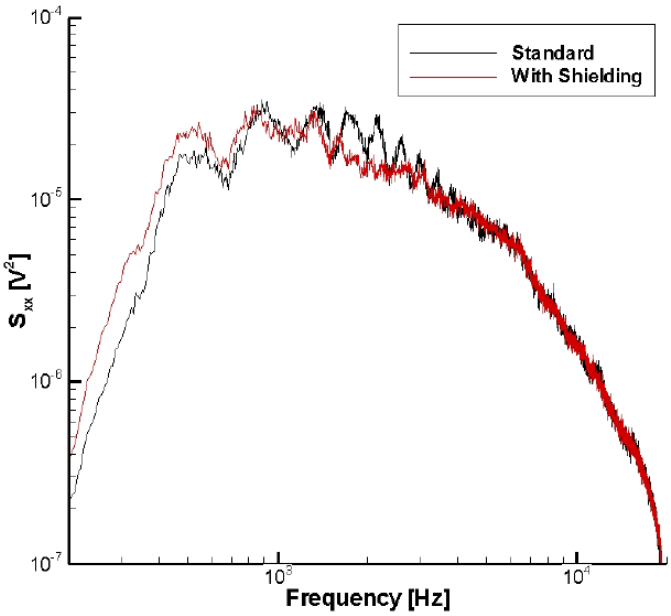

Figure 5.2: Reduction of low frequency oscillations due to additional acoustic treatment of microphones: 90° microphone spectra at 75D

ously sampled PIV images is done in three steps. The first step is to identify the optimal offset locations between two consecutive images. From the calibration of the PIV image frames, a relationship between the pixel spacing and the physical dimensions is obtained. This relationship is known as the scale factor and the second step of the algorithm is to adjust these quantities, as the calibration of the PIV images must be done for each camera separately. Finally the information from all three cameras are combined onto a large grid using a weighted average in the overlap region.

In order to calculate the optimal offsets between the images, the streamwise, fluctuating velocity is computed for the two windows. Since the inspection regions are simultaneously sampled, it is expected that the velocity in the overlap regions is the same within the uncertainty of the measurement (for PIV uncertainty see Appendix A). With this in mind, a least-squares residual was then computed to determine the optimal offset that minimizes the error in the overlap of the two inspection regions. Figure 5.3 shows an example of the

residual map where the minimum value is the position of the optimal offset. In Figure 5.3, it can be seen that the entire window was used to find the optimal offset. This was only done initially, and thus once the approximate optimal offset was known, a smaller window was used to reduce the computational time. The process is then repeated for each snapshot until the values converge. This offset is carried through the rest of the calculations for stitching the inspection regions together.

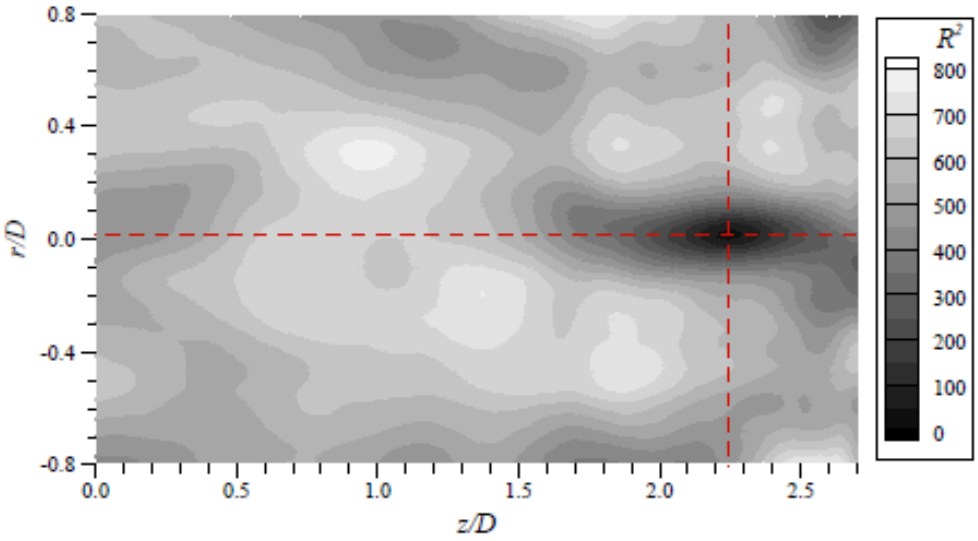

Figure 5.3: Residual map for determining the optimal offset between inspection regions, Shea *et al.* (2014) [207]

The second step in the stitching algorithm is to readjust the scale factors between inspection regions, due to the variability in the calibration procedure. This is done in a similar fashion using a least-squares method. Once again the optimal scale factor is determined by minimizing the residual in the overlap regions. Once the optimal offset is determined, the scale factor is found based on the new overlap region. As the inspection regions are compared in the overlap, the scale factor minimizing the error is the optimal value. Once again, an example of the residuals over a range of scale factors is presented (see Figure 5.4). This process is again repeated for each snapshot until convergence is reached.

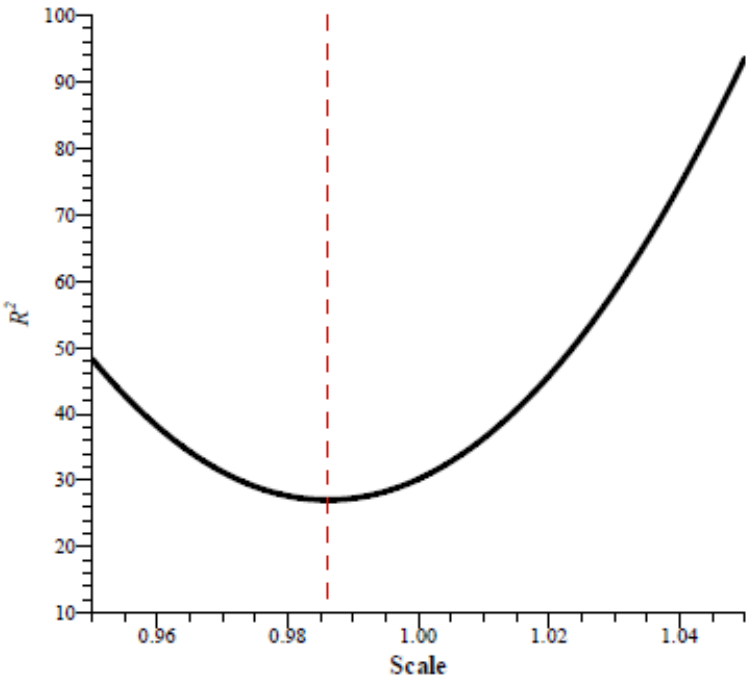

Figure 5.4: Residual plot for determining the optimal scale factor between inspection regions, Shea *et al.* (2014) [207]

After the optimal offsets and scale factors are determined, the final step in the stitching algorithm is to interpolate the overlap information onto the larger grid. This is done for each snapshot, applying the appropriate offset and scale factor. The small windows are combined using a linear weighting in the overlap region. Since there are three cameras in the setup, the offsets and scale factors are determined for cameras 1 and 2, and then for cameras 2 and 3. The last step involves interpolating all of the data onto one large grid giving the full LWPIV image. A single snapshot of the instantaneous streamwise velocity contours from each camera can be seen in Figure 5.5. As can be seen from this figure, the stitching algorithm described is suitable since all images are captured simultaneously and thus the instantaneous velocity is the same in the overlap region of the interrogation windows.

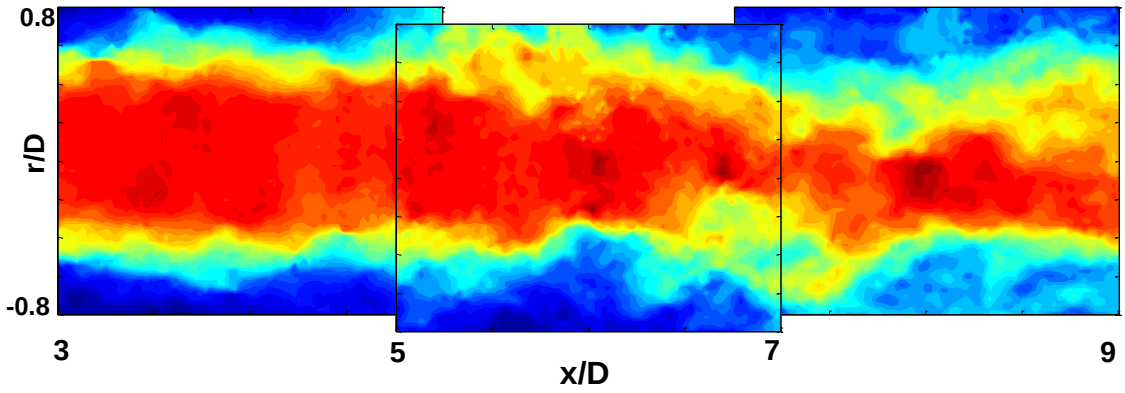

Figure 5.5: Instantaneous streamwise velocity contours for each camera in the LWPIV setup before the stitching algorithm is applied

In the subsequent sections, the data presented is obtained by applying the stitching algorithm to each individual data set. The next sections will look specifically at the full LWPIV in the context of the effects of active flow control on the velocity field and far-field acoustics.

5.2 Velocity Field

The following section focuses on the effects of four different forms of active flow control, both open and closed-loop, as outlined in § 3.3.2 (see Figure 3.21). For the uncontrolled data set (which will be referred to as the baseline case), 500 snapshots are acquired, while each control case contains 300 snapshots. The forcing frequency of the synthetic jet actuation system is 1200 Hz, corresponding to a Strouhal number of 0.30. For the data to be presented, the names of the control cases are abbreviated according to Figures 3.20 and 3.21 in § 3.3.2.

After the stitching algorithm described in § 5.1 is applied, the full large window is obtained for each snapshot. A sample snapshot for the baseline case is seen in Figure 5.6. The masked regions in the figure, indicated by the white rectangles (which are seen in all

subsequent LWPIV plots), represent shadows from the azimuthal arrays of *Kulites* at 6D and 8D downstream. The sensors are located between the PIV plane and the cameras and therefore show up as shadows, and are masked out for this purpose. It is important to note that the sensors themselves are not in the flow field, but are masked to avoid biases in the POD and other subsequent analyses. In order to further validate the stitching algorithm, the second moment (RMS) is shown in Figure 5.7. The seams between the three different interrogation regions can not be seen in the mean or RMS velocity contours. The corresponding RMS plots for each of the control cases can be found in Appendix B. A sample of one fully stitched PIV snapshot for each control case is seen in Figures 5.8 - 5.11.

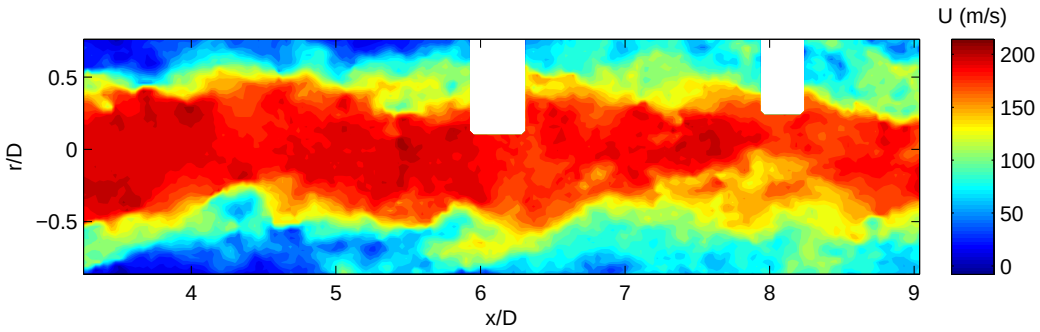

Figure 5.6: Fully stitched LWPIV baseline snapshot: instantaneous streamwise velocity contours

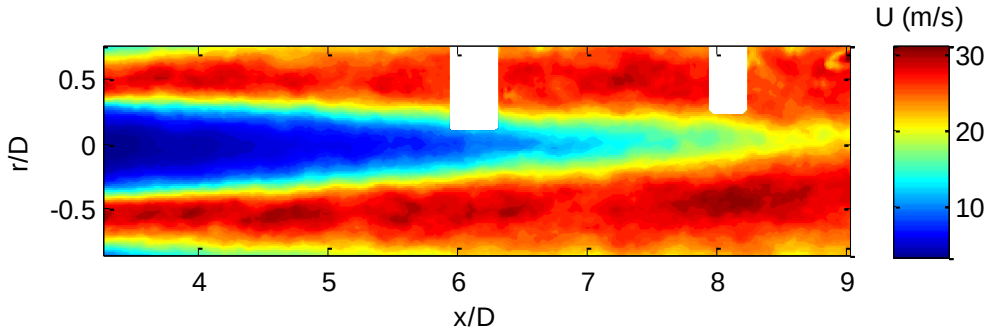

Figure 5.7: Fully stitched LWPIV baseline snapshot: streamwise RMS velocity contours

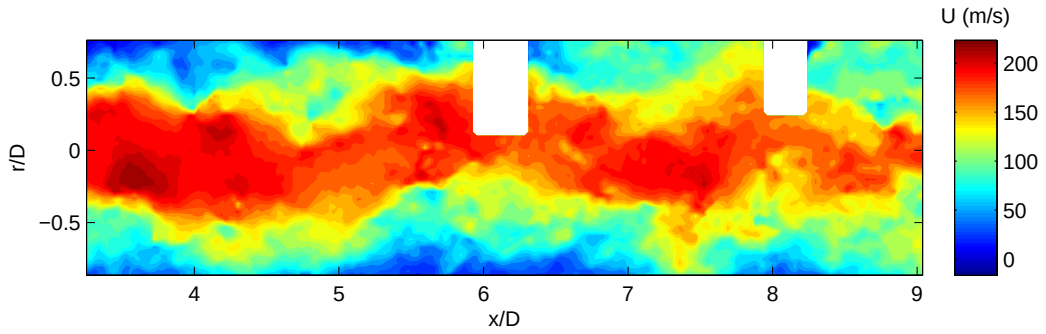

Figure 5.8: Fully stitched LWPIV, OLC1 snapshot: instantaneous streamwise velocity contours

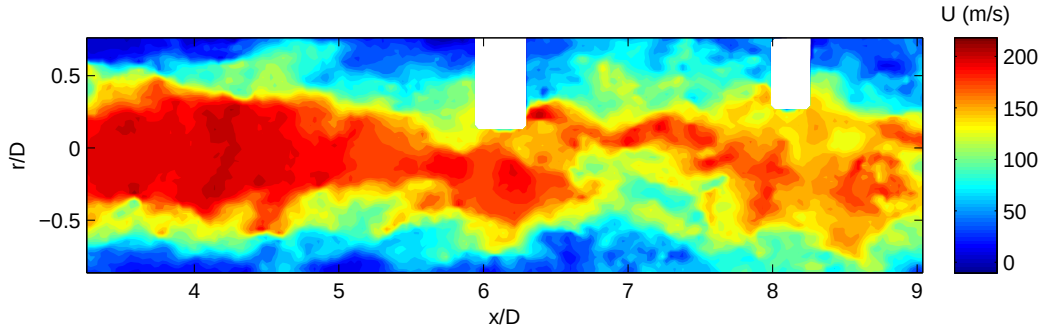

Figure 5.9: Fully stitched LWPIV, OLC2 snapshot: instantaneous streamwise velocity contours

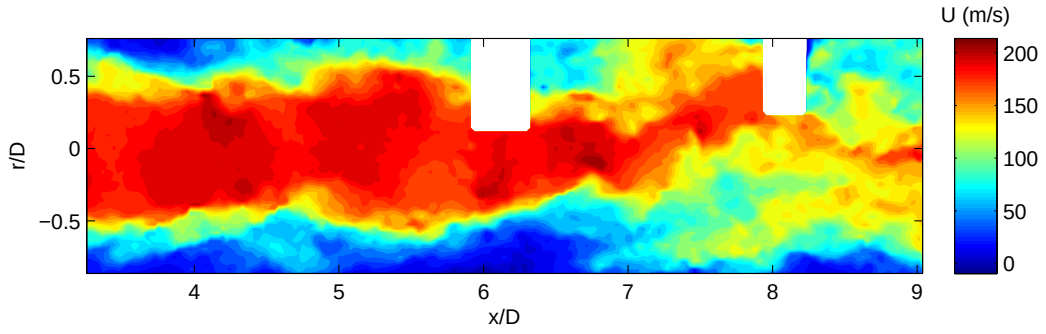

Figure 5.10: Fully stitched LWPIV, CLC1 snapshot: instantaneous streamwise velocity contours

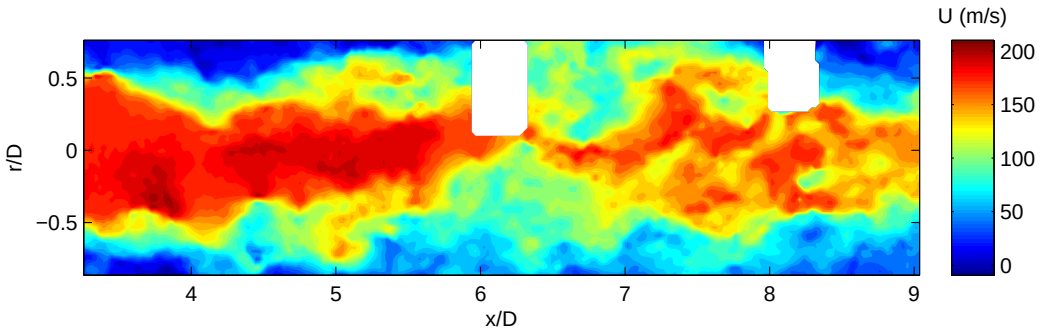

Figure 5.11: Fully stitched LWPIV, CLC2 snapshot: instantaneous streamwise velocity contours

The instantaneous snapshots of the velocity field indicate that the flow control has indeed altered the structures in the flow field in some way, for all cases as compared to the baseline jet. In order to gain a better understanding of how the flow control has altered the velocity field, the mean flow is observed for each of the control cases (in comparison to the uncontrolled jet).

5.2.1 Mean Velocity Flow Field

As indicated by the instantaneous velocity snapshots, the active flow control tends to enhance the mixing of the jet by inducing streamwise vorticity via the actuation input at the nozzle lip. This effect is also observed in the mean flow field, as seen in Figures 5.12 - 5.16. Both the open and closed-loop forcing cases seem to shorten the length of the potential core and cause shear layer expansion as a result of the actuation input.

The direct effects of the control on the mean flow field are somewhat subtle and difficult to see when looking at Figures 5.12 - 5.16. In order to see the effects of the control on the mean flow field more clearly, the mean velocity field of each control case is subtracted from the baseline to obtain a residual mean velocity field of the control, as shown in equation 5.1.

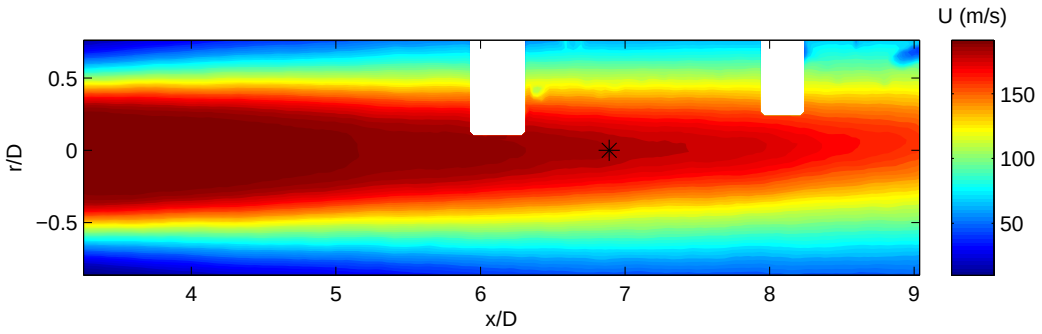

Figure 5.12: Streamwise Velocity Contours of Mean Flow: Baseline

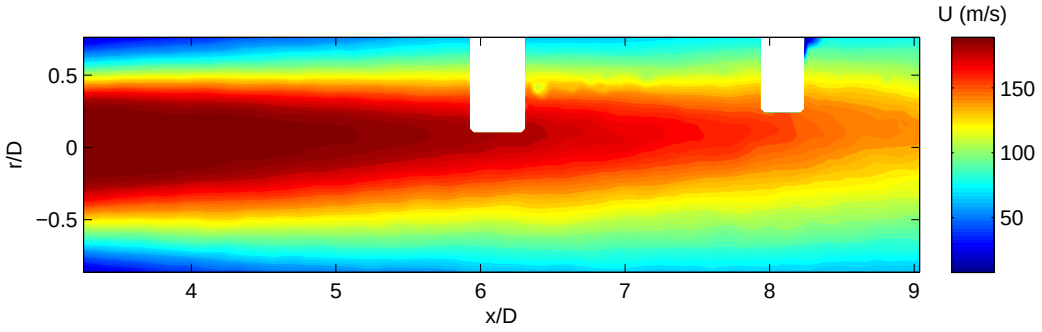

Figure 5.13: Streamwise Velocity Contours of Mean Flow: OLC1

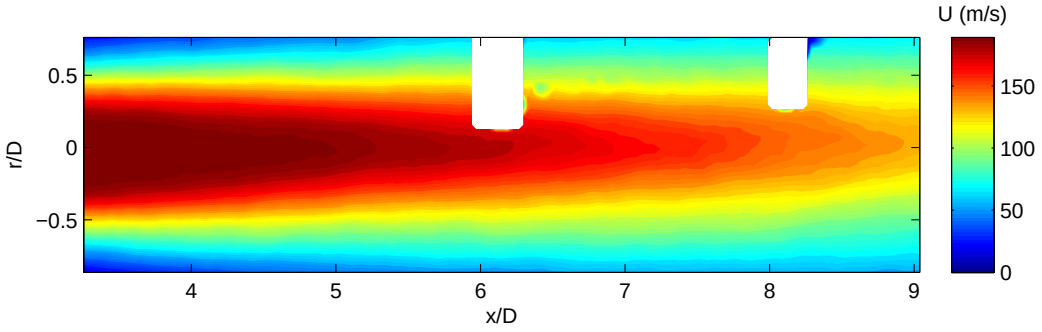

Figure 5.14: Streamwise Velocity Contours of Mean Flow: OLC2

$$\overline{U}_{residual} = \overline{U}_{baseline} - \overline{U}_{control} \tag{5.1}$$

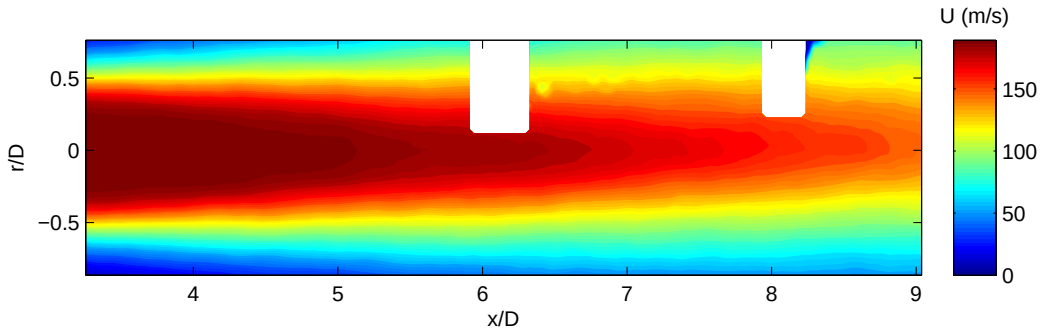

Figure 5.15: Streamwise Velocity Contours of Mean Flow: CLC1

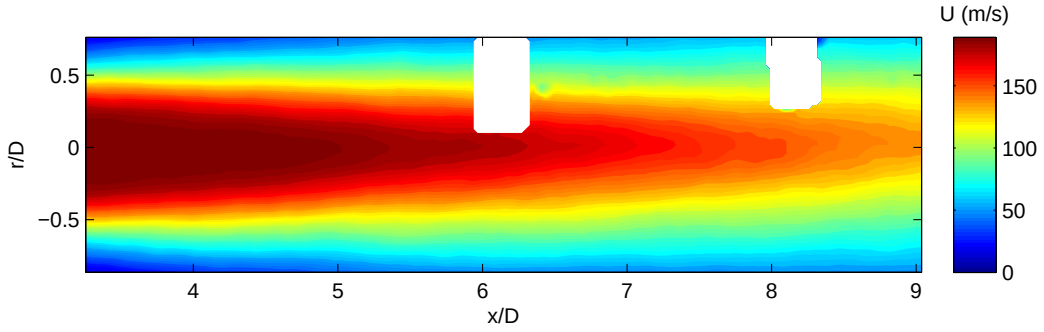

Figure 5.16: Streamwise Velocity Contours of Mean Flow: CLC2

Figures 5.17 - 5.20 show the mean flow residuals with the baseline as the reference (Figure 5.12). For the *OLC1* case in which Fourier-azimuthal mode 1 is implemented, the jet appears to be vectored upwards as a result of the control. This vectoring is not observed in the other control cases, indicating it is something inherent to the *OLC1* control case. The exact reason for this vectoring is not fully understood at this point, however one possible explanation is that the Fourier-azimuthal mode 1 forcing in the open-loop configuration induces an initial condition which causes a slight vectoring of the jet. The is not seen in the other open-loop case, where all actuators are driven in phase. Moreover this is not seen in the *CLC1* case, most likely due to the fact that the closed-loop feedback allows the control system to turn on and off, recovering from the imposed asymmetry.

Since the open-loop forcing is always on, with no feedback, it is possible that the mode

1 forcing causes an inherent vectoring of the jet. The asymmetry of the flow seen in the mean flow residual for the *OLC1* case implies that the mode 1 open-loop forcing has potentially induced a preferred instability in the jet. Another possible explanation for the vectoring of the jet in this particular case, is that some of the actuators failed during the experiments due to excess olive oil residue from PIV seeding. Since the exact reason for the asymmetry in case *OLC1* is unknown, more experiments should be conducted in the future to isolate the differences observed.

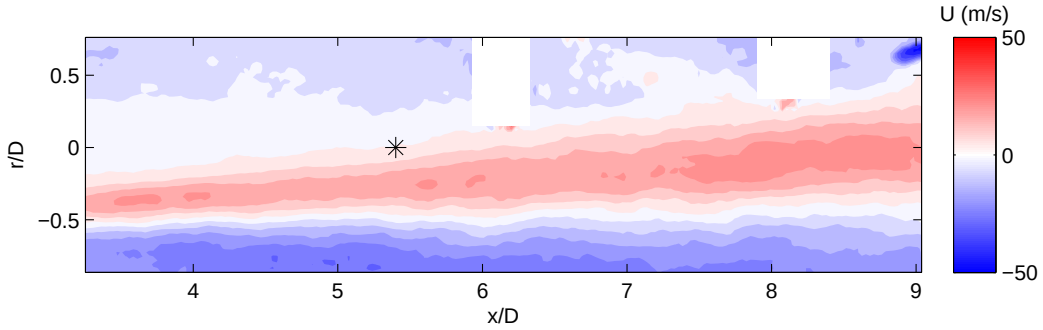

Figure 5.17: Residual Mean Flow: OLC1

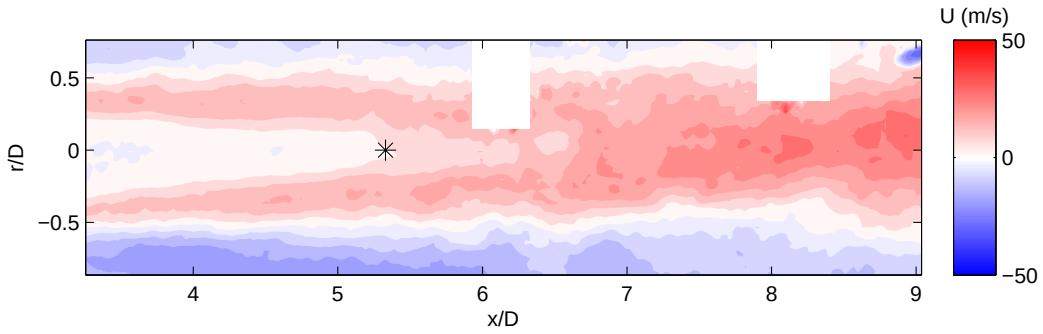

Figure 5.18: Residual Mean Flow: OLC2

The mean residual plots also indicate that both the *OLC2* and *CLC2* cases have a similar effect on the mean flow, while the *CLC1* case leaves the jet relatively unchanged with respect to the other cases. The positive velocity (indicated by red) in the residual plots

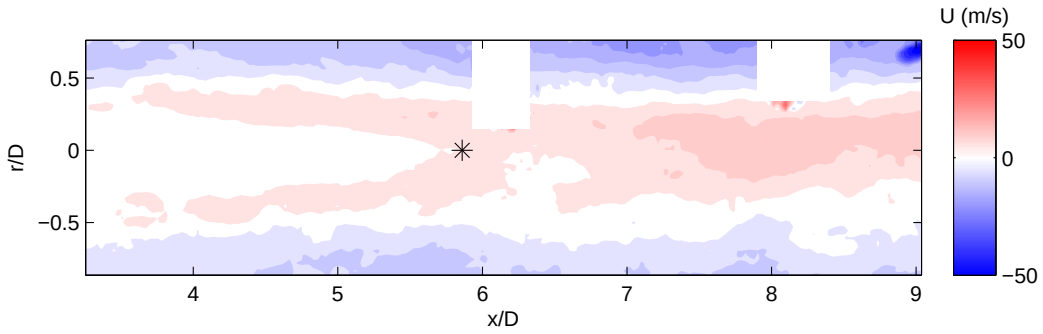

Figure 5.19: Residual Mean Flow: CLC1

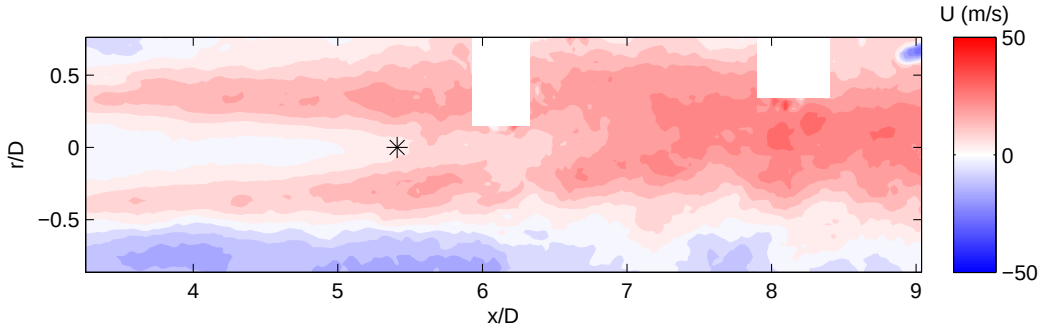

Figure 5.20: Residual Mean Flow: CLC2

represents a decrease in velocity with respect to the uncontrolled jet. This is a result of the imposed actuation which causes enhanced mixing and thus an early collapse of potential core. The negative velocity (indicated by blue) represents an increase in the velocity with respect to the uncontrolled jet. This is primarily seen in the shear layer regions, indicative of shear layer expansion as a result of the control input. The actuation at the nozzle imparts streamwise vorticity around the nozzle lip which causes the structures in the shear layer to mix more rapidly, leading to a large growth in the shear layer. The shear layers therefore collapse on one another sooner as a result, which leads to the early potential core collapse. In order to quantify the change in potential core length as a result of the control, the collapse is defined in the following way, according to Bogey & Bailly (2006) [34].

$$\overline{U}_c(x_c) = 0.95 \times U_j \tag{5.2}$$

Therefore, from equation 5.2, the collapse of the potential core occurs when the mean velocity along the centerline of the jet is 95% of the bulk velocity at the nozzle exit. Based on this definition, the potential core length for the different control cases as compared to the baseline case can be seen in Table 5.1.

Flow Case	*Potential Core Length*, x_c
Baseline	6.89D
OLC1	5.40D
OLC2	5.33D
CLC1	5.86D
CLC2	5.41D

Table 5.1: Potential core length as a result of active flow control

The potential core collapse for the baseline and control cases is also indicated by a black star on Figure 5.12 and Figures 5.17 - 5.20, respectively. These results show that the potential core length has been shortened by approximately $1 - 1.5D$ as a result of the active flow control.

In addition to the mean flow residuals, the effects of the control can also be observed by taking velocity profiles in the transverse direction of the jet at multiple downstream locations. Velocity profiles are taken at 4D and 7D downstream, corresponding to regions before and after the collapse of the potential core. These locations are also chosen so as to avoid the missing data at 6D and 8D. As seen in Figure 5.21, the control causes a reduction in the streamwise velocity in the potential core region (at 4D), indicating a shift in the potential core length, confirmed by the residual plots. Moreover at 7D, Figure 5.21 shows that the shear layer expands as a result of the control, indicated by the increased velocity in the shear layers (at large positive and negative r/D values), with respect to the baseline case. In addition, the velocity profile at 7D clearly shows the vectoring of the jet for the

OLC1 case, as this profile is asymmetric about the centerline (at $r/D = 0$).

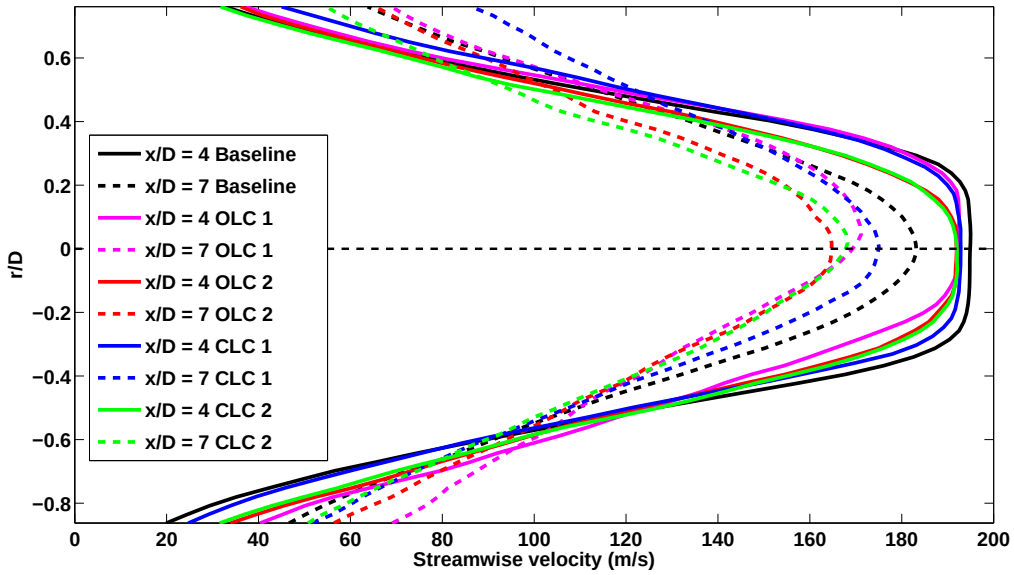

Figure 5.21: Streamwise velocity profiles for baseline and control cases at 4D and 7D downstream

The results presented thus far indicate that control authority over the jet has been achieved using both open and closed-loop flow control with different forms of feedback and actuation. The imposed flow control has caused shear layer expansion through enhanced mixing at the nozzle lip and thereby the potential core is shortened in all control cases, as compared to the uncontrolled, baseline jet. While both open and closed-loop control strategies appear to have similar effects on the flow field in terms of the potential core length, the closed-loop control is more suitable in practical applications. The first reason is that asymmetries in the form of vectoring are not seen in the closed-loop cases. Moreover in a real system, the control strategy which requires less energy input to the system is desired. With respect to the actuation input signal, the open-loop has an RMS value of 3.08 volts, while the closed-loop requires less energy having an RMS value of 2.75 volts. In addition, the closed-loop control draws on intelligence from the system, in this case by continuously

sampling the near-field pressure in real time and feeding this information back to the actuation. These results have shown that closed-loop control is a more desirable form of flow control than open-loop in this particular case. To further assess the specific differences between each of the control cases, the near-field pressure, low-dimensional velocity field, and far-field acoustics are examined in the following sections.

5.3 Near-Field Pressure

The collapse of the potential core at approximately six and eight diameters downstream for the control and baseline cases, respectively, motivates the investigation of the near-field pressure at these locations. In order to make comparisons between the baseline and control cases, with respect to the near-field pressure, the spectral content of the signals will be investigated. This is done by looking at the mean squared second moment statistics, known as the two-sided power spectral density. The power spectral density of a signal is computed by performing the Fourier transform, as outlined by Bendat & Piersol (1971) [27] and Otnes & Enochson (1978) [173]. In the analysis t and f will represent time and frequency, respectively, while subscripts n and f will represent near and far-field, respectively. Therefore given a pressure signal, $p_n(t)$, for example, the two-sided power spectral density is given as follows:

$$S_{nn}(f) = \frac{1}{T}\langle|\hat{p}_n(f)|^2\rangle \tag{5.3}$$

In equation 5.3, $\hat{p}_n(f)$ is the fast Fourier transform (FFT) of the original signal and T is the block length. Therefore, $\langle\bullet\rangle$ implies the ensemble average over the total number of blocks. The FFT of the original signal is computed in the following way:

$$\hat{p}_n(f) = \int_0^T p(t)e^{-i2\pi ft}dt \tag{5.4}$$

As previously mentioned, equation 5.3 represents the two-sided power spectral density function. All of the results presented will be single-sided power spectral densities, denoted as $G_{nn}(f)$ [27, 173]. The single-sided power spectral density is computed by evaluating equation 5.3 over half of the domain. In order to compensate for this loss of energy, the resulting function is multiplied by a factor of two. Therefore, the following is obtained:

$$G_{nn}(f) = 2S_{nn}(f) \quad (0 < f < f_s/2) \tag{5.5}$$

where f_s is the sampling frequency.

Since the *Kulites* are arranged azimuthally, the pressure spectra are presented at each array in order to observe the axisymmetry (or lack thereof) as a result of the different control inputs. The arrangement of the *Kulites* is shown in Figure 5.22, with each color representing a pair of sensors at 6D and 8D, at the same azimuthal position. The near-field is sampled at $15kHz$ and low-pass filtered at $7.5kHz$. The array of sensors at 6D is used for the feedback signal in the flow control implementation. Since the potential core collapses closer to 8D for the baseline case and is shortened to approximately 6D for the control cases, only the 6D spectra will be shown for the control cases to compare to the baseline. The 8D spectra for the control cases can be found in Appendix B. The baseline near-field pressure spectra are observed in Figures 5.23 and 5.24.

In Figures 5.23 and 5.24, the colors correspond to the azimuthal location of each sensor in Figure 5.22. At 6D and 8D for the baseline case, the sensors collapse across the entire frequency band confirming the axisymmetry of the jet without the imposed control. The dominant frequency of the near-field pressure spectra decreases from 6D to 8D as the potential core collapses and jet evolves downstream. Figures 5.25 - 5.28 show the near-field pressure spectra at 6D for each of the control cases. The first important feature to note is the dominant frequency peak at $1200Hz$, corresponding to the forcing frequency of the actuators. Subharmonics of this frequency can be seen throughout the spectra.

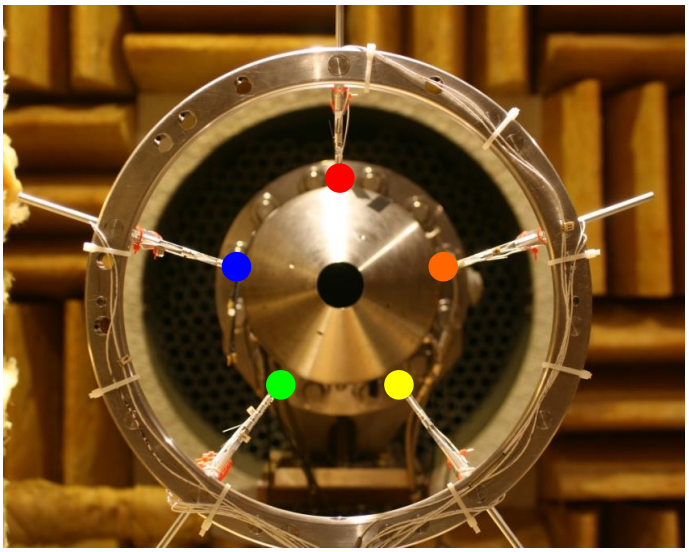

Figure 5.22: Near-field azimuthal pressure array

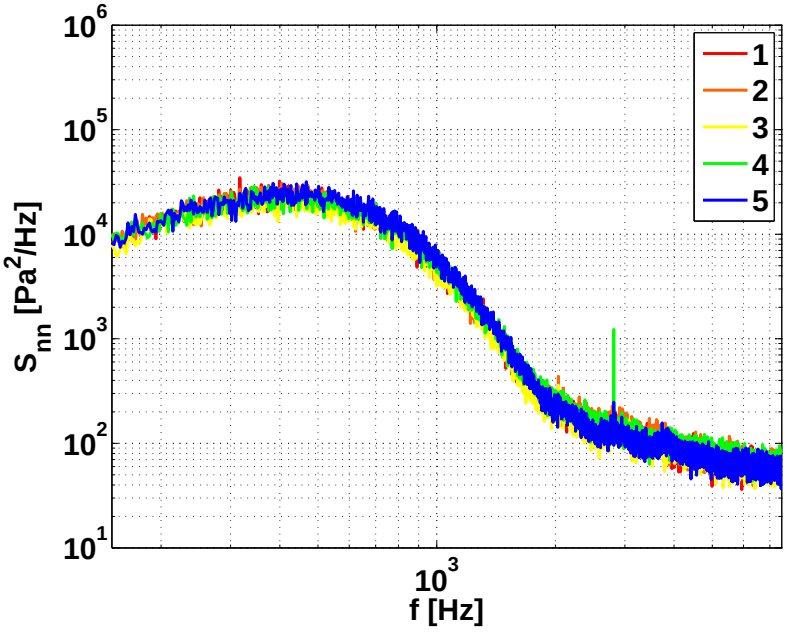

Figure 5.23: Near-field azimuthal pressure spectra: Baseline at 6D

For all control cases, the dominant frequency is preserved however the overall energy has increased, seen by the amplitude of the spectra, as compared to the baseline. This

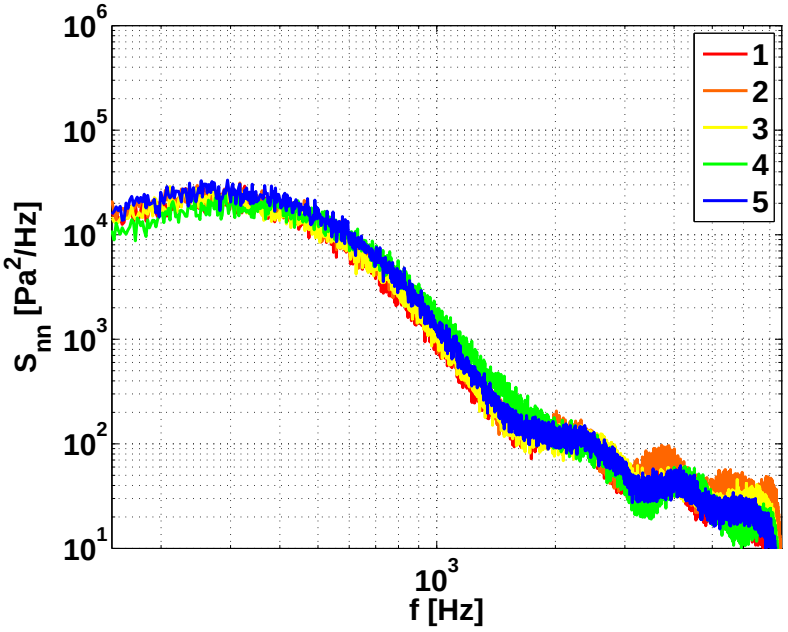

Figure 5.24: Near-field azimuthal pressure spectra: Baseline at 8D

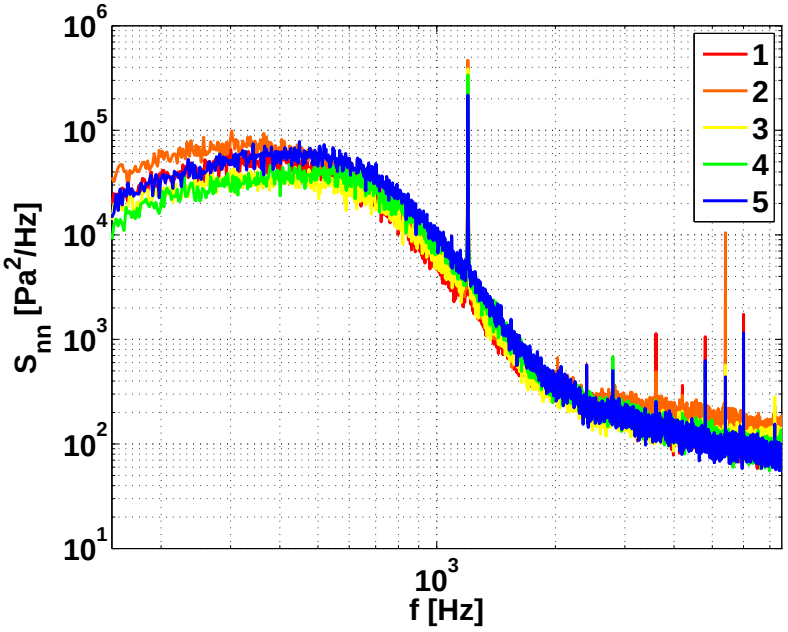

Figure 5.25: Near-field azimuthal pressure spectra: Open-Loop 1 at 6D

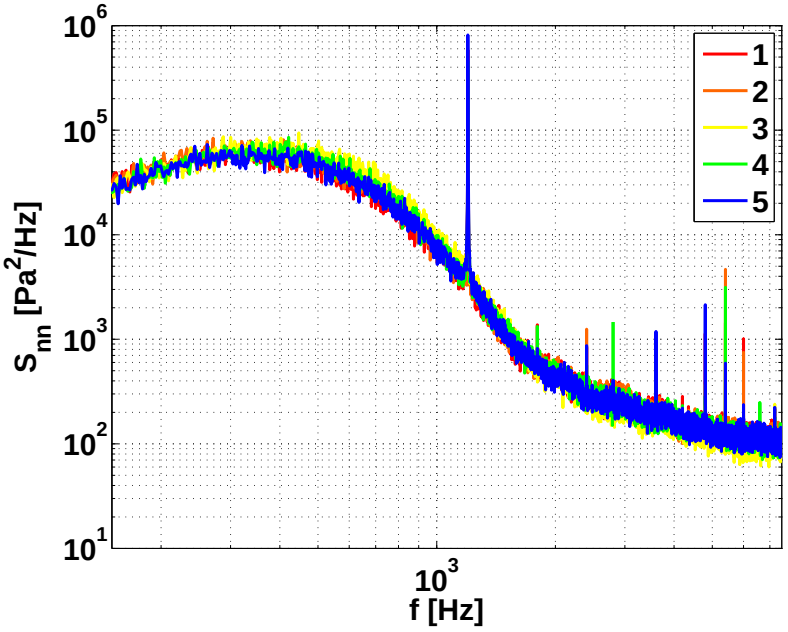

Figure 5.26: Near-field azimuthal pressure spectra: Open-Loop 2 at 6D

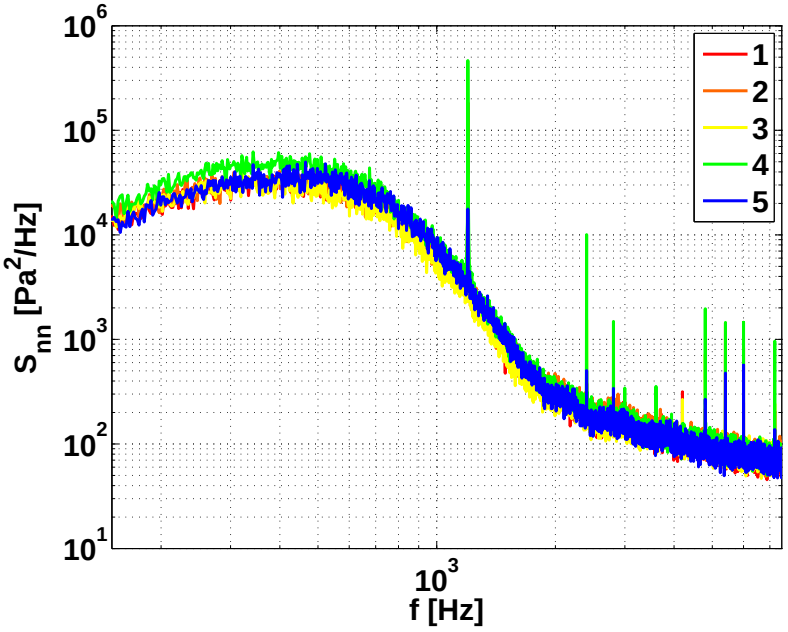

Figure 5.27: Near-field azimuthal pressure spectra: Closed-Loop 1 at 6D

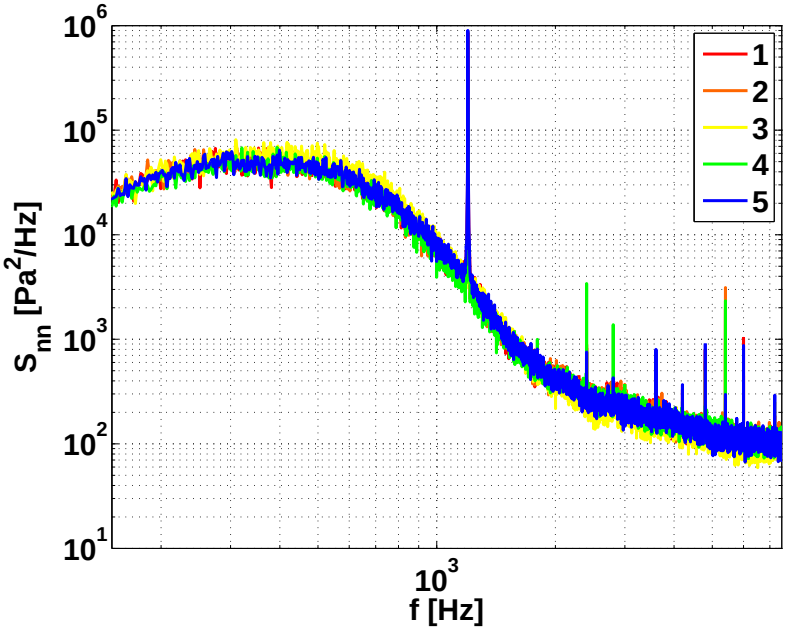

Figure 5.28: Near-field azimuthal pressure spectra: Closed-Loop 2 at 6D

is attributed to the fact that the control has increased the spreading rate of the jet, and ultimately adds energy to the system. All control cases except for the *OLC1* case keep the jet axisymmetric at this downstream location, evident by the collapse of the sensor signals across the entire frequency band. The *OLC1* cases seems to impose an asymmetry, which confirms the vectoring of the jet, seen in the mean residual plots previously shown. Despite the feedback and forcing mechanisms implemented, the other three control cases keep the jet axisymmetric out to 6D downstream, only increasing the energy as a result of the actuation.

5.4 POD Analysis

This section focuses on the application of the POD to the velocity field in order to observe the effects of the control from a low-dimensional standpoint. The POD allows one to obtain the large-scale, highly energetic structures in the flow field. The effects of the control can

therefore be observed by computing the deterministic spatial eigenfunctions, which are the building blocks of the flow field. A low-dimensional representation of the velocity field is also reconstructed from a select number of POD velocity modes, representing a particular amount of overall energy of the system. First, the convergence rate of the eigenvalues is observed, representing the energy distribution of the velocity POD modes.

5.4.1 Modal Convergence

Recalling from equations 4.16 and 4.17 that the summation of the eigenvalues accounts for the total kinetic energy of the system, it is often common practice to examine the convergence rate of the eigenvalues. This is useful for developing reduced-order models which extract a large portion of energy with the fewest number of modes. The convergence rate of the eigenvalues are shown in Figure 5.29 for the different control cases as compared to the baseline. All cases converge at the same rate with the exception of the baseline. For the baseline case, an additional 200 snapshots were acquired and thus converge a bit more slowly as compared to the control cases.

Despite the different number of snapshots between the baseline and control cases, there still exists a comparable convergence of the eigenvalues, recovering approximately 50% of the total kinetic energy with 25 modes (corresponding to 8% of the control modes and 5% of the baseline modes). This is seen more clearly in Figure 5.30. When the energy is normalized by the number of POD modes (*i.e* the number of snapshots), the convergence rate of each case is comparable; this can be seen in Appendix B.3.

Another way to look at the energy with respect to the POD modes is by extracting the individual energy contributions to each of the modes. Looking at the first 10 modes in Figure 5.31, which accounts for between $27\% - 32\%$ of the energy depending on the case (see Figure 5.30), it is observed that none of the individual modes contain more than 6% of the total kinetic energy.

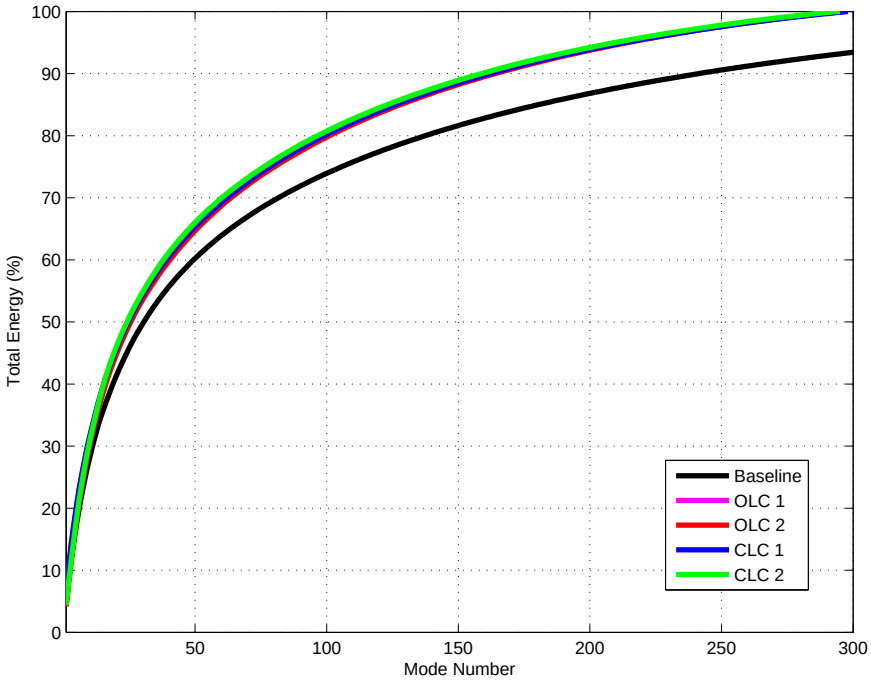

Figure 5.29: Cumulative energy in 300 modes for baseline and control cases

Figure 5.31 indicates a fairly uniform distribution of modes with a noticeable difference in the *OLC1 and CLC1* cases. In particular, these cases contain a large portion of energy in the first two modes as compared to the other cases. The Fourier-azimuthal mode 1 forcing induces an inherent "flapping" motion, captured by the first two POD velocity modes. The strong asymmetry that is imposed with this particular forcing dominates the energy in these first two POD modes.

5.4.2 Spatial Eigenfunctions

The effects of the control on the flow field are observed from the two most energetic spatial POD velocity modes, $\phi_i^{(1-2)}(\vec{x})$. Since there are two spatial dimensions, the eigenfunctions can be represented by the u and v components, corresponding to the streamwise and transverse directions, $\phi_u^{(n)}(\vec{x})$ and $\phi_v^{(n)}(\vec{x})$, respectively. Modes $\phi_i^{(3)}(\vec{x})$ - $\phi_i^{(5)}(\vec{x})$ for each of the

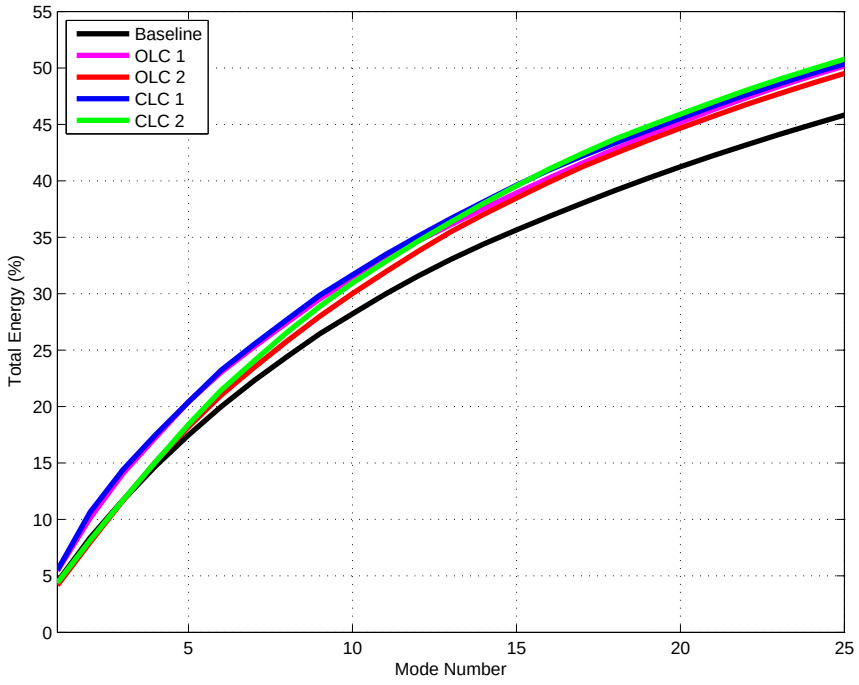

Figure 5.30: Cumulative energy in 25 modes for baseline and control cases

cases can also be found in Appendix B. These spatial eigenfunctions are computed from the fluctuating velocity field, where the mean flow has been subtracted from the instantaneous quantities. The mean flow is sometimes referred to as POD mode 0 in this regard. Looking at the fluctuating velocity is convenient for focusing on the shear layer, where interesting flow interactions are occurring. The first streamwise spatial eigenfunction, $\phi_u^{(1)}(\vec{x})$, for the baseline and control cases are shown in Figures 5.32 - 5.36.

Figures 5.32 - 5.36 show the effects of the different types of active flow control on the large scale structures in the flow field. For the baseline case, the development of large scale structures is not observed until approximately 7D downstream where the potential core begins to collapse. For cases *OLC2 and CLC2*, the development of structures can be seen further upstream as a result of the Fourier-azimuthal mode 0 forcing at the nozzle lip. This is consistent with the fact that the control shortens the potential core length as previously observed. For cases *OLC1 and CLC1*, the Fourier-azimuthal mode 1 forcing is clearly ob-

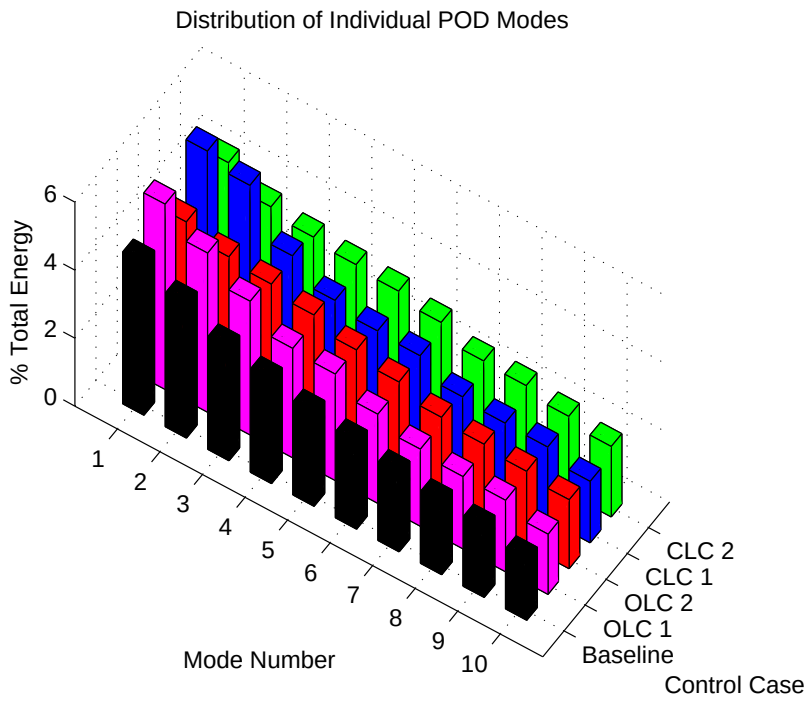

Figure 5.31: Energy distribution of the first 10 POD velocity modes for baseline and control cases

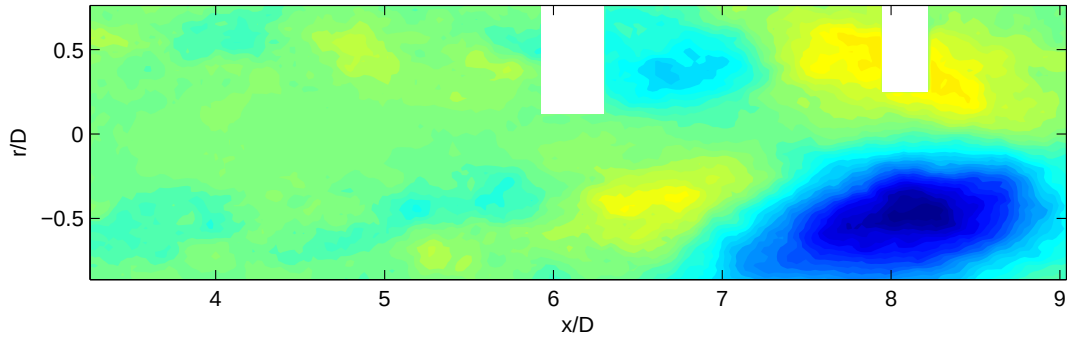

Figure 5.32: POD spatial eigenfunction, $\phi_u^{(1)}(\vec{x})$: Baseline

served by the opposite phase of the small scale structures in the top and bottom portions of the shear layer. Beyond the collapse of the potential core, the structures grow and become less organized due to the interaction of vortices caused by the collapse. Moreover,

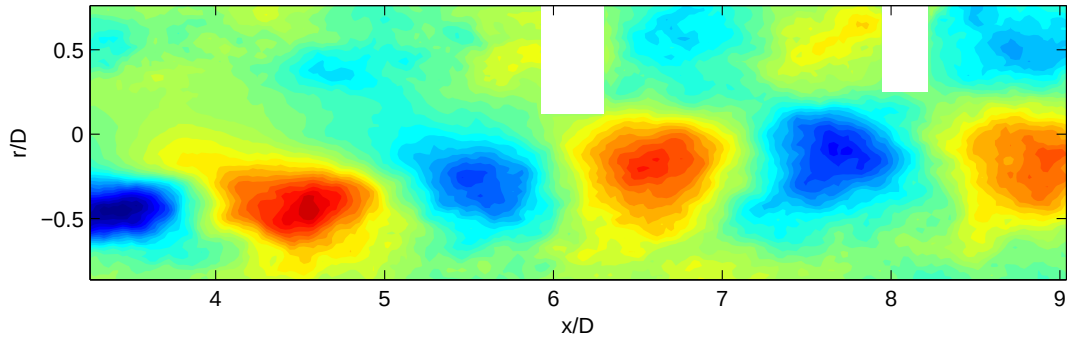

Figure 5.33: POD spatial eigenfunction, $\phi_u^{(1)}(\vec{x})$: OLC1

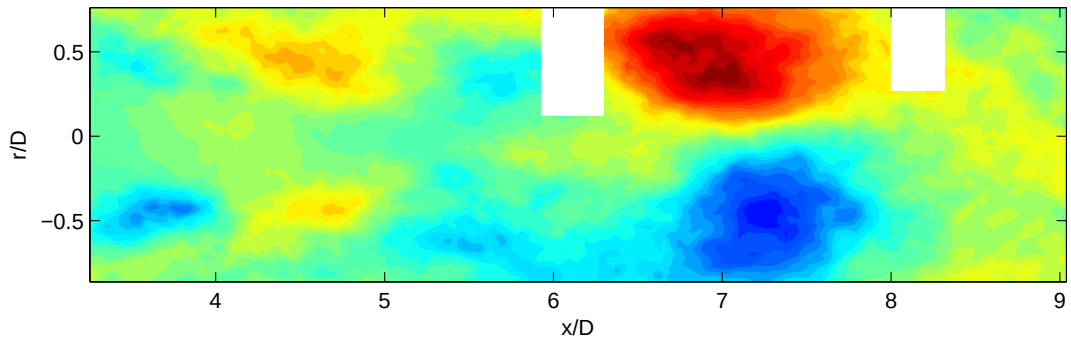

Figure 5.34: POD spatial eigenfunction, $\phi_u^{(1)}(\vec{x})$: OLC2

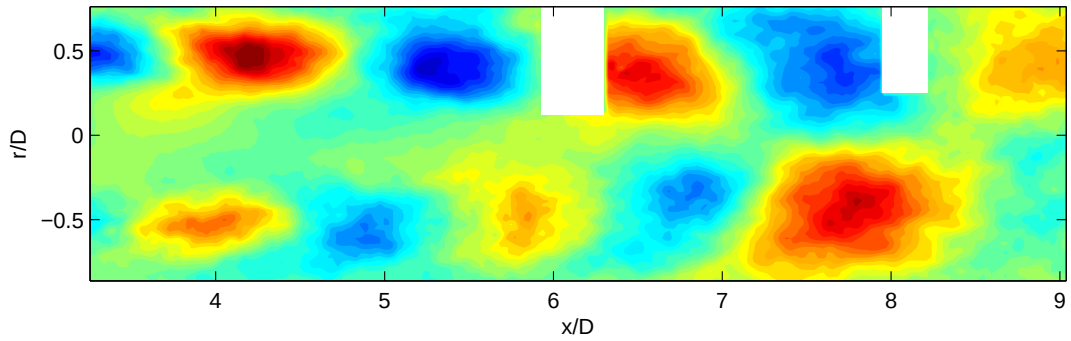

Figure 5.35: POD spatial eigenfunction, $\phi_u^{(1)}(\vec{x})$: CLC1

the strong asymmetry of the structures seen in case *OLC1* again supports the vectoring of the jet, possibly due to the open-loop forcing of Fourier-azimuthal mode 1. Looking more closely at Figure 5.33, the mode 1 forcing frequency can be directly extracted from first

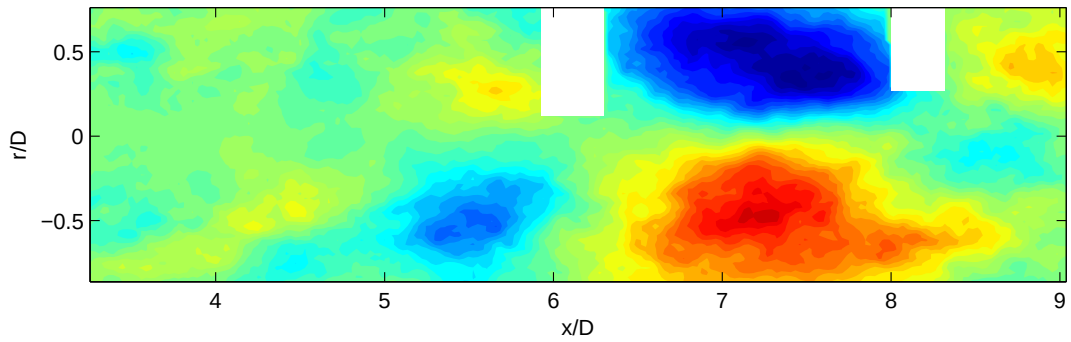

Figure 5.36: POD spatial eigenfunction, $\phi_u^{(1)}(\vec{x})$: CLC2

streamwise POD mode. Assuming a convection velocity in the shear layer of 60% of the bulk velocity ($\sim 120\ m/s$) [35], the forcing frequency can be calculated by observing the spacing of the spatial structures having the same sign. If we assume this to be approximately two jet diameters, then the forcing frequency is calculated to be 1200 Hz, the exact forcing frequency of the synthetic jet actuators. This confirms that the effects of the mode 1 forcing can clearly be extracted from the most energetic POD velocity mode.

The transverse component of the first POD mode, $\phi_v^{(1)}(\vec{x})$, for all cases can be seen in Figures 5.37 - 5.41. Again similar trends are observed for the v component in that the spatial structures of cases *OLC2 and CLC2* resemble that of the baseline, however, more activity is seen further upstream for the control cases, as is expected. Also seen from the v component of the spatial eigenfunctions is the Fourier-azimuthal mode 1 forcing for cases *OLC1 and CLC1*, with case *OLC1* exhibiting the asymmetric behavior as previously observed. For these cases, the Fourier-azimuthal mode 1 forcing keeps the flow structures organized while greatly enhancing the overall mixing in the shear layers.

Similar trends are seen for the second spatial POD mode, where the u component for all cases are seen in Figure 5.42 - 5.46. POD mode 2 inherently has less energy than mode 1, but exhibits similar spatial structures for each of the control cases. Again the dominance of the Fourier-azimuthal mode 1 forcing is clearly observed for cases *OLC1 and CLC1*,

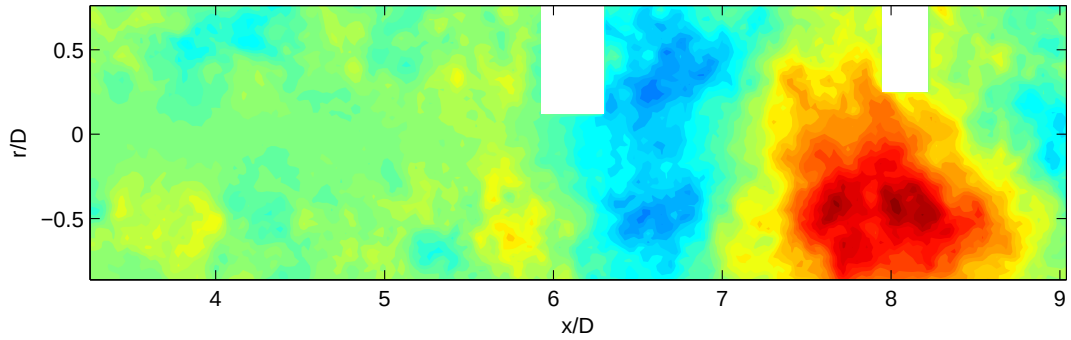

Figure 5.37: POD spatial eigenfunction, $\phi_v^{(1)}(\vec{x})$: Baseline

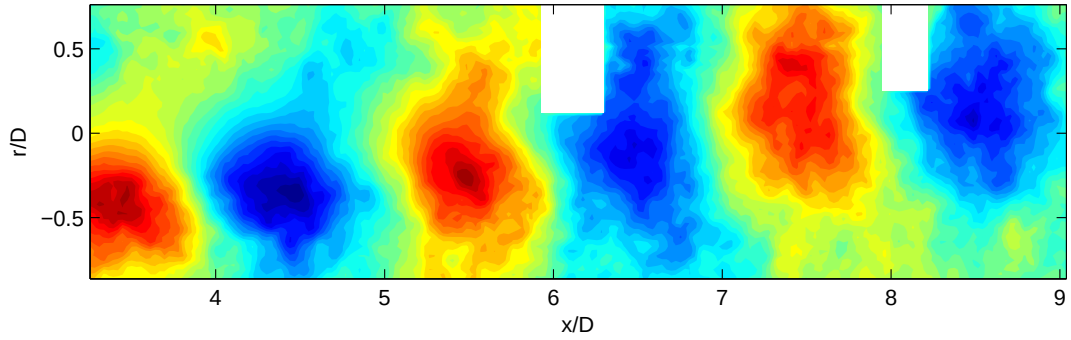

Figure 5.38: POD spatial eigenfunction, $\phi_v^{(1)}(\vec{x})$: OLC1

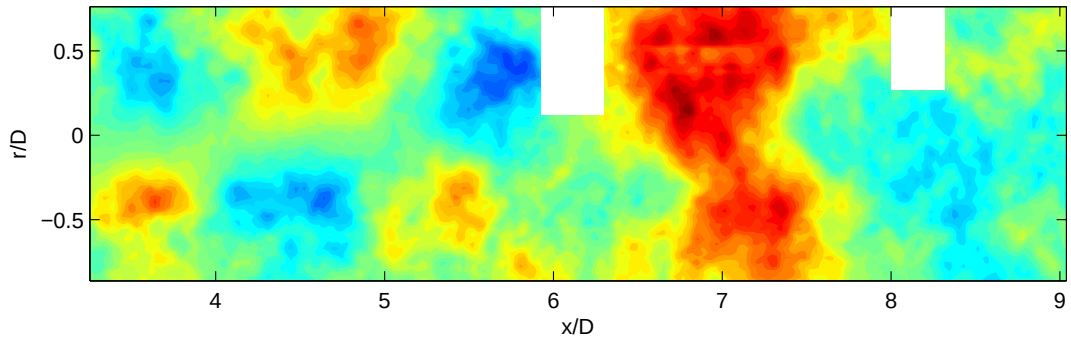

Figure 5.39: POD spatial eigenfunction, $\phi_v^{(1)}(\vec{x})$: OLC2

whereas cases *OLC2 and CLC2* exhibit similar features to that of the baseline. When looking at the v component of the second POD mode in Figures 5.47 - 5.51, similar trends are again observed as compared to the v component of the first POD mode.

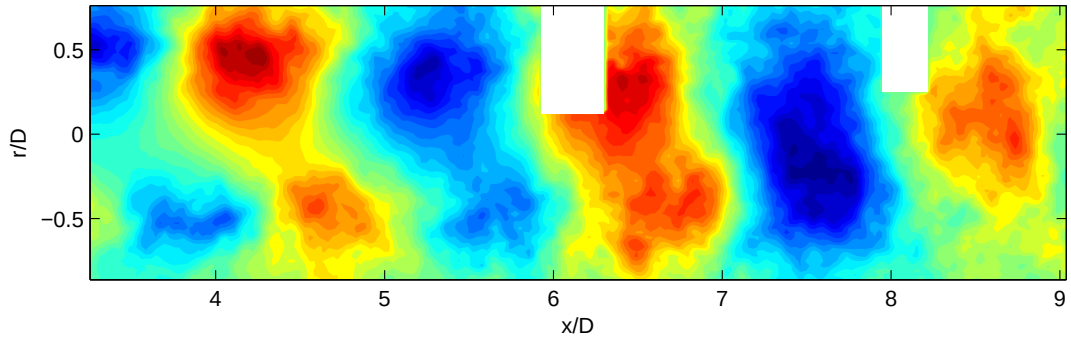

Figure 5.40: POD spatial eigenfunction, $\phi_v^{(1)}(\vec{x})$: CLC1

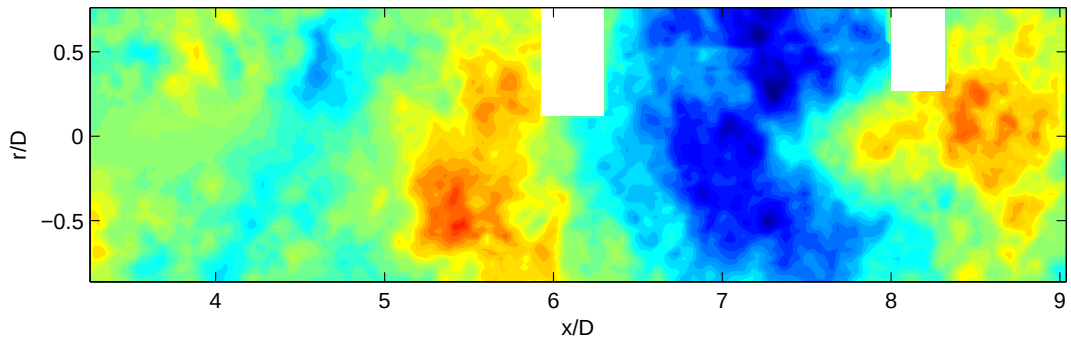

Figure 5.41: POD spatial eigenfunction, $\phi_v^{(1)}(\vec{x})$: CLC2

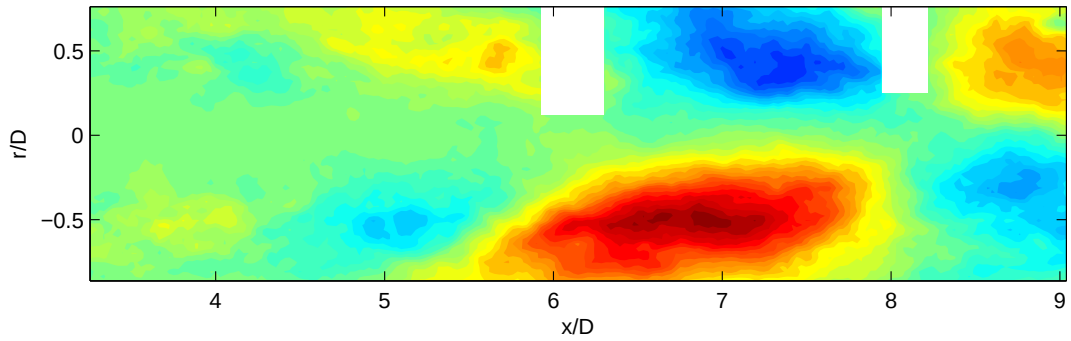

Figure 5.42: POD spatial eigenfunction, $\phi_u^{(2)}(\vec{x})$: Baseline

The results presented have shown that the flow control alters the large scale, highly energetic flow structures by enhancing mixing and decreasing the potential core length. In particular, with cases *OLC1 and CLC1*, the Fourier-azimuthal mode 1 forcing keeps the

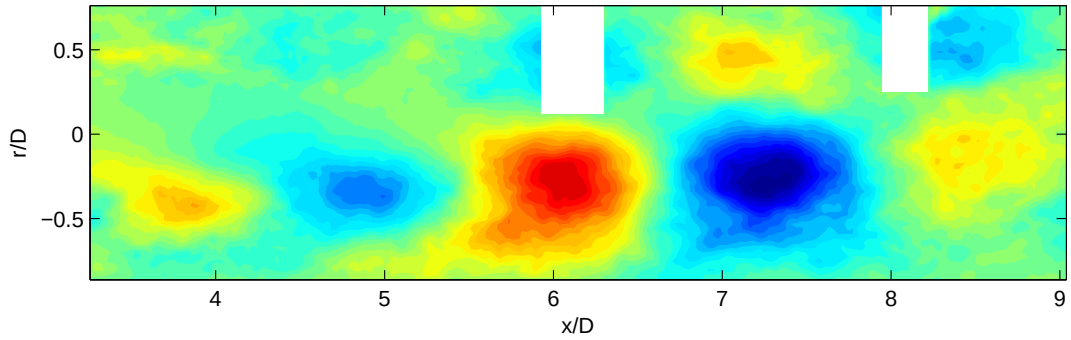

Figure 5.43: POD spatial eigenfunction, $\phi_u^{(2)}(\vec{x})$: OLC1

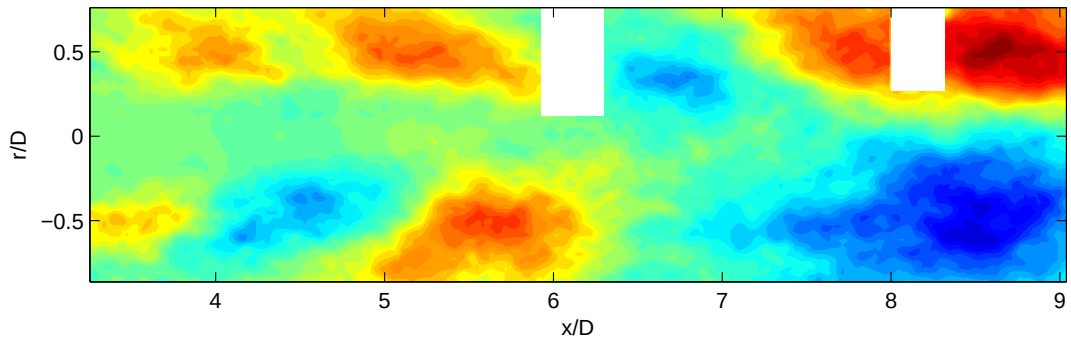

Figure 5.44: POD spatial eigenfunction, $\phi_u^{(2)}(\vec{x})$: OLC2

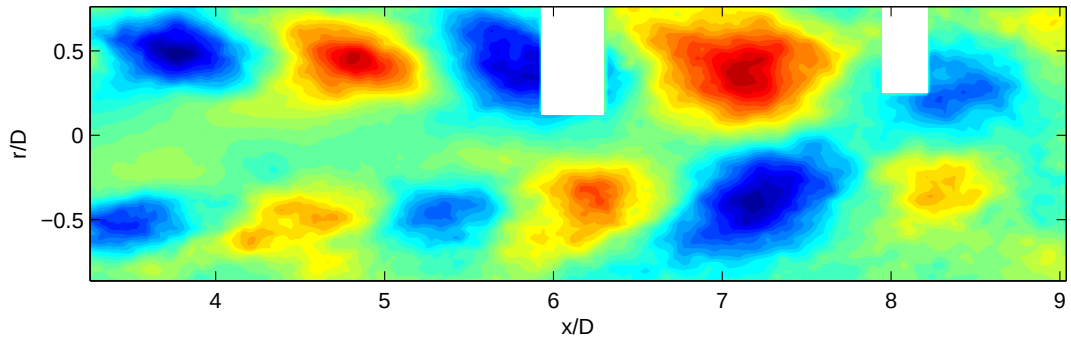

Figure 5.45: POD spatial eigenfunction, $\phi_u^{(2)}(\vec{x})$: CLC1

flow organized while creating small structures propagating through the shear layer. This is evident in both POD modes 1 and 2, for the u and v components alike.

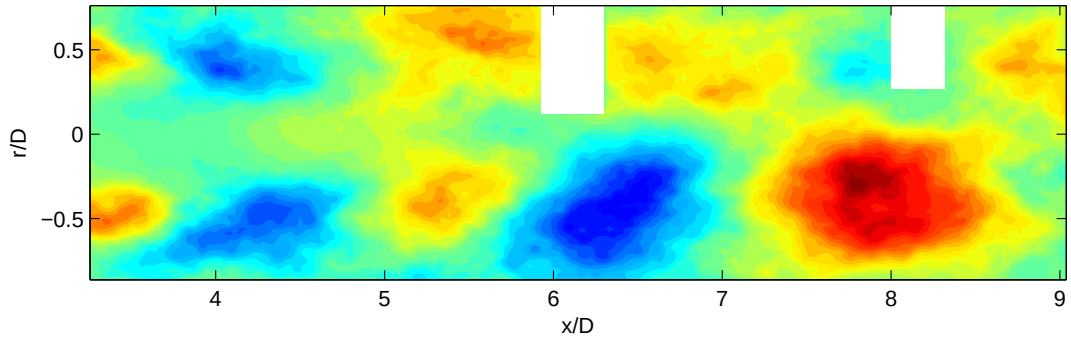

Figure 5.46: POD spatial eigenfunction, $\phi_u^{(2)}(\vec{x})$: CLC2

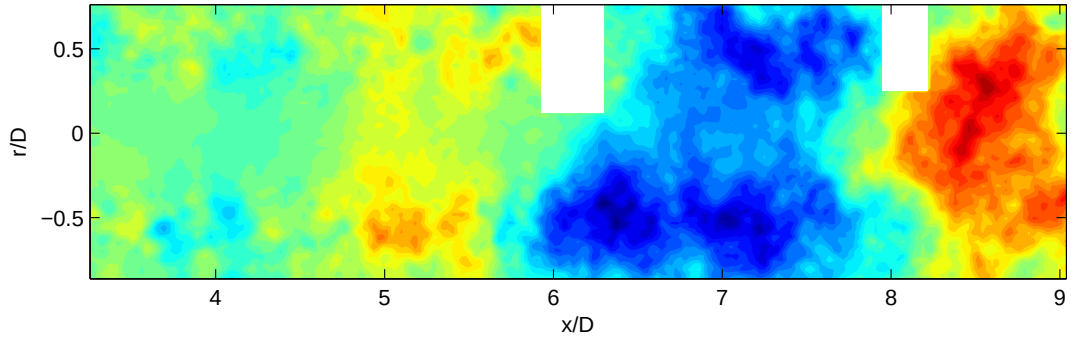

Figure 5.47: POD spatial eigenfunction, $\phi_v^{(2)}(\vec{x})$: Baseline

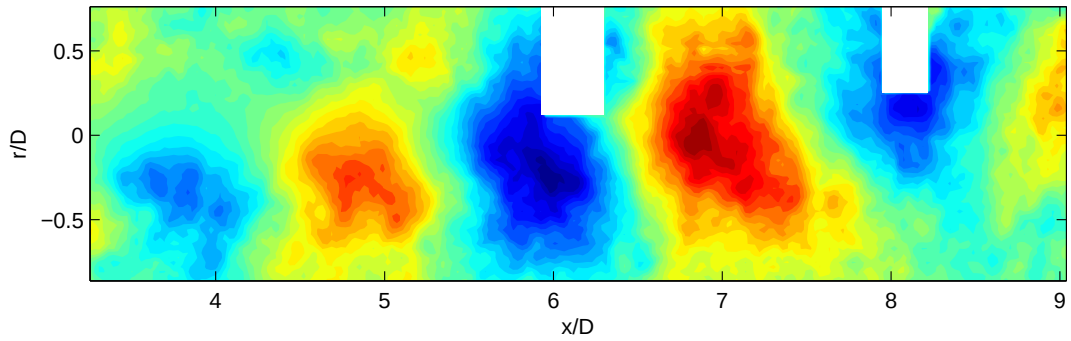

Figure 5.48: POD spatial eigenfunction, $\phi_v^{(2)}(\vec{x})$: OLC1

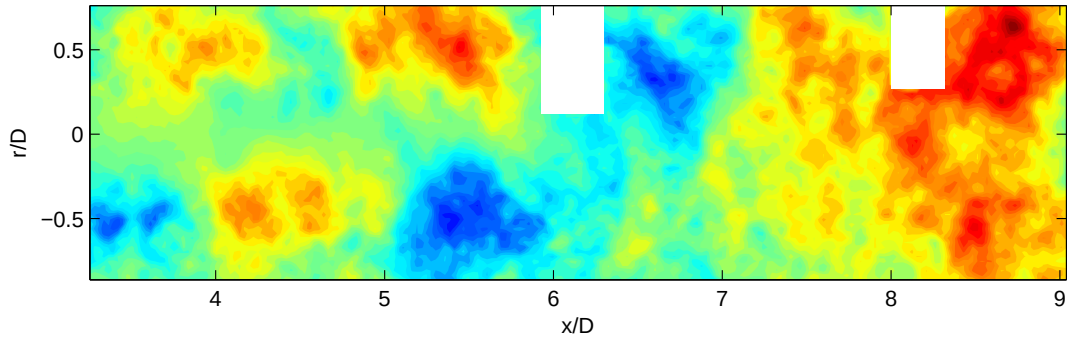

Figure 5.49: POD spatial eigenfunction, $\phi_v^{(2)}(\vec{x})$: OLC2

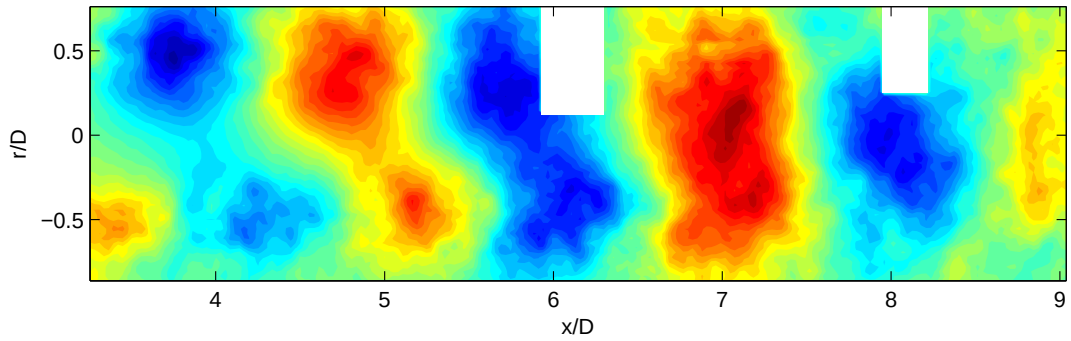

Figure 5.50: POD spatial eigenfunction, $\phi_v^{(2)}(\vec{x})$: CLC1

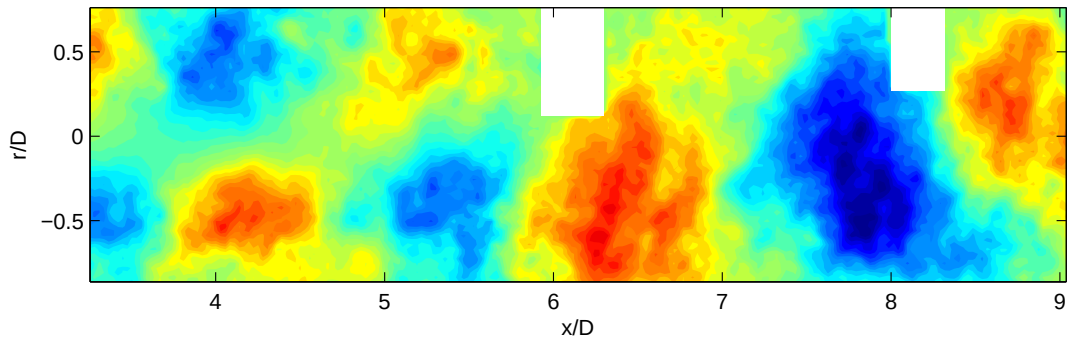

Figure 5.51: POD spatial eigenfunction, $\phi_v^{(2)}(\vec{x})$: CLC2

5.4.3 POD Reconstructions

In order to look at the full (PIV) velocity field from a low-dimensional perspective, reconstructions are performed using a truncated number of POD modes, as described by

equation 4.14. The original full velocity field is rebuilt using all of the POD modes in this equation, for reference. POD reconstructions can be performed for either the instantaneous field or the fluctuating field (in which the mean is subtracted). It has been shown that approximately 50% of the total energy is recovered with only 25 POD modes. Reconstructions are performed on the fluctuating velocity field using 25 POD modes, to see the effects of the control on the low-dimensional velocity field. All reconstructions are compared to the original flow field, where all POD modes are used. The instantaneous velocity field reconstructions using the POD can be found in Appendix B. In all of the figures to be presented, the streamwise fluctuating velocity contours are shown. The POD reconstructions for the baseline and control cases at a single snapshot ($t = 100$) are seen in Figures 5.52 - 5.56.

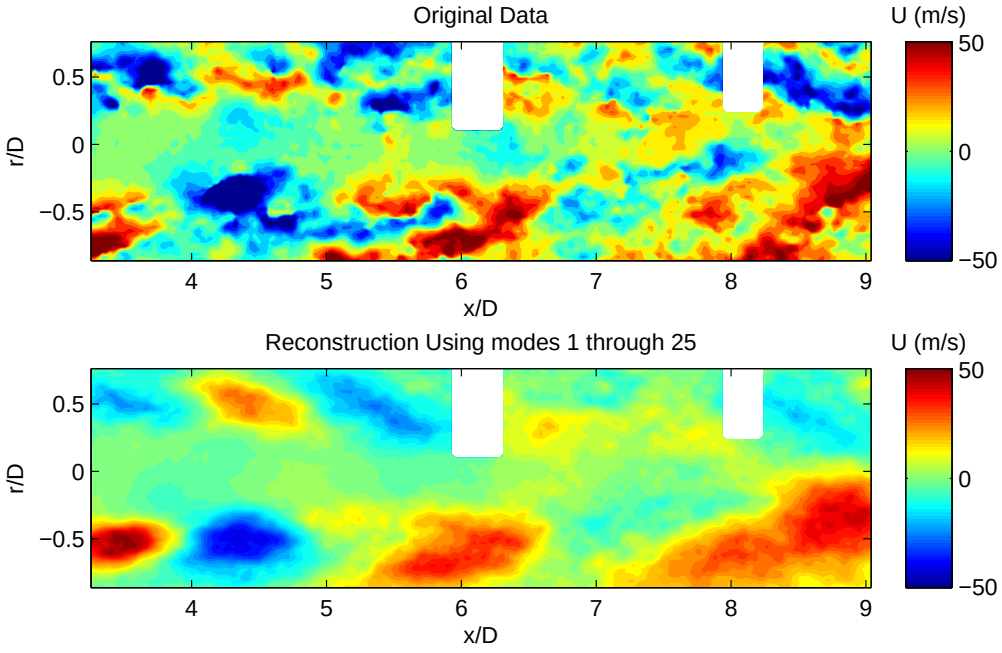

Figure 5.52: Reconstructed fluctuating velocity field: baseline

The POD reconstructions of the fluctuating velocity field form a low-dimensional representation of the flow in terms of the large scale, energetic building blocks of the flow.

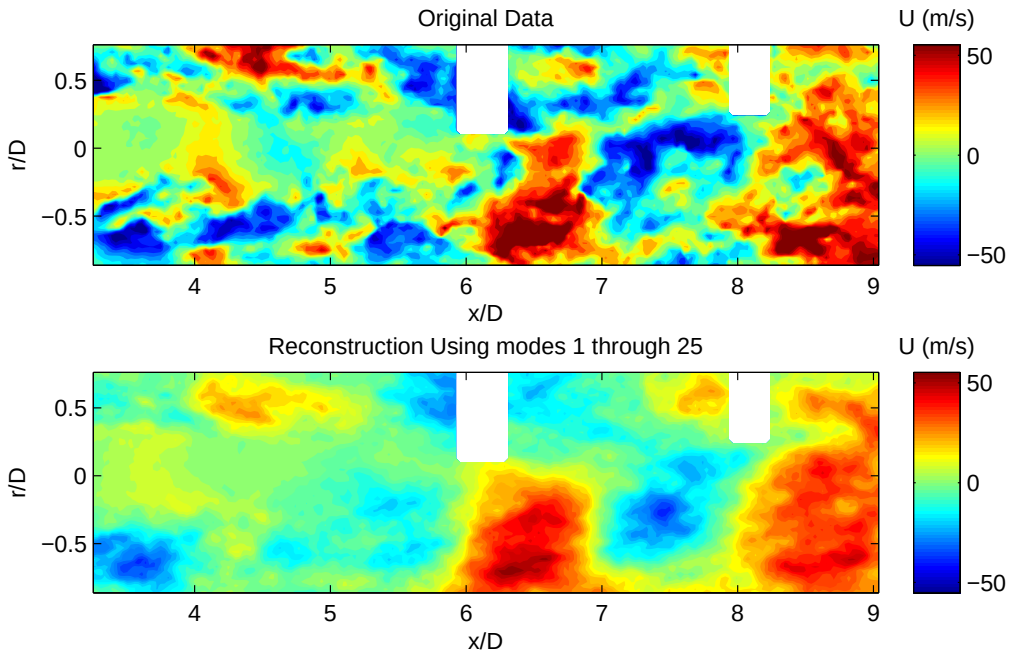

Figure 5.53: Reconstructed fluctuating velocity field: OLC1

For the baseline case in particular, the large scale structures following the shear layer are extracted using the POD. Furthermore, the POD reconstructions show that the control has added structures of various scales to the flow, due to the actuation input. The *CLC1* case seems to have distinct characteristics as compared to the other control cases. This particular case seems to keep the flow organized before the collapse of the potential core, as seen by the flow structures in the shear layer upstream of 6D. Moreover, the Fourier-azimuthal mode 1 forcing causes the potential core to collapse further upstream, as compared to baseline, evident in even a single snapshot.

The POD results clearly display that control authority over the jet has been achieved with each of the control strategies implemented. Through the implementation of the POD as a reduced-order model for the velocity field, the effects of the flow control are observed with respect to the large scale, energetic structures in the flow field. These deterministic eigenfunctions have been significantly altered due to the actuation with both open and

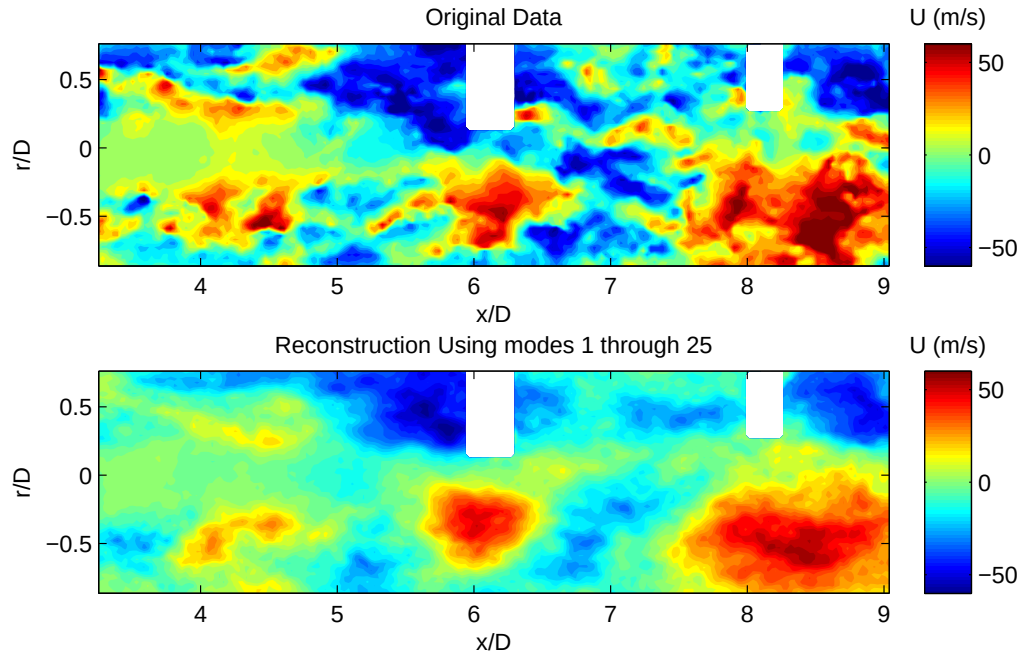

Figure 5.54: Reconstructed fluctuating velocity field: OLC2

closed-loop flow control implemented at the nozzle lip.

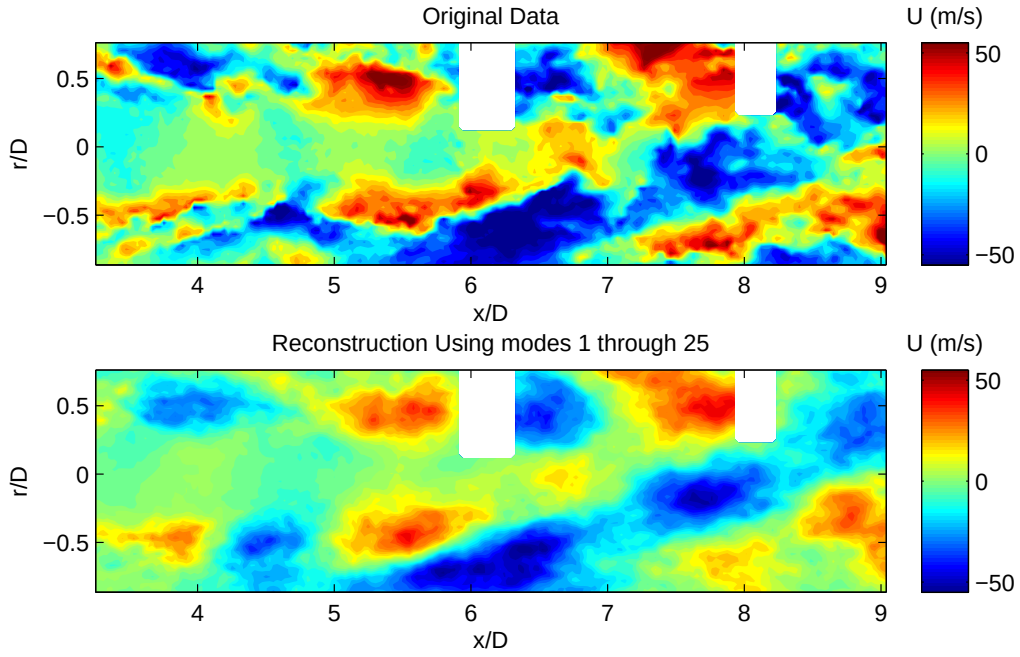

Figure 5.55: Reconstructed fluctuating velocity field: CLC1

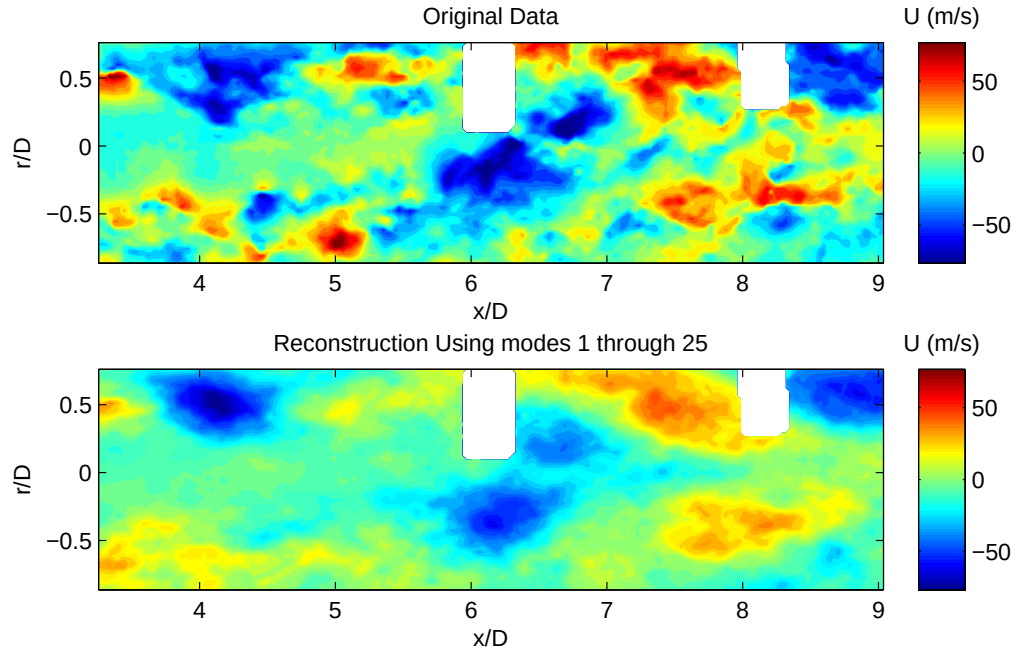

Figure 5.56: Reconstructed fluctuating velocity field: CLC2

5.5 Far-Field Acoustics

In addition to the near-field pressure and velocity fields, the effects of the control can also be observed with respect to the far-field noise. In order to make such comparisons, the power spectral density is computed for each of the far-field microphones. The single-sided power spectral density of each microphone, denoted as $S_{ff}(f)$, is then converted to the sound pressure level (SPL), which is measured in decibels (dB). The formula for calculating the SPL is seen in equation 5.6:

$$SPL_{ff} = 10log_{10}\left(\frac{S_{ff}(f)}{p_{ref}^2}\right) \tag{5.6}$$

where p_{ref} is the reference pressure, quoted by the manufacturer to be $20 \times 10^{-6} \mu Pa$. The microphone configuration can be seen in Figure 5.57. The bottom array of microphones in the configuration are in the same horizontal plane as the jet and will therefore be referred to as the in-plane microphones. The top array of microphones are 15° offset from the horizontal jet plane and therefore these will be known as the out-of-plane or offset microphones.

Figures 5.58 and 5.59 show the SPL for the in-plane and out-of-plane microphones for the baseline case. Each microphone is color-coded according to Figure 5.57. The far-field microphones are sampled at 25 kHz and therefore low-pass filtered at 12.5 kHz to avoid aliasing. As previously mentioned, the uncertainty of the overall sound pressure level is approximately $\pm$ 1 dB with a repeatability of $\pm$ 0.2 dB based on the measurements [134]. The SPL plots indicate that the far-field acoustics are fairly broadband in nature, reflective of the characteristics of the jet. Similar trends can be seen between the in-plane and out-of-plane microphones across the frequency band. The higher sound pressure levels occur at shallow polar angles with respect to the jet axis, due to the cone of coherent noise. The large scale, low frequency structures tend to propagate to these shallow angles, while the

Figure 5.57: Far-field microphone configuration

small scale, high frequency structures are more directed to the steep polar angles. Also, the sound pressure levels are slightly higher for the in-plane microphones than for those at a 15° offset. Figures 5.58 and 5.59 indicate that the far-field acoustics signals collapse at higher frequencies for both arrays of microphones.

In order to quantify the differences in sound pressure level for the various control cases, a directivity plot of the far-field microphones is presented [148]. This plot shows the change in overall sound pressure level (OASPL) at each of the far-field microphones with respect to the baseline (uncontrolled) jet. Figures 5.60 and 5.61 show the OASPL directivity plots for the in-plane and out-of-plane microphones, respectively. The SPL plots for each of the individual control cases can be found in Appendix B.

Figures 5.60 and 5.61 shows that there is an increase in the OASPL for all control cases. However this also indicates that control authority over the jet has been achieved. Moreover, the different control cases seem to each exhibit a specific directivity effect, which is to be

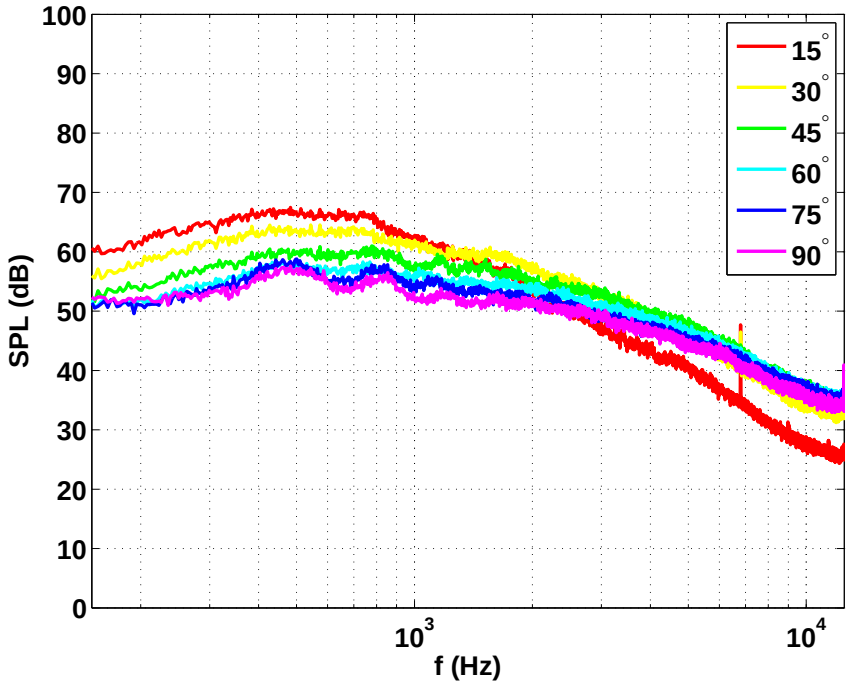

Figure 5.58: In-plane far-field SPL: baseline

expected, as different forcing and feedback mechanisms are provided for the control input. The increased streamwise vorticity created as a result on the actuation increases the high frequency noise, seen at the steep polar angles, both in and out-of-plane with respect to the jet axis. The various types of forcing applied tend to induce additional streamwise vortices and therefore change the structures being propagated to the far-field due to a shift in the potential core length and growth of the shear layer.

Focusing on the microphone at 15° where the sound pressure level is largest, it can be seen that the closed-loop control case in which Fourier-filtered pressure mode 0 is fed back to physically force Fourier-azimuthal mode 1 (*CLC1*), results in an OASPL closest to the baseline. At this microphone, the closed-loop control results in a 1.5 % increase in the OASPL. In addition, an open-loop forcing of Fourier-azimuthal mode 1 seems to be the loudest control case at this particular microphone, resulting in a 2.2 % increase in the OASPL. As was observed from the mean velocity field and POD analysis, with active

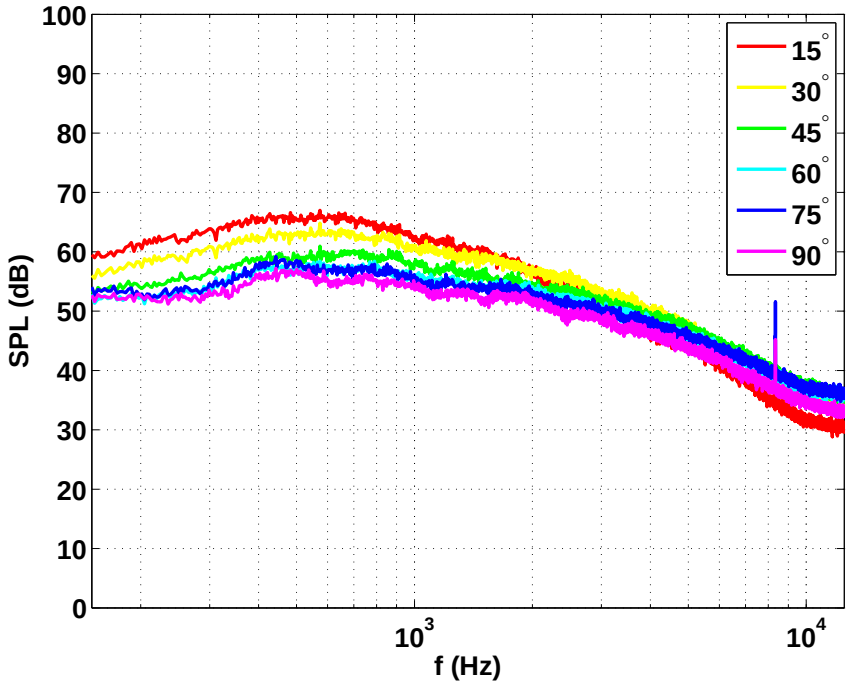

Figure 5.59: Out-of-plane far-field SPL: baseline

flow control (both open and closed-loop), the potential core length has been significantly shortened and a slight increase in the shear layer expansion is also observed. Subtle changes between the open and closed-loop control can be accounted for by the feedback mechanism present in the closed-loop case. These subtle changes clearly result in slight differences in the overall sound pressure levels in the far-field and requires further investigation.

One important conclusion that can be drawn from the OASPL results is that case *CLC1* is the best control case in terms of the far-field noise. While this particular form of flow control does not reduce the far-field noise, it does produce the lowest OASPL of the control strategies implemented. Moreover, the closed-loop control draws on intelligence from the system and uses less energy input to the system as compared to the open-loop. Despite the fact that far-field noise reductions were not achieved, much information has been learned about the flow control strategies implemented.

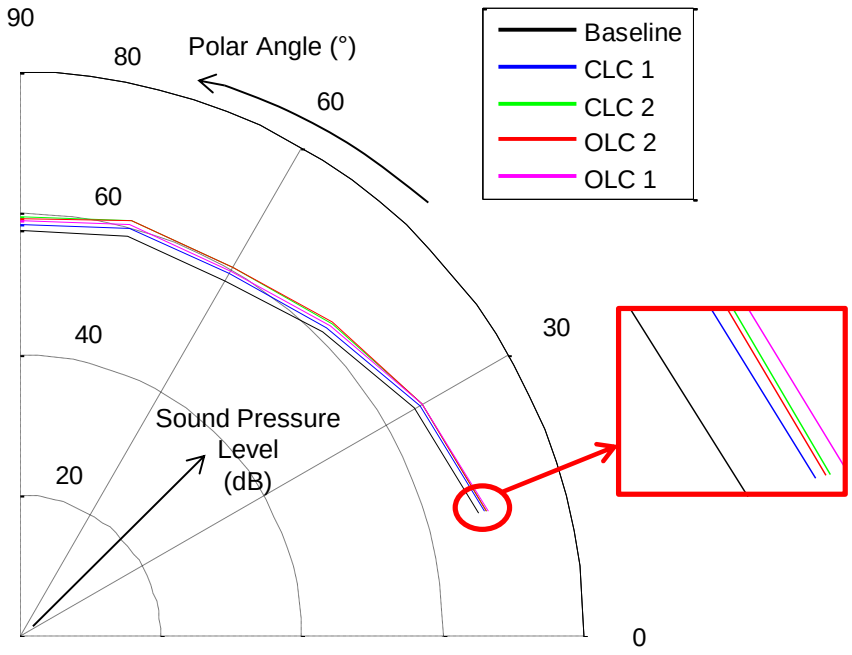

Figure 5.60: Overall sound pressure level directivity: In-plane microphones

5.6 LWPIV Discussions

In the current investigation, a PIV window stitching algorithm has been developed and implemented at Syracuse University to obtain a large PIV window comprising of approximately six jet diameters in the streamwise direction. The data presented has been analyzed to help gain insight into the flow structures being created as a result of the potential core collapse. In addition, simultaneous near and far-field pressure measurements were acquired with both open and closed-loop flow control. Mean velocity contour profiles indicate that the potential core of the jet has been significantly shortened using active flow control. Moreover, since the closed-loop control uses less input energy and draws on intelligence from the flow field, this becomes a more desirable control option than open-loop, for jet noise applications. This is further validated by the fact that the closed-loop control

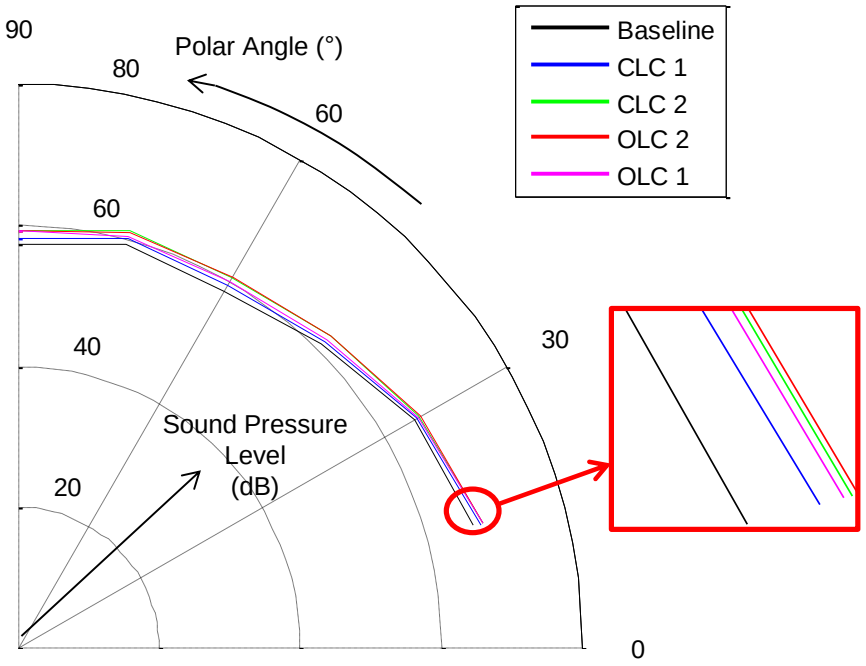

Figure 5.61: Overall sound pressure level directivity: Out-of-plane microphones

case has a lower overall sound pressure level in the far-field across all of the microphones, as compared to the open-loop case. The POD analysis shows that a large amount of the total energy of the system can be recovered with a small number of modes. Looking at the first two POD modes indicates that closed-loop control (specifically case *CLC1*) keeps the flow organized until the collapse of the potential core. The result of the Fourier-azimuthal mode 1 forcing, as a shear layer excitation, can clearly be observed as the small streamwise vortices propagate downstream eventually resulting in the early potential core collapse.

The results presented indicate that control authority has been achieved for the Mach 0.6 jet using active flow control in the form of synthetic jet actuation. This actuation system has been shown to shorten the potential core length by enhancing the mixing in the shear layers of the jet. Through active flow control, the potential core has been shortened by approximately $1 - 1.5D$, as compared to the uncontrolled jet. This is seen in both mean flow

and spatial POD velocity contours in the PIV window. The actuation induces an increased amount of streamwise vorticity which eventually leads to complex vortex interactions during the collapse of the potential core. This leads to a small increase in far-field noise at shallow polar angles and a slightly higher increase at steep polar angles. Moreover, the near-field pressure spectra at six diameters downstream reveals that the jet remains relatively axisymmetric as a result of the flow control. The open-loop flow control shortens the potential core length more than the closed-loop flow control. As the potential core length decreases, the OASPL increases across all far-field microphones. Therefore, it is possible that by organizing the flow to delay the collapse of the potential core, this may in turn reduce the far-field noise. The key is to gain a deeper understanding of the mechanisms responsible for the far-field noise and use this information in conjunction with closed-loop flow control. More advanced control algorithms coupled with novel reduced-order modeling techniques provide a viable framework for jet noise reduction strategies moving forward.

While the LWPIV results provide insights into the effects of active flow control on the flow field and far-field acoustics, the standard PIV does not provide any time-resolved information within the velocity field. The six-diameter interrogation window does allow for the extraction of large scale structures spanning a significant portion of the jet flow in the streamwise plane. The regions before and after the collapse of the potential core are captured by the LWPIV providing useful information about the spatial evolution of the jet's flow field as different control strategies are implemented. In order to address the time-evolution of the jet and ultimately the relationship to the far-field noise, time-resolved PIV (TRPIV) will be the topic of discussion for the next chapter. In the context of understanding and controlling the jet noise, the LWPIV experiments have shown that control authority over the jet is achievable through various types of active flow control through shear layer excitation at the nozzle exit plane. In other words, we have successfully implemented an

$\mathscr{O}(\varepsilon)$ input to the system which achieves an $\mathscr{O}(1)$ response. This is a crucial demonstration for the eventual implementation of active flow control on a real system.

Chapter 6

Time-Resolved PIV Results

The results presented in this chapter focus on the two time-resolved PIV (TRPIV) data sets as outlined in § 2.2.4. Using the time-resolved velocity field coupled with the simultaneously sampled far-field acoustic measurements, low-dimensional flow structures that contribute to the noise are identified through reduced-order modeling techniques. The low-dimensional POD modes of the velocity field which contribute highly to the far-field noise will be denoted as "loud" modes. The relation between the interaction of structures in the flow field and these loud modes will be postulated by observing the low-dimensional, time-resolved flow field. The 2013 TRPIV data set includes the implementation of control to build off of the LWPIV experiments in the context of identifying the loud modes associated with active flow control.

6.1 TRPIV Experimental Overview

As previously stated in § 2.2.4, a 10 kHz time-resolved PIV system is used in both the 2011 and 2013 experiments. While many aspects of the experiments are the same, there are some key differences to be noted. The main difference between these two data sets is, while the 2011 experiments focus on Mach number variation, the 2013 experiments focus on active

flow control for the Mach 0.6 jet. These specific experiments are outlined in § 6.1.1 and 6.1.2, respectively.

6.1.1 2011 TRPIV Experiments

The experiments conducted in 2011 focus primarily on examining the time-dependent flow field for different Mach numbers. Four different Mach numbers were acquired in this set of tests: Mach 0.6, 0.85, 1.0 and 1.2. In addition, open-loop flow control was implemented for the Mach 0.6 case using a Fourier-azimuthal mode 0 forcing (equivalent to case *OLC2* in the LWPIV studies). Flow control was only implemented at Mach 0.6 due to the control authority of the actuation system. A forcing frequency of 1 kHz (corresponding to $St = 0.25$) was used in this particular configuration.

Near-field pressure and far-field acoustics are simultaneously sampled for all TRPIV data sets. Six far-field microphones in the horizontal plane of the jet acquire the acoustic data, while thirteen *Kulites* acquire the near-field pressure with an azimuthal and linear array of sensors. For the PIV, a total of 8,623 snapshots (0.8623 seconds) are acquired for each Mach number at each window location. More information on the specifics of the experimental setup can be found in the works of Low (2012) [148] and Low *et al.* (2013) [149].

6.1.2 2013 TRPIV Experiments

For the experiments conducted in 2013, the focus is shifted to conducting additional types of flow control (as inspired by the LWPIV experiments), as well as gathering information at off-center planes to explore the three-dimensionality of the flow field. In addition, longer record lengths were acquired for statistical convergence, which is crucial for additional analyses to be conducted. For each data set, a total of 15,000 snapshots (1.5 seconds) were acquired. For a select number of test cases, four data sets were taken, for a total of 6

seconds worth of data.

For the active flow control, the same control cases were used as with the LWPIV experiments (*OLC1, CLC1, CLC2*), with the exception of *OLC2*, which was acquired in 2011. For these experiments, a forcing frequency of 1.2 kHz ($St = 0.30$) was used. Once again, in addition to the control experiments, a set of off-center plane measurements, for the uncontrolled jet, was taken. In these tests, ten PIV planes are acquired across the span of the nozzle while keeping the streamwise location fixed. All TRPIV experiments conducted in 2013 are taken at Mach 0.6.

For the near-field pressure and far-field acoustic measurements, similar arrays were used with some slight modifications. An additional array of six microphones were added, as outlined by the LWPIV experiments previously discussed. Also, an additional *Kulite* was added to the linear array, and the azimuthal array was kept the same (see § 2.2 for details).

6.2 2011 TRPIV Results

In order to reduce the far-field noise created by a high-speed jet, one must understand the complex flow structures and interactions, and how these events relate to the acoustics. A key component of this analysis is to identify structures in the velocity field that correlate highly with the far-field pressure signatures. This can be done through the implementation of cross-correlations between near-field velocity and far-field acoustics. Moreover, these correlations can be computed directly if the velocity field is time-resolved.

Since the velocity field is quite complex, containing various length and time scales, low-dimensional modeling in the form of POD is performed to extract the highly energetic, large scale structures. From the decomposition, time-dependent expansion coefficients and spatial eigenfunctions are extracted. The time-dependent expansion coefficients are directly correlated with the far-field acoustics to determine which low-dimensional velocity

modes contribute most highly to the far-field noise. This identification of loud modes then allows one to examine the deterministic spatial structures associated with the potential noise-producing events.

This analysis was performed with the 2011 data set by Low (2012) [148], Low *et al.* (2013) [149], and Berger *et al.* (2012,2013) [30, 31], and will be summarized in the following section. The loud mode identification via the cross-correlation technique motivates the implementation of the OID.

6.2.1 Loud Mode Identification

Initially the loud modes are identified by computing the cross-correlation between the time-dependent, time-resolved velocity POD coefficients and the far-field acoustic microphones signals. The cross-correlation technique is a useful mathematical tool for identifying the similarity between two signals in time, as stated by Otnes & Enochson (1978) [173]. In order to perform the cross-correlations, the cross-spectral density function is first computed in the frequency domain [27, 28]. The cross-spectrum is analogous to the power-spectrum (see equation 5.3) and is defined in the following way:

$$S_{nf}(f) = \frac{1}{T}\langle|\hat{p}_n(f)^* \hat{p}_f(f)|\rangle \tag{6.1}$$

The cross-covariance is computed by taking the inverse Fourier transform of the cross-spectral density function, as shown in the following equation:

$$R_{nf}(\tau) = \int_{-\infty}^{\infty} S_{nf}(f) e^{i2\pi ft} dt \tag{6.2}$$

Finally, the cross-correlation is computed by normalizing the cross-covariance function by the product of the standard deviations of each signal:

$$\rho_{nf}(\tau) = \frac{R_{nf}(\tau)}{\sigma_n \sigma_f} \tag{6.3}$$

In equation 6.3, σ_n and σ_f are the standard deviations of the near and far-field pressure signals, respectively. This technique can be extended to include any two time signals (of the same sampling rate and length). In the analysis to be presented, the signals to be used for cross-correlations include the Fourier-filtered near-field pressure, time-dependent POD velocity coefficients and far-field acoustics.

The first step in identifying the loud modes is to correlate the time-dependent POD velocity coefficients with the near-field pressure. Since the Fourier-filtered mode 0 of the near-field pressure is shown to have a strong correlation with the far-field (refer to § 1.4.2), this will be used to correlate with the POD velocity modes (see Figure 6.1). In performing this correlation, the Fourier-filtered mode 0 of the near-field pressure is computed from the azimuthal array of nine pressure sensors located at 6D downstream. For the time-dependent POD velocity coefficients, the first 100 modes (65% of the total energy) are utilized. A thresholding level of 10% is applied to the corresponding cross-correlations to determine the POD velocity modes having the strongest contribution to the low-dimensional near-field pressure. Several modes have a correlation level above 0.1 as should be expected, since the PIV window from which the POD velocity modes are extracted is at the same downstream location as the near-field pressure sensors [30, 149]. An example of the cross-correlations between the POD velocity modes and the Fourier-filtered mode 0 of the near-field pressure is shown in Figure 6.2. This particular case uses the Mach 0.85 data with the PIV window spanning between 6D and 7.5D in the streamwise direction.

The next step in the analysis is to compute the cross-correlations between the time-dependent POD velocity coefficients and the far-field acoustic signals. If any of the time-dependent POD velocity coefficients are as strongly correlated with the far-field as they are with the near-field, these are identified as loud modes. The equally strong correlation of

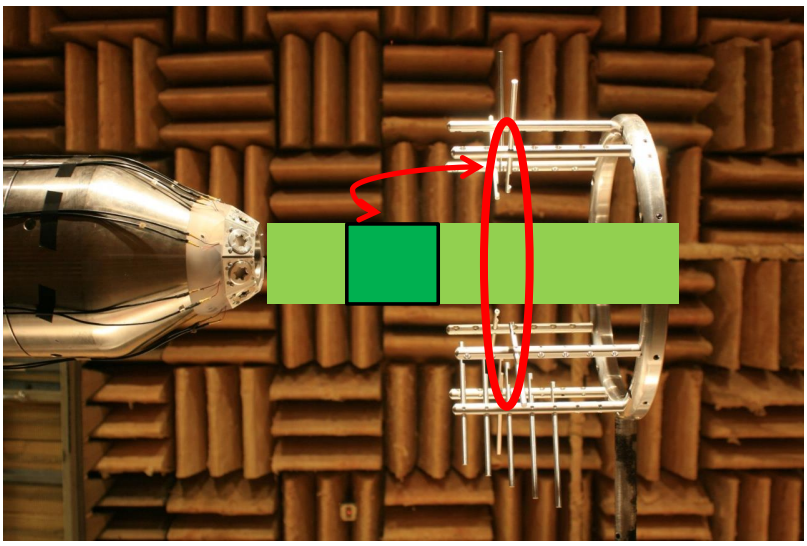

Figure 6.1: Representation of cross-correlation between Fourier-filtered mode 0 of near-field pressure and time-dependent POD velocity coefficients

these velocity modes with both the near and far-field pressure signals indicates that these events are propagating to the far-field, and have strong contributions to the overall noise. Therefore the time-dependent POD velocity coefficients are correlated with each of the far-field microphones individually, as shown in Figure 6.3. Since the microphone at 15° has the strongest correlation with the time-dependent POD velocity coefficients, this will be the microphone used for the remainder of the analysis [148, 149]. These correlations will be known as the velocity-acoustic correlations for the remainder of the discussion. This analysis reveals that depending on the PIV window location and Mach number, only a select number of modes are identified as loud modes.

Looking specifically at the last PIV window location, spanning from 6D to 7.5D in the streamwise direction, the velocity-acoustic correlations are carried out to identify the corresponding loud modes. This particular window location is the most interesting since the flow is highly complex in this region due to the collapse of the potential core. This is also believed to be the region where many noise-producing events are formed. A table

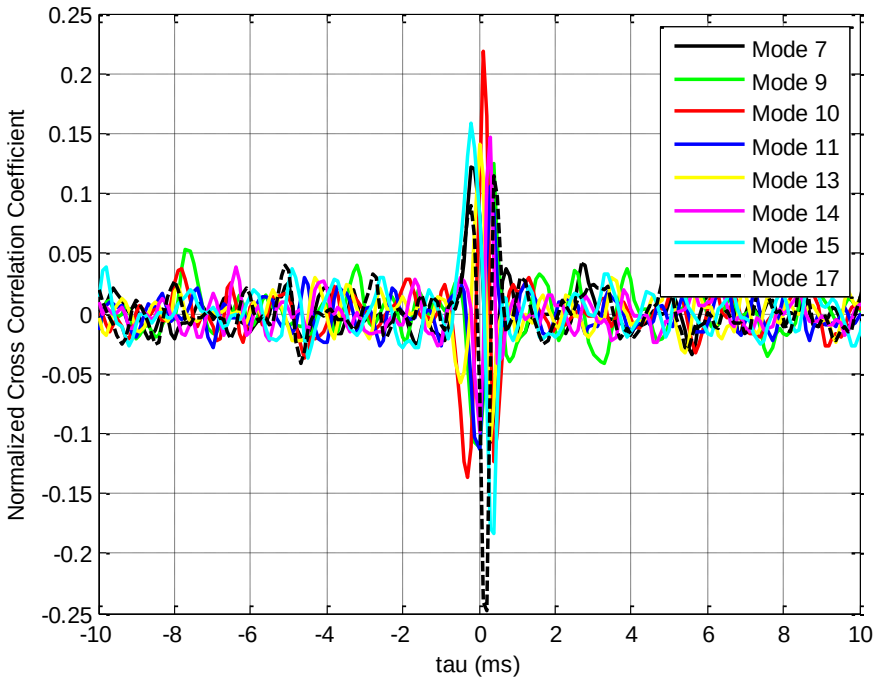

Figure 6.2: Time-dependent POD velocity modes having at least a 10% cross-correlation with the low-dimensional near-field pressure, Berger *et al.* (2013) [30]

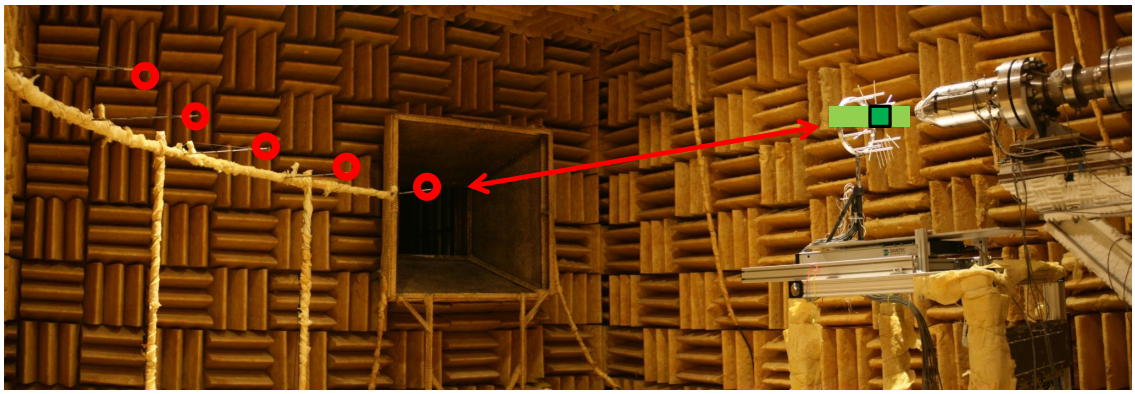

Figure 6.3: Representation of cross-correlation between far-field microphone signals and time-dependent POD velocity coefficients

containing a summary of the loud modes identified for additional test cases, as carried out by Low [148], Low *et al.* [149], and Berger *et al.* [30, 31], can be found in Appendix C.

For the Mach 0.6 case, only two POD velocity modes have a cross-correlation above 10% with the far-field microphone at 15°. As such, modes 6 and 14 are identified as the loud modes for this particular Mach number and PIV window location. The corresponding cross-correlations for this particular case are seen in Figure 6.4. One important feature to notice about these particular loud modes is that the peak of the cross-correlations are of opposite sign, possibly indicative of a phase difference between the two modes. More importantly, these two modes are not the most energetic, indicating the largest noise contributors are characterized by subtleties in the flow field. In fact, modes 6 and 14 contain approximately 2.5% and 1.1% of the total turbulent kinetic energy, respectively.

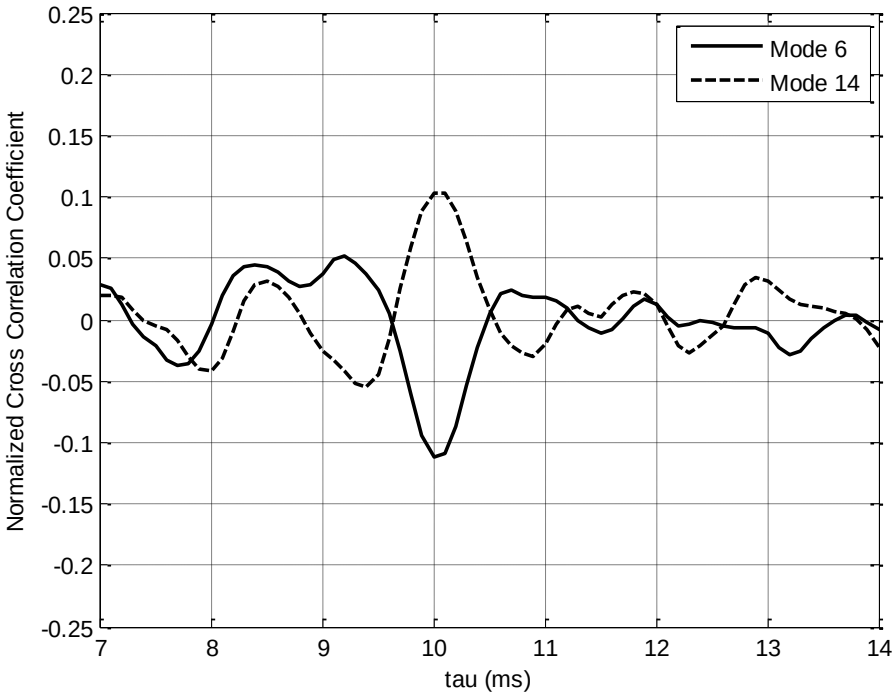

Figure 6.4: Time-dependent POD velocity modes having at least a 10% cross-correlation with the far-field microphone at 15°: Mach 0.6, Low *et al.* (2013) [149]

To complement these findings, the loud modes are also identified for the Mach 0.85 case at the same PIV window location. This time three modes are extracted from the analysis, as

shown in Figure 6.5. Again, these modes are not the most energetic low-dimensional modes but they do strongly contribute to the far-field acoustics, particularly at the 15° microphone.

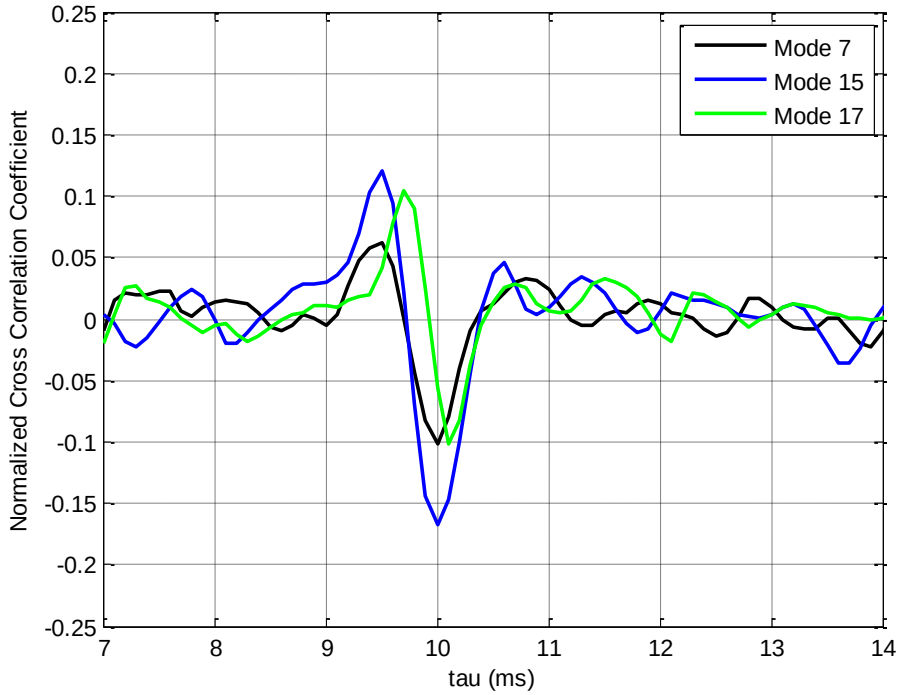

Figure 6.5: Time-dependent POD velocity modes having at least a 10% cross-correlation with the far-field microphone at 15°: Mach 0.85, Berger *et al.* (2013) [30]

The method of cross-correlations provides a means for identifying low-dimensional velocity modes that contribute most highly to the far-field noise. This technique, though effective, remains computationally cumbersome since the cross-correlations must be computed for each individual microphone. As the number of microphones increases (as with the 2013 experiments), this analysis requires additional computations for loud mode identification. Therefore, a more mathematically rigorous technique for identifying the loud modes is desired. The observable inferred decomposition (OID) is employed by using the time-dependent POD velocity coefficients as the source and the far-field microphones as the observer (see § 4.3). A linear mapping between the POD velocity modes and the tem-

poral POD acoustic modes is established to obtain the most acoustically observable modes in the flow field.

To quantify the loud modes using the OID technique, the coefficients of the linear mapping transformation matrix are evaluated. Since the OID uses a low-dimensional representation of the observer, this implies that all far-field microphones are accounted for in the analysis. The largest contributions to the linear mapping matrix are identified as the loud modes using this technique. Recall that the linear mapping matrix is computed using equation 4.42. The OID is first computed for the Mach 0.6 data set, looking at the same PIV window. The coefficients of the linear mapping matrix are plotted for the first 20 POD velocity modes and the first 3 POD acoustic modes as shown in Figure 6.6. The OID analysis shows that the two largest contributors are POD velocity modes 6 and 14, with respect to POD acoustic mode 1. Despite the fact that the POD acoustic modes do not directly represent a particular far-field microphone, a relationship between these quantities is described in the following way. The POD decomposes the far-field microphones in terms of acoustic energy. Since the acoustic energy is higher at the shallow polar angles and lower at the steep polar angles, the first acoustic POD modes is thought to be associated with the 15° microphone while the sixth acoustic POD mode is thought to be associated with the 90° microphone. Therefore velocity POD modes 6 and 14 are most highly correlated with acoustic POD mode 1 (*i.e.* microphone 15°), as seen in Figure 6.6. This result is consistent with the cross-correlation technique, validating the two methods and confirming that modes 6 and 14 are the loud modes at this particular Mach number and window location.

Looking at the OID analysis for the Mach 0.85 data set, the coefficients of the linear mapping matrix are computed to find the loud modes for this particular Mach number. Figure 6.7 again shows the first 20 POD velocity modes and the first 3 POD acoustic modes for the linear mapping matrix. The OID analysis reveals three loud modes for this Mach number and PIV window location. Again the three largest modes correspond to the first

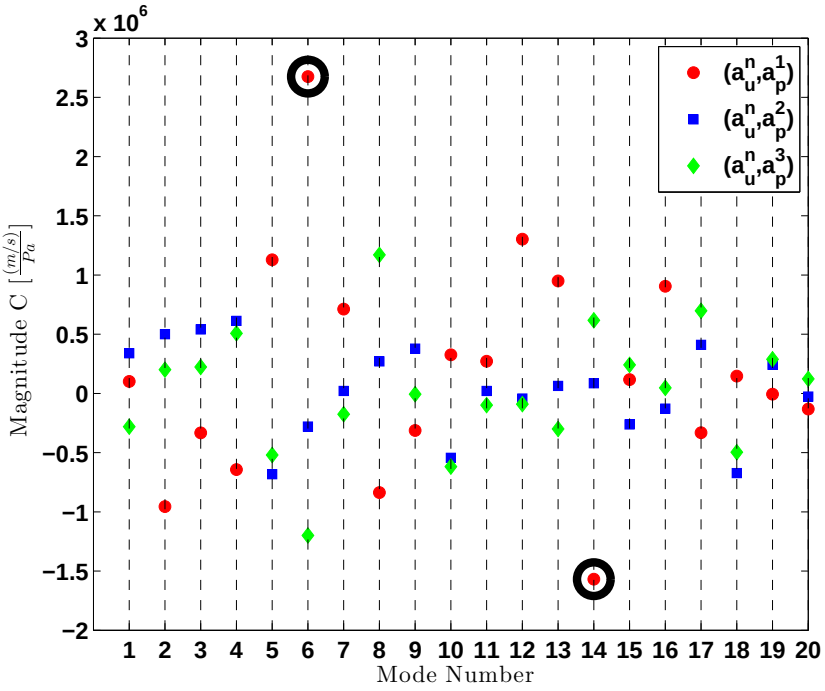

Figure 6.6: Coefficients of the linear mapping matrix for the first 20 POD velocity modes and first 3 POD acoustic modes: Mach 0.6, Berger *et al.* (2013) [30]

acoustic POD mode. The loud modes found from the OID, identified for Mach 0.85 case, are modes 7, 8 and 15. The loud modes computed from the cross-correlation technique are found to be modes 7, 15, and 17. This result implies that the two techniques do not always yield the exact same results in all cases. The differences between these two techniques requires further investigation which is left for future work. Since two of the three loud modes (7 and 15) are found to be the common loud modes for the two techniques at this Mach number, these two modes will be considered as the loud modes for this case. Again, modes 7 and 15 are not the most energetic, containing approximately 2.5% and 1.0% of the total turbulent kinetic energy, respectively.

Building on the work of Low *et al.*, the loud modes for the two different Mach numbers investigated are confirmed by the OID technique. The technique uses the low-dimensional velocity and acoustic fields to identify the most acoustically observable modes in the flow

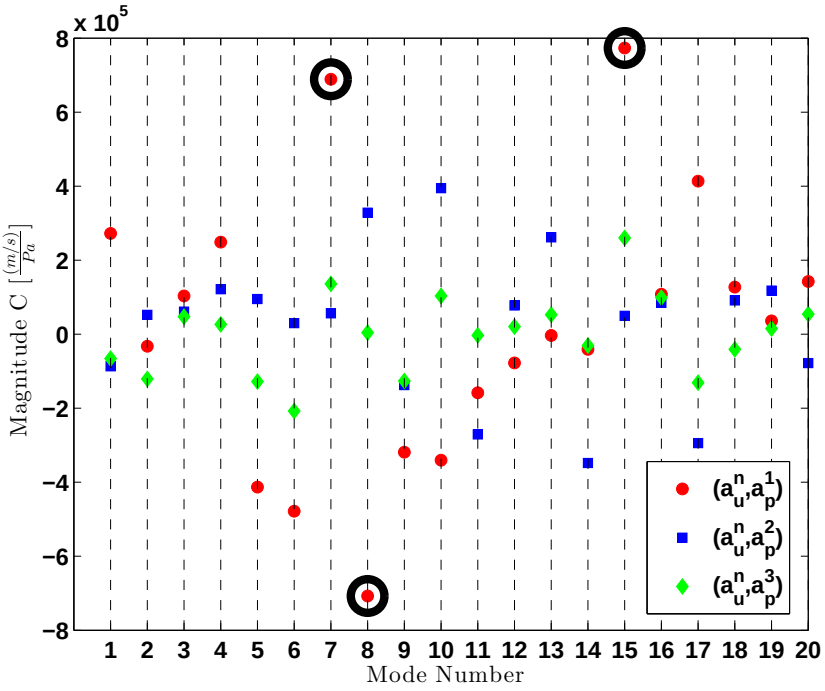

Figure 6.7: Coefficients of the linear mapping matrix for the first 20 POD velocity modes and first 3 POD acoustic modes: Mach 0.85, Berger *et al.* (2013) [30]

field using a linear mapping between the source and observer. Now that these loud modes have been identified, several questions pertaining to the noise-producing events need to be investigated. In particular, what do the spatial structures of these modes look like and how do they relate to the other modes? What do the time-dependent expansion coefficients look like? Is there something noticeable about the time-evolution of the loud modes as compared to the other low-dimensional modes? Are the loud modes for the different Mach numbers somehow related? Is there a deterministic eigenfunction in the flow field that is responsible for the largest contribution to the far-field noise? As soon as some of these questions are addressed, one can begin to think about controlling these modes using active flow control techniques. It is important to remember that the loud modes are not the only contributors to the far-field noise, however they do seem to be the *largest* contributors, and as such should be investigated in further detail. The next section focuses specifically on the

spatial eigenfunctions associated with the loud modes and addresses the correlations that may exist between the loud modes at the two different Mach numbers.

6.2.2 Spatial Eigenfunctions and Modal Correlations

Presented in this section are the spatial eigenfunctions of the velocity POD modes for the Mach 0.6 and Mach 0.85 data sets, for the PIV window spanning from $6D$ to $7.5D$ downstream. The streamwise and transverse eigenfunctions ($\phi_u^{(n)}(\vec{x})$ and $\phi_v^{(n)}(\vec{x})$, respectively) are plotted separately for both Mach numbers for comparison. The spatial eigenfunctions for Mach 0.6 are found in Figures 6.8 and 6.9, while the Mach 0.85 case is presented in Figures 6.10 and 6.11.

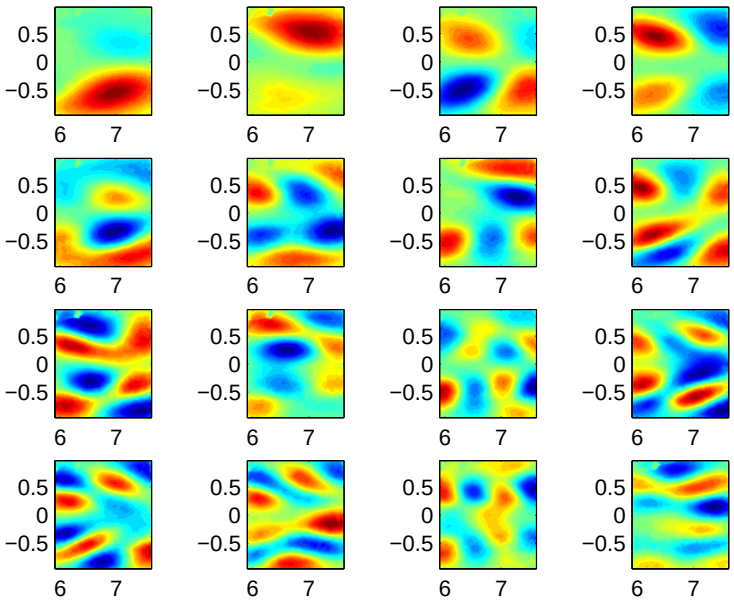

Figure 6.8: First 16 spatial eigenfunctions, $\phi_u^{(n)}(\vec{x})$ for Mach 0.6: abscissa $= x/D$, ordinate $= r/D$

In all of these cases, the first sixteen spatial eigenfunctions are presented starting with modes one through four in the first row from left to right, ending with mode sixteen in the

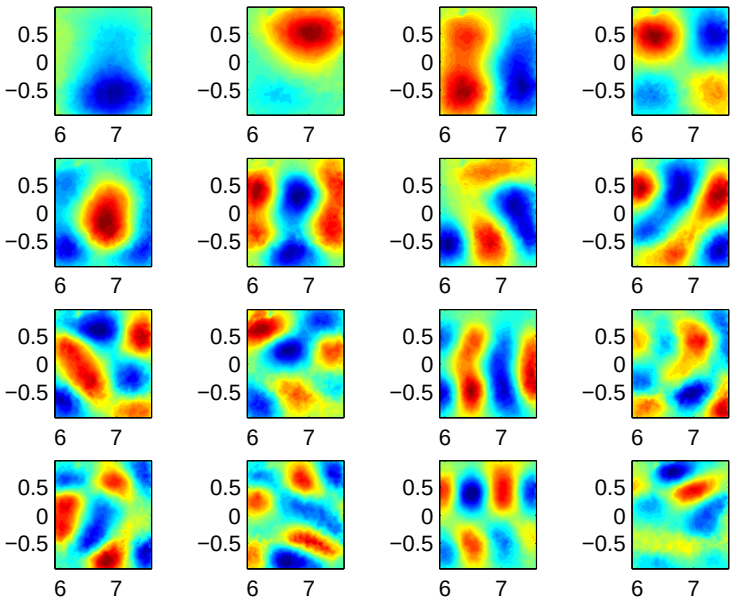

Figure 6.9: First 16 spatial eigenfunctions, $\phi_v^{(n)}(\vec{x})$ for Mach 0.6: abscissa $= x/D$, ordinate $= r/D$

bottom right corner. The abscissa is x/D and the ordinate is r/D for these four figures. Looking more closely at the loud modes, that is modes 6 and 14 for Mach 0.6, and modes 7 and 15 for Mach 0.85, their spatial structures seem to be distinct from all other modes. This is seen by the unique arrangement of structural patterns, which requires further investigation. Moreover, there is a strong similarity between mode 6 for Mach 0.6 and mode 7 for Mach 0.85. The same is also true for mode 14 for Mach 0.6 and mode 15 for Mach 0.85. Perhaps there is a distinct low-dimensional set of spatial structures that are associated with the largest noise sources, invariant of the Mach number.

In order to quantify the similarities between the loud modes at the two different Mach numbers, a correlation is carried out between the modes. To see the similarity in the modes qualitatively first, Figure 6.12 shows the u and v components of the loud modes for the two different Mach numbers. From a qualitative perspective, the loud modes for the two

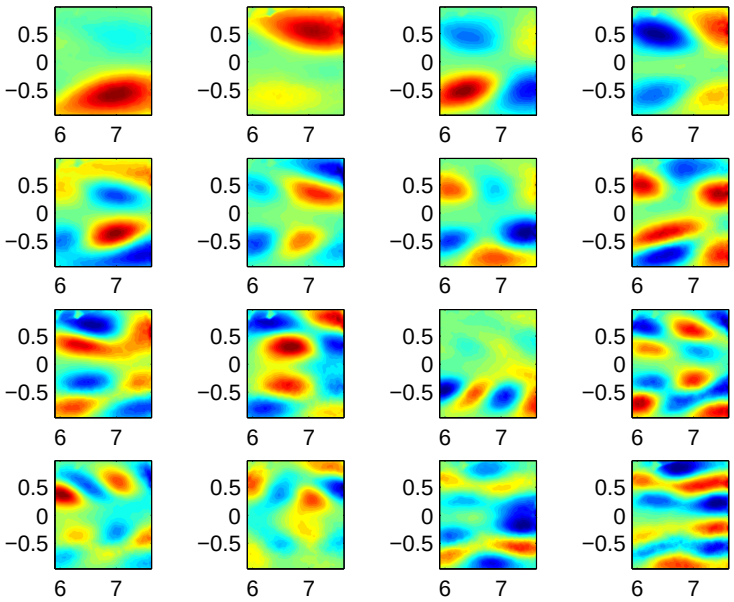

Figure 6.10: First 16 spatial eigenfunctions, $\phi_u^{(n)}(\vec{x})$ for Mach 0.85: abscissa $= x/D$, ordinate $= r/D$

different cases exhibit similar characteristics, for both components. One important feature to notice is that with the u and v components of modes 14 and 15, the spatial eigenfunctions are out of phase. This is because the integral eigenvalue problem of the POD determines the spatial eigenfunctions to within a phase and thus it is the structure that is of importance and not the sign. To determine how similar the loud modes are from a quantitative perspective, a correlation between the modes must be performed.

Recalling the governing constraints of the POD, it is known that the spatial eigenfunctions which are the basis functions, are orthogonal (and more specifically, orthonormal), meaning their inner product is equal to either one or zero (see equations 4.4 and 4.9). Therefore if the dot product of any spatial eigenfunction is taken with itself, the result will be one. Moreover if the dot product is taken between all modes, the result will be the identity matrix. An example of this is shown with the first 20 modes of the Mach 0.6 case, in

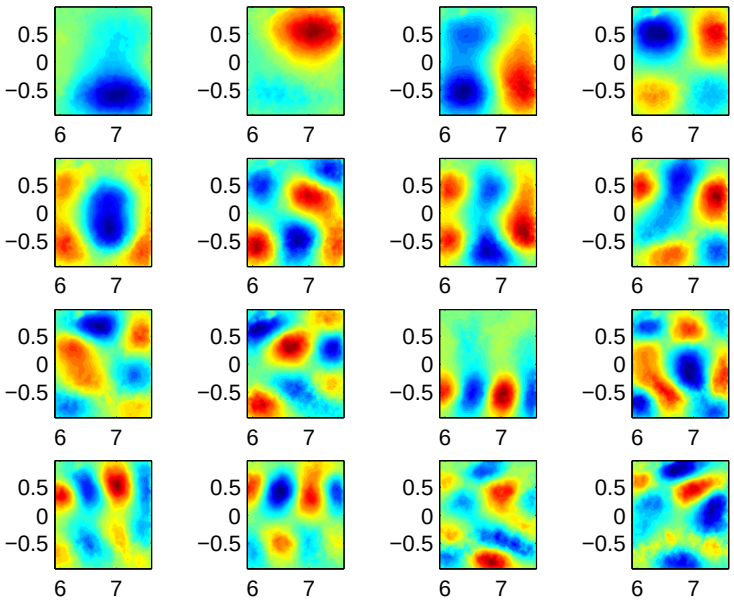

Figure 6.11: First 16 spatial eigenfunctions, $\phi_v^{(n)}(\vec{x})$ for Mach 0.85: abscissa $= x/D$, ordinate $= r/D$

Figure 6.13. As expected the result of this correlation is the identity matrix. The correlation between the first 20 modes for the Mach 0.6 and Mach 0.85 cases is then computed to quantitatively show the similarity between the loud modes.

Figure 6.14 shows a correlation level of 0.9 between modes 6 and 7, and a correlation level of 0.7 between modes 14 and 15. Figure 6.14 also reveals some interesting characteristics about the relationship between the Mach 0.6 and Mach 0.85 cases, from a low-dimensional perspective. The same mode numbers are well correlated between the two cases, until the first loud mode, at which point there is a shift in the modal correlation. The modes seem to correlate well again after this point until the next loud mode. This mode shifting in the loud modes between Mach numbers might be an inherent feature of the noise-producing events. According to Berger *et al.* (2012) [31], for the Mach 1.0 data, mode 16 appears to be the loud mode, using the cross-correlation technique. The OID has

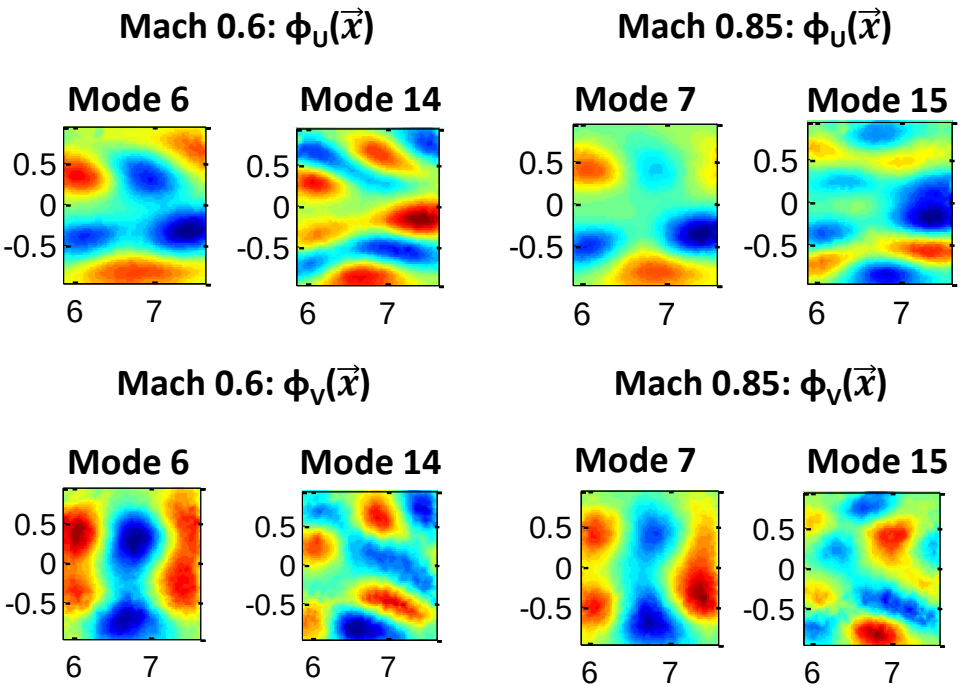

Figure 6.12: Loud Modes for Mach 0.6 and Mach 0.85: abscissa $= x/D$, ordinate $= r/D$

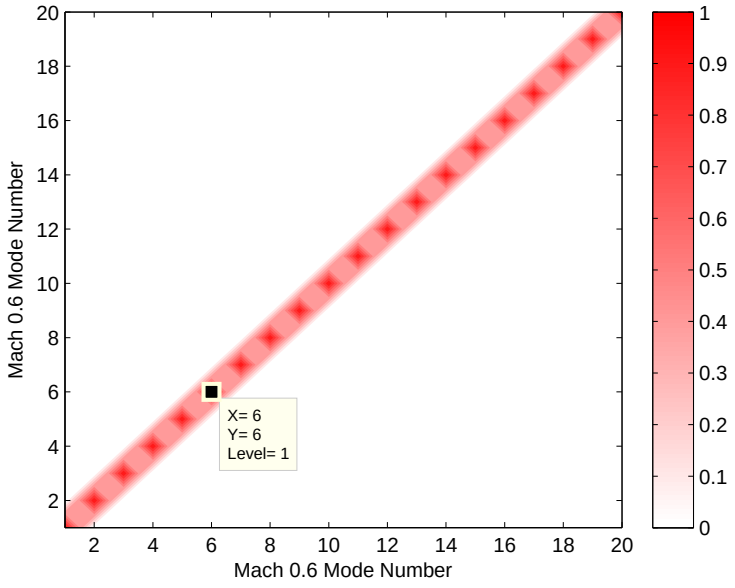

Figure 6.13: Modal correlation of the first 20 spatial eigenfunctions for the Mach 0.6 case

not yet been performed on this data set, however this result seems consistent with the loud mode shifting conjecture at increased Mach numbers. Regardless of this mode shift, the spatial structures of the loud modes remains quite similar, indicating there is something special about these particular modes with respect to the noise.

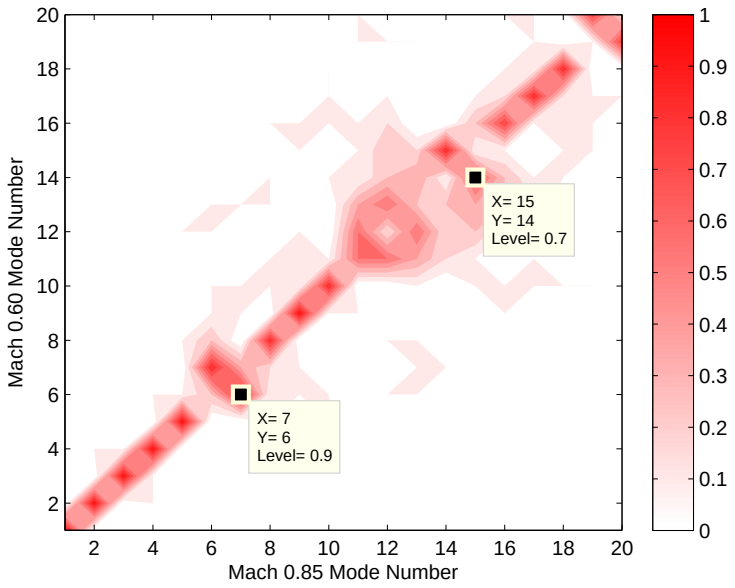

Figure 6.14: Modal correlation of the first 20 spatial eigenfunctions for Mach 0.6 and Mach 0.85

The similarity between the loud modes can also be determined by taking each component of the spatial eigenfunction separately. In doing so it is found that modes 6 and 7 for Mach 0.6 and 0.85, respectively, yield a correlation level of 0.9 for both the u and v components. Modes 14 and 15 for Mach 0.6 and 0.85, respectively, have a correlation level of 0.8 for the u component and 0.6 for the v component. These correlations are presented in Figures 6.15 and 6.16.

The spatial structure of the low-dimensional loud modes leads to some initial thoughts regarding the interaction of structures that have the most significant contributions to the far-field noise. In order to fully develop these thoughts, it is important to remember that

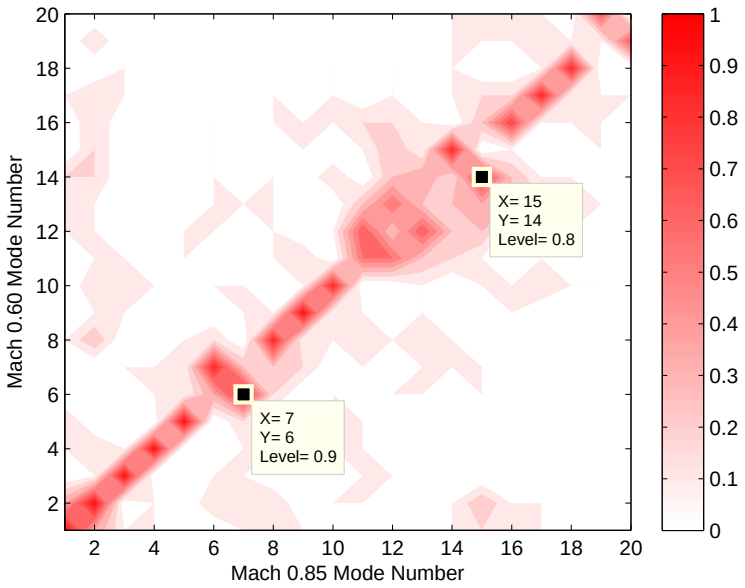

Figure 6.15: Modal correlation of the first 20 spatial eigenfunctions ($\phi_u^{(n)}(\vec{x})$) for Mach 0.6 and Mach 0.85

these structures are not only evolving in *space*, but also in *time*. Since the measurements conducted are time-resolved, the time-dependence of the velocity field is studied, focusing on the relationship between loud modes and the far-field acoustics. For the analysis presented, velocity POD mode 6 will be the focus, keeping in mind that this is not the only contribution to the noise, but that it has been shown to be the strongest contribution using the analysis techniques described. The analysis of the other loud modes in this context will be the focus of future work.

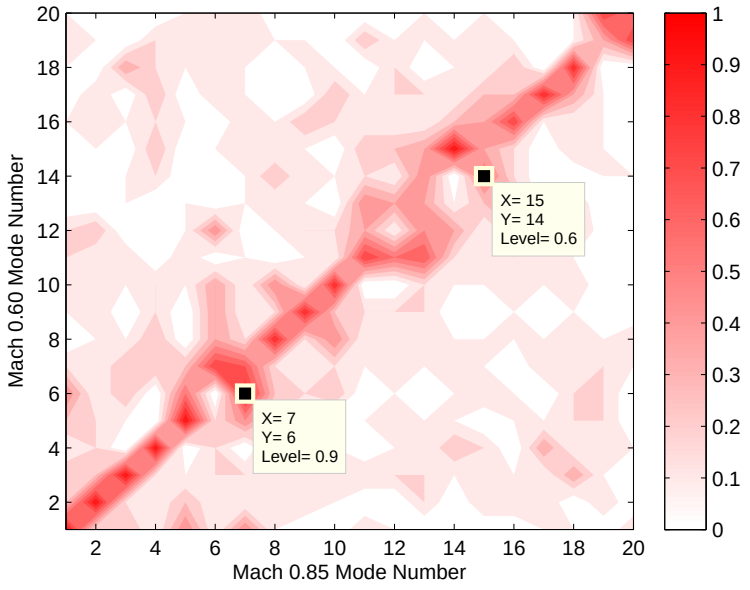

Figure 6.16: Modal correlation of the first 20 spatial eigenfunctions ($\phi_v^{(n)}(\vec{x})$) for Mach 0.6 and Mach 0.85

6.3 Loud Mode Time-Dependence

In order to track the events of the loud modes, it is necessary to observe the time-dependent POD expansion coefficient corresponding to mode 6. In general the temporal POD modes of the velocity field are rich in spectral content, thus the temporal and spatial modes are investigated to gain a better understanding of the physics associated with the loud mode. Figure 6.17 shows the time-dependent, time-resolved POD expansion coefficient corresponding to mode 6. As previously mentioned, the temporal POD modes are spectrally rich in nature. The auto-spectra of modes 6 and 14 can be found in the work of Low *et al.* (2013) [149]. For the analysis to be presented, the first 50 *ms* of the full record length of 0.8623 seconds (862.3 *ms*) is considered. The first 50 *ms* for temporal POD mode 6 is presented in Figure 6.18. Looking at a small subset of the original time series will allow for the extraction of useful information as we track the spatial structure of the loud mode in time. The first 50 *ms* for temporal POD modes $1 - 10$ (with the exception of mode 6) are presented in Appendix C.2.

The spatial and temporal evolution of the loud mode is observed by reconstructing the velocity field using only mode 6. This reconstruction, performed using equation 4.14, yields the fluctuating velocity field using only mode 6. The mean is then added to the fluctuating contribution to reconstruct the instantaneous velocity field. In order to clearly see the structures propagating through the field, the instantaneous field is viewed in the convective time frame, as shown in the work of Bonnet *et al.* (1994) [35]. For a high-speed axisymmetric jet, the convective speed is assumed to be approximately 60% of the bulk flow at the exit [35, 224]. In this case, the convection velocity is Mach 0.36, taken to be the speed in the shear layer of the jet. The convection speed is subtracted from the instantaneous velocity to obtain the convective velocity field, as shown in equation 6.4.

$$\tilde{u}_{conv} = \tilde{u} - (0.6 \times U_j) \tag{6.4}$$

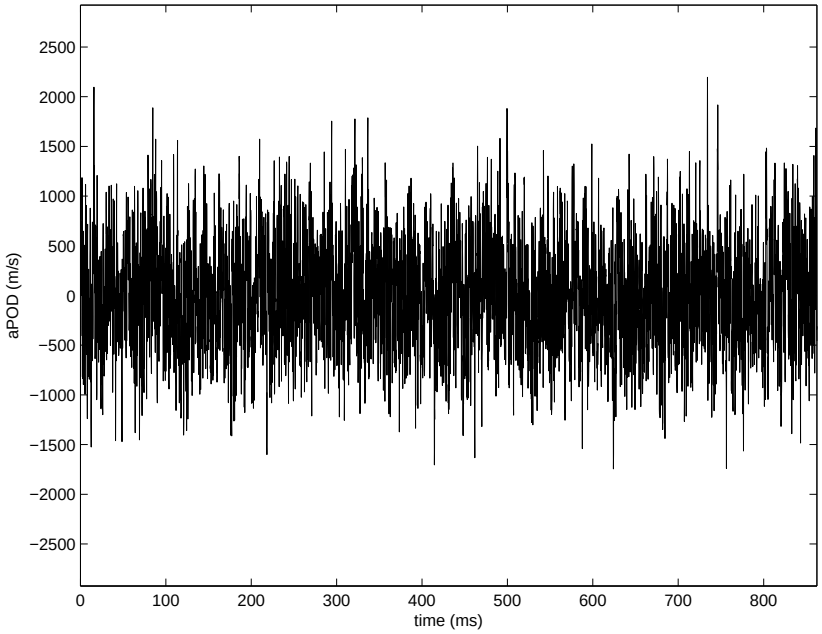

Figure 6.17: Mode 6 time-dependent POD expansion coefficient

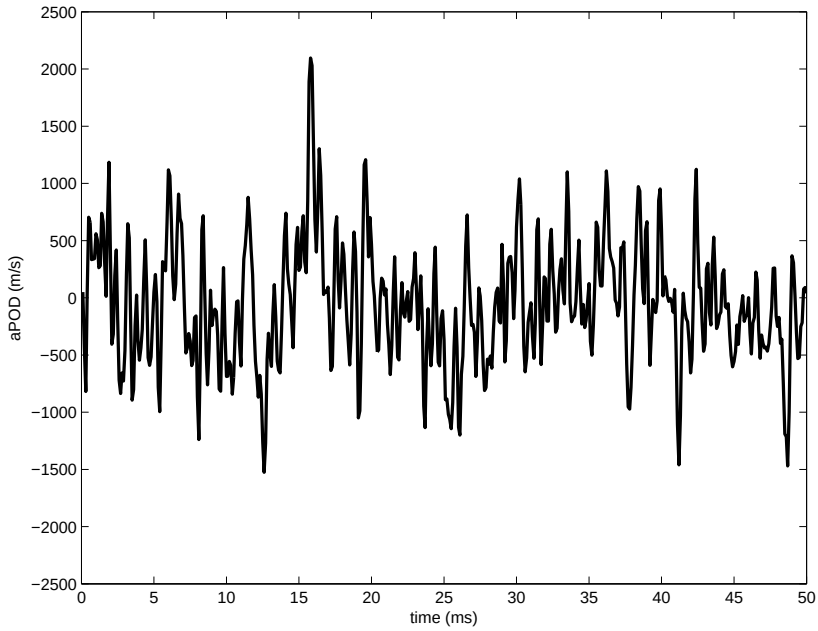

Figure 6.18: Mode 6 time-dependent POD expansion coefficient for the first 50 *ms*

Therefore the velocity in the flow field will be observed with reference to the shear layer, which is not moving in the convective frame. All velocity reconstructions of the loud mode will be presented in the convective frame.

6.3.1 Near-Field Diagnostics to Far-Field Acoustics

First, the full original velocity field in the convective frame is presented for a single snapshot (using all POD modes for reconstruction) in Figure 6.19. The two-component velocity is represented by the vectors, which are plotted on top of the streamwise velocity contours for emphasis. The complexity of the flow field motivates the low-dimensional representation using the loud mode, as previously discussed. Within the extracted 50 *ms* for POD mode 6, there are several snapshots where interesting behavior in the flow physics is observed at random points in time. The identification of individual low-dimensional spatiotemporal events contributing to far-field noise is a daunting task and thus additional techniques have been employed to aid in the process. The idea is to approach the problem using two independent techniques and begin to analyze key features of the flow field that may account for noise-producing events.

The method of relating near-field diagnostics to far-field acoustics is currently being studied in the context of noise source identification for high-speed jets. This work is being conducted at Syracuse University by Lewalle *et al.* (2013,2014) [135, 137, 138] and Kan *et al.* (2013,2014) [115–118]. The flow field is characterized by velocity and velocity derivative quantities, denoted as diagnostics. These diagnostics are then correlated with the far-field acoustic signals (microphones) using wavelet filtering. Several spatial locations within the velocity field are sampled and using the time-frequency information from the wavelet filtering, highly correlated diagnostics are traced back to the flow field in both time and space. The particular diagnostic and correlation level is tracked throughout the analysis. It has been found that the diagnostics with the largest contribution to

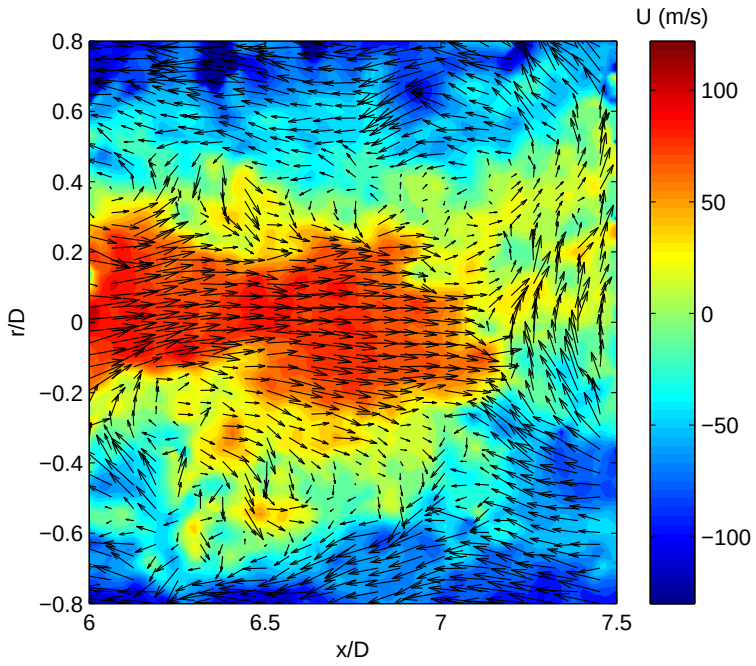

Figure 6.19: Original velocity field in the convective time frame at $t = 15.8$ *ms*

the far-field acoustics are streamwise velocity, transverse velocity, Reynolds stress, two-dimensional vorticity, two-dimensional divergence, Q-criterion, and the determinant of the two-dimensional rate of strain [115, 117, 137]. Since this method resolves the diagnostics in both time and space, a movie for the first 50 *ms* has been created to show the contributions of the diagnostics to the far-field acoustics. This movie can be found at: http://lcs3.syr.edu/faculty/lewalle/jetnearfield/index.html, and instantaneous snapshots have been extracted for comparisons with the current results [135]. In the movie, M denotes the far-field microphones, K the near-field *Kulites*, and D for the diagnostics. In terms of the colors for the diagnostics, the Q-criterion is represented with red, and shades of blue and green are related to vorticity and other similar diagnostics. The contour lines represent the contributions of the diagnostics to the cross-correlation with the far-field acoustics, in time, frequency and space. The diagnostic contributions are intermittent, which is to be expected.

This movie indicates that there are several instances with a large amount of activity followed by sometimes long periods with no activity at all. Occasionally, the highly active events are long in duration, $\mathcal{O}(1\ ms)$, while other times they can be quite short, $\mathcal{O}(0.1\ ms)$. Using this movie as a reference, snapshots from the mode 6 reconstructions are extracted when a large amount of diagnostic activity is present. From these mode 6 reconstructed snapshots, those with irregular flow structures are extracted for further investigation. Preliminary results indicate that a time of particular interest using both approaches occurs around $t = 15.7\ ms$. Two instantaneous snapshots are taken at $t = 15.7\ ms$ and $15.8\ ms$ from the diagnostics movie to display the amount of near-field activity (see Figures 6.20 and 6.21). Additional highly active snapshots for $t = 16.3\ ms$ and $23.6\ ms$ can be found in Appendix C for reference.

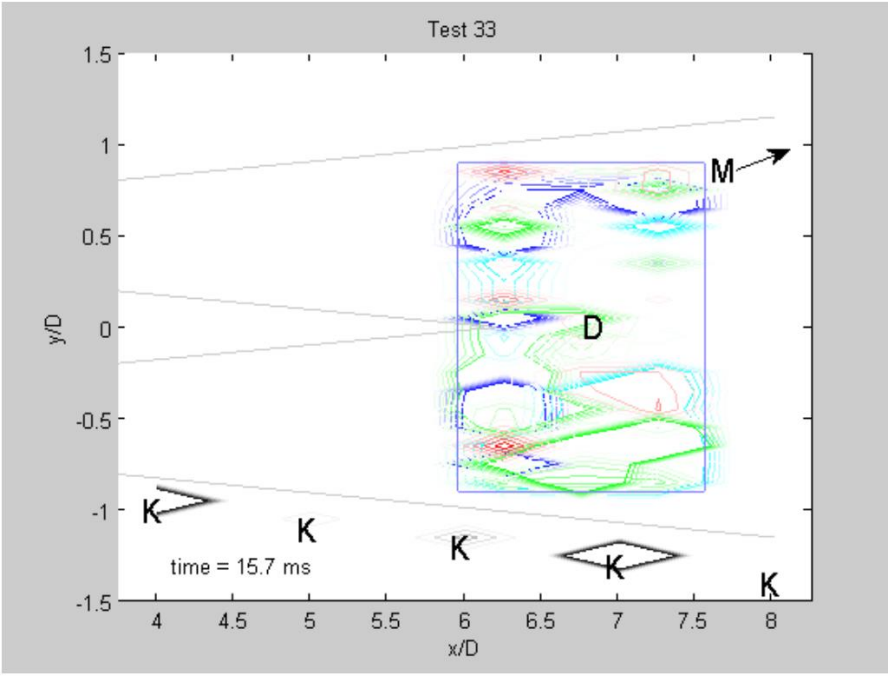

Figure 6.20: Near-field diagnostics at $t = 15.7\ ms$ [135]

To complement the snapshots presented, which show large amounts of diagnostic activity, an additional snapshot is chosen to demonstrate the lack of activity at intermittent

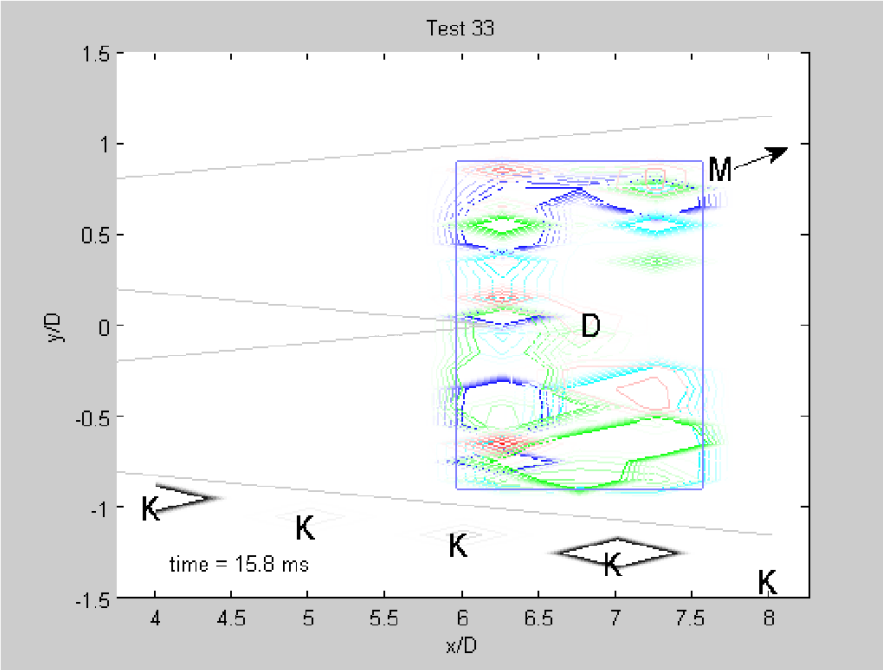

Figure 6.21: Near-field diagnostics at $t = 15.8\ ms$ [135]

points in time. Figure 6.22 shows a snapshot at $t = 20.0\ ms$, where there is no diagnostic activity present. Once again, this means there are no diagnostic quantities in the velocity field that are contributing, in a recognizable way, to the far-field acoustics at this particular instant in time. Analogous representations will be presented and interpreted for the mode 6 reconstructions in the next section.

6.3.2 Reconstructed Velocity Field

The mode 6 reconstructions are shown for the same two snapshots ($t = 15.7\ ms$ and $15.8\ ms$) in order to see what the actual low-dimensional flow field looks like during this time of high diagnostic activity. The convective velocity is once again represented with vectors which are now plotted on top of streamwise or transverse velocity contours to emphasize the structures in both directions. In addition to the reconstructed velocity field, the

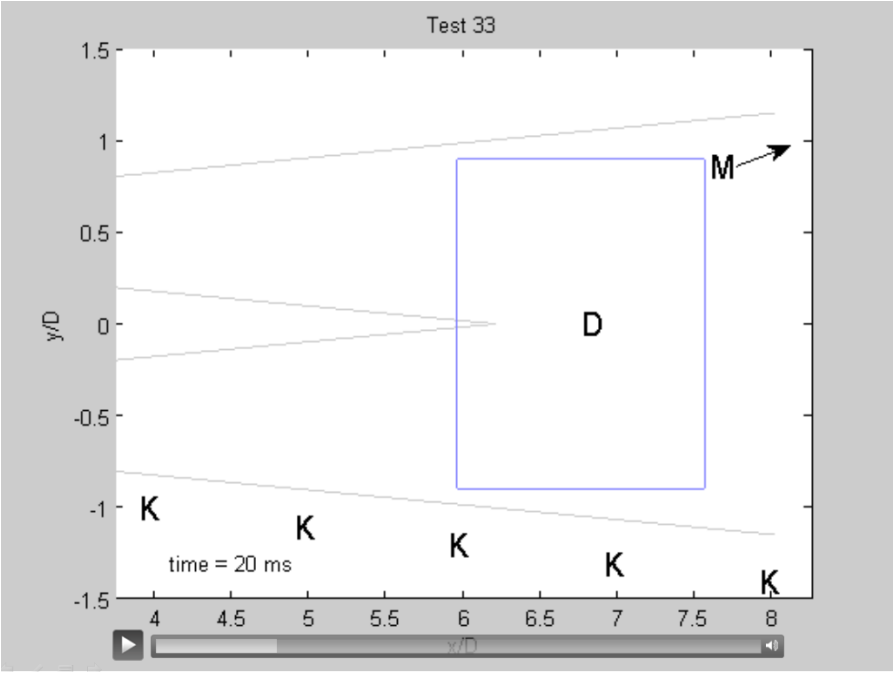

Figure 6.22: Near-field diagnostics at $t = 20.0\ ms$ [135]

corresponding point in time with respect to the temporal POD coefficient is also shown. Before presenting these particular snapshots of interest, the snapshot at $t = 20.0\ ms$ is shown in Figure 6.23, to complement that of Figure 6.22, shown previously. Figure 6.23 does not appear to reveal any interesting features of the flow physics, as confirmed by the diagnostic technique (Figure 6.22).

The mode 6 reconstructions for $t = 15.7\ ms$ and $15.8\ ms$, plotted with streamwise velocity contours are shown in Figures 6.24 and 6.25, respectively. These particular snapshots are characterized by large perturbations in the velocity field as seen by the contortion of structures. This behavior only lasts for a few snapshots and occurs intermittently in time. The contortion of the structures is qualitatively quite different from that of Figure 6.23. Moreover, the initial conjecture that there is something inherently unique about this particular flow structure is consistent with the diagnostics presented in Figures 6.20 and 6.21, which display a large amount of activity correlating highly with the far-field acoustics. We

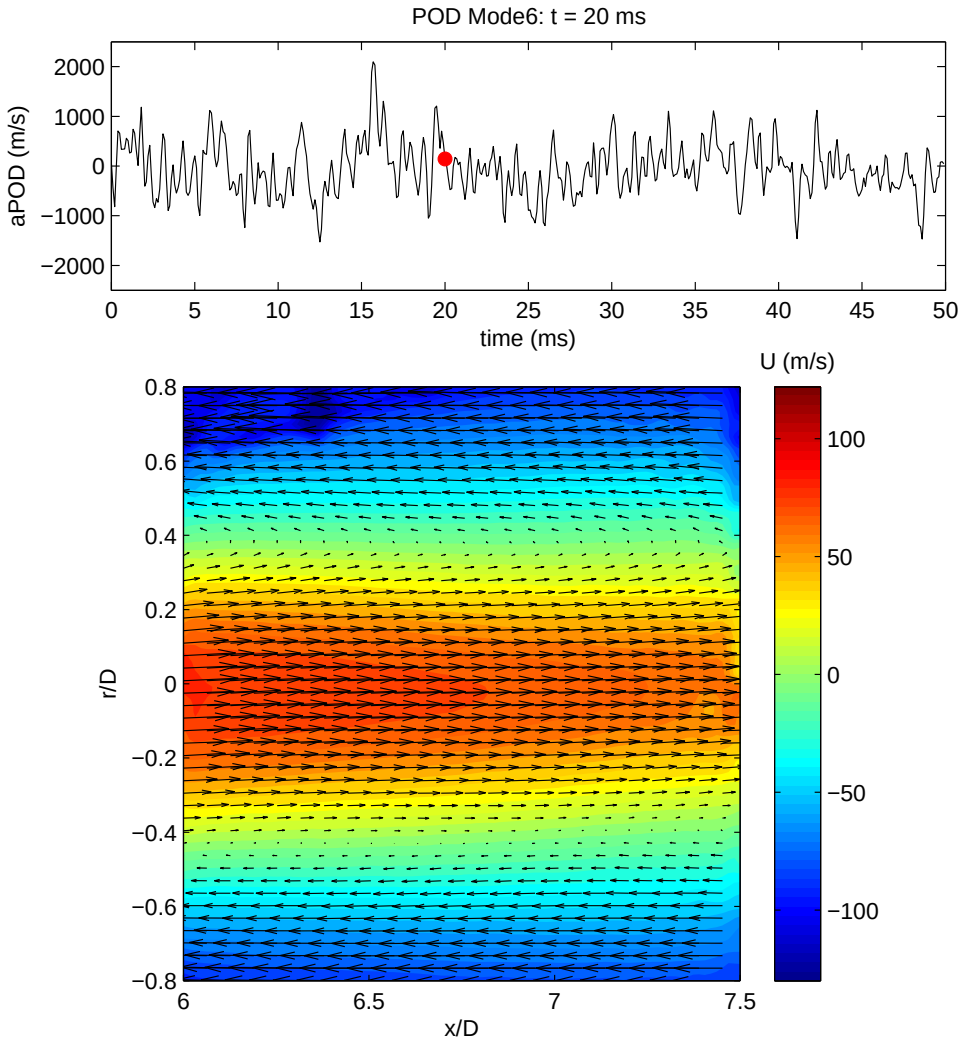

Figure 6.23: Mode 6 reconstruction in the convective time frame at $t = 20.0\ ms$

hypothesize that this contorted structure seen in Figures 6.24 and 6.25 might represent an event or interaction of structures in the flow field that is responsible for a large portion of the far-field noise. The most interesting point to be made is that the two completely independent techniques reveal the same snapshot in time, which contributes highly to the far-field acoustics. This conjecture is of course an initial thought based on the tools and

analysis at hand. Further investigations into some of these ideas is required, however these results provide a starting point for future analyses.

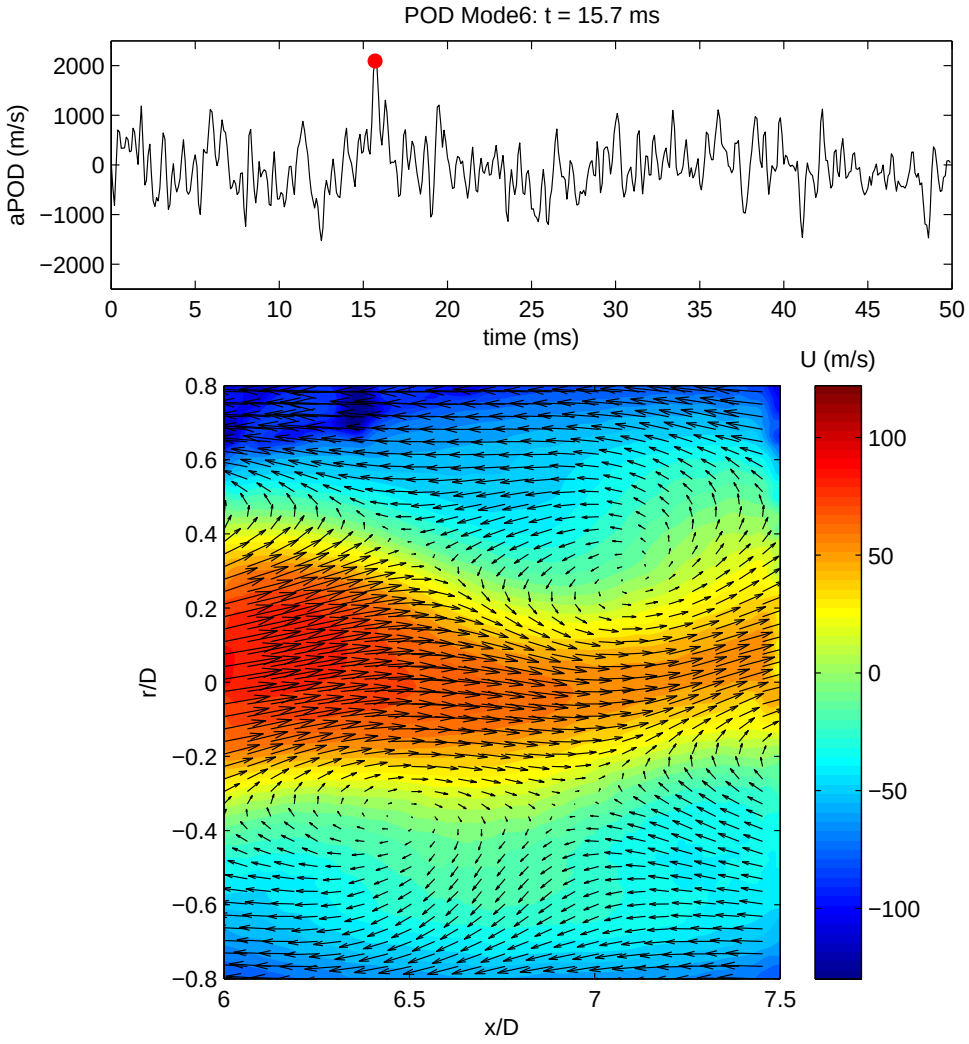

Figure 6.24: Mode 6 reconstruction in the convective time frame at $t = 15.7$ *ms*, with streamwise velocity contours

Looking more closely at Figures 6.24 and 6.25, it is observed that the contortion of structures is spatially asymmetric, indicating some interesting interactions are most likely occurring. Keeping in mind that the PIV plane is a two-dimensional view of a highly

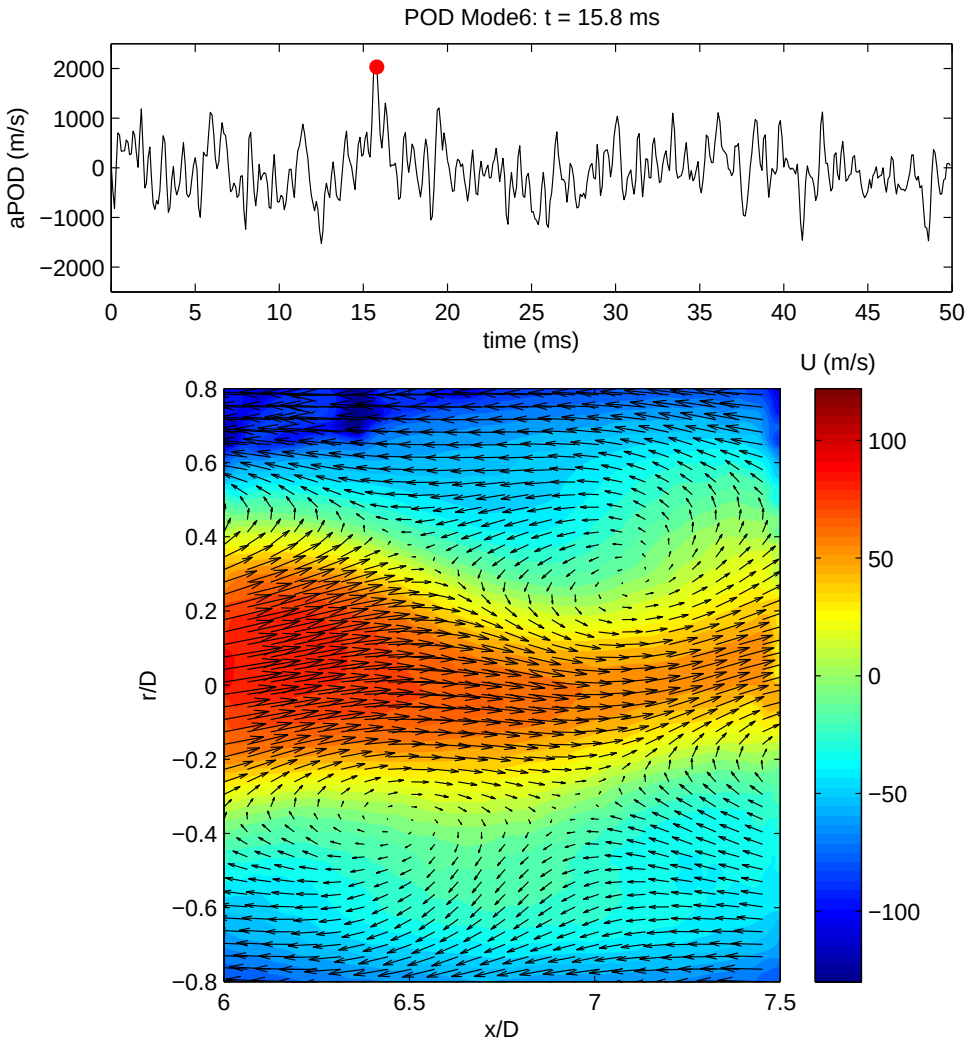

Figure 6.25: Mode 6 reconstruction in the convective time frame at $t = 15.8$ *ms*, with streamwise velocity contours

three-dimensional field, one can imagine vortices interacting as a result of the potential core collapse causing high strain stretching and contortions in all three dimensions. The structures seen in the figures presented could be a two-dimensional projection of such interactions. Moreover, this highly irregular flow structure occurs at the largest peak of the time-dependent expansion coefficient, in this particular range of time. Coupling this with

the diagnostic analysis leads to the hypothesis that irregular flow structures in time and space, that are characterized by the low-dimensional loud mode, are the most efficient contributors to the far-field noise. These short duration, contortions in the loud mode could assist in identifying the full three-dimensional interaction of structures responsible for the noise-producing events. As with the diagnostics, similar trends are observed at $t = 16.3\ ms$ and $23.6\ ms$, and these results can be found in Appendix C. The results presented in Figures 6.24 and 6.25 are now shown with transverse velocity contours in Figures 6.26 and 6.27.

The transverse velocity contours reveal large scale flow structures, which appear to be most dominant at these particular snapshots in time. The strong radial component that is observed could possibly represent a radial ejection of fluid caused as a result of the interaction of vortices. This idea couples nicely with initial conjecture that the interaction of streamwise vortices is causing the contortion of structures in the streamwise direction and ejection of fluid in the radial direction. This is of course a hypothesis based on the two-component results presented along the centerline of the jet.

Up to this point, it has been shown that POD mode 6 of the velocity field is identified from the OID analysis as the loud mode. The contortion of structures in the flow field at particular instances in time are believed to be potential sources of far-field noise, as supported by the diagnostics technique. An important question regarding the temporal behavior of mode 6 still needs to be addressed. Are these flow structures unique to this low-dimensional mode or are similar structures observed for the other modes? The diagnostics technique has identified $t = 15.7\ ms$ as important instance in time with respect to the potential noise-producing events in the near-field. Therefore, this snapshot is examined for modes 5 and 7 to see if similar flow structures are present at this time.

Figures 6.28 and 6.29 present the velocity reconstructions for modes 5 and 7 respectively at $t = 15.7\ ms$. Neither of these modes show contortions of structures as that seen

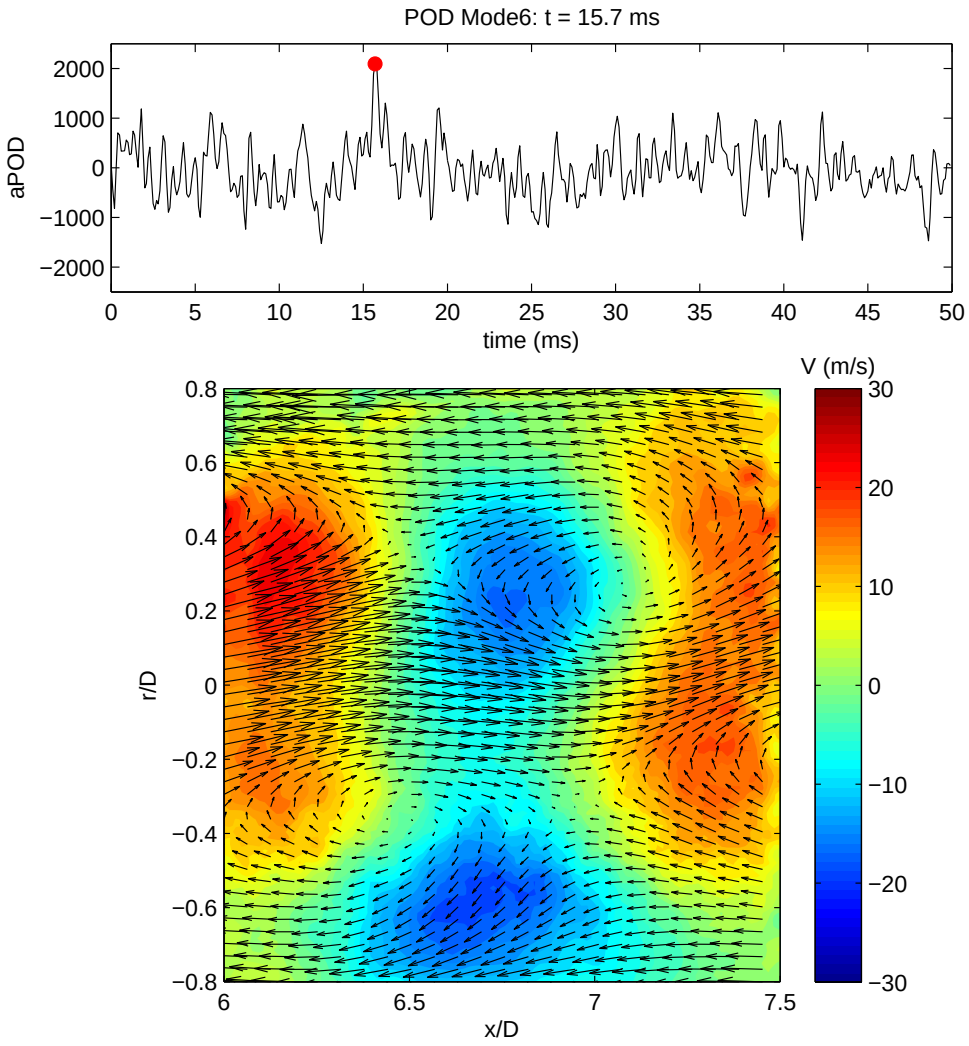

Figure 6.26: Mode 6 reconstruction in the convective time frame at $t = 15.7$ *ms*, with transverse velocity contours

with mode 6. This is also true for modes 1 through 4 at this particular snapshot (see Appendix C). The fact that the behavior seen in mode 6 is unique to that mode, at an instant in time where noise-producing events are believed to be occurring, implies that this behavior is worth investigating further. It is important to keep in mind that the full PIV velocity field is formed from the summation of *all of the modes*. The analysis presented suggests that from

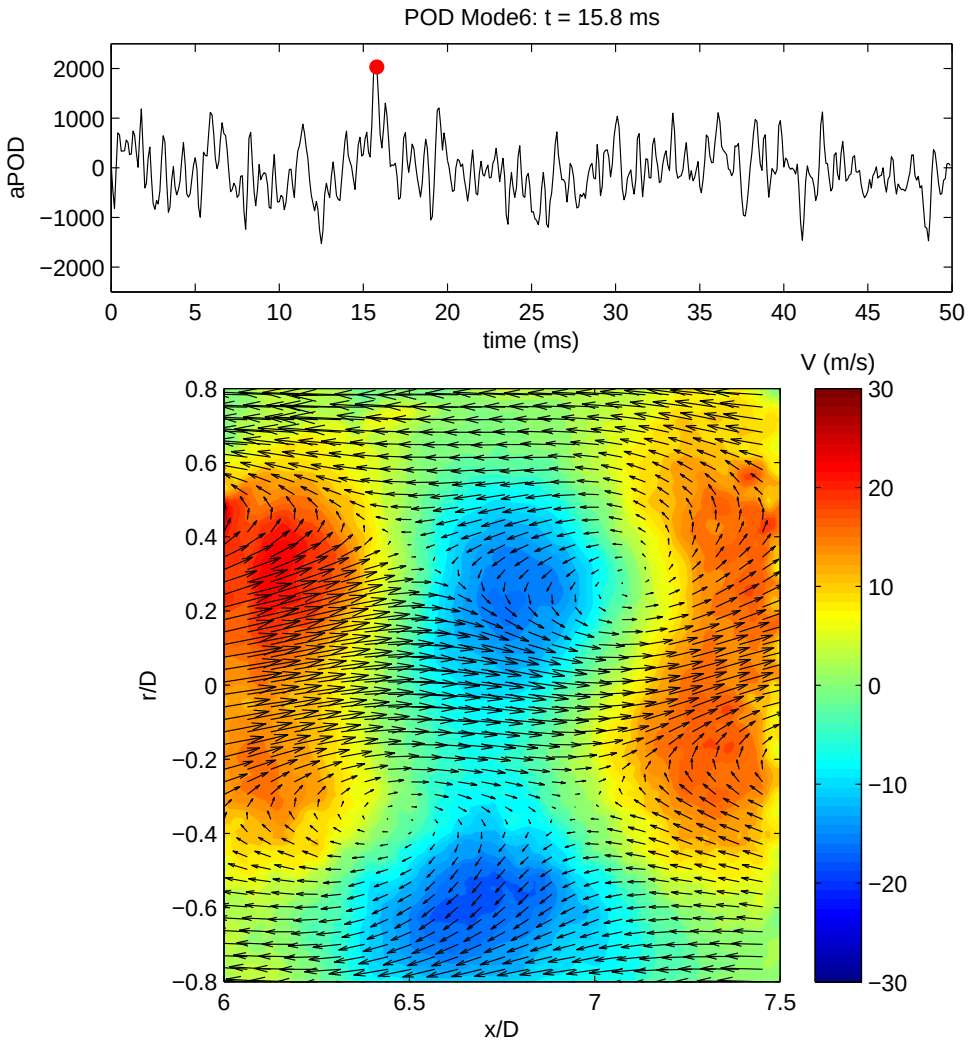

Figure 6.27: Mode 6 reconstruction in the convective time frame at $t = 15.8$ *ms*, with transverse velocity contours

a low-dimensional standpoint, the spatial structures that have the strongest contributions to the far-field noise have been identified. To further validate that the other low-dimensional modes do not exhibit the flow features intrinsic to mode 6, a ten mode reconstruction of the convective velocity field is presented both with and without mode 6 taken into the formulation. Figure 6.30 shows a ten mode reconstruction of the flow field at $t = 15.7$ *ms*

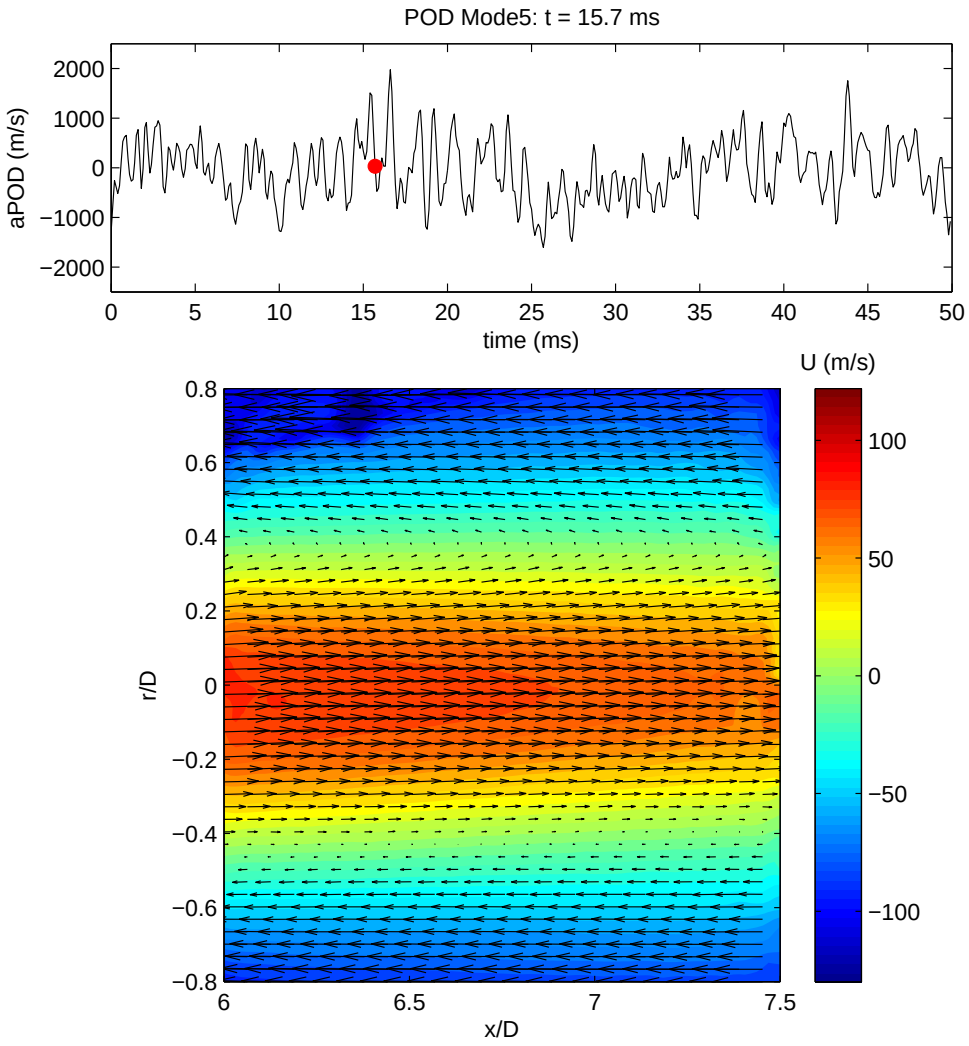

Figure 6.28: Mode 5 reconstruction in the convective time frame at $t = 15.7$ *ms*, with streamwise velocity contours

including mode 6. With a full ten mode reconstruction, the contortion present in mode 6 is clearly observed at this snapshot. This would indicate that mode 6 seems to dominate the flow field, consistent with previous observations. To confirm this, the flow field is reconstructed from the first ten modes, with mode 6 filtered out, shown in Figure 6.31. The filtering of mode 6 confirms that this particular mode dominates the overall flow field at

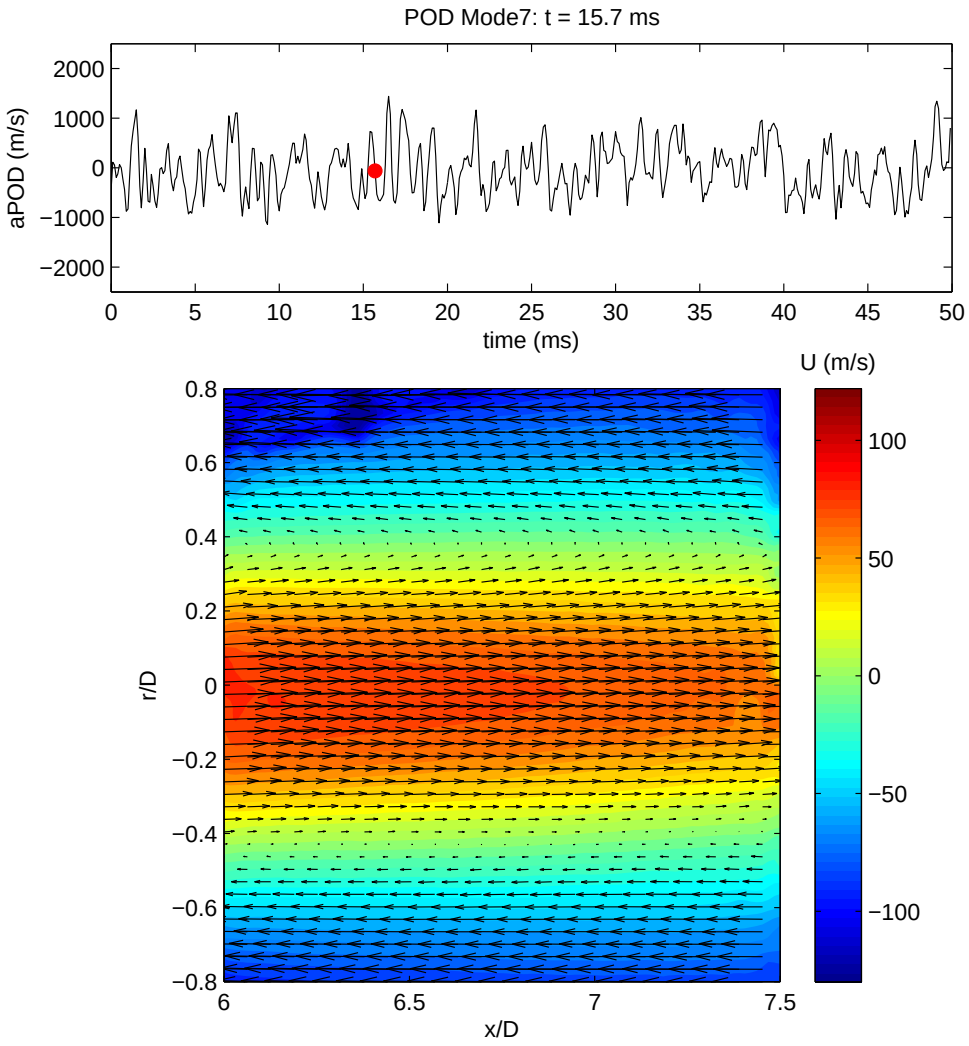

Figure 6.29: Mode 7 reconstruction in the convective time frame at $t = 15.7$ *ms*, with streamwise velocity contours

this snapshot in time. The significant reduction in the contortion of structures in the other nine modes validates that there is an interesting interaction occurring here directly related to the loud mode. The claim is not that mode 6 is the only mode responsible for the noise-producing events, but rather it provides the greatest contribution from a low-dimensional perspective in terms of kinetic energy.

Based on the results presented in this section, the OID technique can be applied to the controlled jet in order to determine the loud modes as a result of the active flow control. This couples with the concepts of control discussed in § 5 using the LWPIV, and the loud mode identification through OID discussed in this section. The 2013 TRPIV results involving the active flow control are presented in the following section.

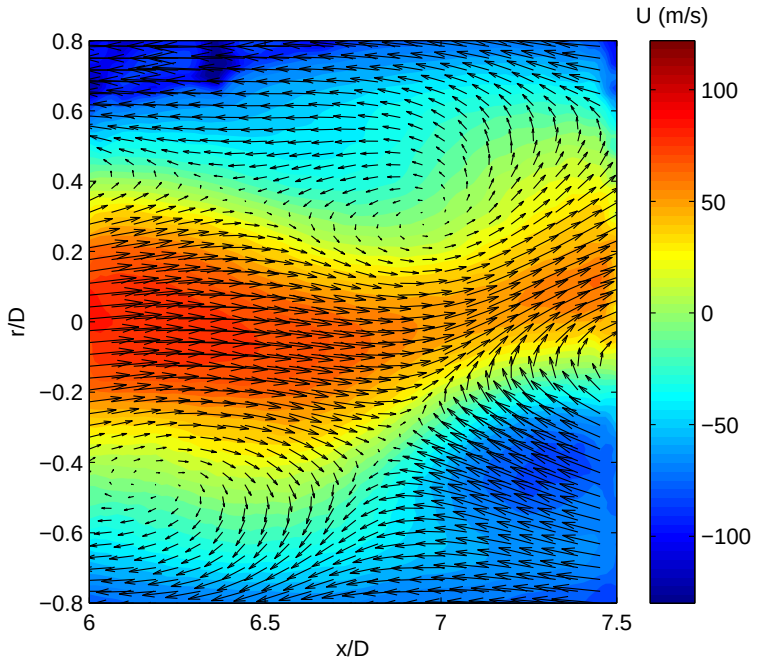

Figure 6.30: Reconstruction of modes 1 through 10 in the convective time frame at $t = 15.7$ *ms*, with streamwise velocity contours

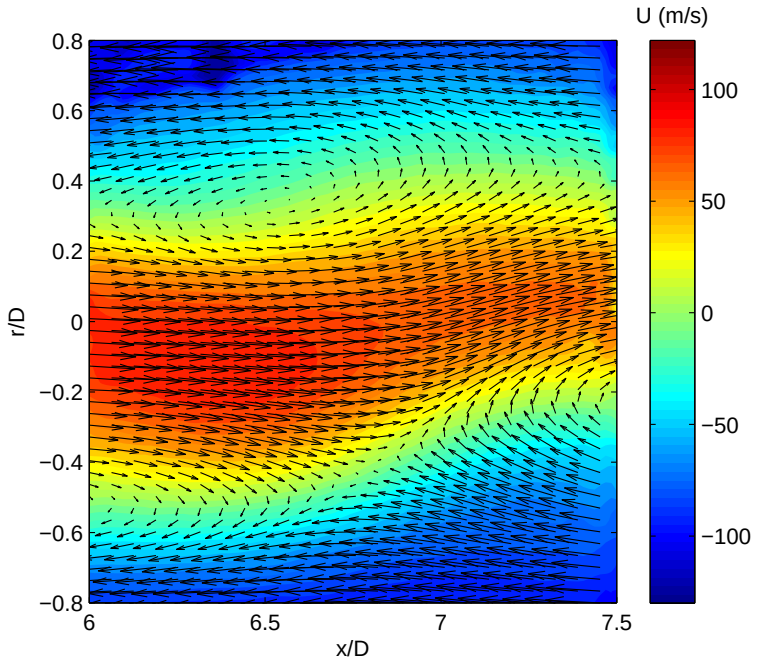

Figure 6.31: Reconstruction of modes 1 through 10, mode 6 filtered, in the convective time frame at $t = 15.7$ *ms*, with streamwise velocity contours

6.4 2013 TRPIV Results

The TRPIV experiments conducted in 2013 comprise a large data set involving several different tests ranging from active flow control to extended window sizes and off-center plane measurements. In the context of the work presented thus far, this section will focus primarily on the active flow control results. A detailed description of the other experiments conducted can be found in the work of Berger *et al.* (2014) [29]. The different types of flow control implemented in this set of experiments directly follows the strategies outlined in § 5 for the LWPIV experiments. Therefore cases *OLC1, CLC1 and CLC2* are performed in this set of experiments and case *OLC2* is taken from the 2011 experiments to complete the set.

The *OLC1* case was acquired at several downstream locations, however the two closed-loop cases were only acquired at one single downstream location. This is due to the time sensitivity of the experimental testing as well as the limited number of synthetic jet actuators. Due to the fact that the PIV requires seeding of the bulk flow, olive oil residue easily becomes trapped in the actuation glove, causing the actuators to fail quite often. Therefore actuators had to be switched out quite frequently due to the large amount of excess olive oil.

The results presented will focus on the PIV window spanning from 4D to 5.5D downstream, along the centerline of the jet in the streamwise direction. This is the furthest downstream location that could be acquired for the control cases with this particular setup, due to the design of the new pressure ring. Recall, that the new pressure ring is more rigid and thus the placement of the *Kulites* is more precise than the 2011 experiments. For the closed-loop experiments, the ring could not be removed since the sensors in the azimuthal array are used for feedback in the control loop. This is an issue that will need to be addressed for future experiments.

6.4.1 Relation to LWPIV Results

To justify shifting the analysis from the LWPIV to the smaller window TRPIV in the context of studying control, the two data sets are compared using the spatial POD modes of the velocity field. Since there will of course be windowing effects present with a smaller window (as in the TRPIV), a window of the same size as the TRPIV is extracted from the LWPIV data set. After this window is extracted, the POD is performed and compared to the TRPIV modes (POD) using the correlation of the spatial eigenfunctions as previously presented. The first sixteen spatial eigenfunctions using the POD are compared for the baseline cases of the TRPIV and LWPIV at the same window location. The spatial eigenfunction for the TRPIV and the extracted LWPIV are shown in Figures 6.32 and 6.33. The first few modes seem to correlate quite well as expected, since for the same window location, the deterministic spatial structures from a low-dimensional viewpoint should be the same. Once again, recall that the POD solves for these basis functions to within a phase and thus it is the shape of the structures that is most important.

The correlation between these modes are computed and the results are shown in Figure 6.34. From this analysis, it is shown that the first 7 modes correlate quite well (correlation levels ranging from 0.6 to 0.8), indicating the spatial structures are similar as expected. The lack of high correlation beyond this point could be accounted for by windowing effects and the lack of full convergence in the POD modes with the LWPIV data set. A summary of the correlations between the first sixteen modes can be found in Appendix D.

An additional LWPIV data set containing an order of magnitude more snapshots for statistical convergence was collected at two different Mach numbers (0.6 and 0.85), for the uncontrolled jet, by Shea *et al.* (2014) [207]. In this work, the extracted LWPIV modes are correlated with the 2011 TRPIV results. For more information regarding the relationship between the LWPIV and TRPIV spatial eigenfunctions, please refer to the work of Shea *et al.* [207].

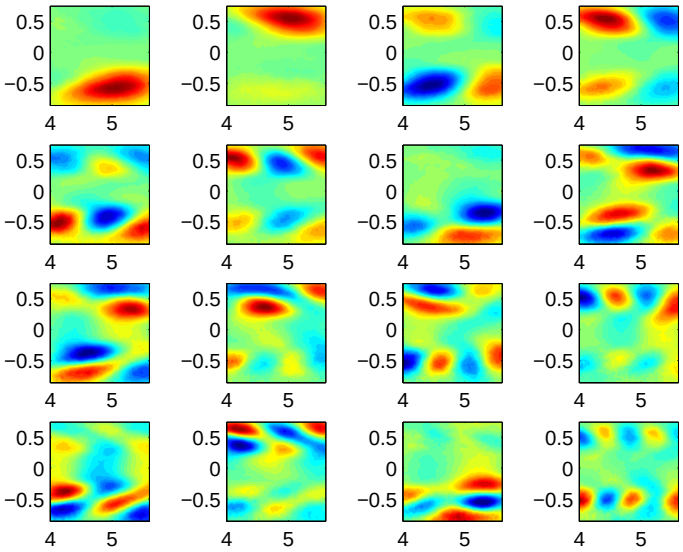

Figure 6.32: First 16 spatial eigenfunctions, $\phi_u^{(n)}(\vec{x})$ for TRPIV (baseline): abscissa $= x/D$, ordinate $= r/D$

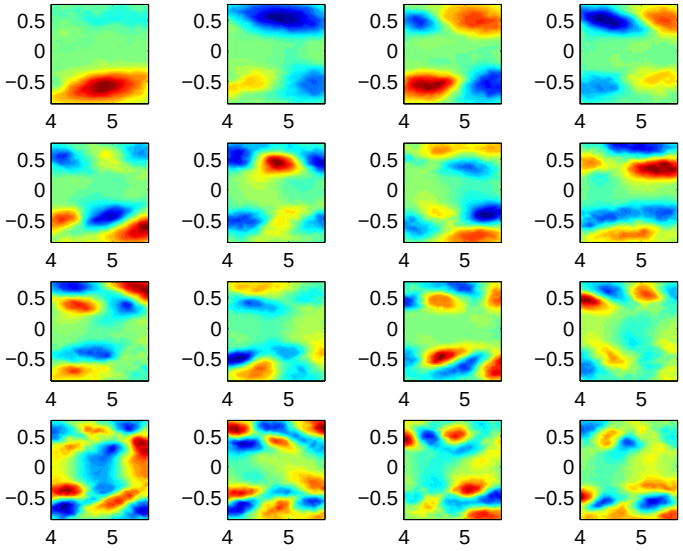

Figure 6.33: First 16 spatial eigenfunctions, $\phi_u^{(n)}(\vec{x})$ for extracted LWPIV (baseline): abscissa $= x/D$, ordinate $= r/D$

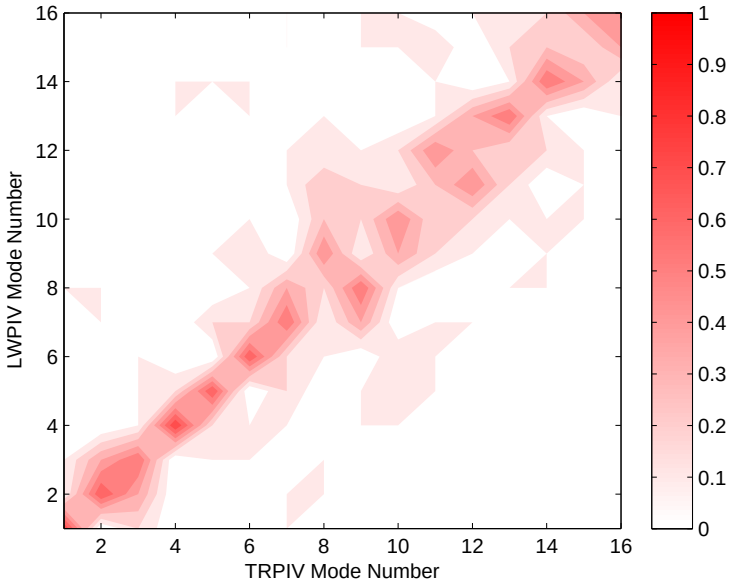

Figure 6.34: Modal correlation of the first 16 spatial eigenfunctions, $\phi_i^{(n)}(\vec{x})$, for the TRPIV and extracted LWPIV cases (baseline)

6.4.2 Near-Field Pressure and Far-Field Acoustics

For near-field pressure measurements, the new pressure ring is implemented with a total of fourteen *Kulites* arranged in an azimuthal array at 6D (with nine sensors) and a linear array with sensors from 4D to 6.5D (with a 0.5D spacing). The configuration of *Kulites* using the new pressure ring can be seen in Figure 6.35. The azimuthal array of sensors at 6D are used for the closed-loop feedback and the sensor located at 6D in the linear array is also part of the azimuthal array, as indicated by the blue dot in Figure 6.35. The near-field pressure spectra are plotted for each sensor in the two arrays for the baseline case.

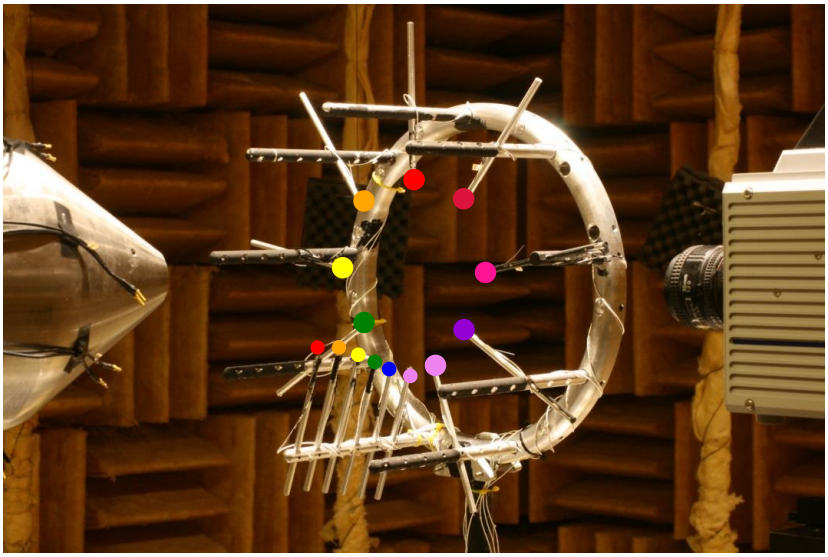

Figure 6.35: Near-field *Kulite* configuration showing linear and azimuthal sensor arrays

Figure 6.36 shows the pressure spectra for the azimuthal near-field array for the baseline case. As indicated by the figure, the sensor signals collapse across most of the frequency band where the dominant jet frequencies are present. For the linear array of sensors, the pressure spectra is shown in Figure 6.37. The spectra of the linear array of sensors indicates a shift in the dominant frequency as the jet evolves downstream and the potential core

begins to collapse. The effects of the control on the near-field pressure spectra are similar to the results presented for the LWPIV experiments (see § 2.2.4). Since this is not the current focus of this section, the near-field pressure spectra for the control cases can be found in Appendix D.

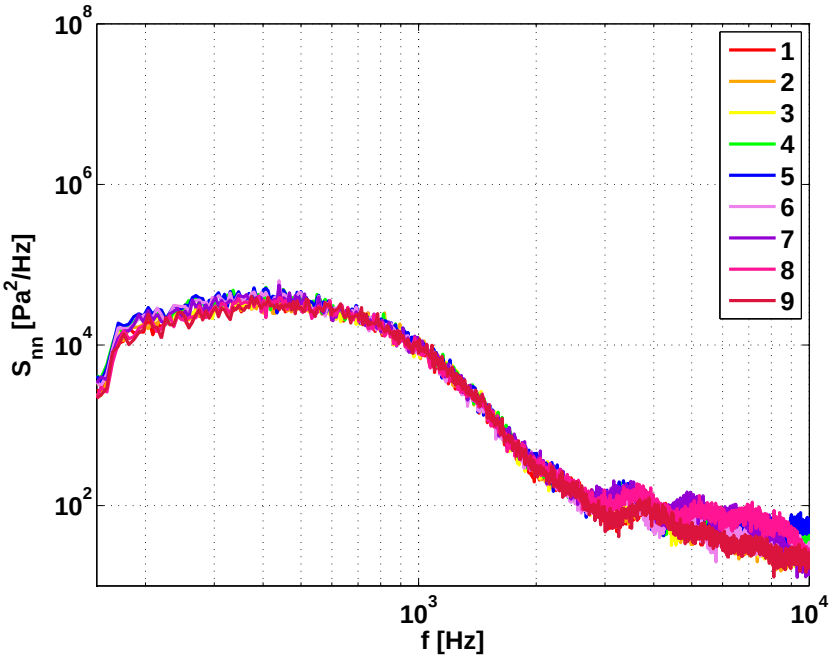

Figure 6.36: Near-field pressure spectra, azimuthal array (baseline)

Figure 6.38 shows the far-field SPL for the in-plane microphones, for the baseline case. Once again, similar trends are seen for the out-of-plane microphone and the effects of the control are similar to that of the LWPIV results (§ 2.2.4). The remainder of the far-field SPL results can be found in Appendix D.

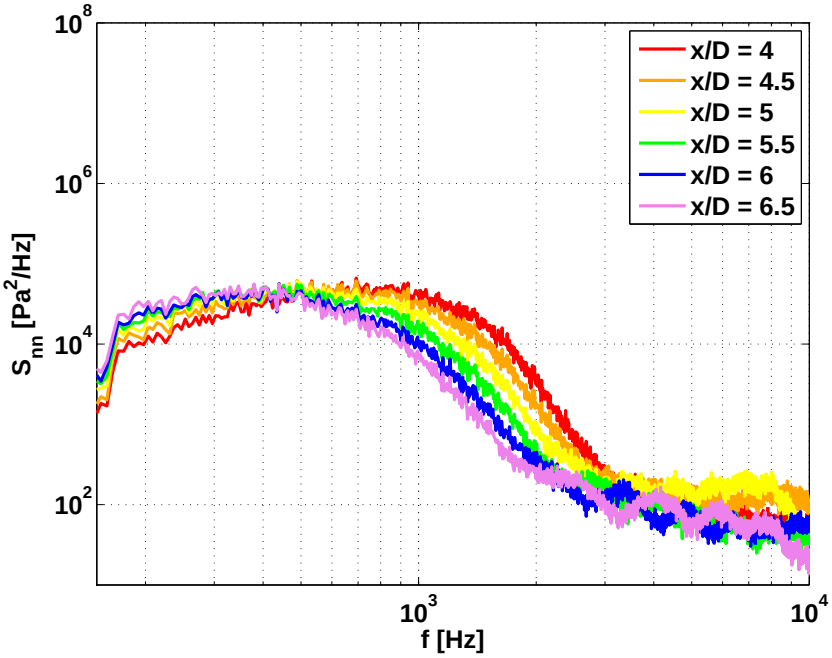

Figure 6.37: Near-field pressure spectra, linear array (baseline)

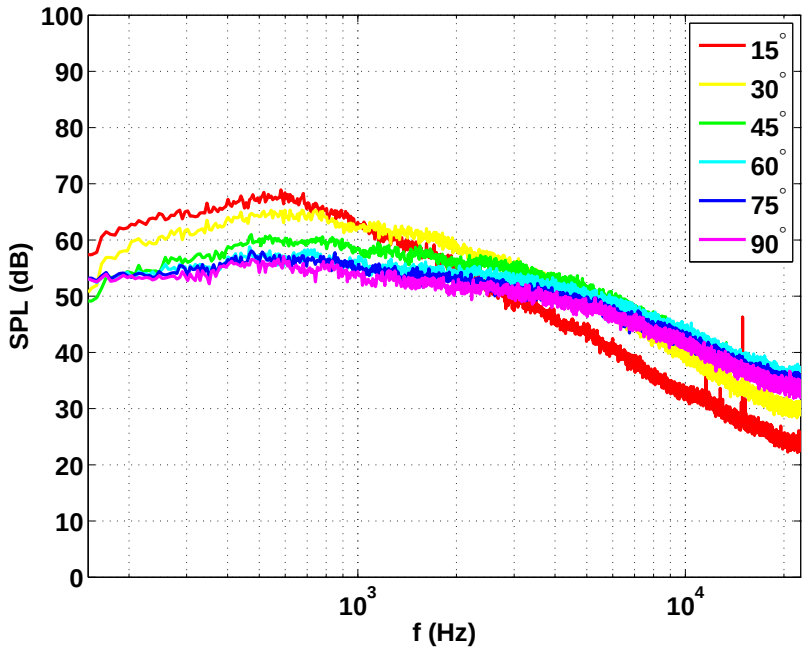

Figure 6.38: Far-field SPL, in-plane microphones (baseline)

6.5 TRPIV Velocity Field

The data presented in this section will focus on the identification of loud modes through the OID, as a result of the active flow control. This is done using the TRPIV experiments since the OID modes can be computed directly from the time-resolved, temporal POD velocity modes. This combines the concepts previously discussed in this chapter with the results from the LWPIV experiments. For the control cases, some additional post-processing has been done on two of the data sets. A slight misalignment of the PIV laser caused randomly distributed spurious vectors in the *OLC1* case. As such, a technique known as Gappy POD has been applied to minimize the amount of spurious vectors in the velocity field. For the *OLC2* case, which is taken from the 2011 TRPIV experiments, the window size is slightly different from the 2013 TRPIV experiments and thus a smaller window is extracted for consistency across all control cases.

6.5.1 Open-Loop Control Post-Processing

An instantaneous snapshot of streamwise velocity contours for the *OLC1* case is shown in Figure 6.39. The spurious vectors are seen in the potential core and lower portion of the shear layer. The goal is to fill in the data using the information known from the mean field and spatial eigenfunctions from the POD. In the statistical sense, an accurate representation of the flow field can be constructed in the regions where there is missing or incorrect data. This concept is known as Gappy POD and will be implemented to repair this data set. The Gappy POD technique is further explained by Bui-Thanh *et al.* (2004) [42], Wilcox (2006) [253], Murray & Ukeiley (2007) [168], Vendl & Fassbender (2010) [238] and Ruscher *et al.* (2013) [193]. The Gappy POD has been applied to the *OLC1* case using the *Orange HSD* code developed by Ruscher at Syracuse University [194]. The resulting instantaneous snapshot with Gappy POD applied is shown in Figure 6.40. The spurious vectors have been eliminated as a result of the Gappy POD and thus the technique has been applied to

the entire data set for further analysis.

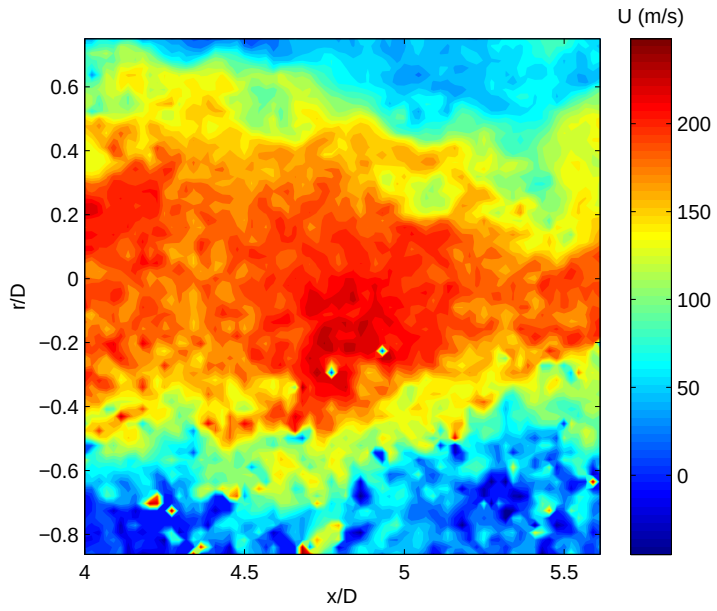

Figure 6.39: Instantaneous snapshot of streamwise velocity contours for case *OLC1*

For the *OLC2* case taken during the 2011 TRPIV experiments, a smaller window to match the 2013 results is extracted. Once again, the *Orange HSD* tool is used to extract the necessary data [194]. A snapshot of the streamwise instantaneous velocity contours taken from the extraction is shown in Figure 6.41. This open-loop control case completes the set of control cases, analogous to those studies for the LWPIV experiments. Instantaneous velocity snapshots for the two closed-loop control cases are shown in Appendix D for completeness.

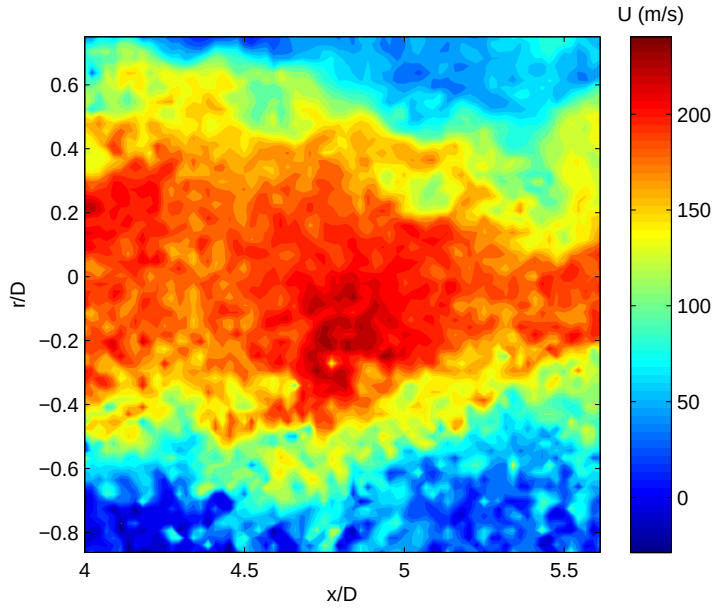

Figure 6.40: Instantaneous snapshot of streamwise velocity contours for case *OLC1* with the application of Gappy POD

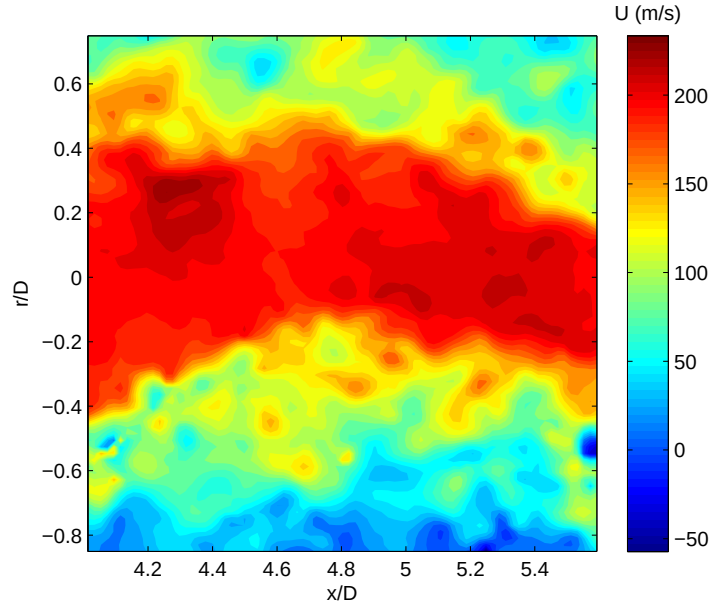

Figure 6.41: Instantaneous snapshot of streamwise velocity contours for case *OLC2*, taken from the 2011 TRPIV experiments

6.5.2 Mean Flow Field

As with the LWPIV results, the mean flow residual is computed in order to see the effects of the various control inputs on the velocity field. For reference the mean flow represented by streamwise velocity contours is shown for the baseline case in Figure 6.42. The effects of the control on the mean velocity field via the mean flow residuals are shown in Figures 6.43 - 6.46.

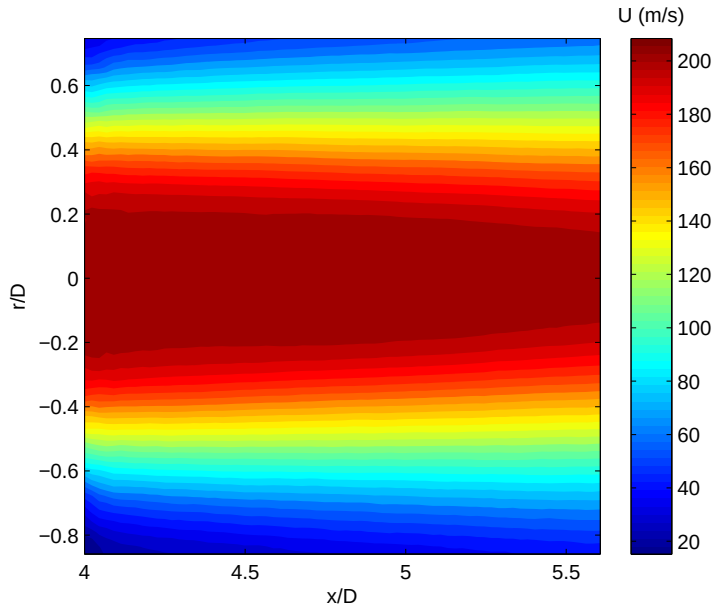

Figure 6.42: Streamwise velocity contours of the mean velocity field for the baseline case

For all flow control cases, actuation input at the nozzle lip results in a shortened potential core length as observed with the LWPIV data. For the *OLC1* case, the Fourier-azimuthal mode 1 forcing imposes a noticeable asymmetry in the flow field, which was also found to be the case in the LWPIV results. This confirms the idea that the open-loop forcing of Fourier-azimuthal mode 1 breaks up the dominant axisymmetric mode 0 through the "flapping" induced by the control input at the nozzle lip. The *OLC2* case greatly enhances mixing resulting in a shortened potential core length and noticeable shear layer expansion. This

is again consistent with the results shown for the LWPIV. Both closed-loop control cases seem to keep the flow relatively symmetric, while decreasing the potential core length and causing shear layer growth. The *CLC2* case seems to have a great effect on the flow field as compared to the *CLC1* case, as shown by the contour levels in the figures. The mean flow residuals are fairly consistent with those presented for the LWPIV experiments, with the exception of the *OLC1* case. Recall that for this case in the LWPIV, a strong vectoring of the jet was observed as a result of the control. Once again, this requires further investigation, however it is clear that Fourier-azimuthal mode 1 forcing imparts a strong asymmetry in the flow field due to the actuation input. To complement the mean flow residual plots presented, velocity profiles for the different control cases are presented with reference to the baseline case. Figure 6.47 shows the mean flow velocity profiles for all cases, taken at 5D downstream. The decrease in streamwise velocity along the centerline for all control cases, as compared to the baseline, confirms the decrease in potential core length as a result of the control. Within the potential core region, cases *OLC2 and CLC1* seem to exhibit similar behavior, as do cases *OLC1 and CLC2*.

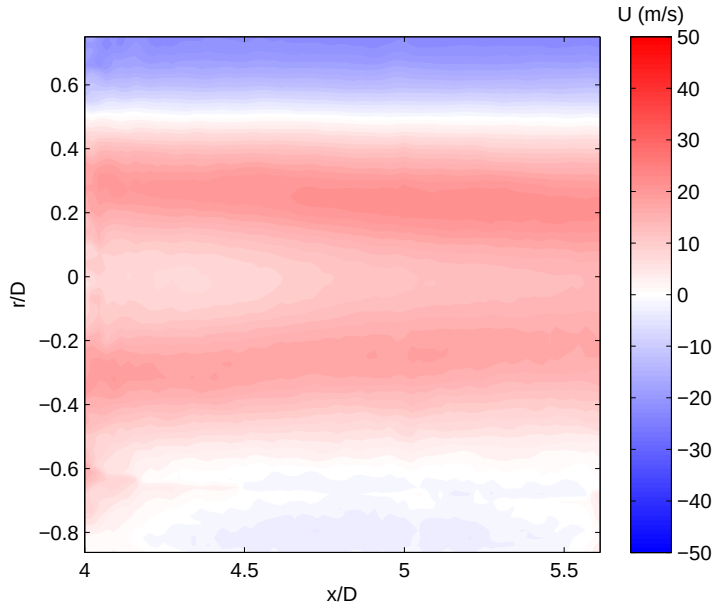

Figure 6.43: Mean flow residual of streamwise velocity for *OLC1*

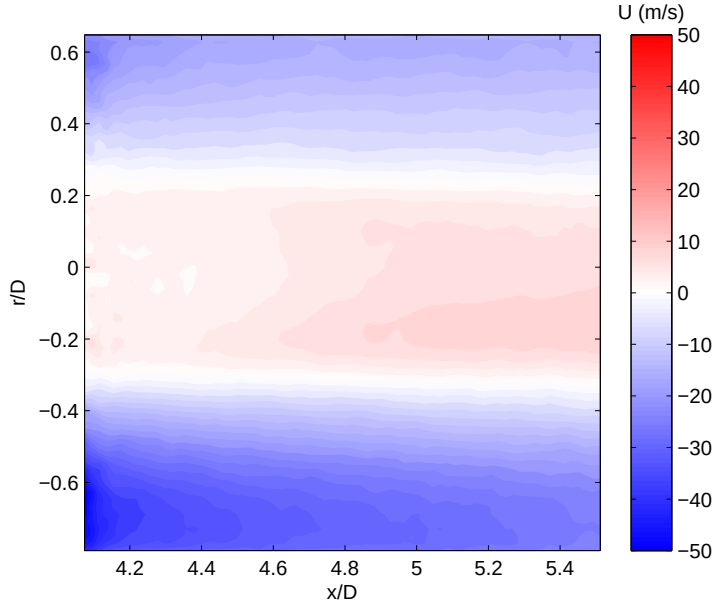

Figure 6.44: Mean flow residual of streamwise velocity for *OLC2*

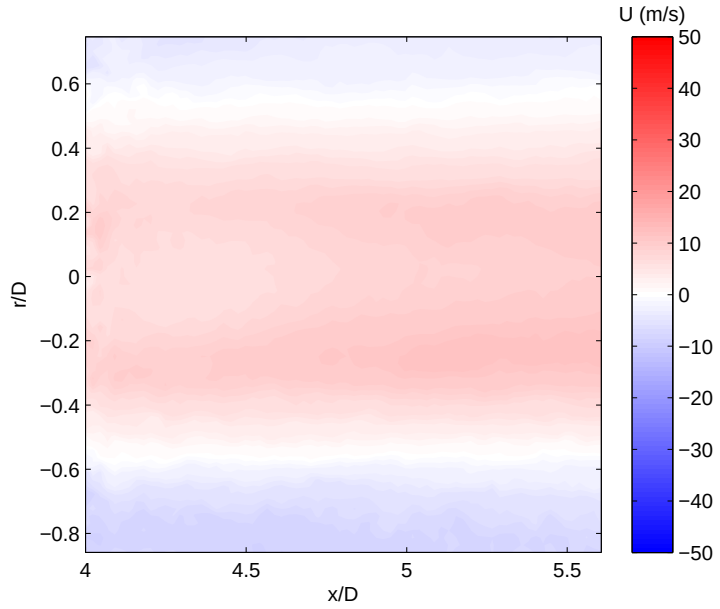

Figure 6.45: Mean flow residual of streamwise velocity for *CLC1*

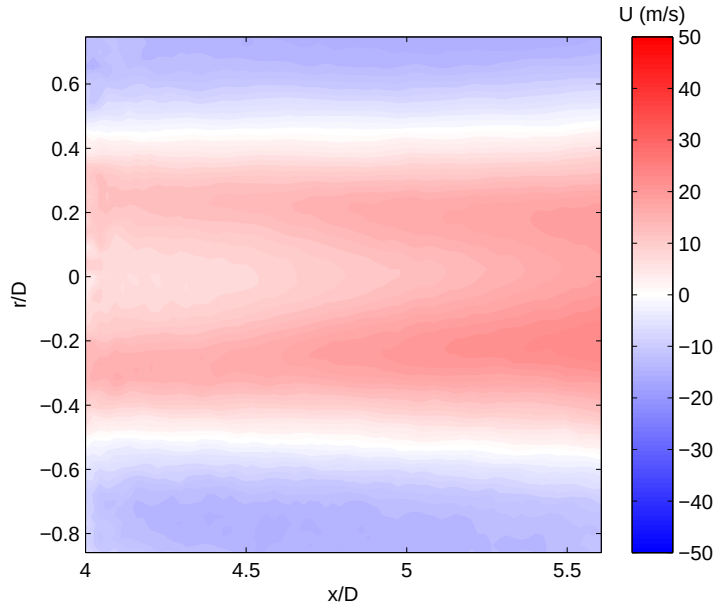

Figure 6.46: Mean flow residual of streamwise velocity for *CLC2*

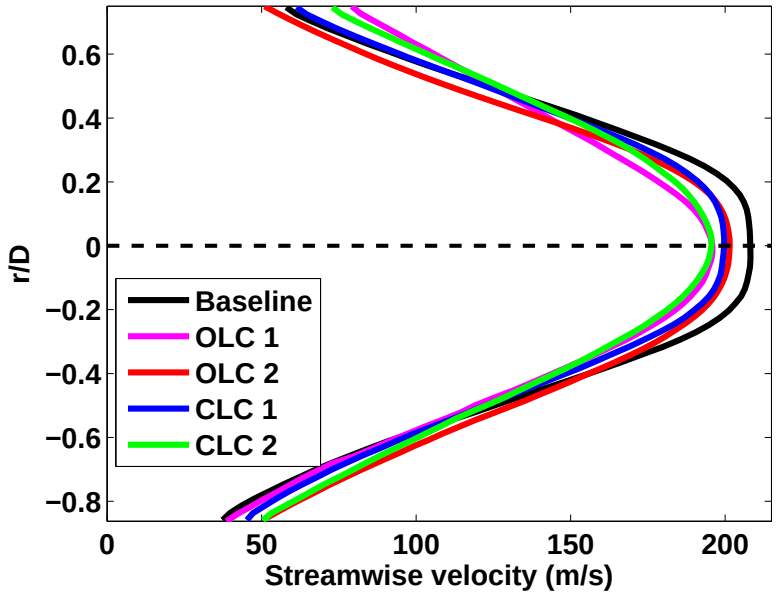

Figure 6.47: Mean flow velocity profiles taken at 5D downstream

6.6 Low-Dimensional Velocity Modes

The last portion of the analysis focuses on identifying the loud modes for the control cases using the OID technique previously presented. Once again, to have a better understanding of the large-scale, energetic flow structures, the POD is first performed on the velocity field to obtain the spatial and temporal POD modes. The convergence rate of the control cases and the baseline are presented for 5000 POD modes, shown in Figure 6.48. The baseline and two closed-loop control cases converge at the same rate, while case *OLC2* converges faster and case *OLC1* converges slower, as compared to the other cases. Looking at the first 25 modes, shown in Figurer 6.49, anywhere from 41% to 52% of the total energy is recovered with this number of modes.

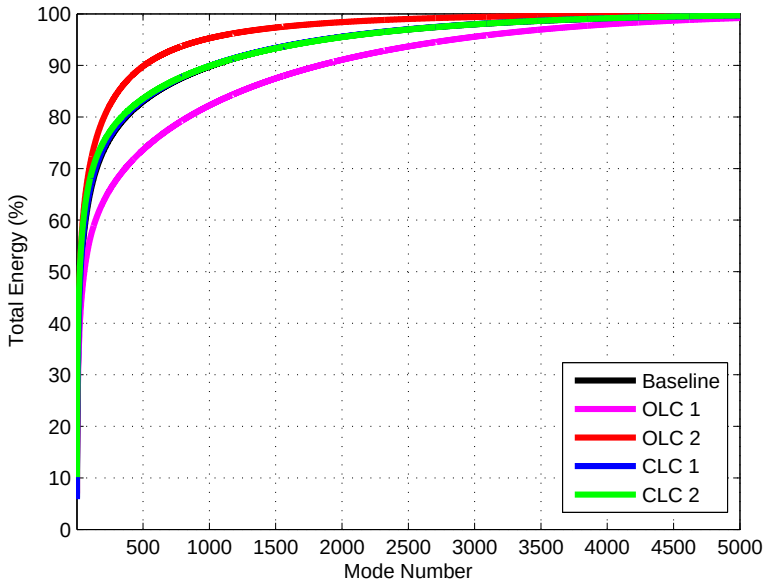

Figure 6.48: Cumulative energy in 5000 modes for the baseline and control cases

To see how the energy is distributed within the first ten modes for the control and baseline cases, the individual energy contributions are presented in Figure 6.50. Depending on the case, the first ten modes contain between 30% and 40% of the total energy. The most

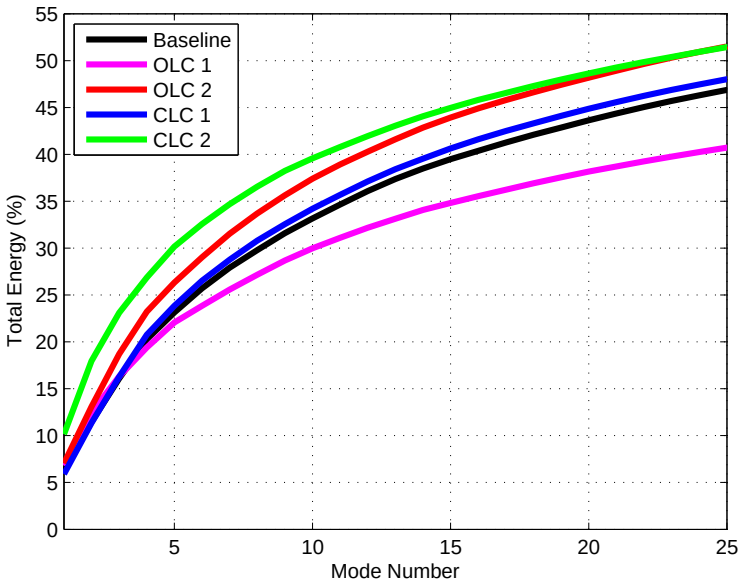

Figure 6.49: Cumulative energy in 25 modes for the baseline and control cases

notable feature of the distribution of energy within the first ten modes is seen for the *OLC2* case. For this particular control case, the first two modes contain a much larger portion of energy as compared to the other cases. The Fourier-azimuthal mode 0 forcing appears to dominate the energy in the first two POD modes in this case.

The most important aspect of the POD analysis in this case is the extraction of the loud modes through the OID. The spatial eigenfunctions computed from the POD (for the control cases) are not presented in this section but can be found in Appendix D for reference. The spatial POD modes for the baseline case are presented in Figure 6.32, shown previously.

6.6.1 Loud Mode Identification for Control

The OID analysis is performed on each TRPIV control data set in order to identify the loud modes, which arise as a result of the active flow control. Recall that the number of OID

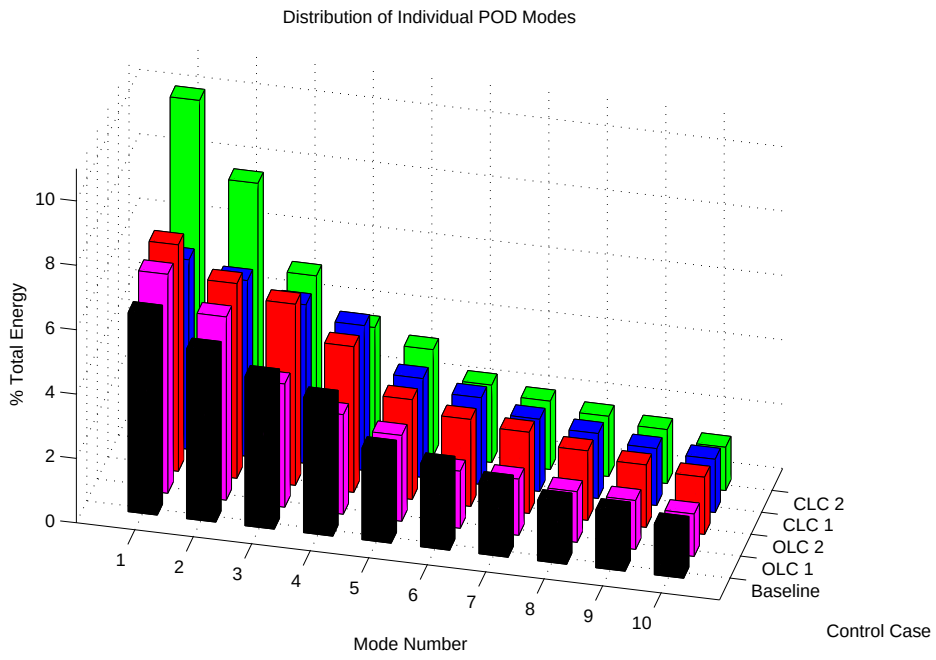

Figure 6.50: Energy distribution of the first 10 POD velocity modes for baseline and control cases

modes is a function of the number of observers, *i.e.* the number of far-field microphones. For this set of experiments, twelve OID modes are yielded from the analysis. One loud mode is identified for each control case and the corresponding spatial POD velocity mode is presented in Figure 6.51. The two control strategies which implement a Fourier-azimuthal mode 0 forcing (cases *OLC2* and *CLC2*), exhibit POD velocity mode 1 as the loud mode. This implies that the control input dominates the flow field and ultimately causes the most energetic mode to have the largest contribution to the far-field noise. The two control cases which implement a Fourier-azimuthal mode 1 forcing (cases *OLC1* and *CLC1*) exhibit different POD velocity modes as the loud modes. In any case, these control cases do not seem to be dominated by the control input but rather induce some sort of mode shifting that is being tracked by the OID analysis, with respect to the strongest contributions to the far-field noise.

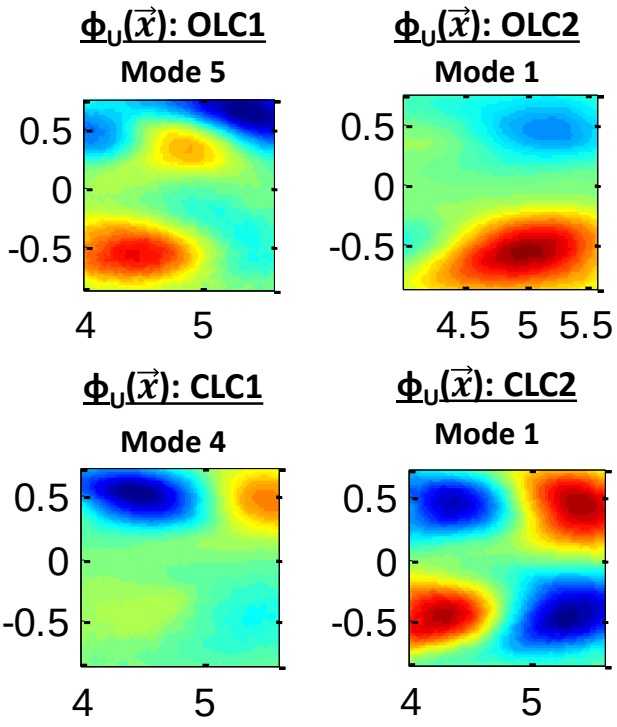

Figure 6.51: Loud modes for the control cases represented by the corresponding spatial POD velocity modes

These preliminary results do not necessarily provide any new information regarding specific structures or events that account for the largest contributions to the far-field noise. However, it can be concluded that the control does have an impact on which POD velocity mode is associated with the loud mode. The effects of the control are more complex than originally anticipated, especially with respect to the noise-producing events, as identified through the OID analysis. What can be said for now is that the Fourier-azimuthal mode 0 forcing causes POD velocity mode 1 to be the loud mode with both open and closed-loop control. This implies that with this type of actuation input, the most energetic POD velocity mode strongly correlates with the far-field acoustics. The Fourier-azimuthal mode 1 forcing however, creates a more subtle interaction with respect to the events correlated with the far-field noise.

Looking at the POD velocity modes that are found to be the loud modes, one might notice that similar spatial structures exists between mode 4 for the *CLC1* case and mode 1 for the *CLC2* case. To further investigate this observation, the correlation between the two modes is computed and shown in Figure 6.52. From this analysis, it has been determined that mode 4 for the *CLC1* case has a 70% correlation with mode 1 for the *CLC2* case. This implies that the two closed-loop control cases, despite having different actuation inputs and different feedback signals, have loud modes that are quite similar in spatial structure, from a low-dimensional energy perspective. Perhaps this structure is similar in nature to that of mode 6 for the baseline case, however no strict conclusions can be drawn this early on in the analysis. The investigation of the loud modes for the various control cases will be left for future work at this point. The coefficients of the linear mapping matrix which aid in the identification of the loud modes are presented in Appendix D.

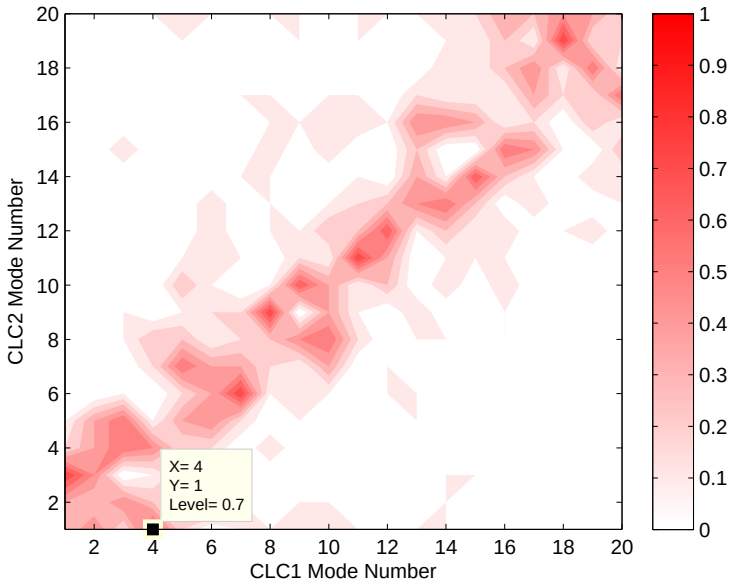

Figure 6.52: Modal correlation for the first 20 POD modes between the two closed-loop control cases

6.7 TRPIV Discussions

The results presented in this chapter have demonstrated the ability to identify individual low-dimensional velocity modes which have the highest correlation to the far-field acoustics, through reduced-order modeling techniques such as POD and OID. Moreover, for the baseline jet, the low-dimensional velocity field is reconstructed using this loud mode to identify possible noise-contributors in both time and space. The diagnostic analysis tools of Kan and Lewalle [116, 117, 135, 137, 138] have identified specific instances in time where the near-field activity correlates highly with the far-field acoustic signatures. These concepts are coupled with the loud mode identification to track possible noise-producing events in the velocity field. The results presented have shown that a large contortion of structures in the streamwise direction and radial ejection in the transverse direction (for POD mode 6), at a particular instance in time ($t = 15.7\ ms$), could be a significant contribution to the far-field noise. Once again this is confirmed using both the OID and diagnostic approaches. It is possible that this interaction of structures ties back to the proposed "leap-frogging" of vortex rings (see Figure 1.3) as proposed by Glauser (1987) [79]. Perhaps the lead vortex upstream bursts through the slower moving vortex downstream resulting in contortion in the streamwise direction and radial ejection of fluid in the transverse direction. This is of course only an initial conjecture at this point, however what is known for sure, is that there is some unique interaction occurring in time for this particular spatial mode that is contributing highly to the far-field noise. The specific interaction of structures at this point can not be confirmed and therefore must be further investigated.

Moreover, it has been found through the correlation of spatial eigenfunctions, that there are similar low-dimensional velocity modes between the two different investigated Mach numbers. The increase in Mach number causes a shift in the loud mode but yet the spatial structure of this mode remains quite similar. This leads to the initial idea that there may be some specific low-dimensional POD velocity mode that is responsible for the largest

contributions to the far-field noise, invariant of the Mach number. To confirm this theory, the spatial and temporal nature of mode 7 for the Mach 0.85 case must be investigated in the context of the work presented for mode 6 (at Mach 0.6). If similar behavior is observed, further conclusions can then be drawn regarding the loud mode, for differing Mach numbers. Moreover, the temporal coefficients of the loud modes for the two Mach numbers can be compared using cross-correlation and cross-spectral techniques.

One specific point of interest for future work in this regard, is to examine different excerpts in time using both the loud mode tracking and diagnostic approaches. It is believed that the contortions of structures seen for mode 6 occur at several points in time. Therefore it would be interesting to the compare the spatial and temporal nature of such events. Presumably such interactions in the flow field are occurring frequently at various length and time scales. The key is to understand how this directly relates to the far-field noise, as we have begun to decipher in this study.

Another point of interest for future work is to study the full three-dimensional flow field. The studies presented here look at two-dimensional slices of the flow field and even though much insight has been gained, it is known that the noise-producing events and associated interactions occur in three-dimensional space. One way to begin to explore the three-dimensionality of the flow field is to look at interrogation regions off of the center plane of the jet. This will provide some insight into how the flow field changes across the span of the nozzle in the radial direction. Some of these measurements have already been taken during the 2013 TRPIV experiments and are currently being processed and analyzed. The preliminary off-center plane measurements are presented in the following section.

6.7.1 Off-Center Plane Measurements

Off-center plane measurements have been taken for the Mach 0.6 uncontrolled jet to gain a better understanding of the three-dimensionality of structures, in the context of identifying

noise-producing events. The following data set contains ten measurements planes taken across the span of the nozzle with 0.125D (0.25 inches) spacing between planes (with the exception of the left-most plane, being 0.25D from its neighboring plane). The sixth window from the left corresponds to the center plane of the jet ($r/D = 0$). The PIV window spans from 3D to approximately 5D downstream in the streamwise direction. The instantaneous streamwise velocity contours for each of the measurements planes are shown in Figure 6.53. In each image, the ordinate is r/D and the abscissa is x/D. These measurements are not phase aligned, but give an idea of how the flow evolves in the radial direction, going from one end of the nozzle lip to the other.

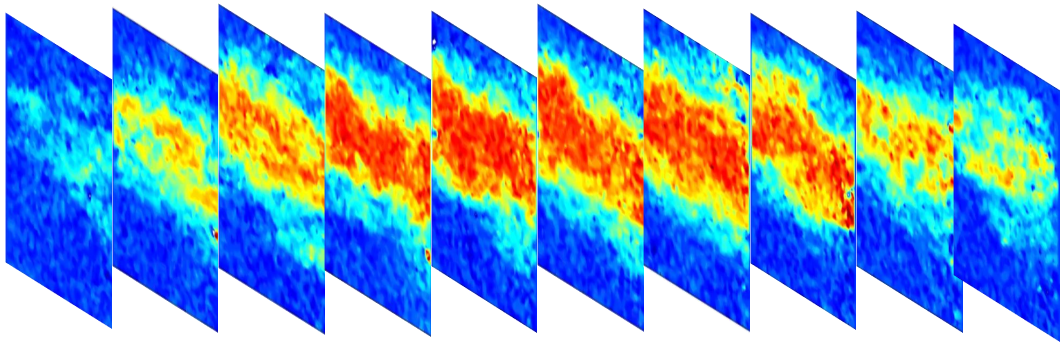

Figure 6.53: Instantaneous streamwise velocity contours for off-center plane measurements: ordinate: r/D; abscissa: x/D [29]

Snapshot POD has been applied to each of the PIV windows to see how the low-dimensional spatial structures develop across the nozzle in the radial direction. The streamwise contours for the first four spatial POD velocity modes are shown in Figure 6.54. Slices in the $r-\theta$ plane of the jet would indicate that these POD modes resemble spatial Fourier modes, which is consistent with previous findings (see Hall & Glauser (2009) [91]). Moreover, the first few POD modes indicate an organization of structures in the radial direction. It is not until mode 4 that disorganization in the structures is observed at the edge of the nozzle (the outer PIV windows). These first few POD modes give a general sense of the large scale, energetic structures in the flow field, in the radial direction across the span of

the jet.

The off-center plane measurements provide some initial insight into the three-dimensionality of the velocity field, which is key in understanding the complex flow physics, especially those structures and interactions directly related to the far-field noise. The goal of this data set is to apply the OID in an effort to understand the nature of the noise-producing events in the radial direction of the jet. Additionally, the time dependence of these modes can also be observed. A more in depth analysis of the off-center plane measurements can be found in the work of Berger *et al.* (2014) [29].

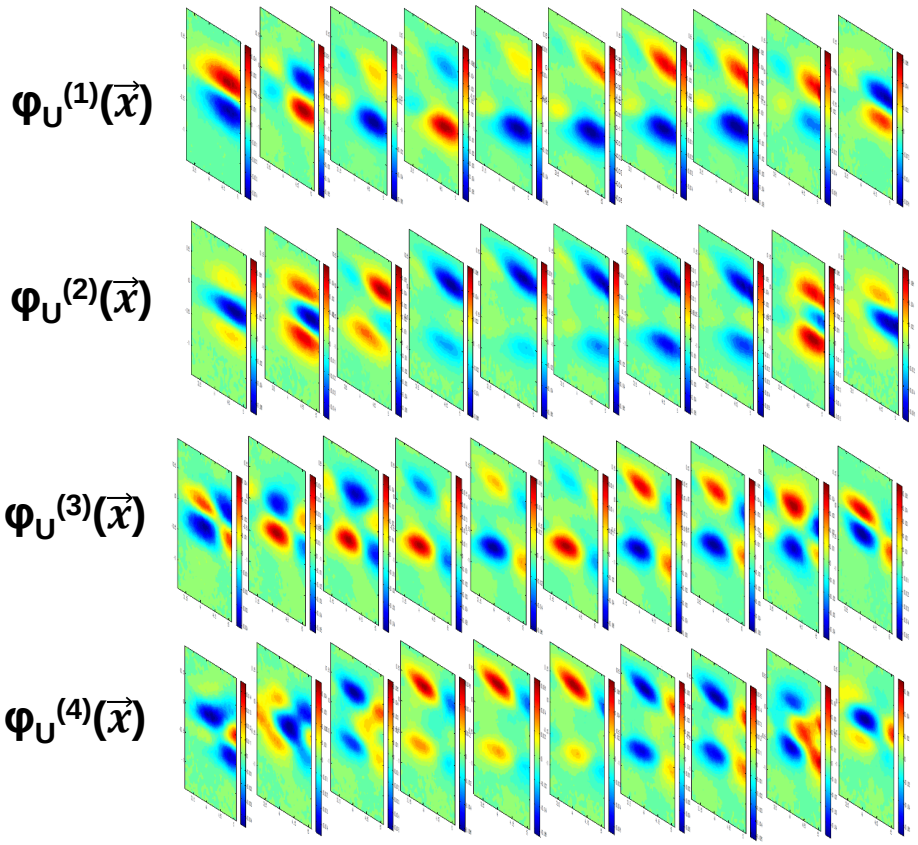

Figure 6.54: First four spatial POD modes in the radial direction: ordinate: r/D; abscissa: x/D [29]

Chapter 7

Conclusions

Within the context of understanding and controlling the noise-producing events responsible for the far-field noise in a high-speed jet, a series of experiments have been conducted in the Syracuse University anechoic chamber and jet facility. The work presented builds on extensive studies in the jet noise community, specifically from experiments conducted within the Syracuse University research group [90, 148, 182, 227]. It has been shown that the entrainment of ambient fluid into the jet's bulk flow causes instabilities at the nozzle lip, eventually leading to an interaction of flow structures at various length and time scales. The complex flow physics governed by the non-linear turbulence and how this eventually leads to large pressure fluctuations in the far-field is still not completely understood. In this spirit, two very important aspects of the jet noise problem are, understanding the flow physics in the context of the far-field noise, and controlling the noise-producing events by using information from the flow field. The work presented aims at coupling these two concepts in an overall effort to reduce the far-field noise through active flow control strategies.

The full jet flow field is highly three-dimensional and governed by non-linear turbulence interactions at various scales. One way to attempt to understand the nature of the noise-producing events is to reduce the dimension of the problem by constructing low-dimensional models which capture the dominant flow physics in terms of the turbulent

kinetic energy. If the flow field can be understood from a low-dimensional viewpoint, one can begin to develop some intuition about the development of dominant flow features in both time and space.

These reduced-order modeling techniques are then coupled with experiments which employ flow control to manipulate the flow field and the interaction of structures, to ultimately alter the far-field pressure fluctuations responsible for noise production. In this context, a relationship between the near and far-field pressure signatures have motivated the investigations of closed-loop flow control using real-time, near-field pressure as the feedback mechanism. Moreover, the velocity field is observed with the addition of flow visualization techniques in the form of PIV.

In order to gain a deeper understanding of the relationship between the interaction of structures in the flow field and the far-field acoustics, the near-field velocity, as well as the near and far-field pressure, are simultaneously sampled. While flow control is also implemented in the current studies, a great deal of post-processing in the form of reduced-order modeling is also conducted to explore the spatial and temporal nature of the large-scale, highly energetic structures in the flow field.

The first set of experiments involving the LWPIV indicate that with the active flow control, we have demonstrated significant control authority over the jet. Moreover the LWPIV itself provides an inspection region of the velocity field encompassing the collapse of the potential core. This region of the jet, characterized by the strong interaction of the shear layers, resulting in vortex stretching, merging and breakdown, is believed to be the major contributor to noise-producing events. Using open and closed-loop flow control in the form of synthetic jet actuation at the nozzle lip, with near-field pressure as the feedback mechanism, an $\mathscr{O}(1)$ response has been produced from an $\mathscr{O}(\varepsilon)$ input. Despite the fact that no noise reductions are observed in the far-field, a great amount of control authority has been shown, using a relatively simple control scheme. The active flow control shortens

the potential core length (by as much as 1.5D) while expanding the shear layer, by means of enhancing the mixing at the nozzle exit. Moreover, the closed-loop control draws on intelligence from the system in the form of the near-field pressure sensors and uses less energy input to the system as compared to the open-loop control. In addition, the closed-loop control (*CLC1*) is the quietest of the control cases, indicating this form of the active flow control should be further investigated [32] (see Appendix E).

In the context of ultimately reducing far-field jet noise on a real system, having control authority over the jet is a very important component. However, equally if not more important, is understanding what mechanisms to control specifically. That is to say, an understanding of the flow structures and interactions responsible for the far-field noise is of the upmost importance. In this spirit, the focus is shifted to the second set of experiments in which TRPIV is acquired simultaneously with near and far-field pressure, both with and without control. A time-resolved representation of the velocity will allow us to evaluate the interaction of flow structures in time and space. Once again due to the complexity of the flow field, reduced-order models are employed to obtain a low-dimensional representation of the jet's velocity field. Using the POD, which finds a set of basis functions that decomposes the flow to maximize the mean squared kinetic energy, a low-dimensional representation of the flow field is established. This is then coupled with the OID technique to find a linear relationship between the low-dimensional velocity field (source) and low-dimensional acoustic field (observer). The modes with the highest correlation in this linear mapping are coined as "loud" modes in the flow and contribute significantly to the far-field acoustics.

For the TRPIV experiments, it has been shown that the OID is an effective technique for extracting the loud POD modes. Moreover, the TRPIV allows for the tracking of the structure of these modes in both time and space. *It was found that there exists a strong correlation between the spatial structures of the loud POD modes for the Mach 0.6 and*

Mach 0.85 jets. This implies that we may have identified a low-dimensional, loud spatial structure, invariant of the Mach number. In this spirit, a technique which correlates near-field velocity diagnostics with far-field acoustics through wavelet filtering [117, 137], has been developed to track contributions to the noise in frequency, time and space. Coupling these two techniques, large streamwise contortions and radial ejections of the loud mode are found at specific instances in time. Since the diagnostic approach points to the same instant in time where the loud mode exhibits interesting behavior, the initial hypothesis is that there is an interaction of structures at this point that may be a noise-producing event. Specifically looking at mode 6, the loud mode associated with the Mach 0.6 jet at 6D downstream, the contortion of the structures in the streamwise direction and ejection of fluid in the radial direction (around $t = 15.7\ ms$) could tie back to some previous conjectures regarding the noise-producing events. This seemingly high strain, short duration event might be related to the "leap-frogging" of vortices, as initially proposed by Glauser [79]. Whether this is a coincidence or not is unclear at this point, however we do know for sure that some unique interaction of structures in this particular low-dimensional mode is correlating particularly highly with the far-field acoustics. These preliminary findings which potentially suggest a specific noise-producing event in time and space must be further investigated by coupling the diagnostic and loud mode techniques more efficiently.

In the final set of experiments, flow control is implemented in conjunction with TRPIV in order to combine the analyses of the previous two experiments. *The data set allows for the comparison of the effects of flow control for the time-resolved jet flow field.* In this spirit, the OID analysis is performed on this data set to identify potential loud modes as a result of the control input. The Fourier-azimuthal mode 0 forcing, in either the open or closed-loop configurations, causes the most energetic POD mode 1 to be the dominant noise contributor. The Fourier-azimuthal mode 1 forcing leads to more complex flow interactions and thus the loud modes are no longer the most energetic POD modes, but rather higher order modes,

as seen in the uncontrolled jet. The differences in the loud modes for the mode 0 versus mode 1 forcing are not completely understood at this point. However, the loud modes of the two closed-loop control cases exhibit a 0.7 correlation level in the spatial structures. This indicates that there may be a specific spatial structure that has the highest contribution to the noise, associated with the closed-loop control. This could in fact be analogous in some way to the unique structure of mode 6 for the uncontrolled jet.

Through the experiments and analysis performed in the current study, control authority has been achieved over the jet using various types of actuation input at the nozzle lip. Potential noise-producing events in the form of low-dimensional loud modes have been identified using various reduced-order modeling techniques. Moving forward, coupling the reduced-order modeling results and the flow control applications to reduce the far-field noise is the ultimate goal. The results presented herein are not suggesting that the loud modes are the only contributions to the far-field noise but rather, they provide a low-dimensional representation of the largest contributions to the noise. The insights gained from the analyses discussed should provide new insights into the mechanism and interactions of structures in the velocity field that eventually lead to large pressure fluctuations in the acoustic field. This work examines the velocity field from a two-dimensional perspective and thus to enhance the validity of our conjectures and deepen our understanding of the results, the full three-dimensional flow field should also be investigated. In this spirit, some recommendations for future work will be briefly discussed in the next section.

7.1 Future Work

The complexity of the jet noise problem motivate the necessity for further investigations into the concepts presented in this body of work. Building on the analysis techniques used to identify the loud modes, longer record lengths should be studied in conjunction with the diagnostic approaches, to see how frequently and to what extent the contortion of structures

in the loud mode is occurring. The current study looked at the first 50 *ms* of an 800 *ms* time series. Presumably, the behavior found at 15.7 *ms* occurs at many later instances in time, but how similar are these structures and do the diagnostic techniques continue to pick up these events? Within the context of exploring the spatial structure of the loud modes in time, the windowing effects of the small TRPIV interrogation region remain a concern in terms of looking at the full flow field. It is therefore of interest to identify loud modes from the LWPIV experiments by lagging the pressure signal. The time-resolved nature of the current studies allow these computations to be performed directly, but this can also be done using the LWPIV results.

To address the issue of three-dimensionality, there are a few approaches in mind to be considered for future experiments and analyses. The first concept which has briefly been presented, involves looking at off-center plane measurements with TRPIV. It has been shown by Berger *et al.* (2014) [29] that the time-resolved nature of the structures across the span of the nozzle in the radial direction could provide some new and important insights to understand the noise-producing events. These results motivate additional attempts at capturing the full three-dimensional flow field by acquiring time-resolved PIV measurements in the $r-\theta$ plane of the jet. Having TRPIV measurements in the streamwise plane (with various downstream and radial positions), coupled with the $r-\theta$ plane at various streamwise locations, will provide new insights into the fully three-dimensional flow field. Loud mode identification can be applied in this context to see the interaction of the noise-producing events in the overall flow field. These experimental results can then be coupled with large eddy simulations (LES), through the current collaborations with Gaitonde *et al.* at The Ohio State University.

Lastly, we seek to develop an algorithm for efficiently coupling the OID and diagnostic approaches presented herein. Conjectures regarding the noise-producing events have been made in the context of this framework but the development of a specific metric to identify

such events and interactions is desired. For example, we can observe the mode-filtered vorticity or rate of strain as a function of time to gain a better understanding of the flow interactions with respect to the noise. As a proposed first step moving forward, we can attempt to suppress the loud mode (*i.e.* mode 6) by incorporating it into the feedback loop of the control through its estimation in real-time with near-field pressure. Regardless of the specific technique(s) moving forward, we can conclude that the sources of jet noise are indeed subtle in nature and thus understanding the full three-dimensional flow field to the best of our ability is paramount in ultimately reducing the far-field noise.

Appendix A

PIV Uncertainties: LWPIV & TRPIV

For both PIV experiments conducted, error in the measurements exist as a result of the optical technique used to acquire the velocity fields. The errors associated with PIV arise as a result of measuring the particle displacement between snapshots for a given image pair. The sources of displacement error, as outlined in Chapter 5.5 of Raffel *et al.* (1998) [187], are the particle image diameter ($\delta x_{\text{PI-DIA}}$), particle image displacement ($\delta x_{\text{PI-DIS}}$), camera resolution (δx_{RES}), background noise (δx_{NOISE}), and gradients across the interrogation window (δx_{GRAD}). It has been shown that the largest source of error is attributed to the gradient in the flow field [206]. Therefore, this quantity will be computed for the LWPIV and TRPIV experiments [187, 206].

For the LWPIV experiments, the interrogation window is 32×32 pixels and the particle image diameter is approximately 3 pixels. This gives a particle displacement of 8 pixels between snapshots in the potential region of the jet. In the shear layer of the jet, the largest mean velocity gradient was found to be approximately $15 m/s$ between two adjacent velocity vectors. This corresponds to a gradient of 0.055 pixels/pixel. Referring to Raffel *et al.* [187], the RMS-uncertainty of the gradients is therefore 0.25 pixels. The total displacement uncertainty is calculated using the following equation:

$$\delta x = \sqrt{(\delta x_{\text{PI-DIA}})^2 + (\delta x_{\text{PI-DIS}})^2 + (\delta x_{\text{RES}})^2 + (\delta x_{\text{NOISE}})^2 + (\delta x_{\text{GRAD}})^2} \tag{A.1}$$

In the above equation, δx_{GRAD} is the dominant contribution and thus the other quantities can be neglected in the calculation [206]. For the LWPIV, the pixel displacement is 8 and thus the associated error is calculated to be approximately 3.1%.

For the TRPIV experiments, the interrogation window is 16×16 pixels, with a particle image diameter of 1 pixel and a particle displacement of 4 pixels. In this experiment, the largest mean velocity gradient in the shear layer of the jet is approximately $5m/s$ between two adjacent velocity vectors. This corresponds to a gradient of 0.0061 pixels/pixel. The resulting uncertainty is therefore 0.055 pixels. According to equation A.1, the associated error is found to be approximately 1.4%.

These uncertainties are heavily dependent on local gradients in the flow field and the pixel displacement at a particular location in the flow field. For more information regarding the uncertainty associated with PIV measurements, refer to Raffel *et al.* [187].

In addition, the time between laser pulses is set to be 4 μs for the Mach 0.6 jet, such that each particle moves approximately one quarter of the interrogation region. This Δt is based on the bulk velocity in the potential core and thus the highest uncertainties are associated with the velocity in the shear layer.

Appendix B

LWPIV Supplemental Figures

This section contains supplemental plots for the LWPIV data set, found in § 5. Presented here are RMS plots for the control cases, spatial POD modes of the velocity field, and far-field sound pressure levels.

B.1 RMS of the Velocity Field

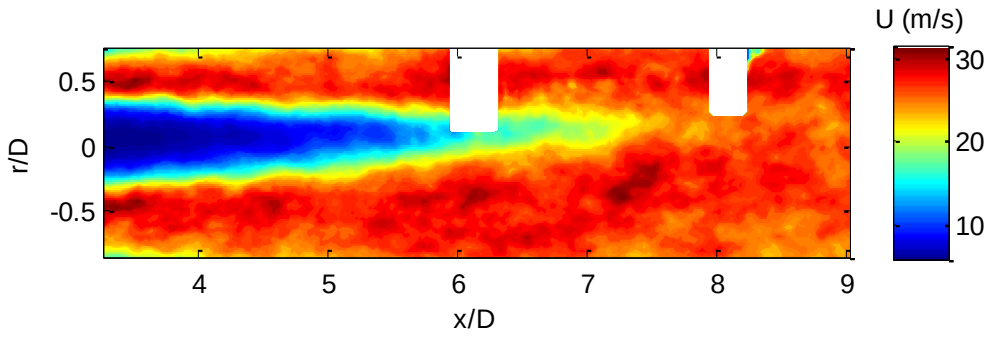

Figure B.1: Fully stitched LWPIV, OLC1 snapshot: streamwise RMS velocity contours

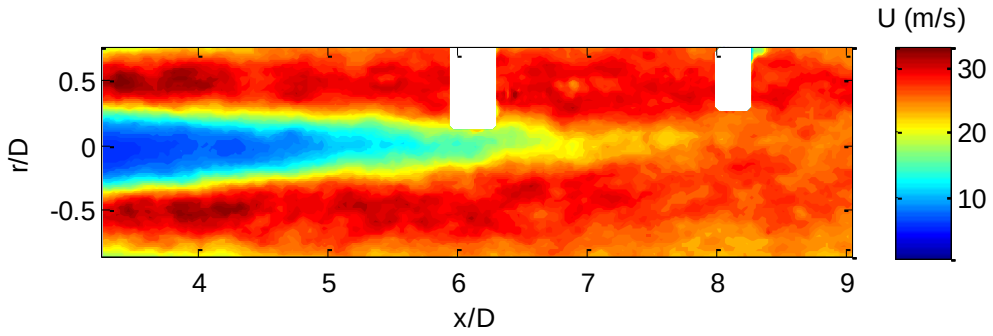

Figure B.2: Fully stitched LWPIV, OLC2 snapshot: streamwise RMS velocity contours

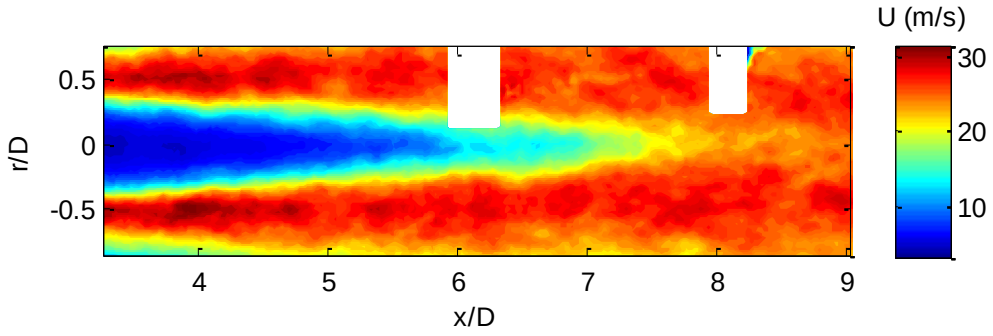

Figure B.3: Fully stitched LWPIV, CLC1 snapshot: streamwise RMS velocity contours

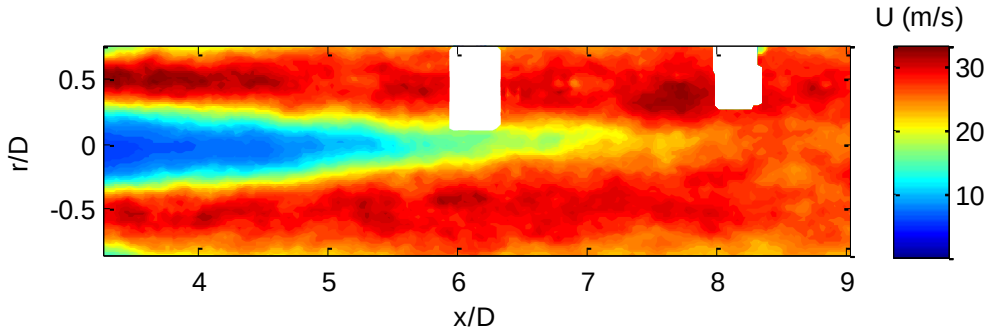

Figure B.4: Fully stitched LWPIV, CLC2 snapshot: streamwise RMS velocity contours

B.2 Near-Field Pressure Spectra

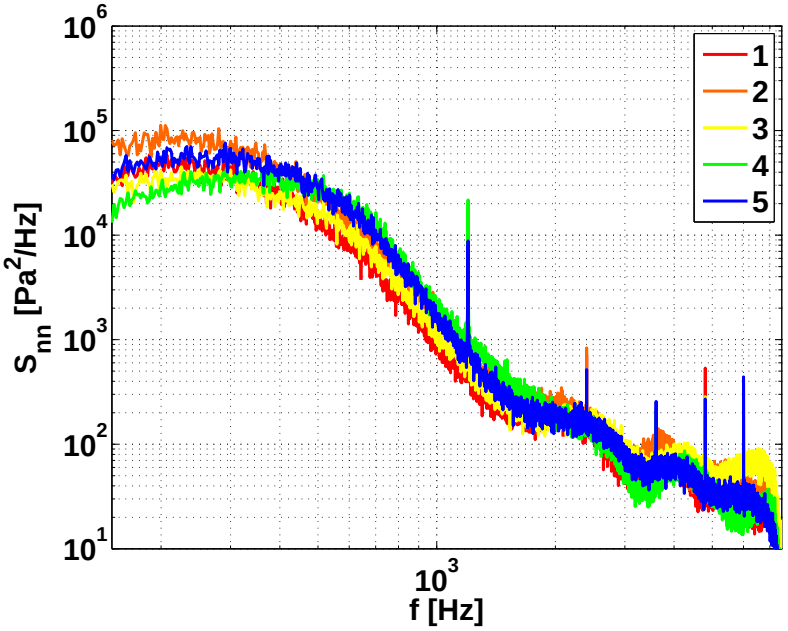

Figure B.5: Near-field azimuthal pressure spectra: Open-Loop 1 at 8D

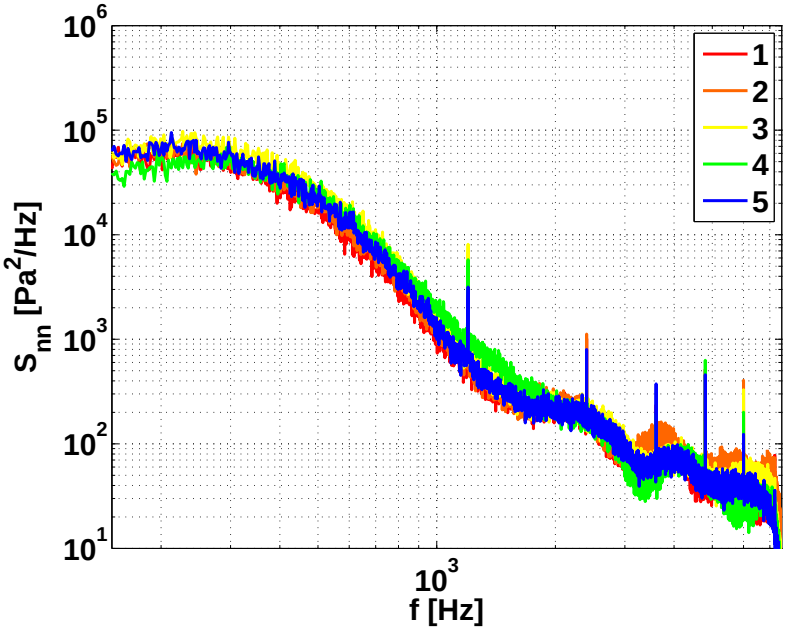

Figure B.6: Near-field azimuthal pressure spectra: Open-Loop 2 at 8D

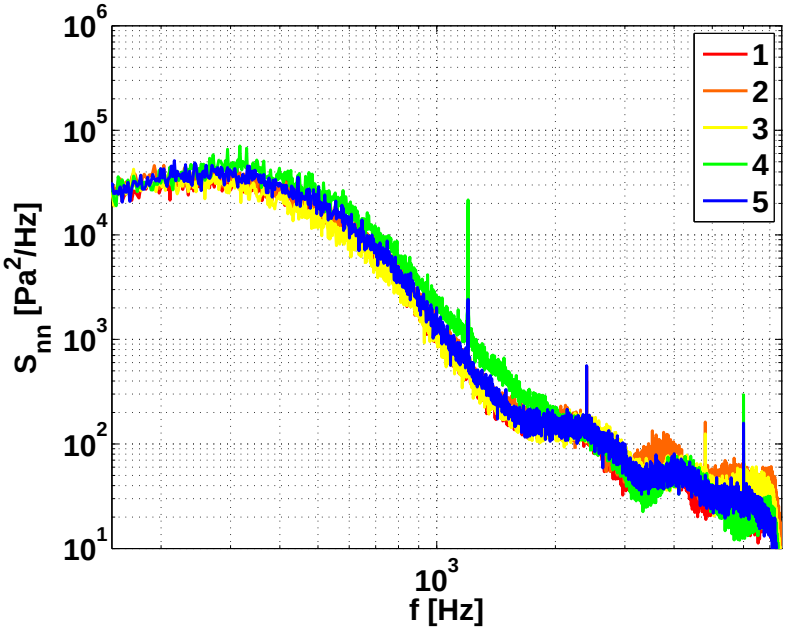

Figure B.7: Near-field azimuthal pressure spectra: Closed-Loop 1 at 8D

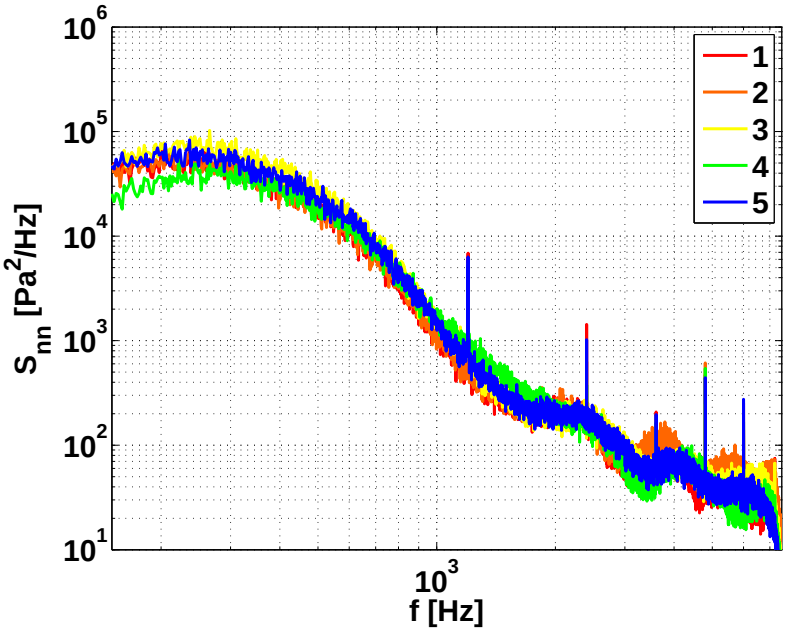

Figure B.8: Near-field azimuthal pressure spectra: Closed-Loop 2 at 8D

B.3 POD Convergence Rates

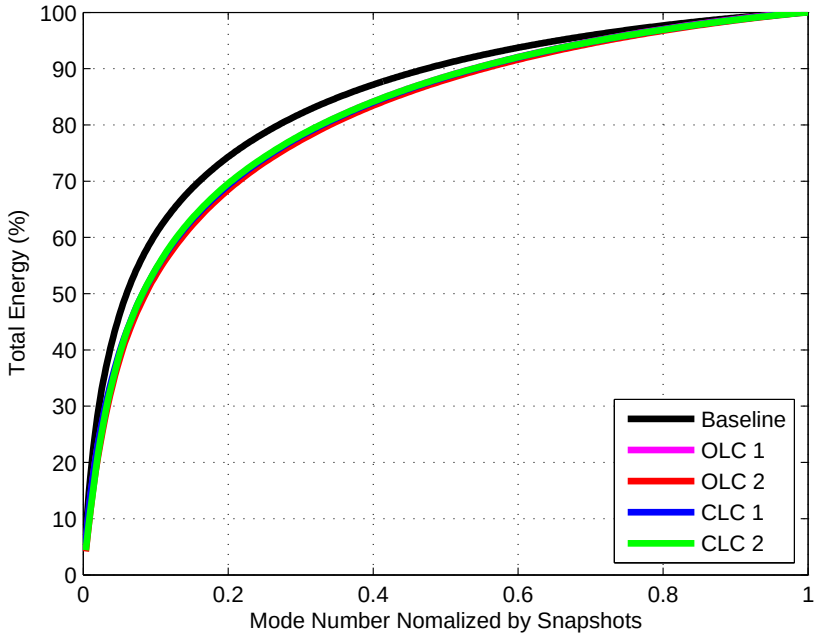

Figure B.9: Convergence rate of POD modes normalized by the number of snapshots

B.4 POD Spatial Eigenfunctions

The spatial eigenfunctions are further categorized by the u and v components.

B.4.1 Streamwise POD spatial eigenfunctions, $\phi_u^{(n)}(\vec{x})$

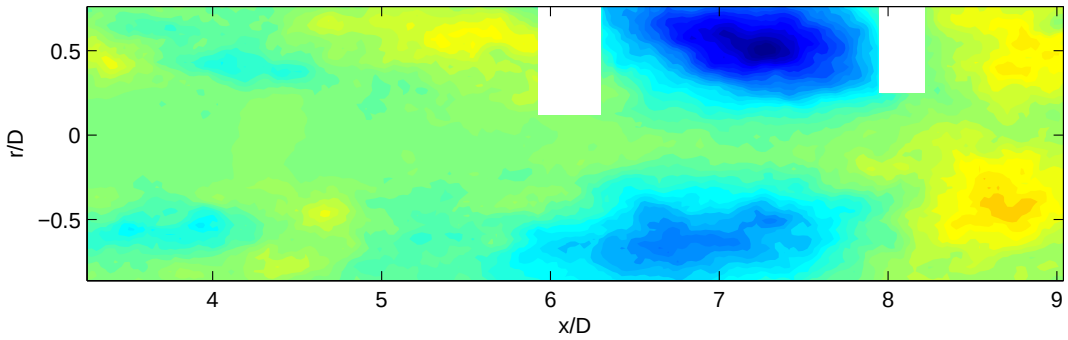

Figure B.10: POD spatial eigenfunction, $\phi_u^{(3)}(\vec{x})$: Baseline

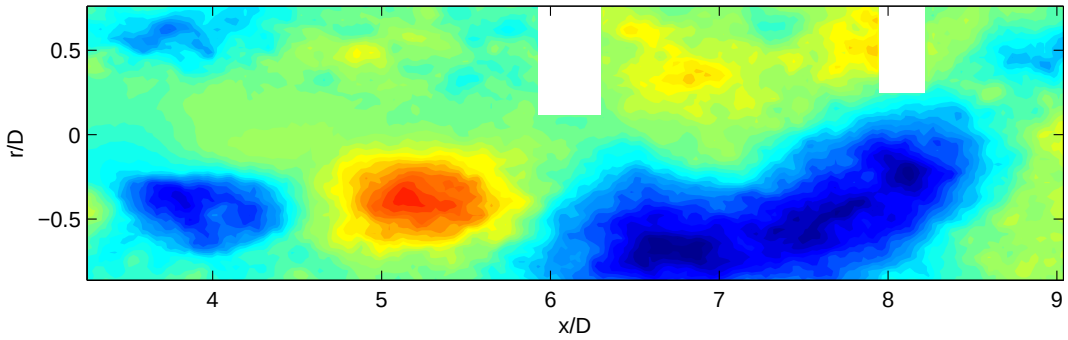

Figure B.11: POD spatial eigenfunction, $\phi_u^{(3)}(\vec{x})$: OLC1

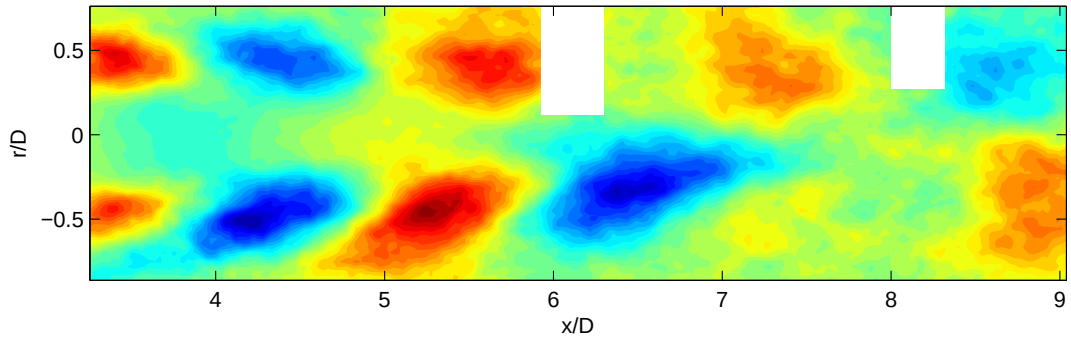

Figure B.12: POD spatial eigenfunction, $\phi_u^{(3)}(\vec{x})$: OLC2

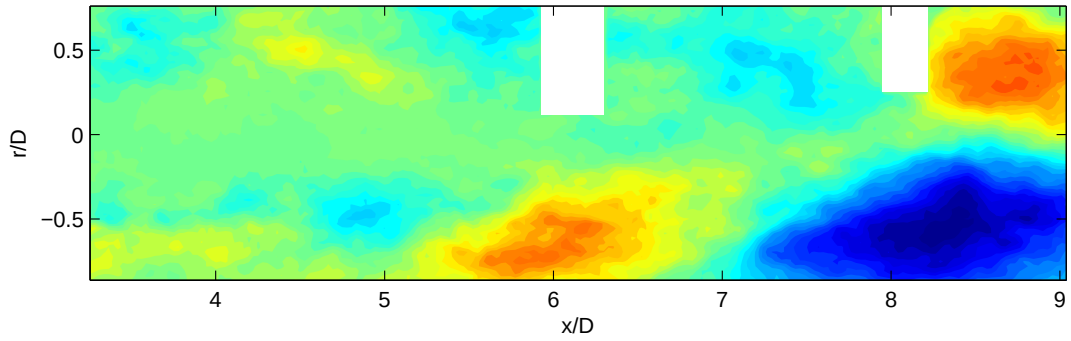

Figure B.13: POD spatial eigenfunction, $\phi_u^{(3)}(\vec{x})$: CLC1

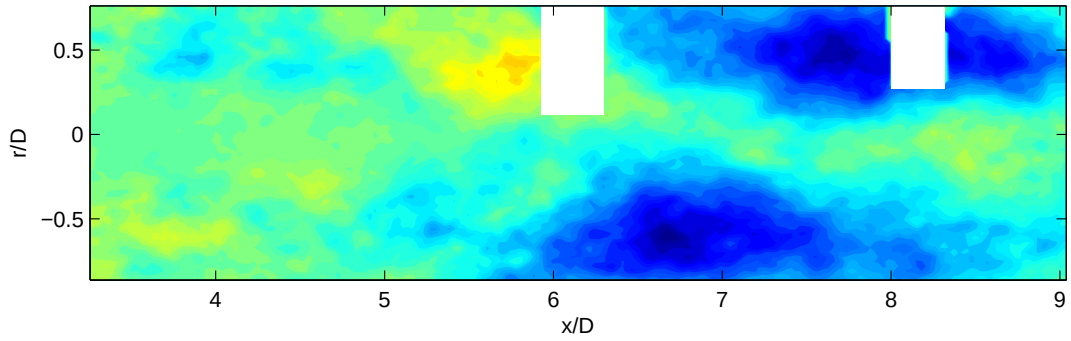

Figure B.14: POD spatial eigenfunction, $\phi_u^{(3)}(\vec{x})$: CLC2

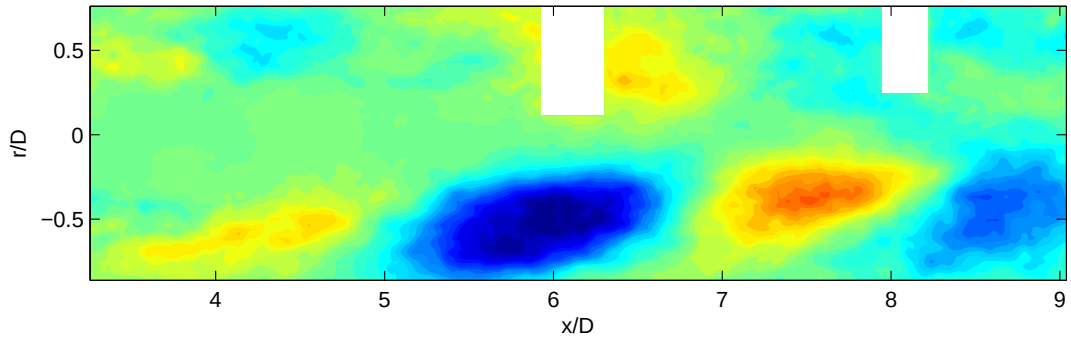

Figure B.15: POD spatial eigenfunction, $\phi_u^{(4)}(\vec{x})$: Baseline

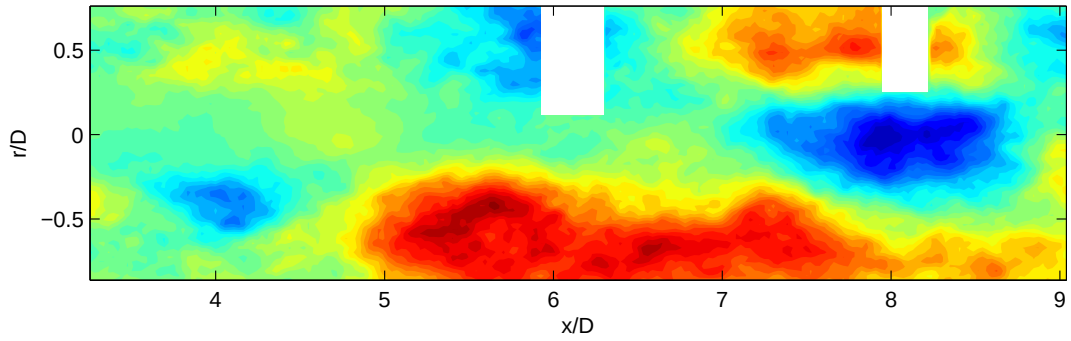

Figure B.16: POD spatial eigenfunction, $\phi_u^{(4)}(\vec{x})$: OLC1

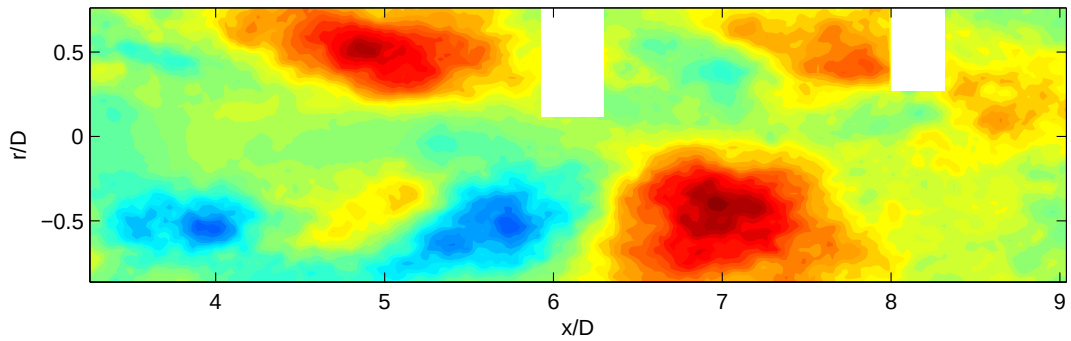

Figure B.17: POD spatial eigenfunction, $\phi_u^{(4)}(\vec{x})$: OLC2

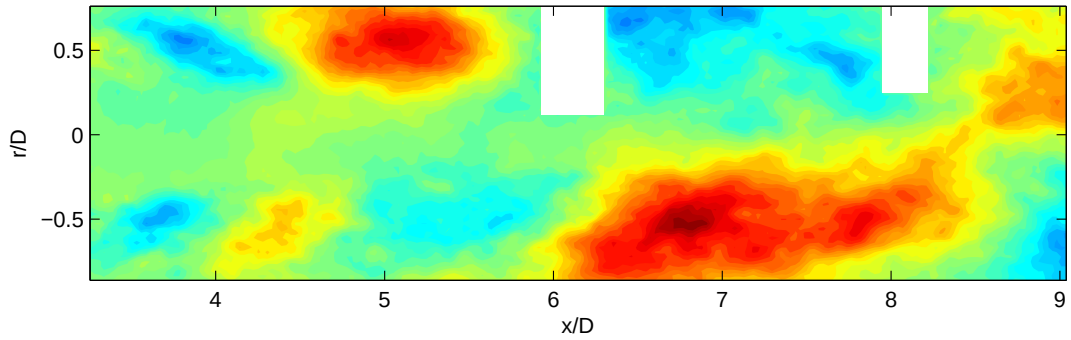

Figure B.18: POD spatial eigenfunction, $\phi_u^{(4)}(\vec{x})$: CLC1

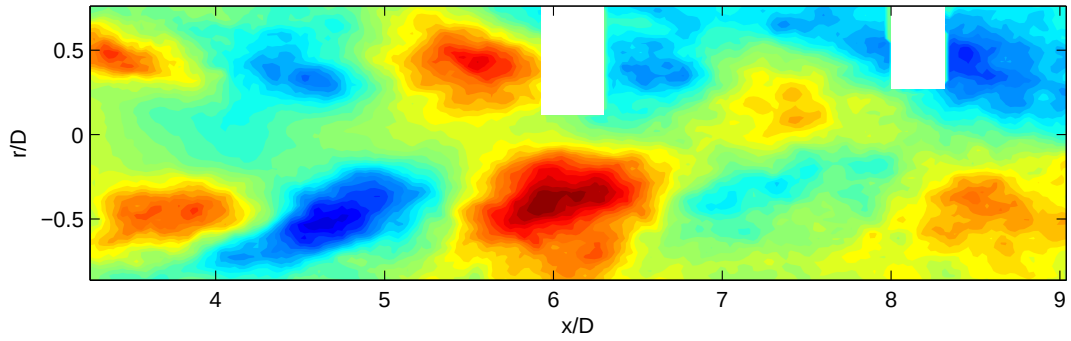

Figure B.19: POD spatial eigenfunction, $\phi_u^{(4)}(\vec{x})$: CLC2

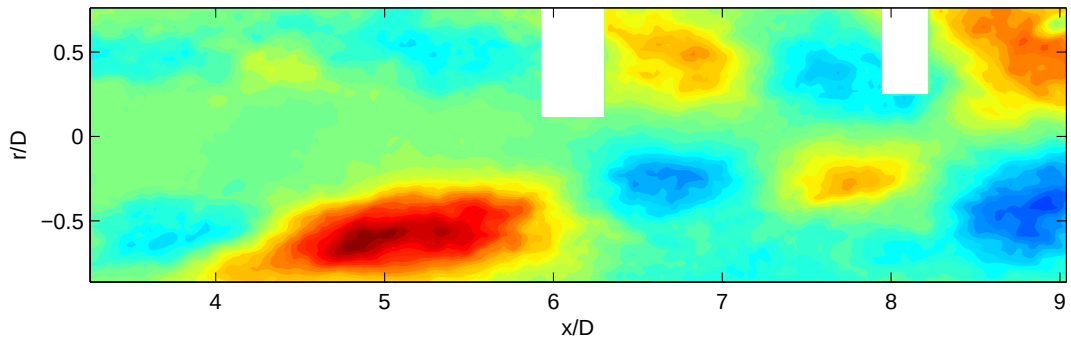

Figure B.20: POD spatial eigenfunction, $\phi_u^{(5)}(\vec{x})$: Baseline

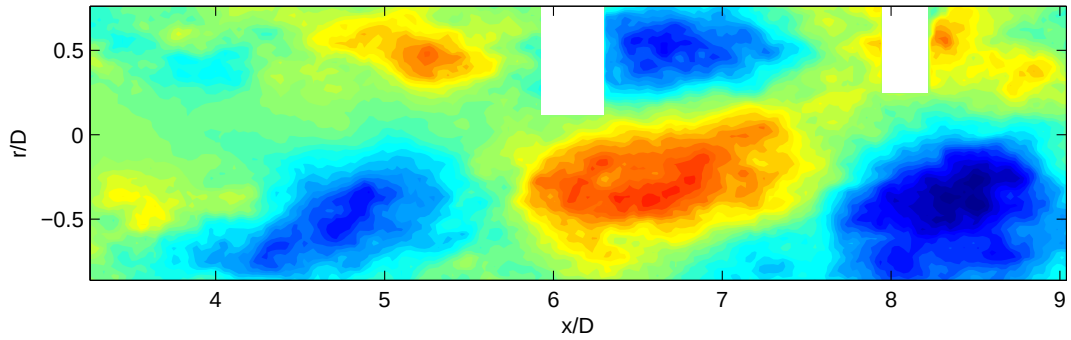

Figure B.21: POD spatial eigenfunction, $\phi_u^{(5)}(\vec{x})$: OLC1

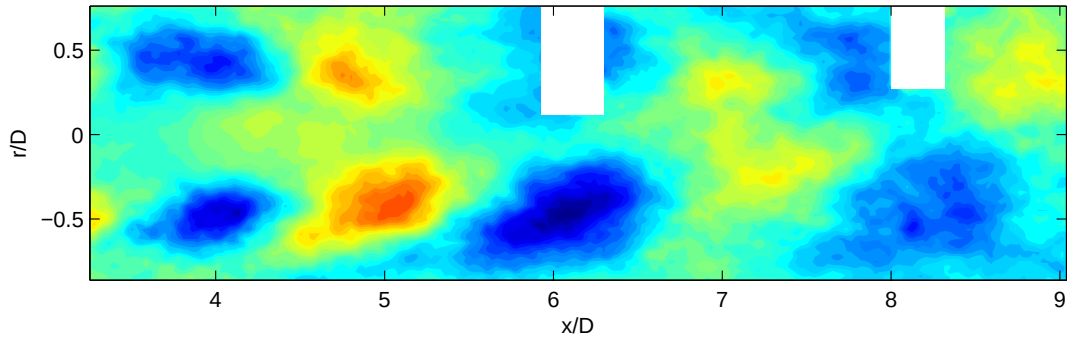

Figure B.22: POD spatial eigenfunction, $\phi_u^{(5)}(\vec{x})$: OLC2

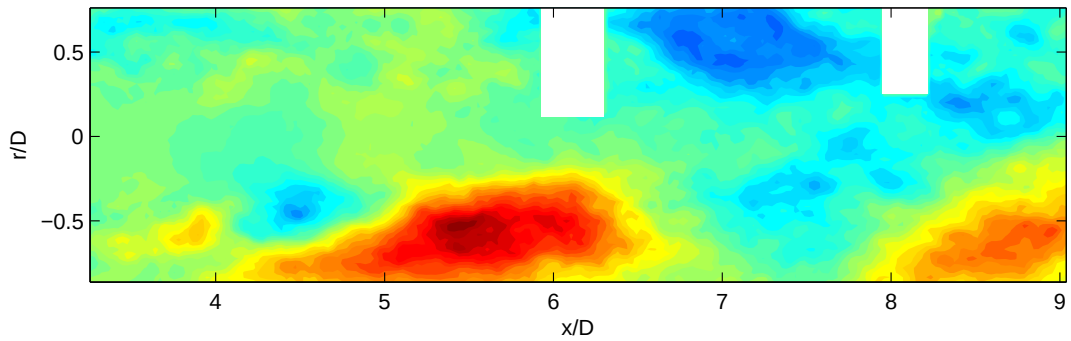

Figure B.23: POD spatial eigenfunction, $\phi_u^{(5)}(\vec{x})$: CLC1

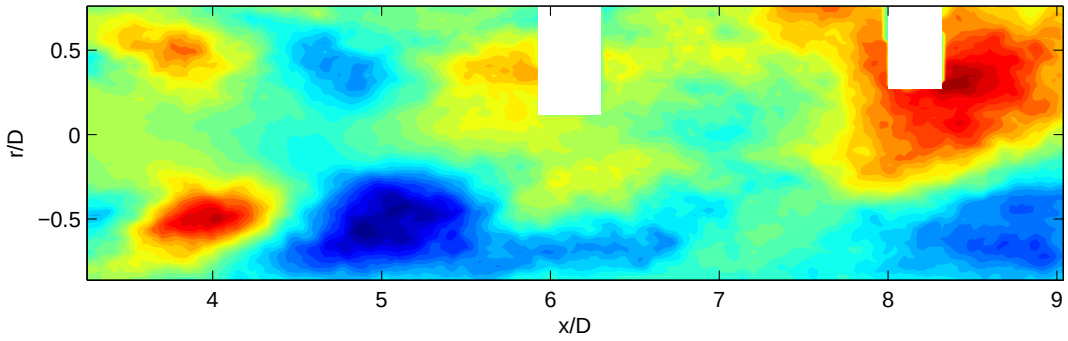

Figure B.24: POD spatial eigenfunction, $\phi_u^{(5)}(\vec{x})$: CLC2

B.4.2 Transverse POD spatial eigenfunctions, $\phi_v^{(n)}(\vec{x})$

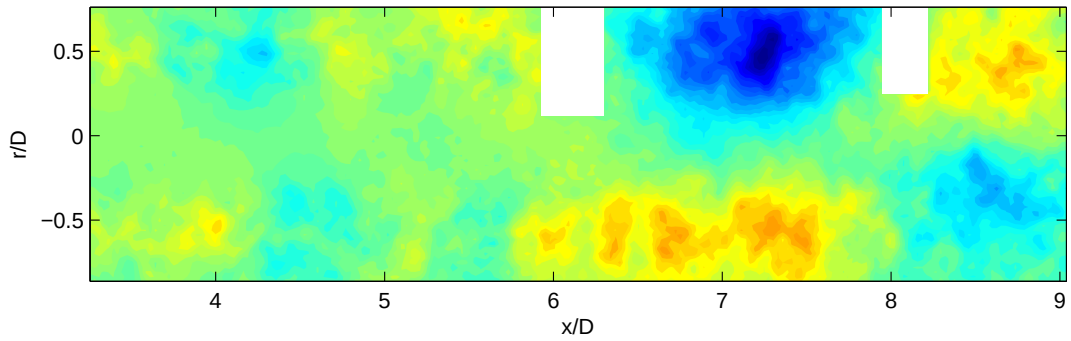

Figure B.25: POD spatial eigenfunction, $\phi_v^{(3)}(\vec{x})$: Baseline

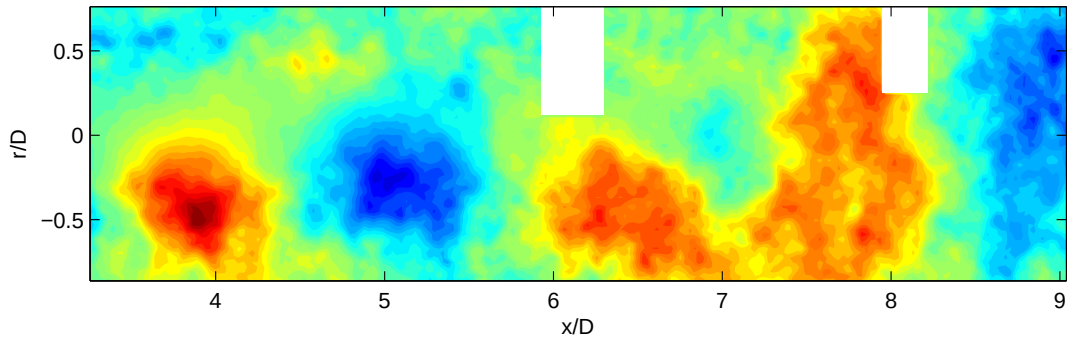

Figure B.26: POD spatial eigenfunction, $\phi_v^{(3)}(\vec{x})$: OLC1

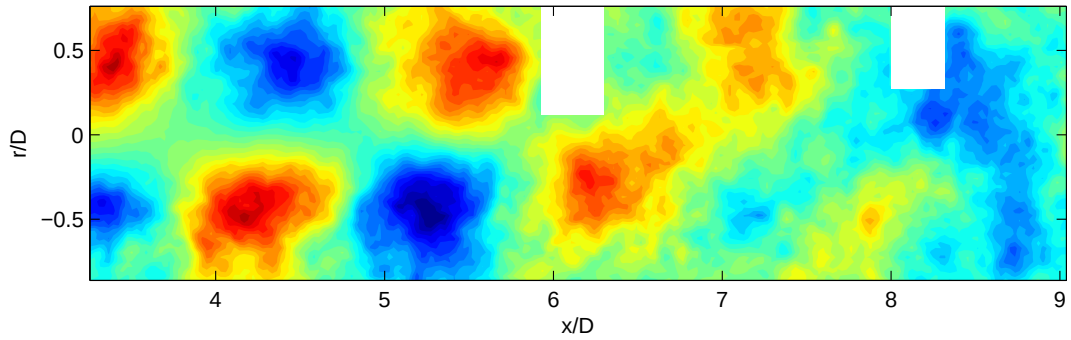

Figure B.27: POD spatial eigenfunction, $\phi_v^{(3)}(\vec{x})$: OLC2

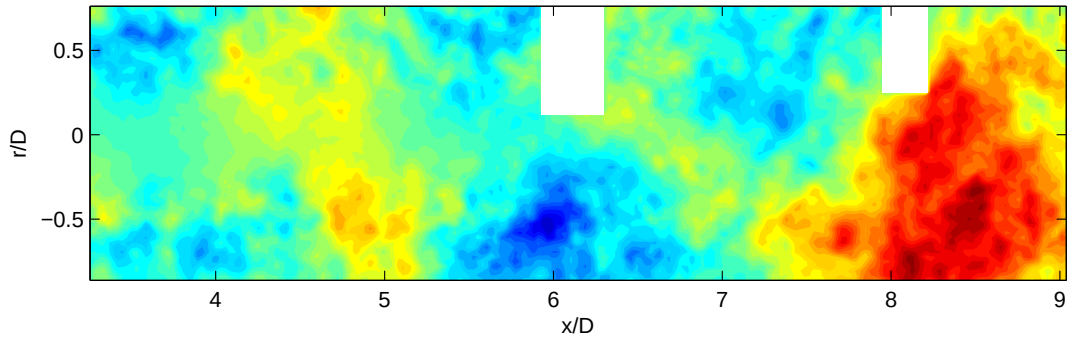

Figure B.28: POD spatial eigenfunction, $\phi_v^{(3)}(\vec{x})$: CLC1

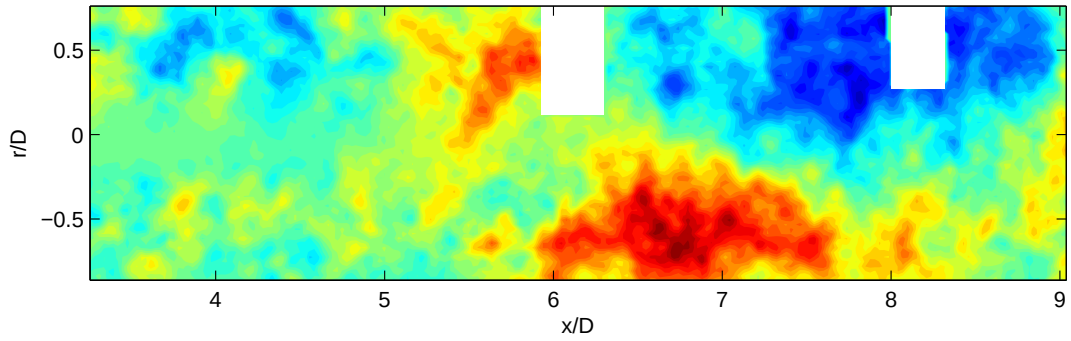

Figure B.29: POD spatial eigenfunction, $\phi_v^{(3)}(\vec{x})$: CLC2

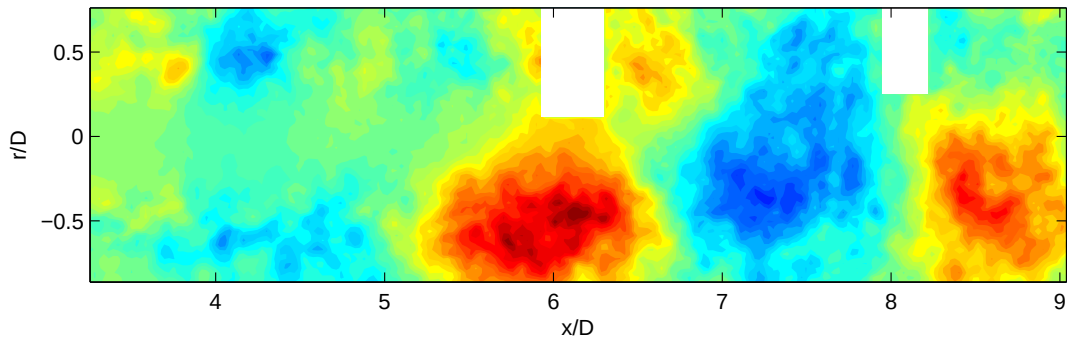

Figure B.30: POD spatial eigenfunction, $\phi_v^{(4)}(\vec{x})$: Baseline

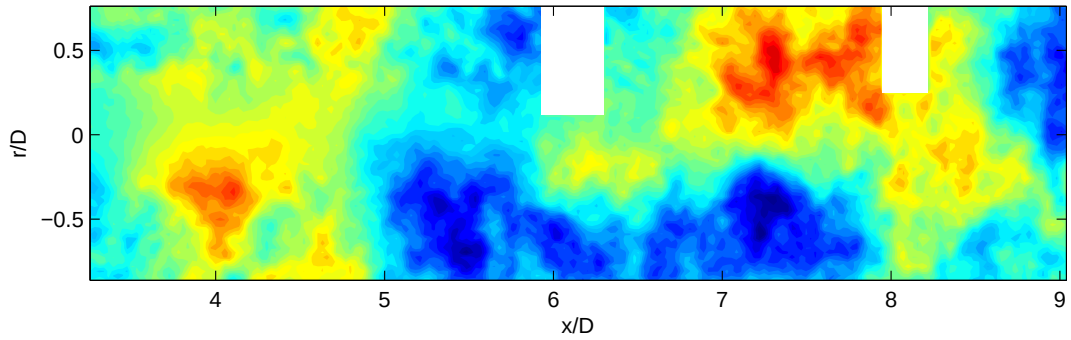

Figure B.31: POD spatial eigenfunction, $\phi_v^{(4)}(\vec{x})$: OLC1

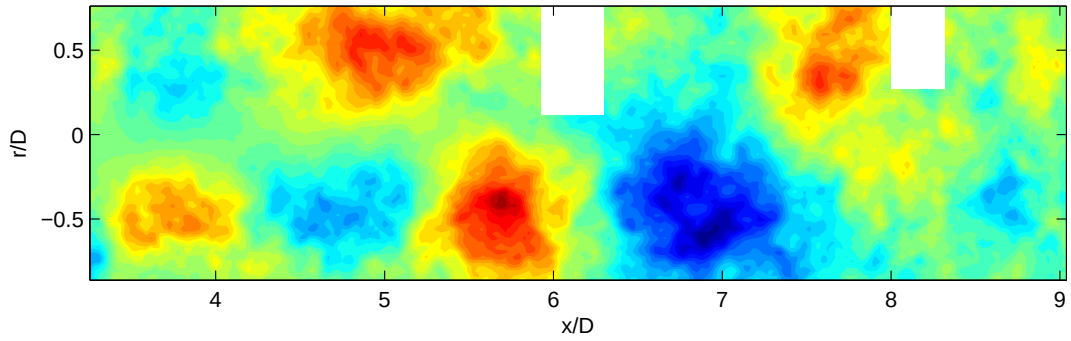

Figure B.32: POD spatial eigenfunction, $\phi_v^{(4)}(\vec{x})$: OLC2

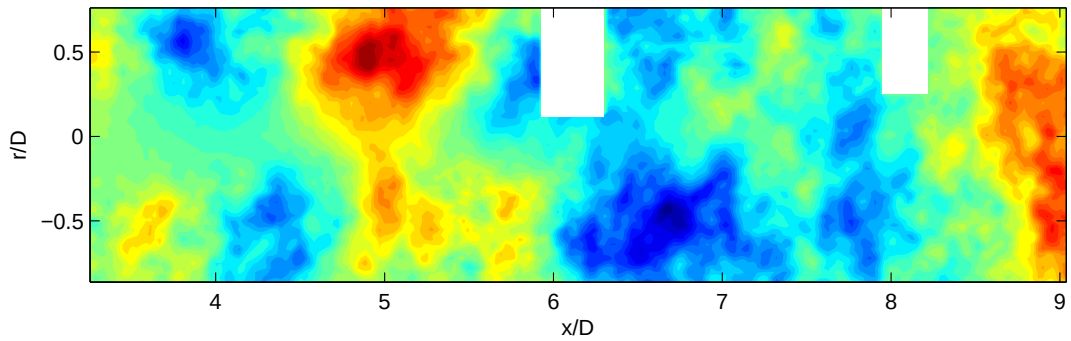

Figure B.33: POD spatial eigenfunction, $\phi_v^{(4)}(\vec{x})$: CLC1

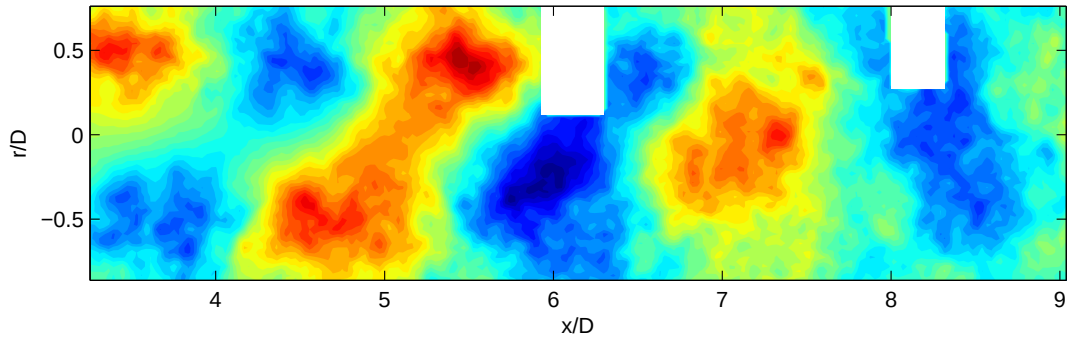

Figure B.34: POD spatial eigenfunction, $\phi_v^{(4)}(\vec{x})$: CLC2

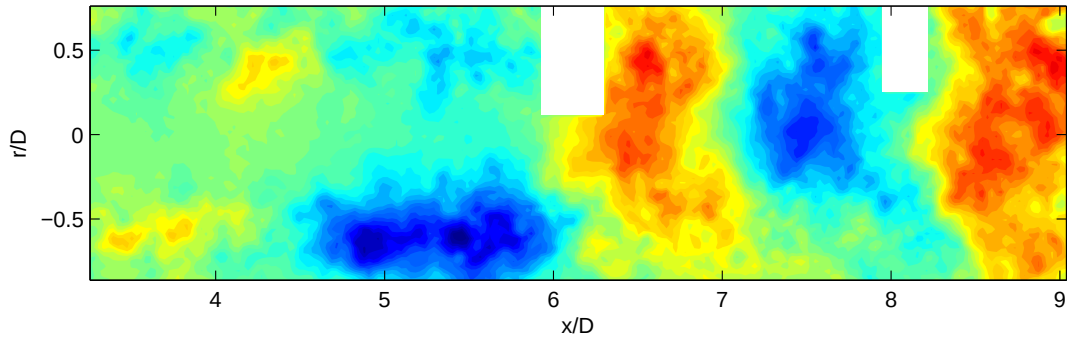

Figure B.35: POD spatial eigenfunction, $\phi_v^{(5)}(\vec{x})$: Baseline

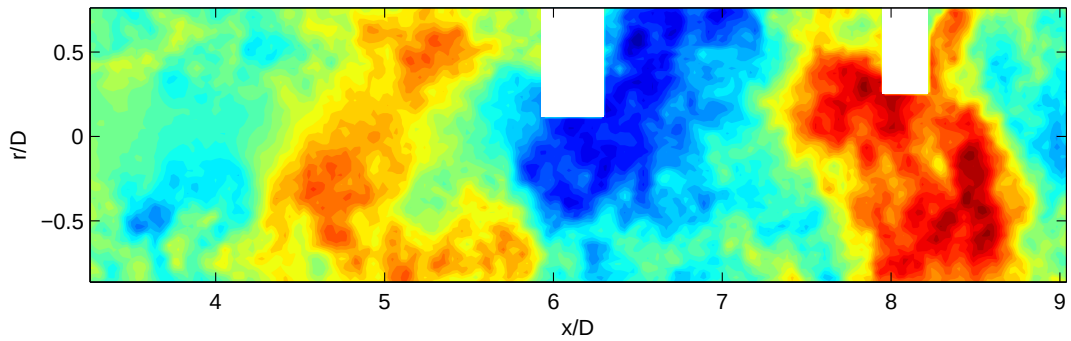

Figure B.36: POD spatial eigenfunction, $\phi_v^{(5)}(\vec{x})$: OLC1

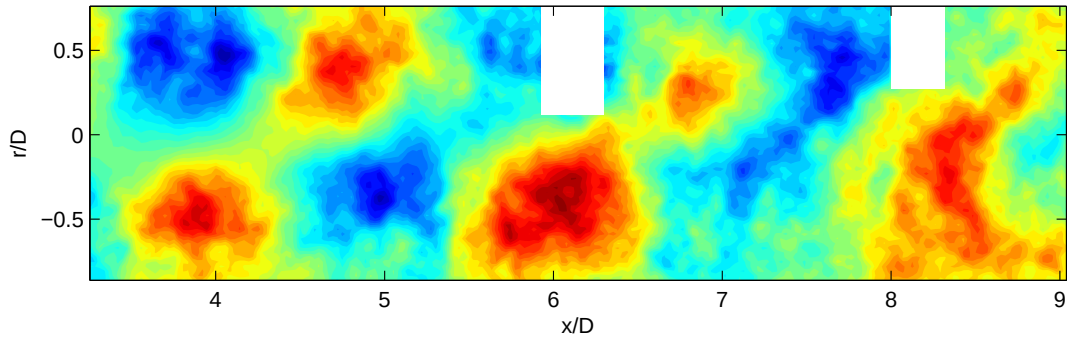

Figure B.37: POD spatial eigenfunction, $\phi_v^{(5)}(\vec{x})$: OLC2

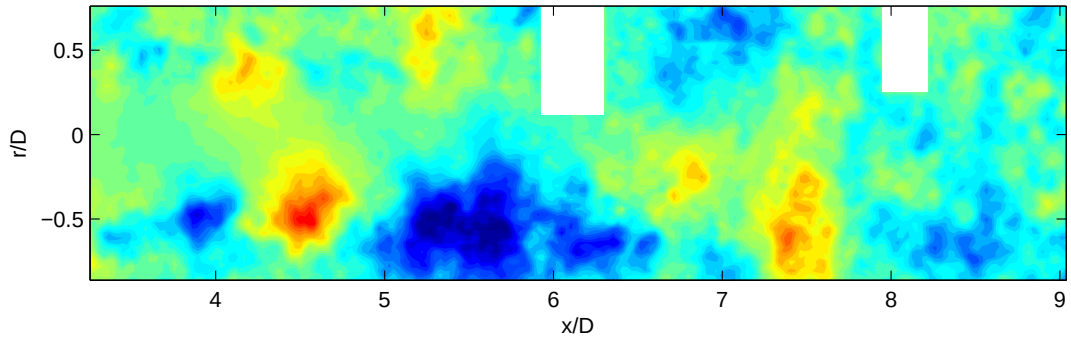

Figure B.38: POD spatial eigenfunction, $\phi_v^{(5)}(\vec{x})$: CLC1

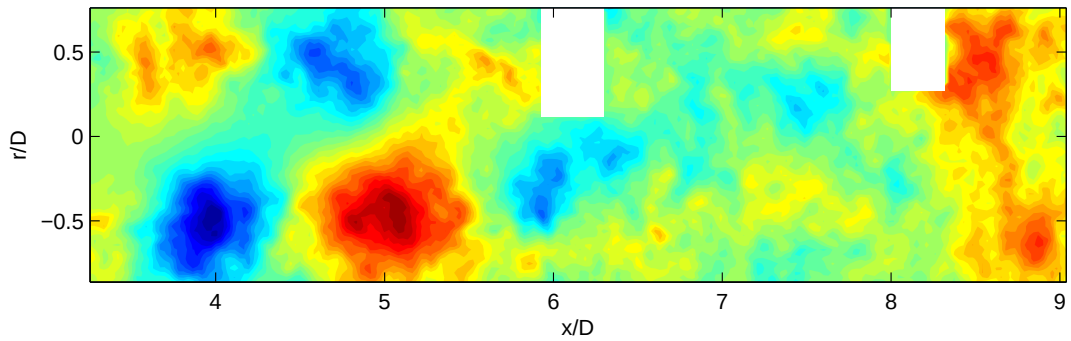

Figure B.39: POD spatial eigenfunction, $\phi_v^{(5)}(\vec{x})$: CLC2

B.5 Reconstructed Instantaneous Velocity Fields

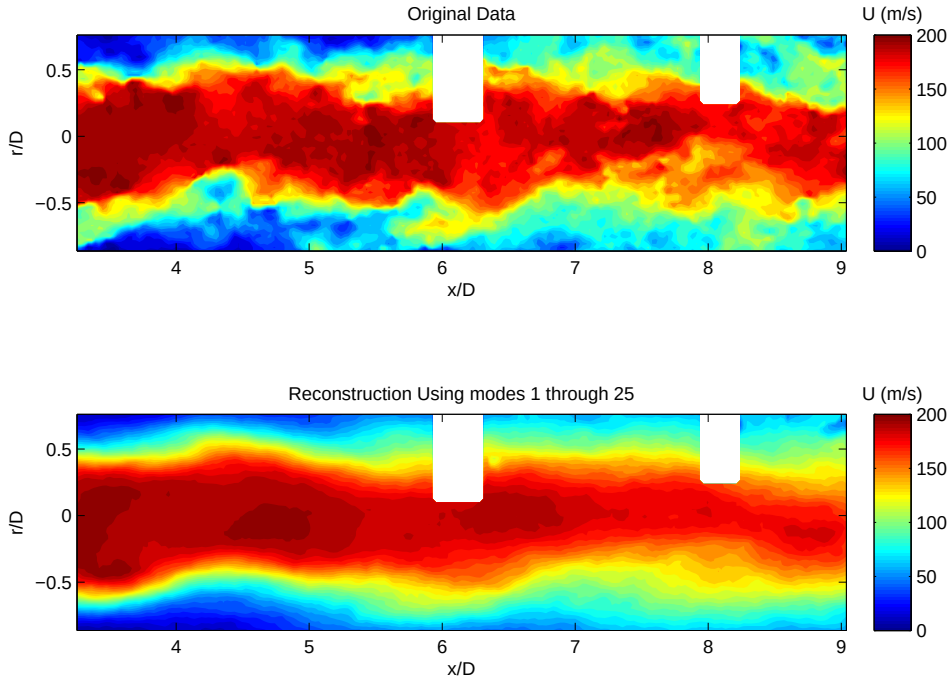

Figure B.40: Reconstructed Instantaneous Velocity Field: Baseline

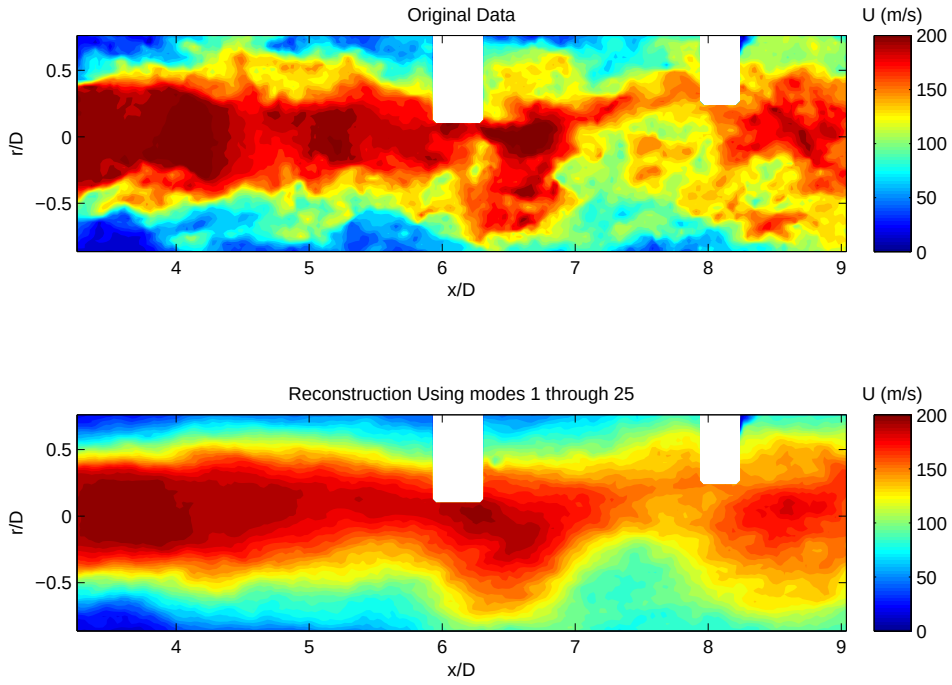

Figure B.41: Reconstructed Instantaneous Velocity Field: OLC1

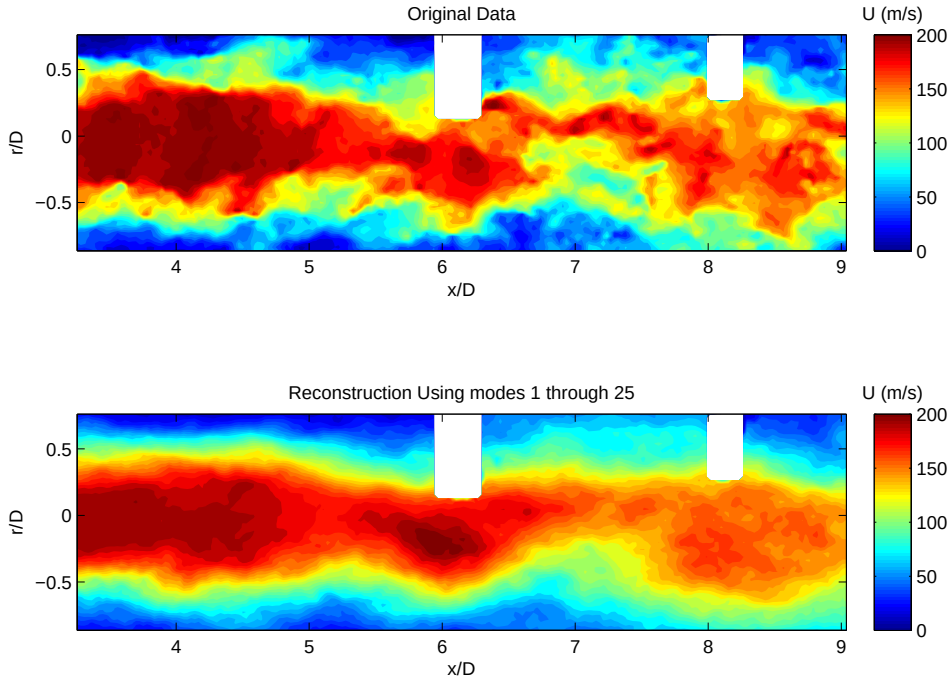

Figure B.42: Reconstructed Instantaneous Velocity Field: OLC2

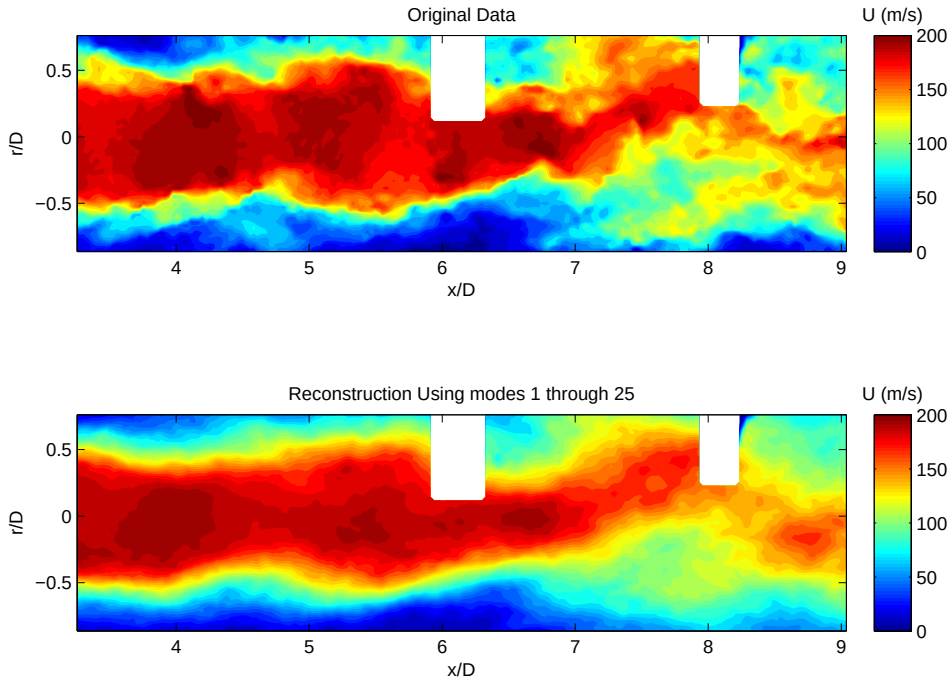

Figure B.43: Reconstructed Instantaneous Velocity Field: CLC1

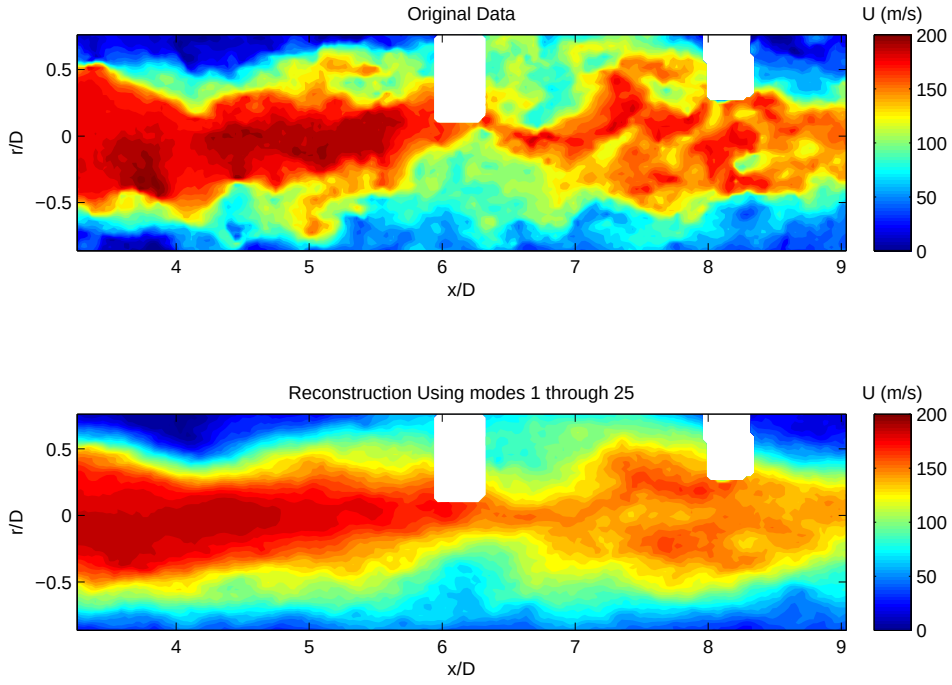

Figure B.44: Reconstructed Instantaneous Velocity Field: CLC2

B.6 Far-Field Sound Pressure Levels

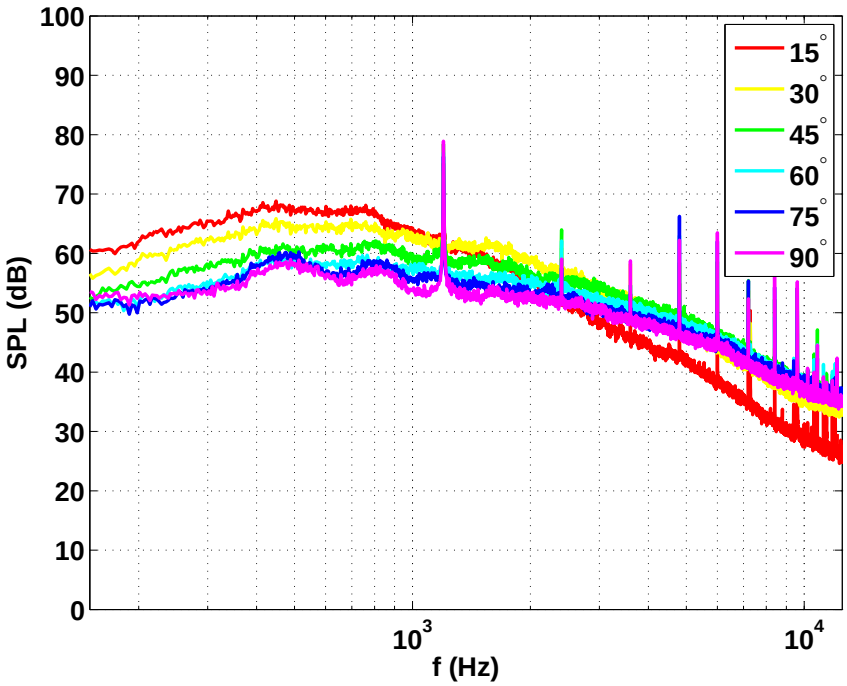

Figure B.45: In-plane far-field SPL: OLC1

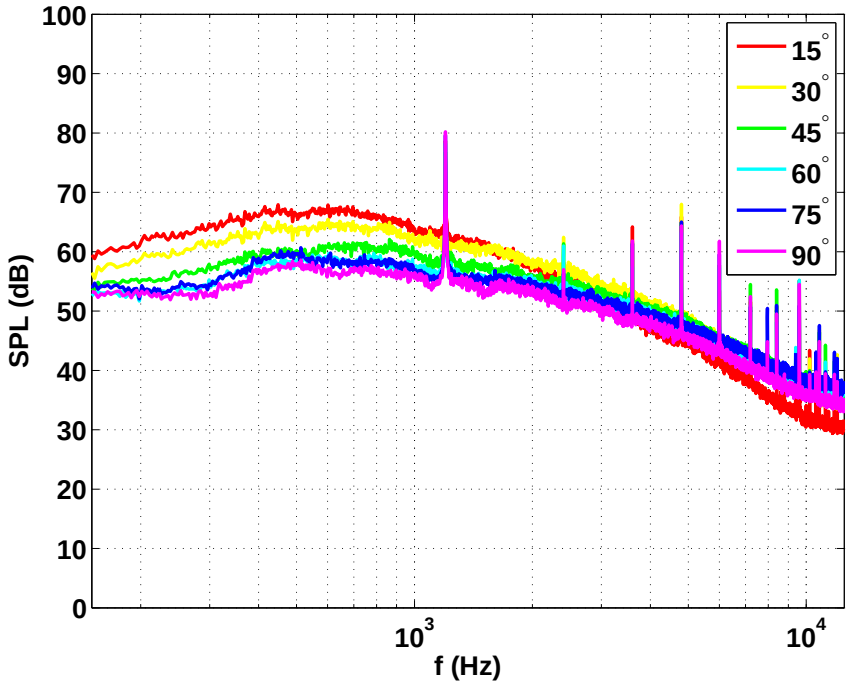

Figure B.46: Out-of-plane far-field SPL: OLC1

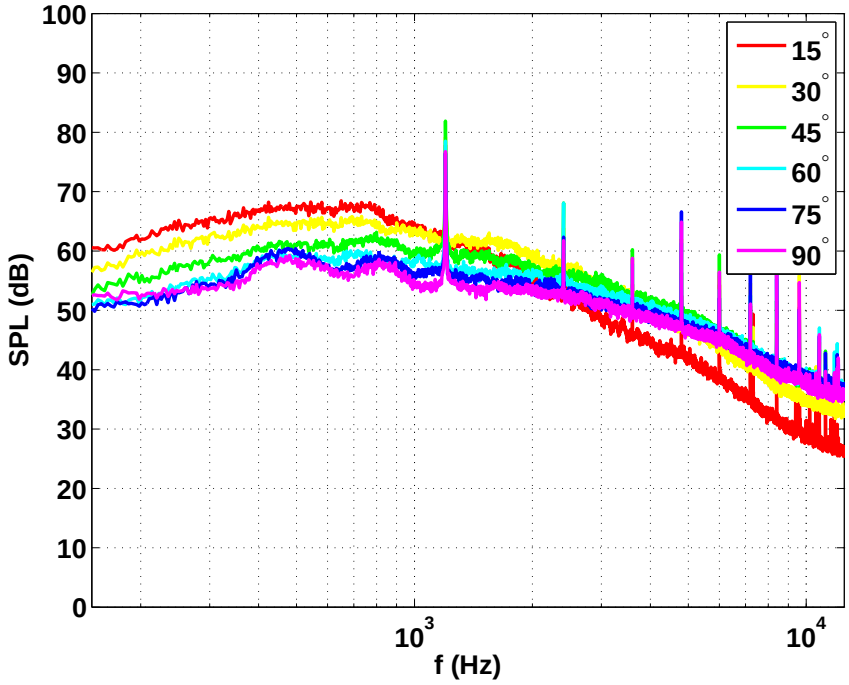

Figure B.47: In-plane far-field SPL: OLC2

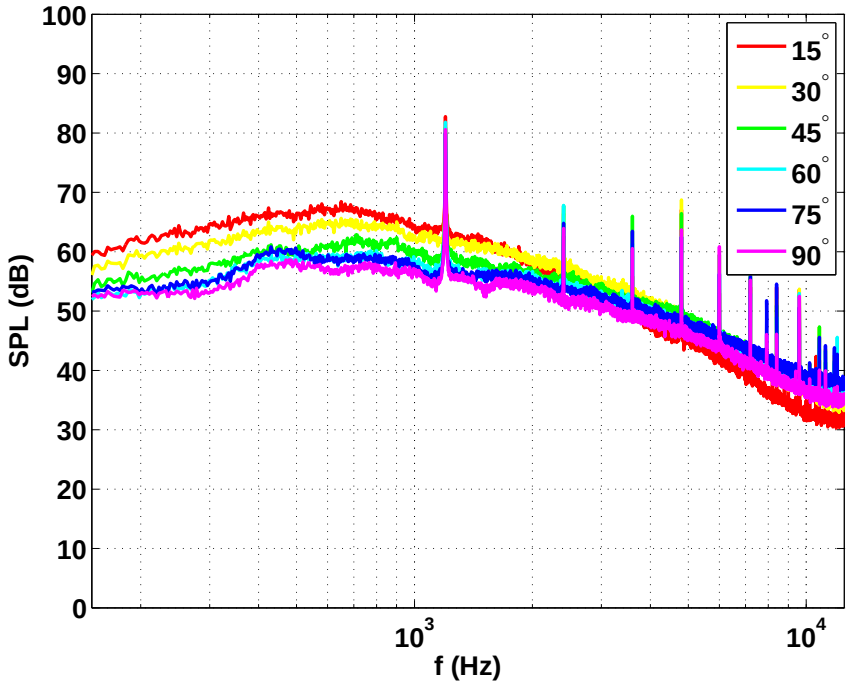

Figure B.48: Out-of-plane far-field SPL: OLC2

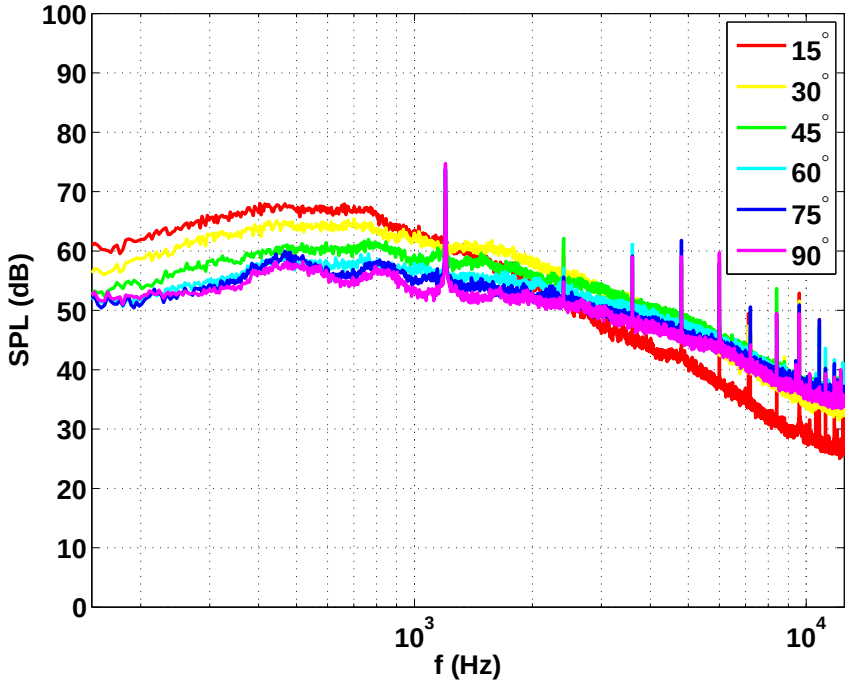

Figure B.49: In-plane far-field SPL: CLC1

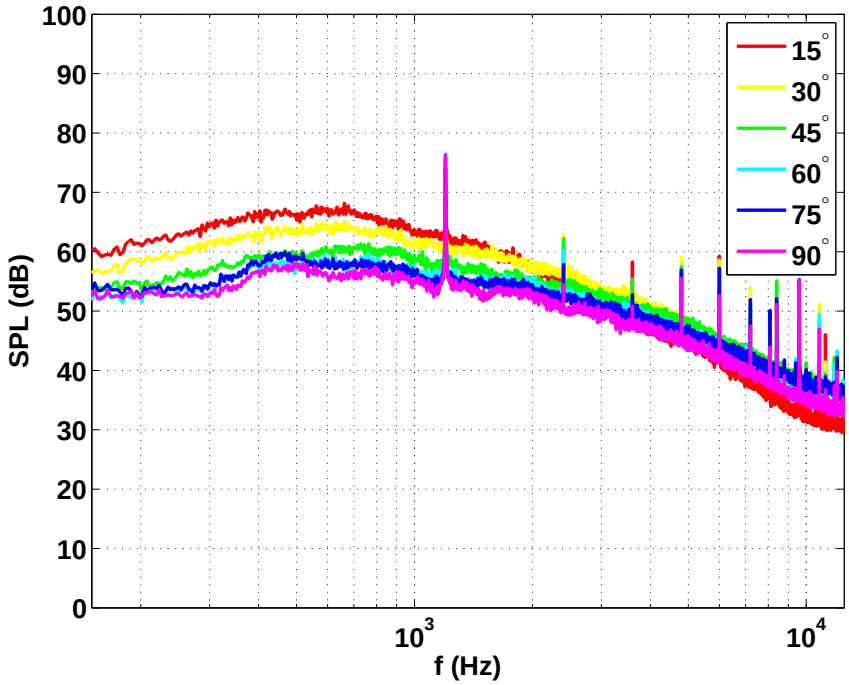

Figure B.50: Out-of-plane far-field SPL: CLC1

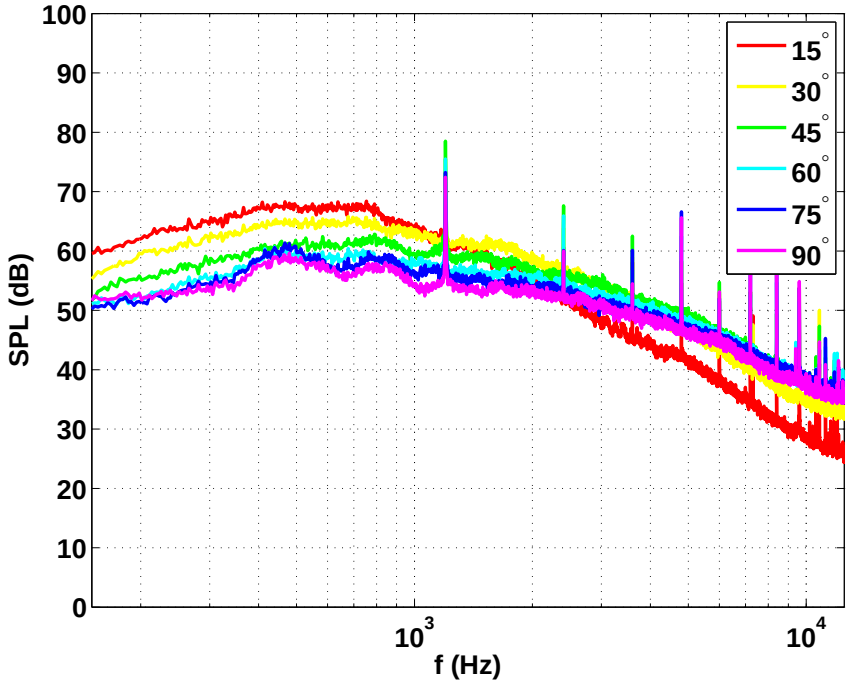

Figure B.51: In-plane far-field SPL: CLC2

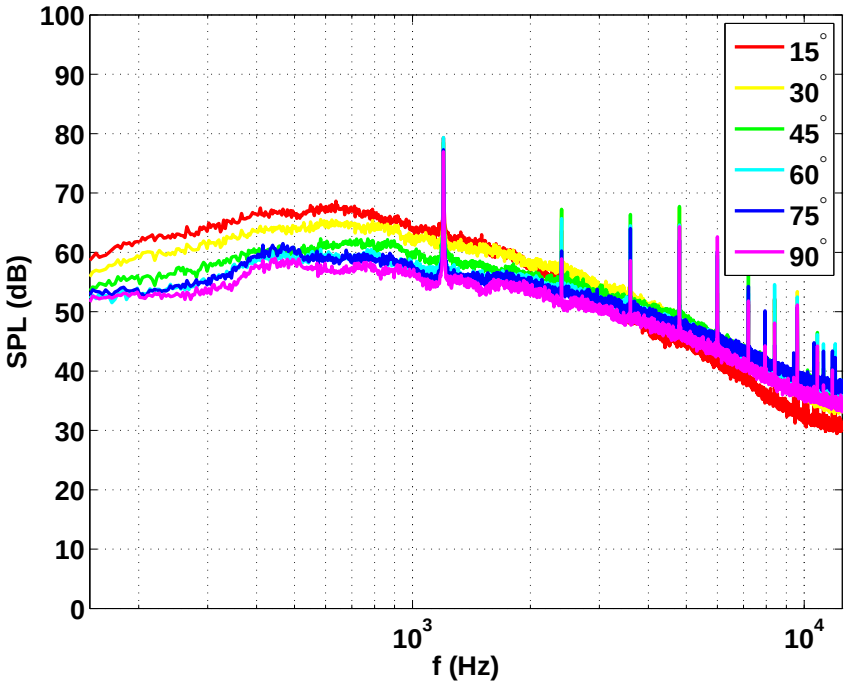

Figure B.52: Out-of-plane far-field SPL: CLC2

Appendix C

2011 TRPIV Supplemental Figures

C.1 Summary of Loud Modes

Mach Number	*Window Location* (x/D)	*Loud Mode*(s)
0.60	5–6.5	6
0.60	6–7.5	6, 14
0.85	6–7.5	7, 15
1.00	6–7.5	16

Table C.1: Loud modes for different Mach numbers and window locations

C.2 Time-Dependent POD Expansion Coefficients

This section presents the temporal POD coefficients for the Mach 0.6 data set at $x/D = 6 - 7.5$.

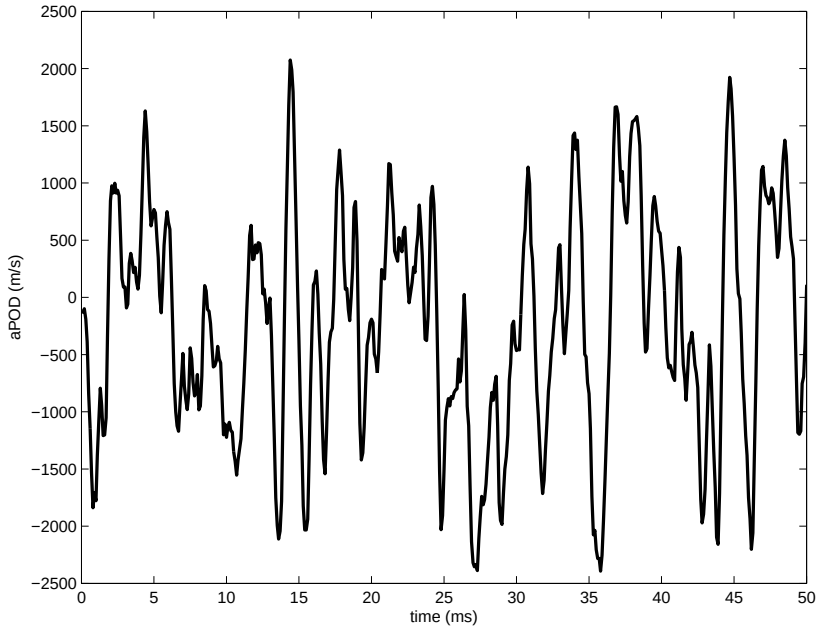

Figure C.1: Mode 1 time-dependent POD expansion coefficient for the first 50 *ms*

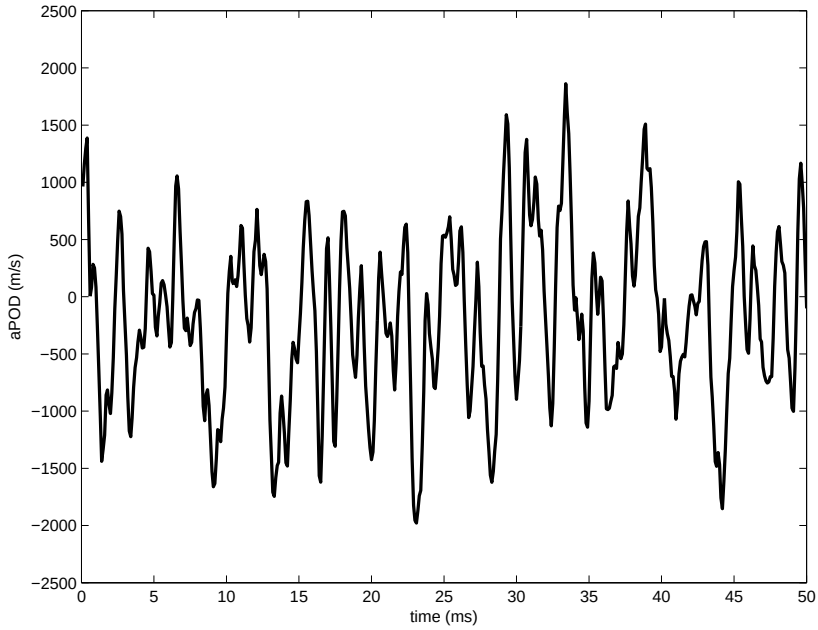

Figure C.2: Mode 2 time-dependent POD expansion coefficient for the first 50 *ms*

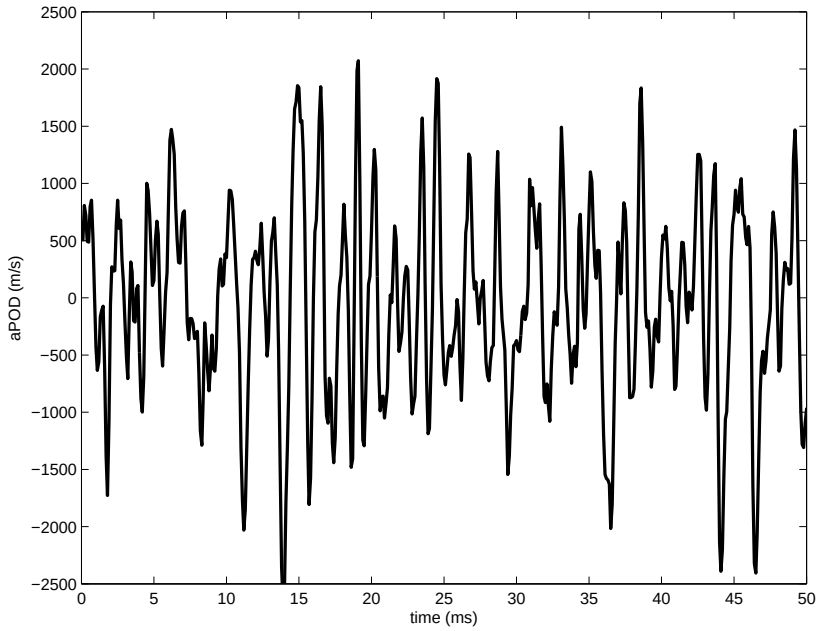

Figure C.3: Mode 3 time-dependent POD expansion coefficient for the first 50 *ms*

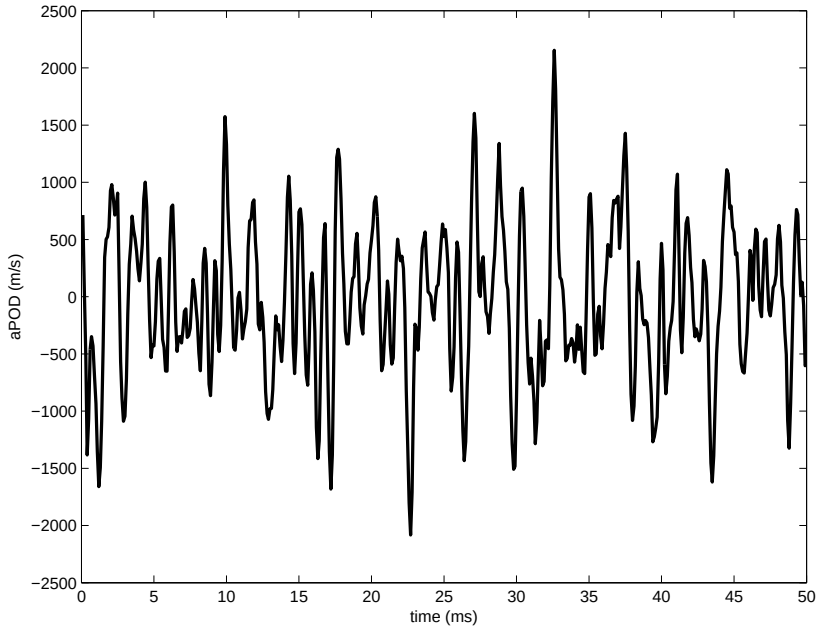

Figure C.4: Mode 4 time-dependent POD expansion coefficient for the first 50 *ms*

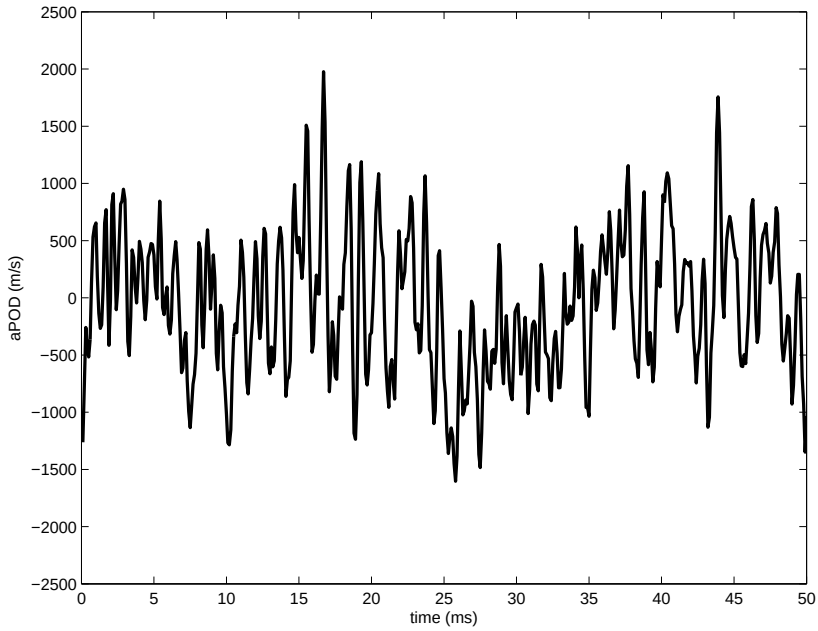

Figure C.5: Mode 5 time-dependent POD expansion coefficient for the first 50 *ms*

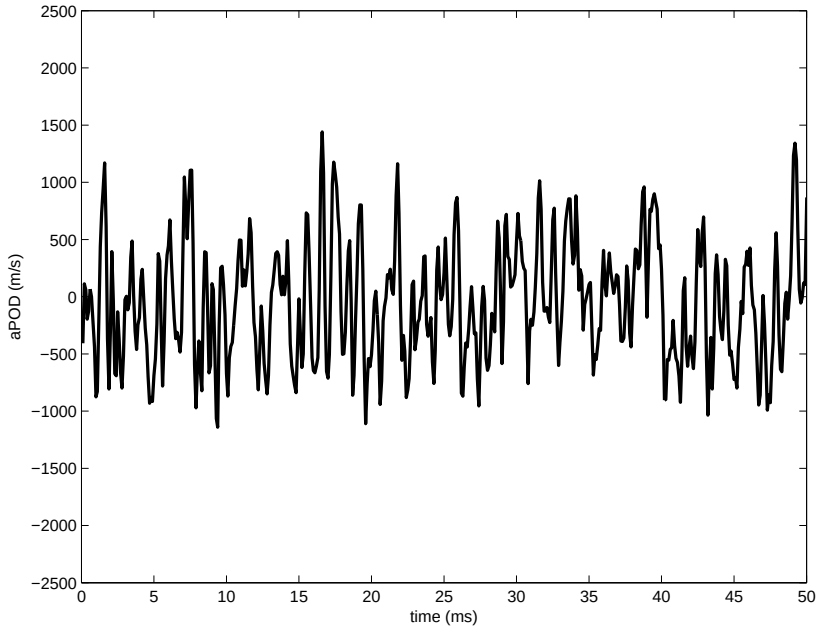

Figure C.6: Mode 7 time-dependent POD expansion coefficient for the first 50 *ms*

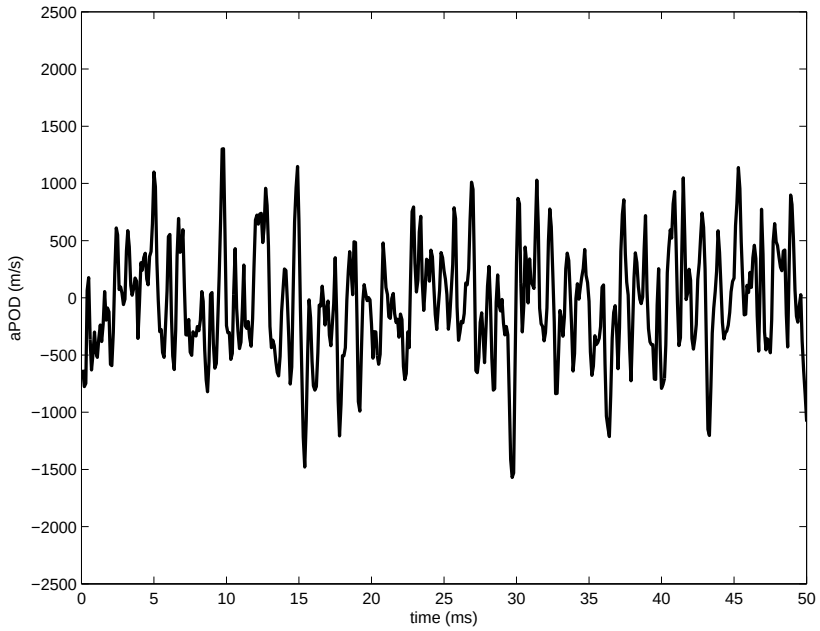

Figure C.7: Mode 8 time-dependent POD expansion coefficient for the first 50 *ms*

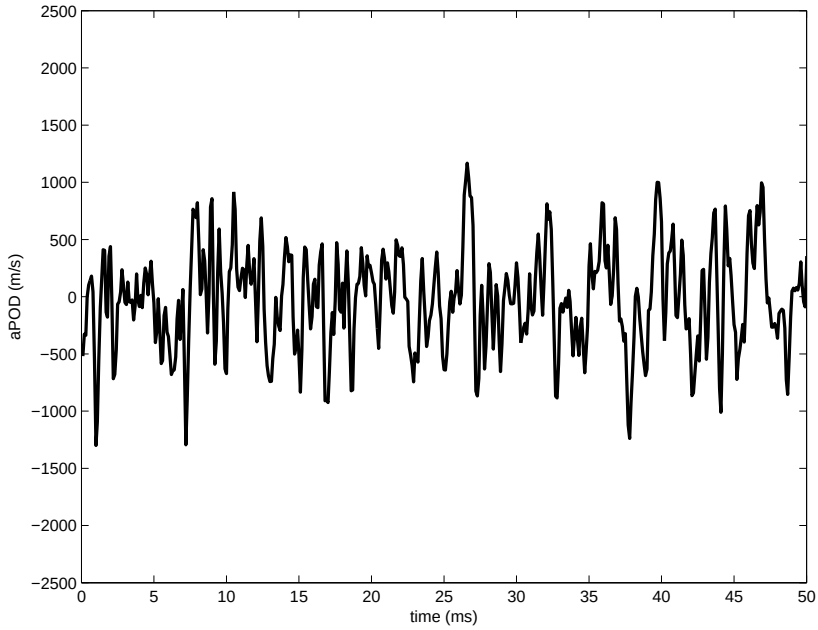

Figure C.8: Mode 9 time-dependent POD expansion coefficient for the first 50 *ms*

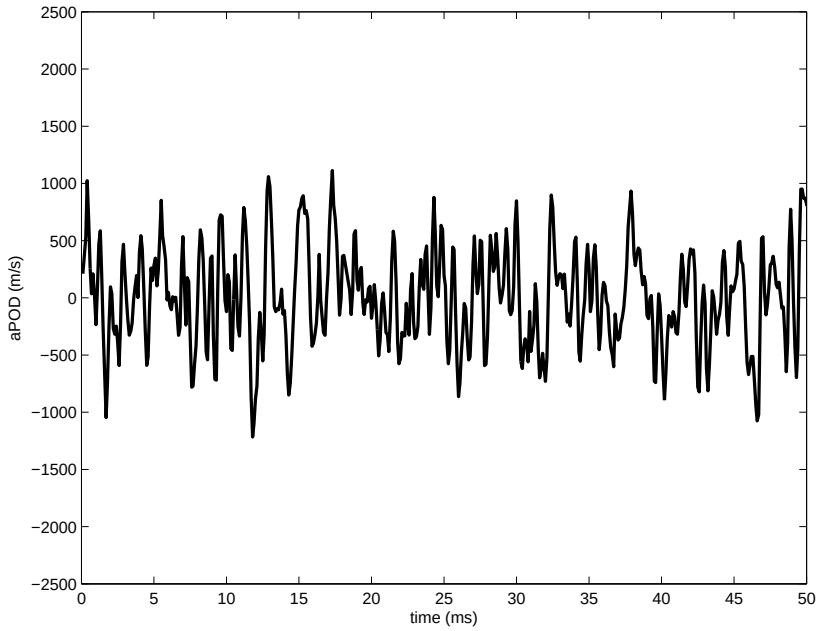

Figure C.9: Mode 10 time-dependent POD expansion coefficient for the first 50 *ms*

C.3 Near-Field Diagnostics to Far-Field Acoustics

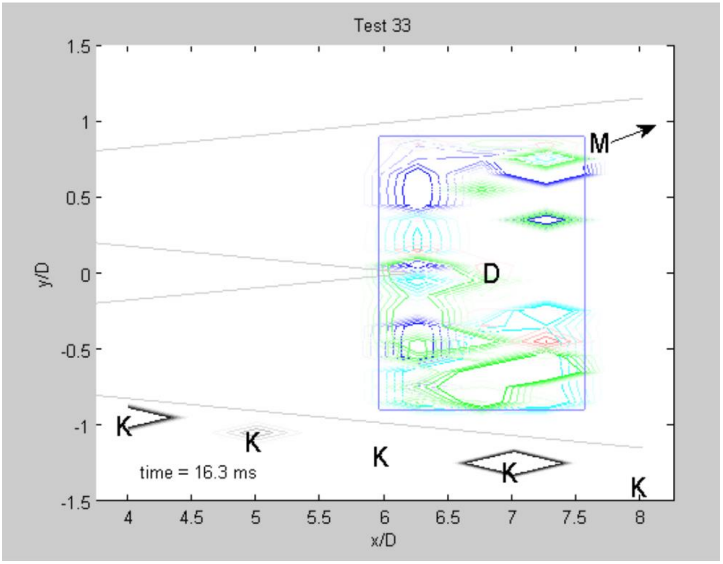

Figure C.10: Near-field diagnostics at $t = 16.3$ *ms* [135]

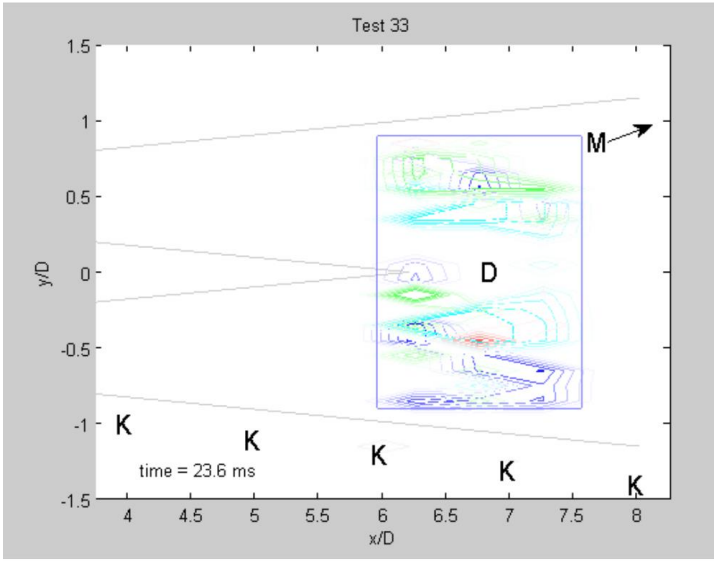

Figure C.11: Near-field diagnostics at $t = 23.6$ *ms* [135]

C.4 Time-Dependent POD Reconstructions

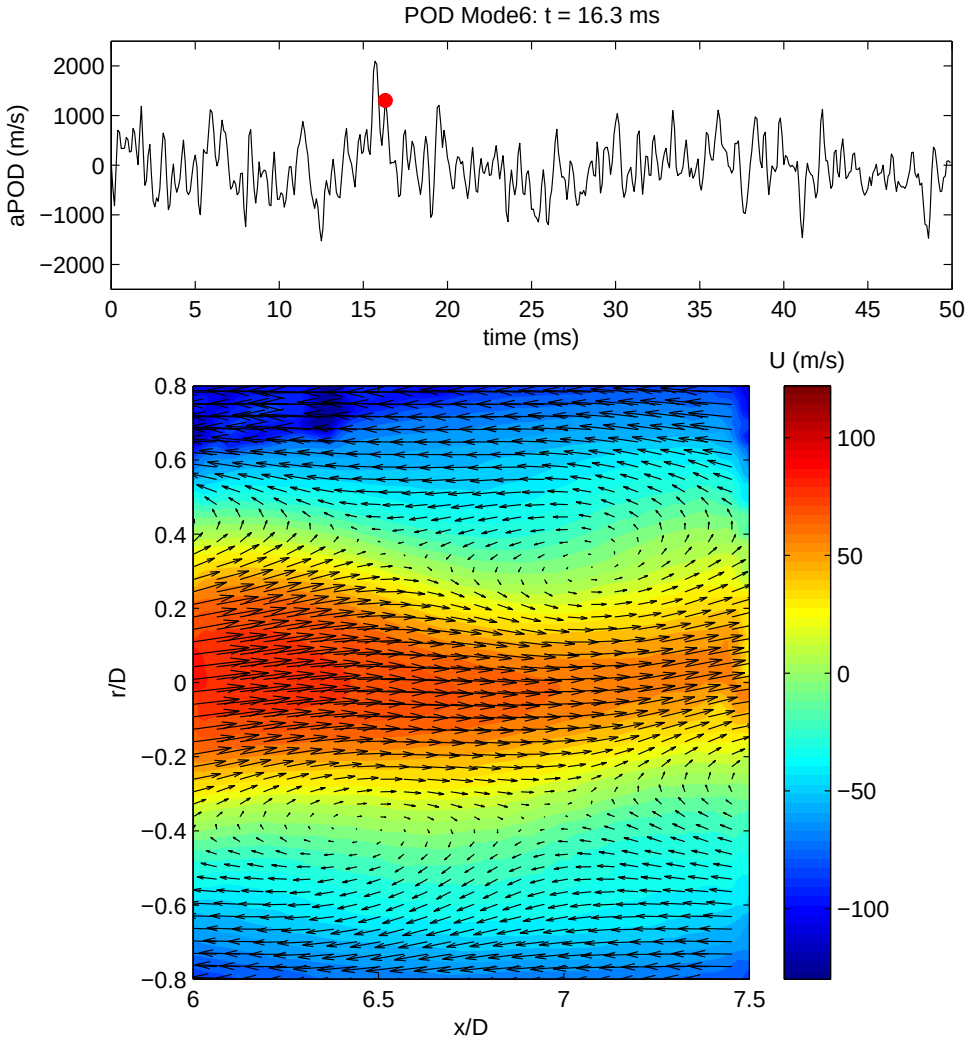

Figure C.12: Mode 6 reconstruction in the convective time frame at $t = 16.3$ *ms*, with streamwise velocity contours

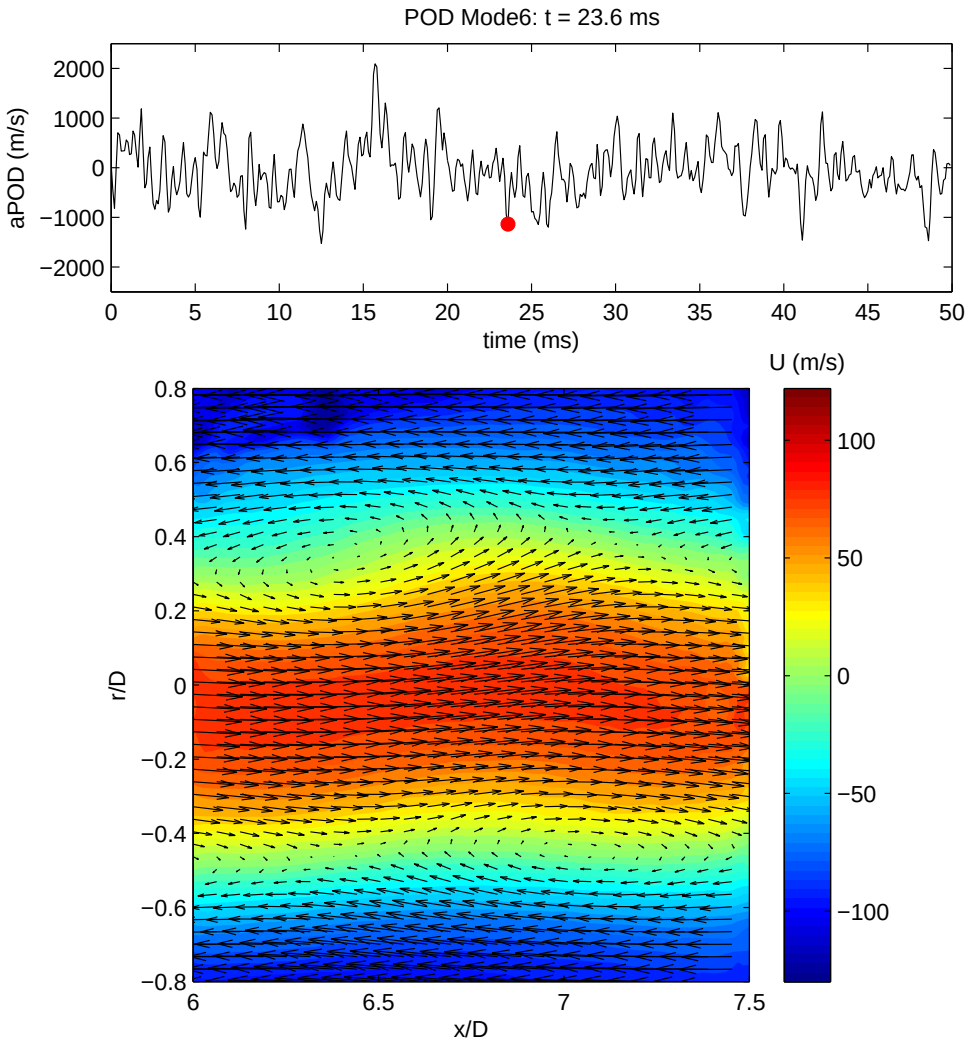

Figure C.13: Mode 6 reconstruction in the convective time frame at $t = 23.6\ ms$, with streamwise velocity contours

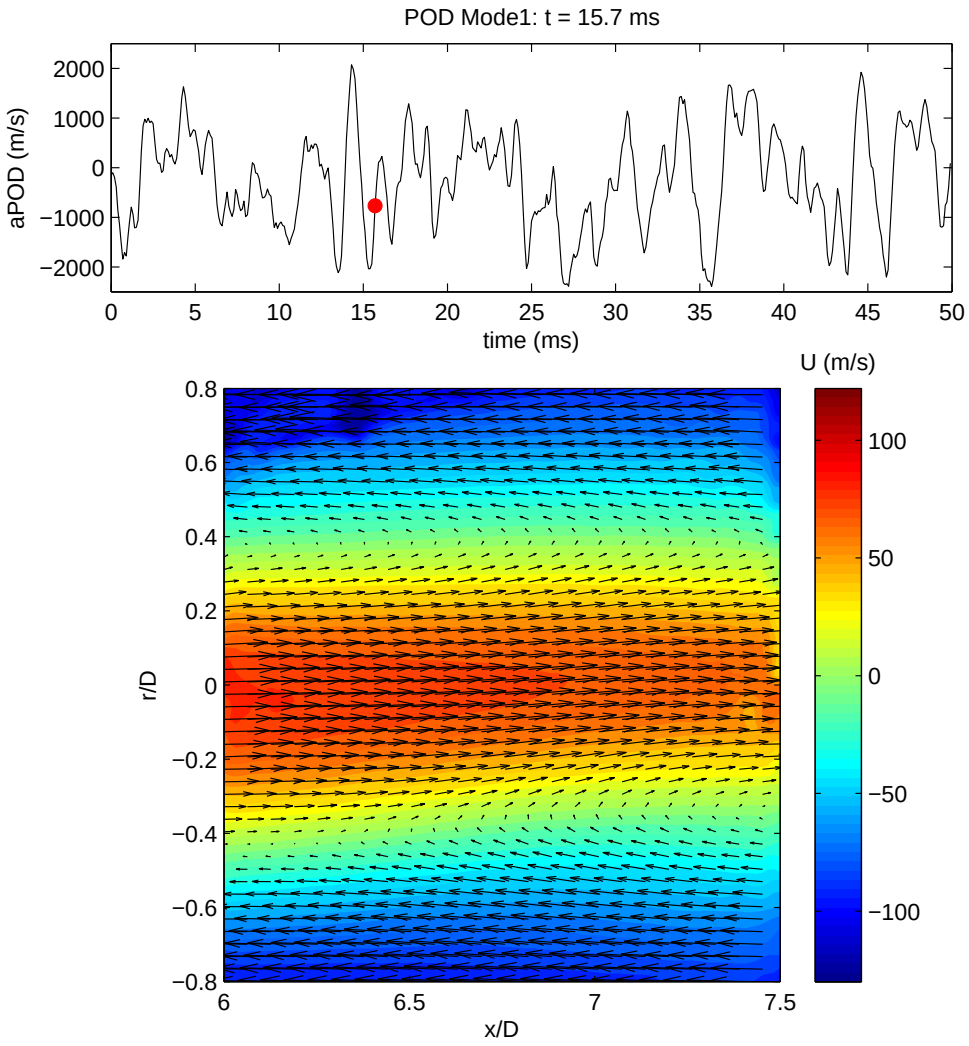

Figure C.14: Mode 1 reconstruction in the convective time frame at $t = 15.7$ *ms*, with streamwise velocity contours

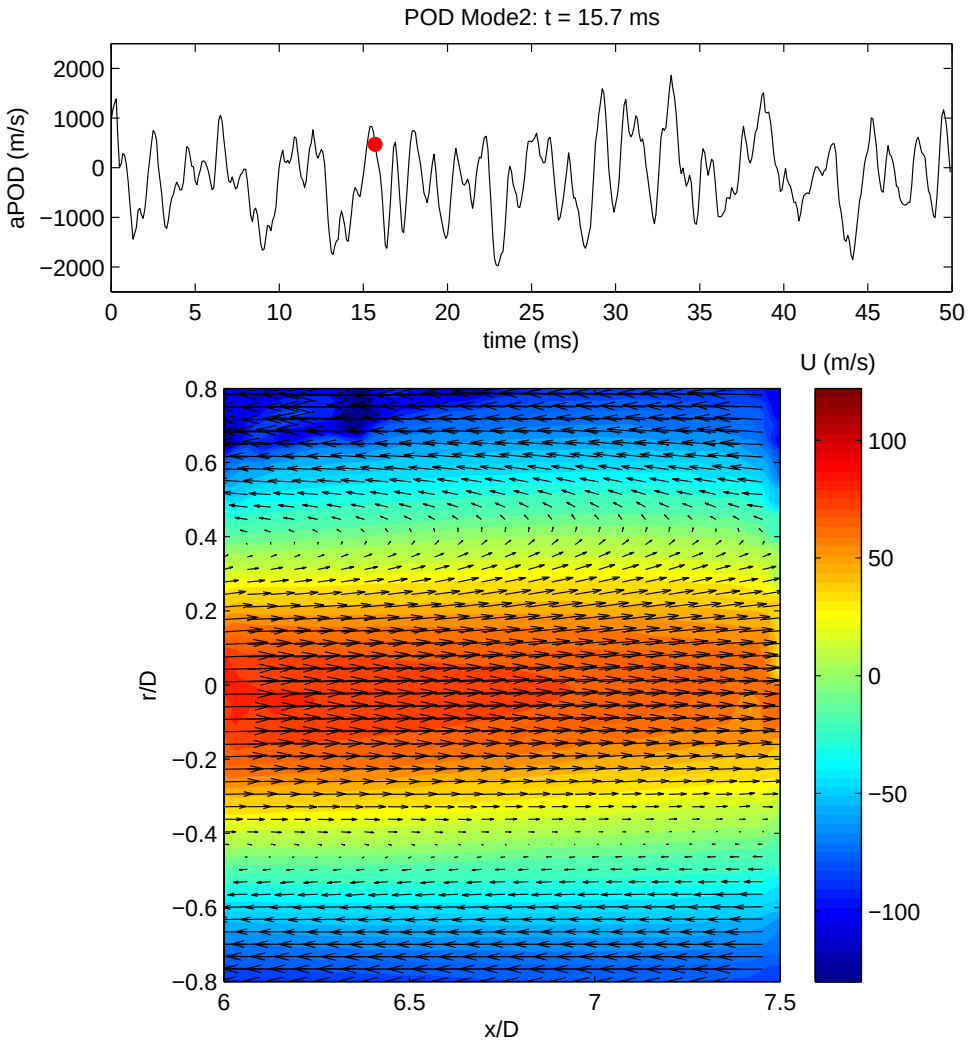

Figure C.15: Mode 2 reconstruction in the convective time frame at $t = 15.7$ *ms*, with streamwise velocity contours

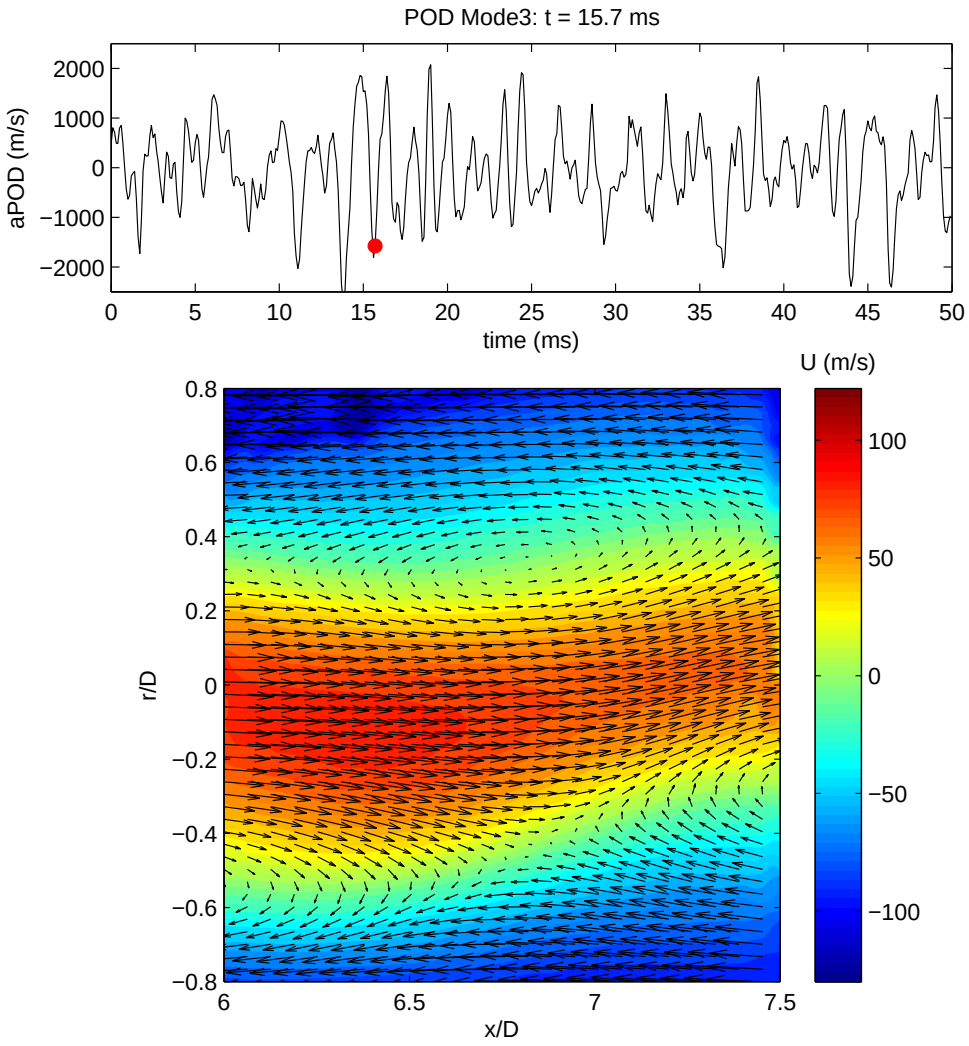

Figure C.16: Mode 3 reconstruction in the convective time frame at $t = 15.7$ *ms*, with streamwise velocity contours

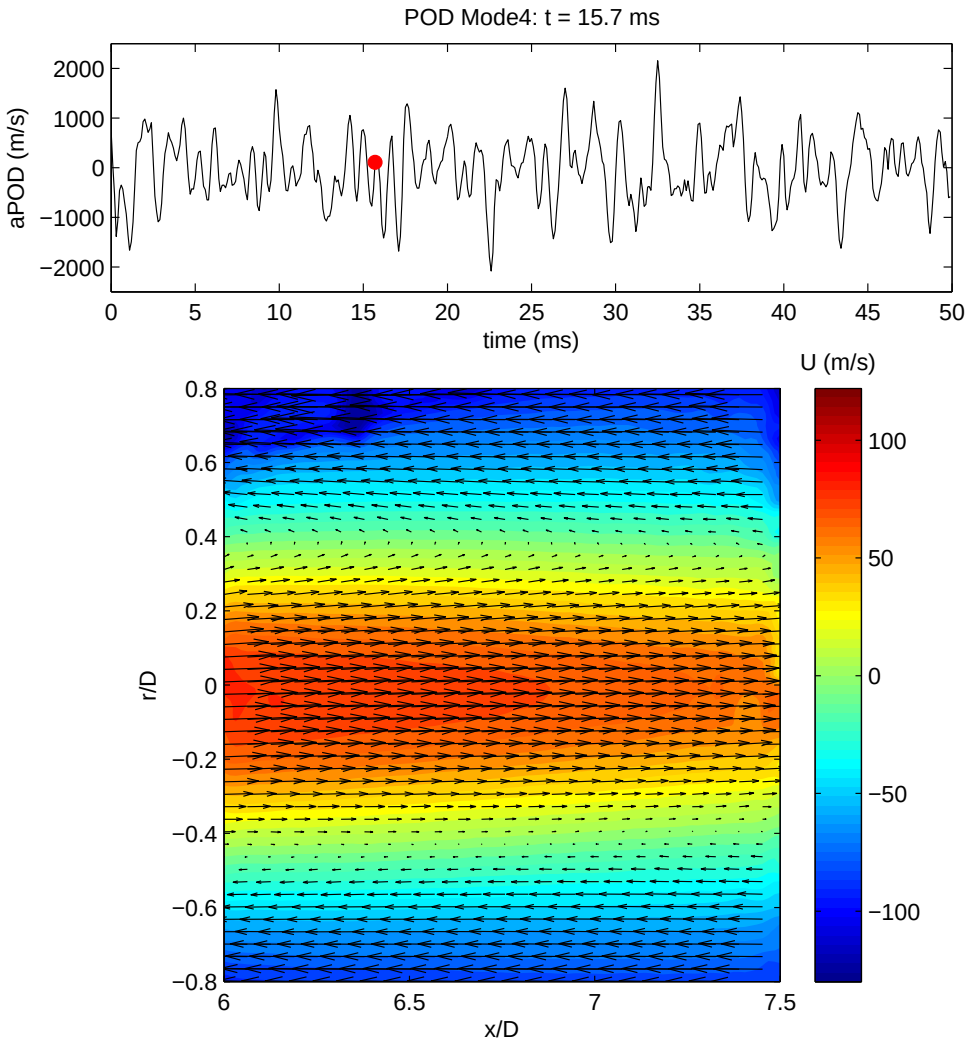

Figure C.17: Mode 4 reconstruction in the convective time frame at $t = 15.7$ *ms*, with streamwise velocity contours

Appendix D

2013 TRPIV Supplemental Figures

D.1 TRPIV and LWPIV Relationship

Mode Number	*Correlation Level*
1	0.8
2	0.7
3	0.6
4	0.8
5	0.7
6	0.7
7	0.6
8	0.2
9	0.1
10	0.5
11	0.3
12	0.3
13	0.6
14	0.6
15	0.2
16	0.4

Table D.1: Modal correlation for the first 16 spatial eigenfunctions: TRPIV and extracted LWPIV (baseline)

D.2 Near-Field Pressure Spectra

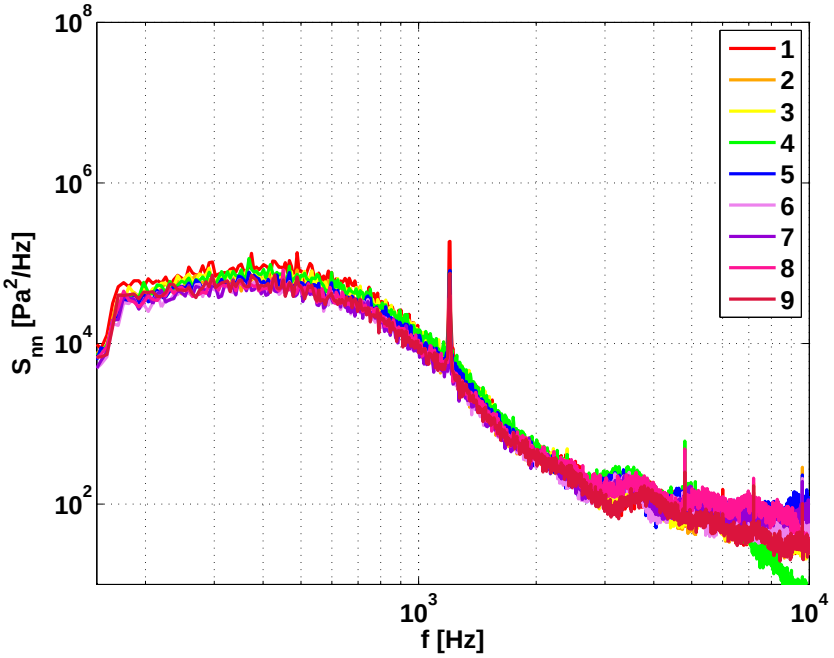

Figure D.1: Near-field pressure spectra, azimuthal array (OLC1)

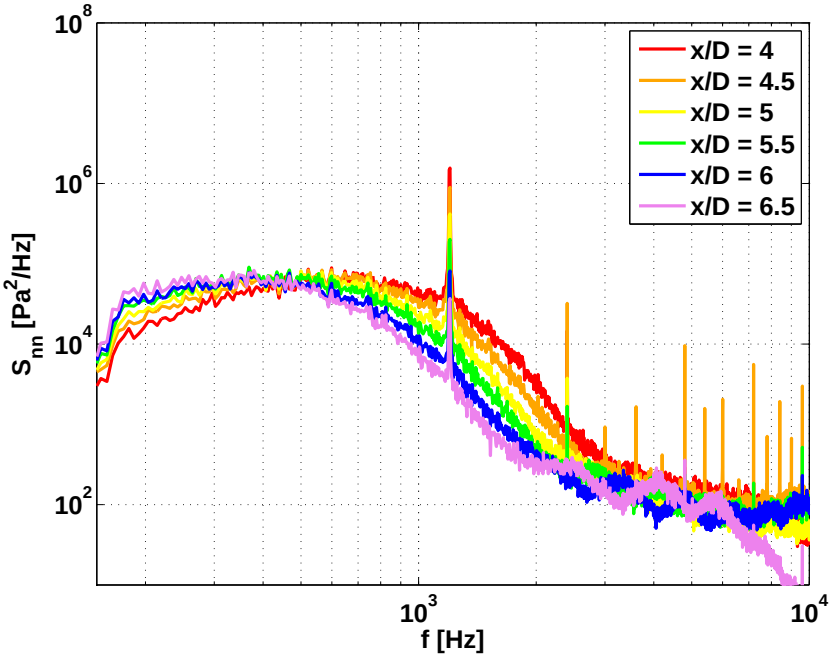

Figure D.2: Near-field pressure spectra, linear array (OLC1)

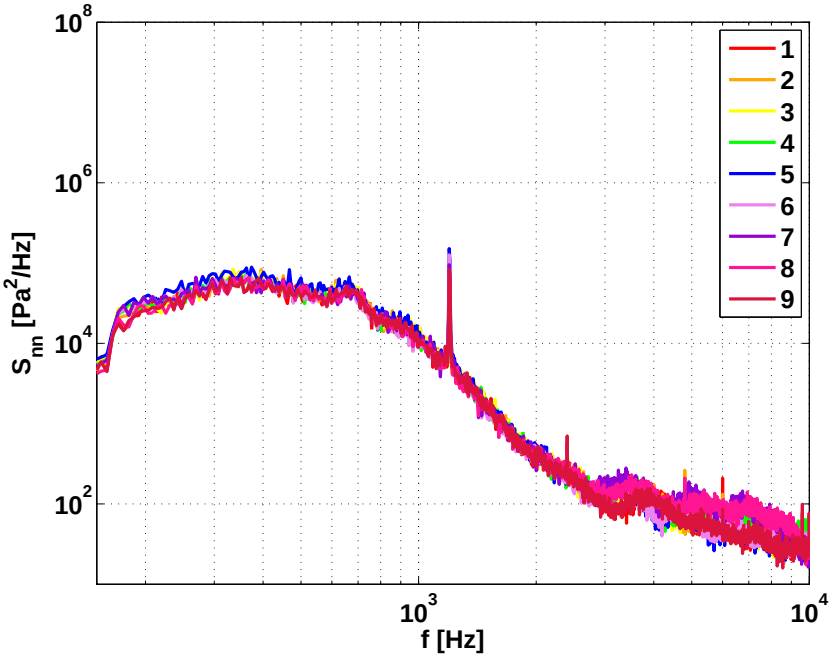

Figure D.3: Near-field pressure spectra, azimuthal array (CLC1)

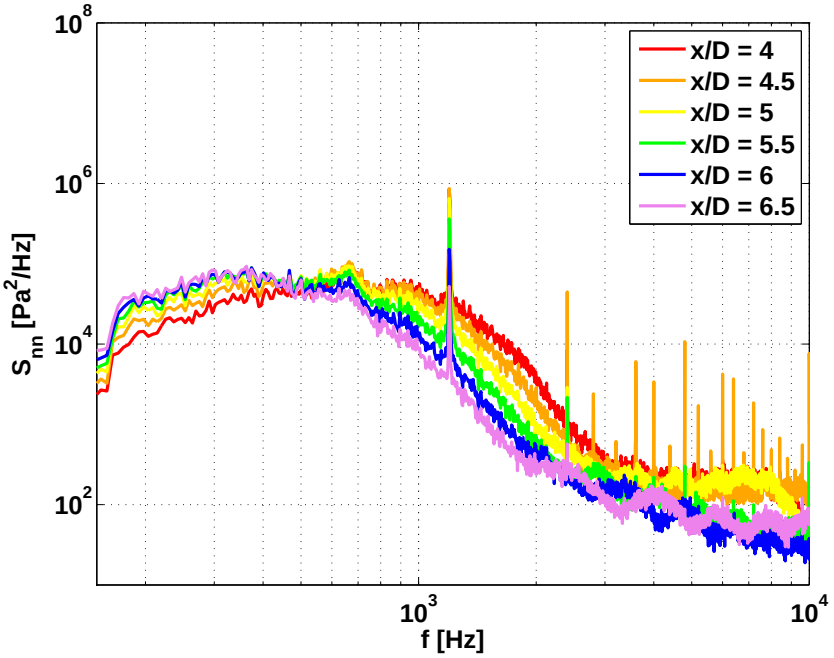

Figure D.4: Near-field pressure spectra, linear array (CLC1)

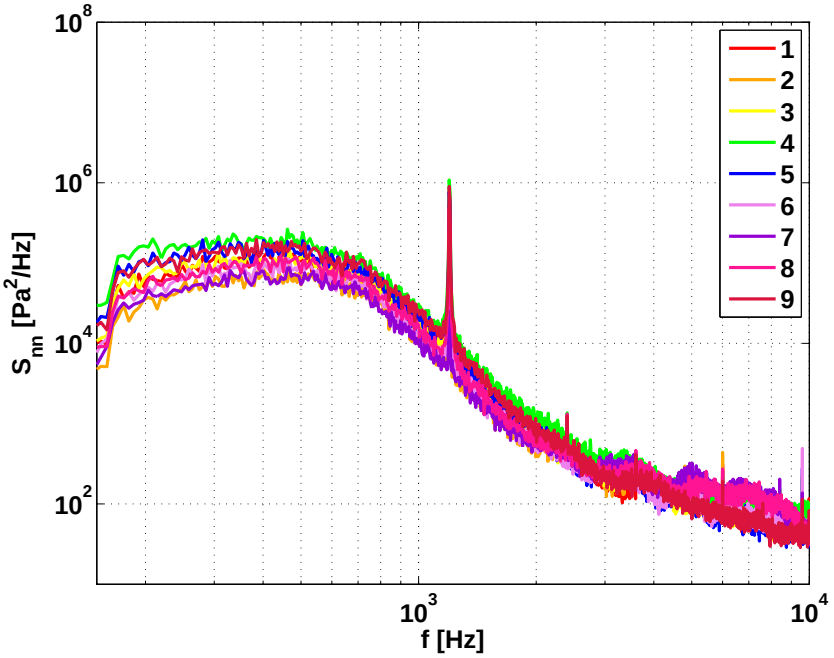

Figure D.5: Near-field pressure spectra, azimuthal array (CLC2)

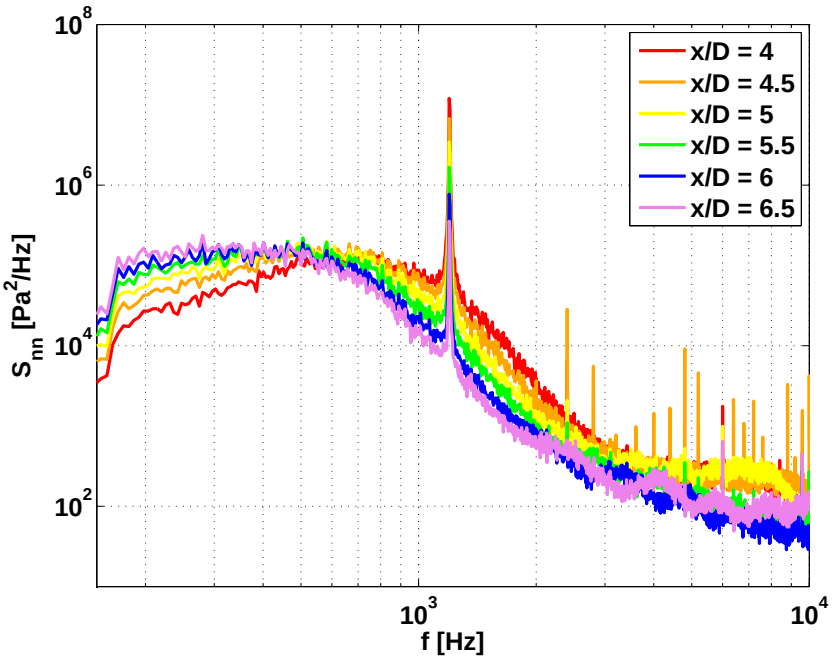

Figure D.6: Near-field pressure spectra, linear array (CLC2)

D.3 Far-Field Acoustics

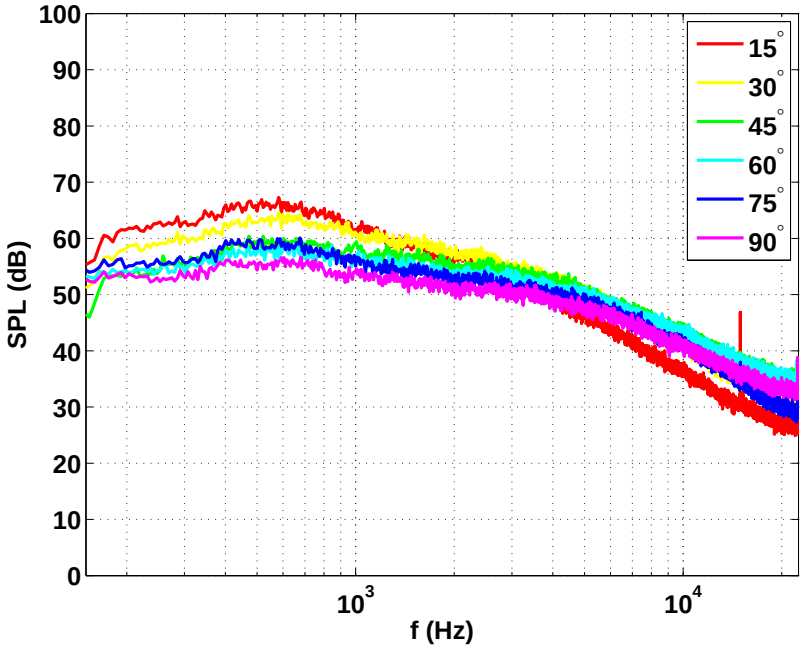

Figure D.7: Far-field SPL, out-of-plane microphones (baseline)

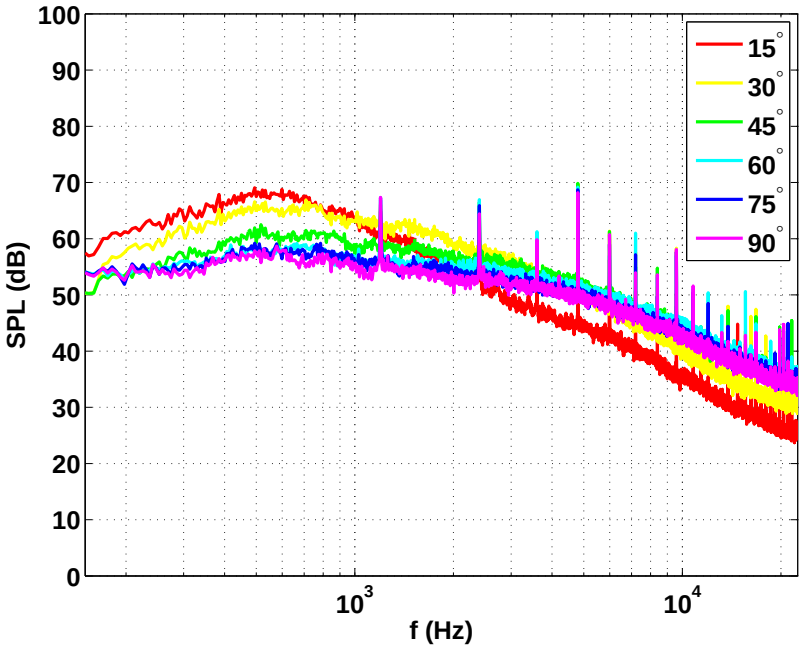

Figure D.8: Far-field SPL, in-plane microphones (OLC1)

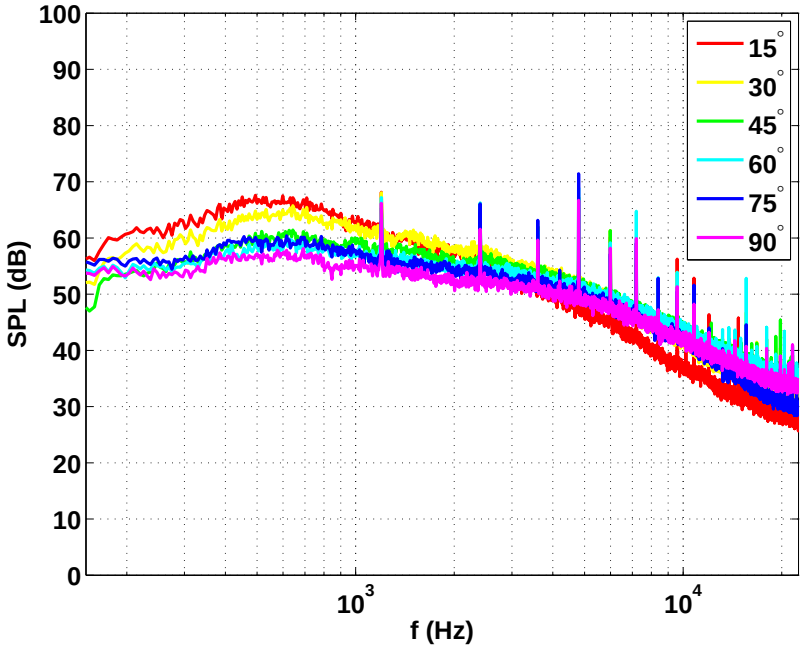

Figure D.9: Far-field SPL, out-of-plane microphones (OLC1)

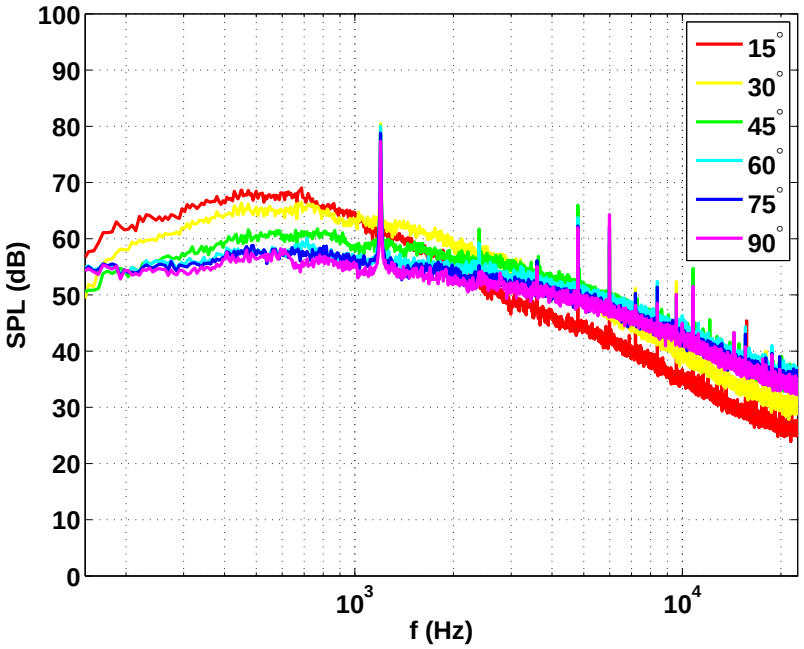

Figure D.10: Far-field SPL, in-plane microphones (CLC1)

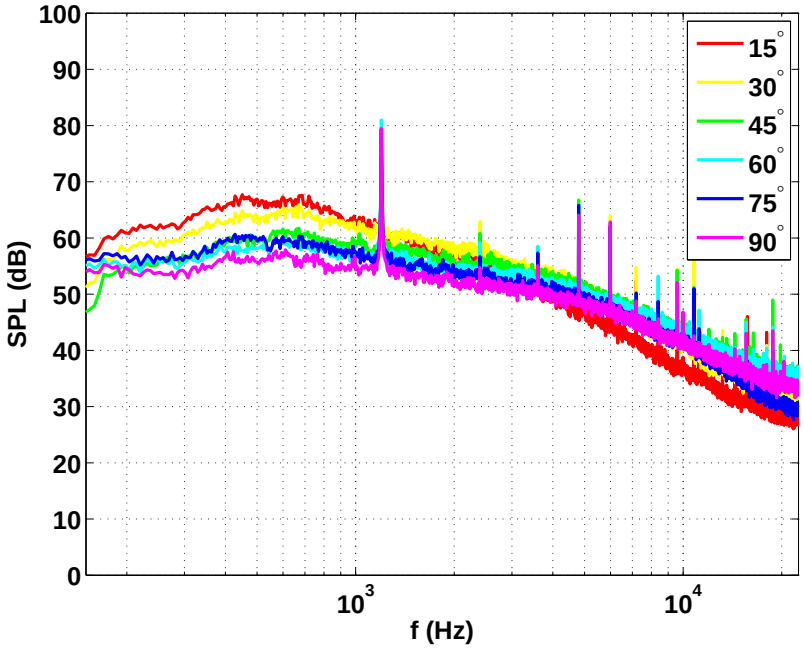

Figure D.11: Far-field SPL, out-of-plane microphones (CLC1)

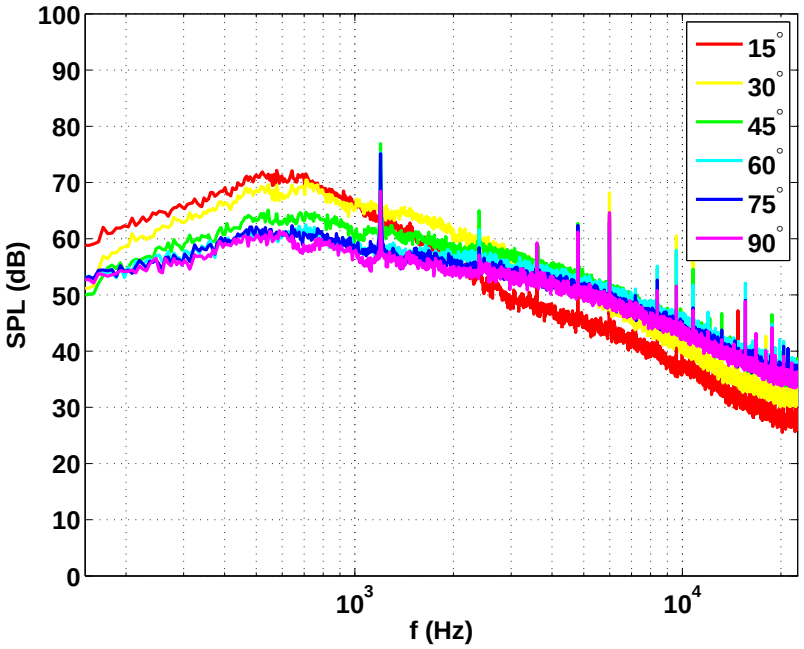

Figure D.12: Far-field SPL, in-plane microphones (CLC2)

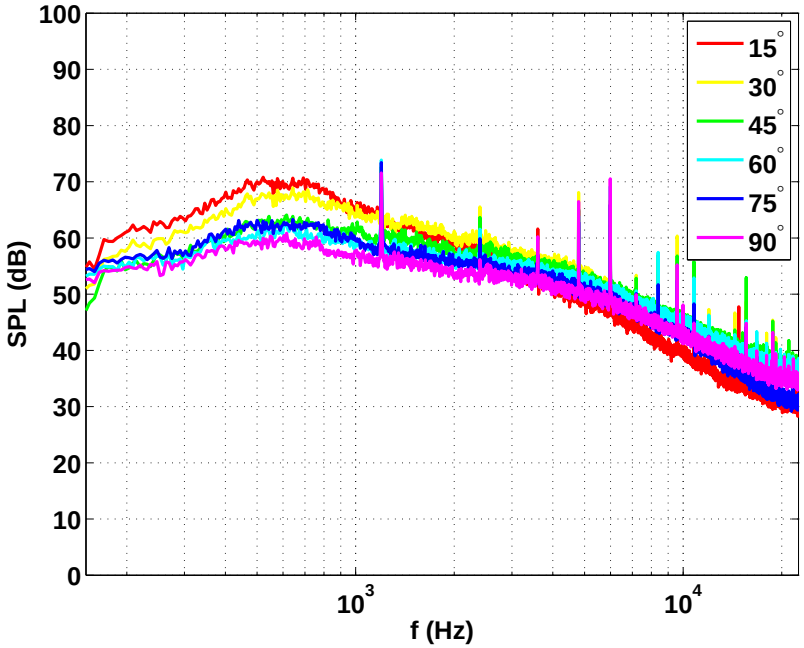

Figure D.13: Far-field SPL, out-of-plane microphones (CLC2)

D.4 Instantaneous Velocity Field

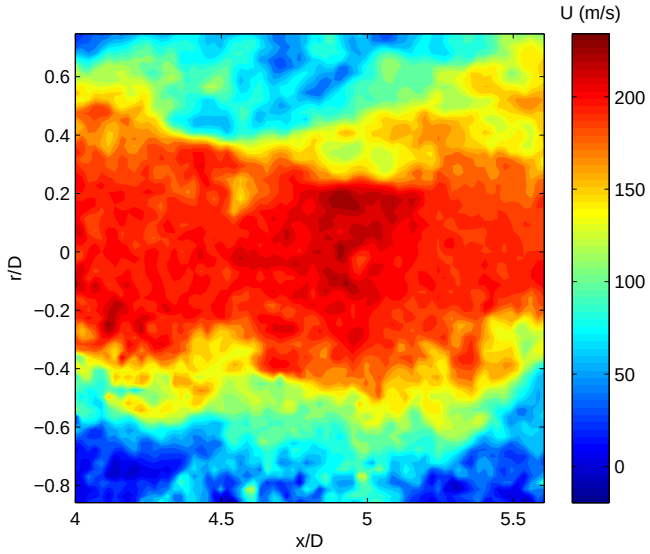

Figure D.14: Instantaneous snapshot of streamwise velocity contours for case *CLC1*

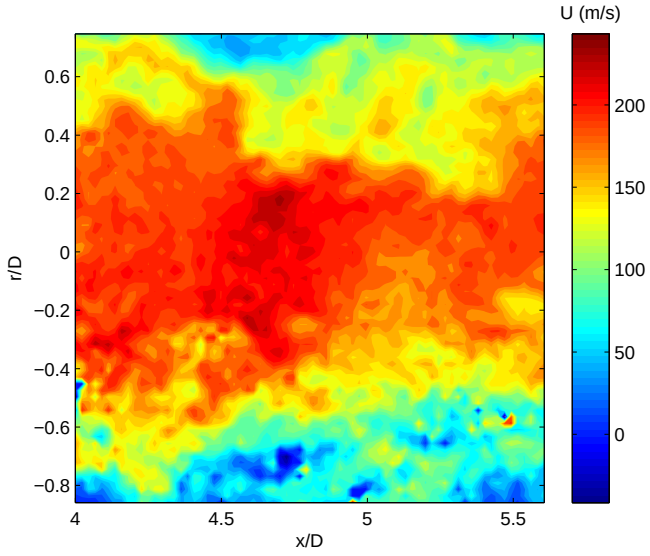

Figure D.15: Instantaneous snapshot of streamwise velocity contours for case *CLC2*

D.5 POD Spatial Eigenfunctions

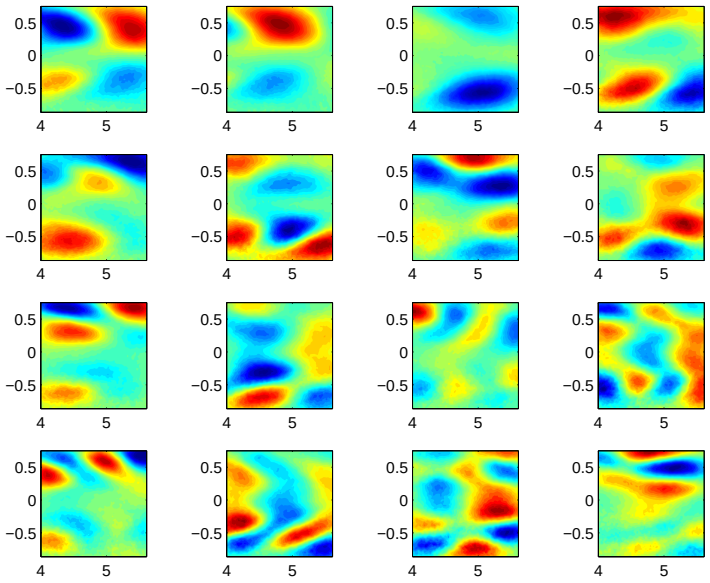

Figure D.16: First 16 spatial eigenfunctions, $\phi_u^{(n)}(\vec{x})$ for TRPIV (OLC1): abscissa $= x/D$, ordinate $= r/D$

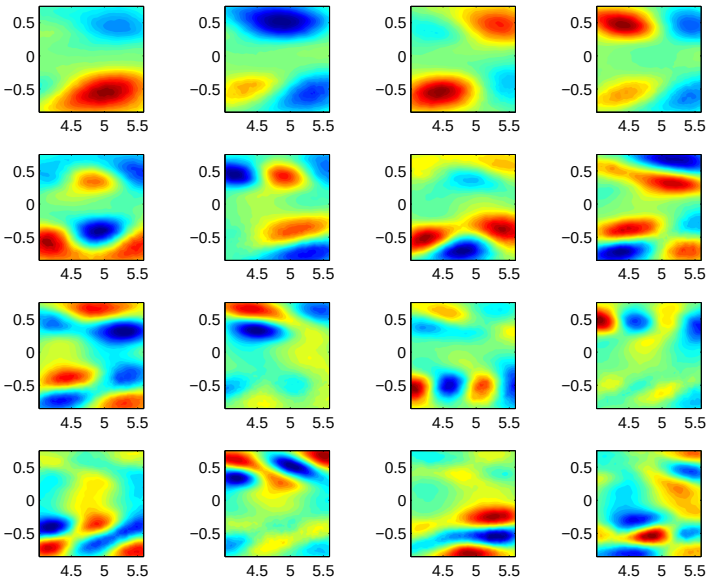

Figure D.17: First 16 spatial eigenfunctions, $\phi_u^{(n)}(\vec{x})$ for TRPIV (OLC2): abscissa $= x/D$, ordinate $= r/D$

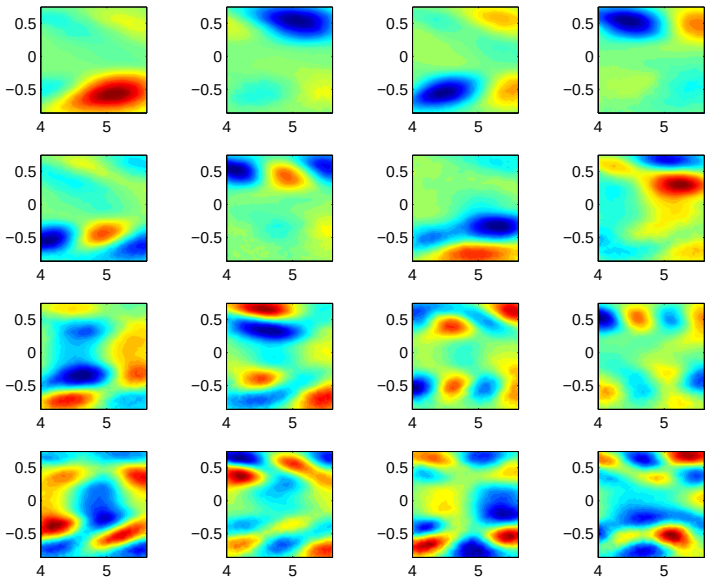

Figure D.18: First 16 spatial eigenfunctions, $\phi_u^{(n)}(\vec{x})$ for TRPIV (CLC1): abscissa $= x/D$, ordinate $= r/D$

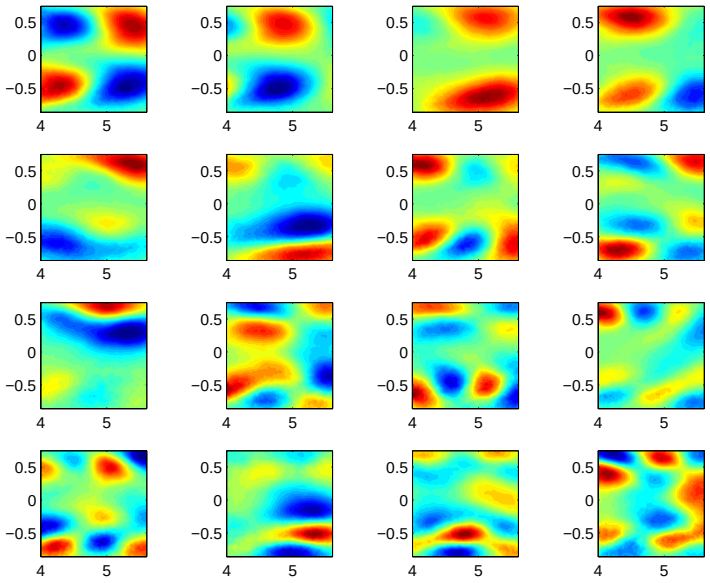

Figure D.19: First 16 spatial eigenfunctions, $\phi_u^{(n)}(\vec{x})$ for TRPIV (CLC2): abscissa $= x/D$, ordinate $= r/D$

D.6 OID Control: Coefficients of Linear Mapping Matrix

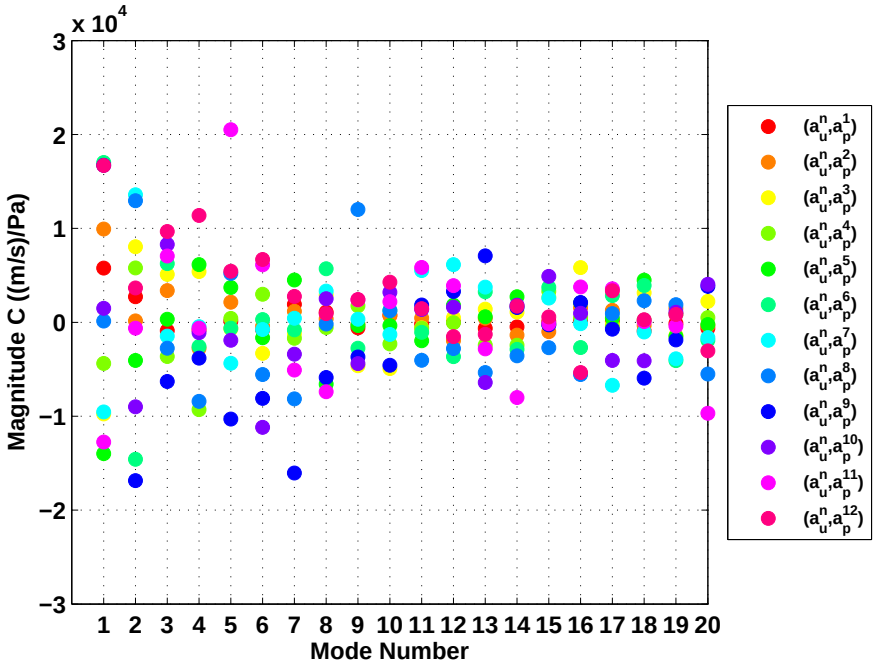

Figure D.20: Coefficients of the linear mapping matrix for the OID: *OLC1*

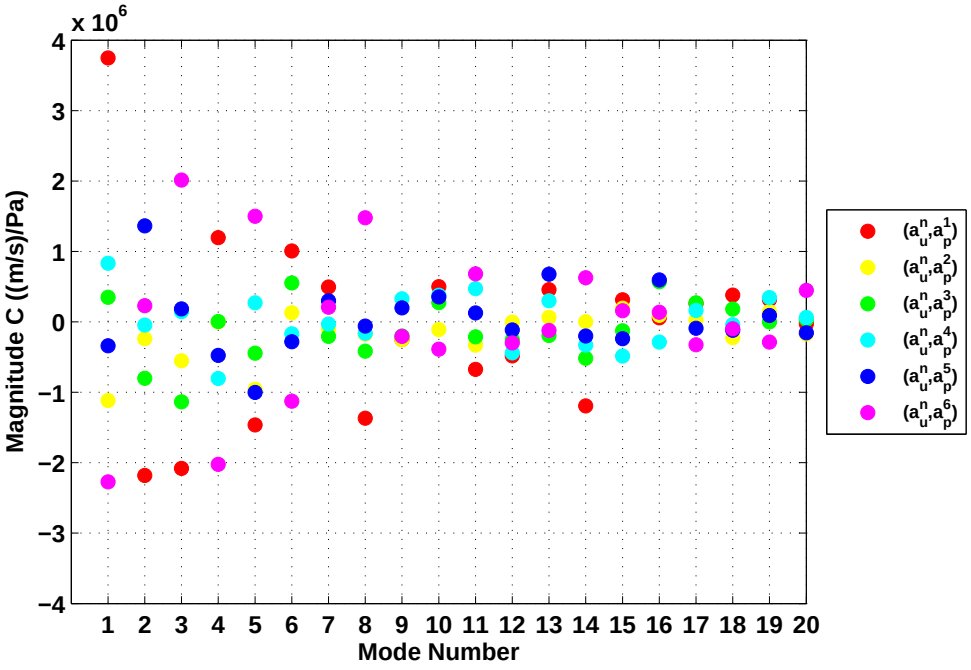

Figure D.21: Coefficients of the linear mapping matrix for the OID: *OLC2*

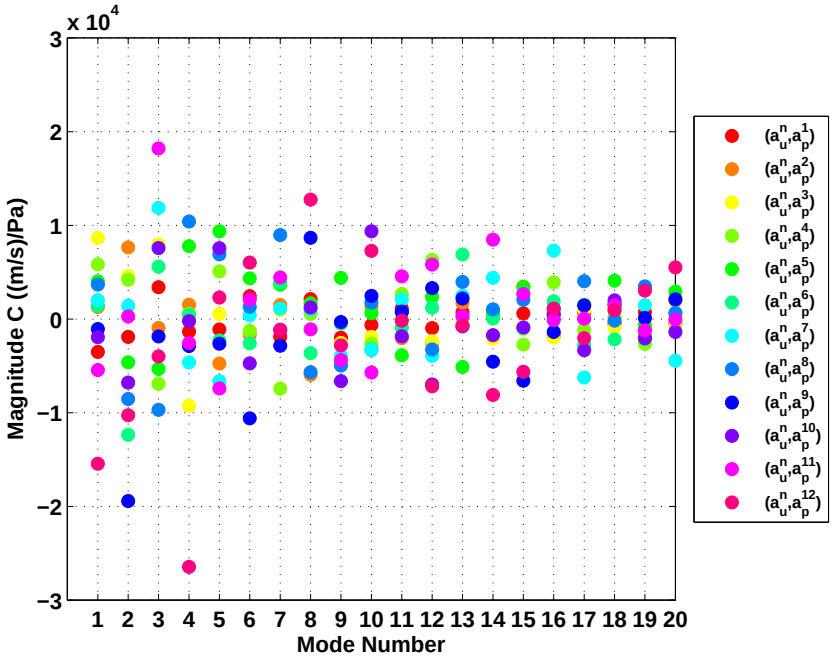

Figure D.22: Coefficients of the linear mapping matrix for the OID: *CLC1*

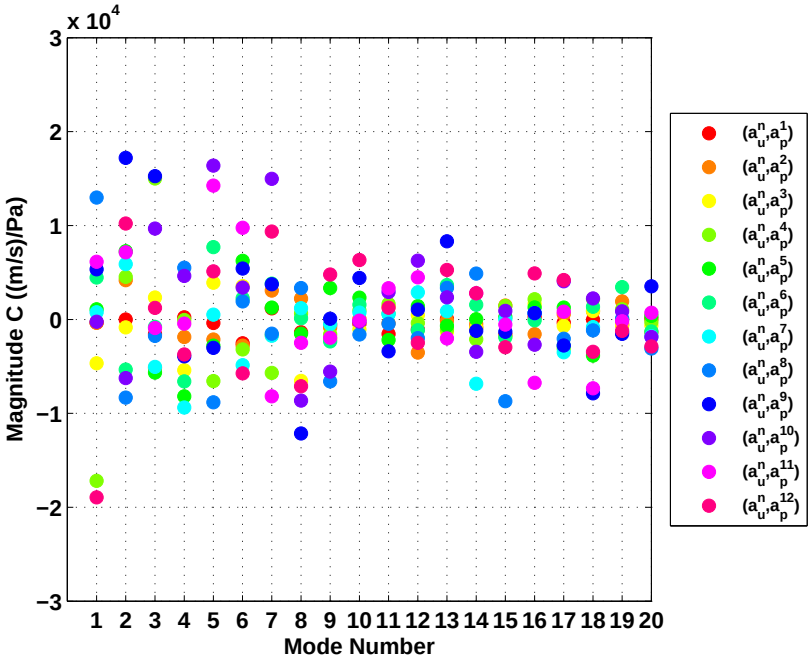

Figure D.23: Coefficients of the linear mapping matrix for the OID: *CLC2*

Appendix E

Submission for review to the *Journal of Flow Turbulence and Combustion*

Noname manuscript No.
(will be inserted by the editor)

Active Flow Control for High Speed Jets with Large Window PIV

Zachary P. Berger · Patrick R. Shea · Matthew G. Berry · Bernd R. Noack · Sivaram Gogineni · Mark N. Glauser

Received: date / Accepted: date

Abstract The current work investigates a Mach 0.6 jet flow field with particle image velocimetry (PIV) and simultaneously sampled near and far-field pressure. Two component velocity measurements are taken in the streamwise plane of the jet. Three cameras are placed such that each interrogation window is captured simultaneously and stitched together to obtain a six diameter PIV window. In addition, active flow control is applied using an actuation glove comprised of synthetic jet actuators. Both open and closed-loop control are applied in different physical forcing configurations. For closed-loop control, hydrodynamic pressure from the near-field array of sensors is fed back to the actuation system in real time. The large window PIV allows one to examine how the flow field is affected by the flow control. Low-dimensional modeling techniques, in the form of proper orthogonal decomposition, are performed in order to obtain a better understanding of the large scale, energetic events in the flow field. It has been found that active flow control changes the potential core length and shear layer expansion, which affects the overall sound pressure levels in the far-field.

Keywords Jet Noise · Aeroacoustics · Active Flow Control · Particle Image Velocimetry · Reduced-Order Modeling

Z.P. Berger (✉) , P.R. Shea, M.G. Berry, M.N. Glauser
Syracuse University, Syracuse, NY 13244 USA
E-mail: zpberger@syr.edu

P.R. Shea
E-mail: prshea@syr.edu

M.G. Berry
E-mail: mgberry@syr.edu

M.N. Glauser
E-mail: mglauser@syr.edu

B.R. Noack
Institute PPRIME, Poitiers, F-86036 Cedex, France
E-mail: bernd.noack@uni-poitiers.fr

S. Gogineni
Spectral Energies, LLC., Dayton, OH 45431 USA
E-mail: sgogineni@spectralenergies.com

1 Introduction

In recent years, the aerospace community has invested an increasingly large amount of time and resources into research focusing on the jet noise problem. For commercial applications, environmental pollution and increasing amounts of air traffic make jet noise reduction a high priority. From the military perspective, tactical maneuvers and the hearing loss experienced by aircraft carrier flight deck crews motivate an increased interest in the jet noise problem. Moreover, due to increasingly stringent noise regulations on aircraft in both the private and commercial sectors, jet noise research is more important than ever. The International Civil Aviation Organization (ICAO) is not only calling for quieter aircraft, but according to Viswanathan & Pilon [56], the studies should focus on gaining insight into noise source mechanisms and low-noise designs. The turbulence community continues to be at the forefront of these studies, focusing on noise source identification and far-field acoustic noise suppression.

The nonlinear mechanisms associated with noise source generation are still not completely understood in the context of jet noise. From a general perspective, noise generation is created by the turbulent entrainment of ambient fluid as it interacts with the exhausted jet plume. This is a result of the instabilities created at the nozzle lip, which then lead to vortex interactions evolving downstream. These vortex interactions give rise to large pressure fluctuations in the near-field. This then leads to large acoustic signatures in the far-field (Tinney [52]). Also, it has been shown by Hall and Glauser [20] and Seiner [44] that the coherent structures just beyond the collapse of the potential core provide the strongest contributions to the far-field noise. In addition, it has been shown that large scale, low frequency structures tend to propagate towards the shallow polar angles with respect to the jet axis. The small scale, high frequency structures tend to propagate radially towards the steep polar angles. This is known as F and G-spectrum, respectively, as outlined by Mollo-Christensen *et al.* [36] and Tam and Chen [50].

The study of coherent structures in turbulent flows has been studied extensively by Crow and Champagne [12], Brown and Roshko [8] and Winant and Browand [57]. Lumley was among the first to develop a low-dimensional approximation of a flow field in order to extract coherent structures based on the turbulent kinetic energy [34]. The approach is commonly known as proper orthogonal decomposition (POD) and has been studied extensively within the turbulence community. Glauser and George conducted some of the first studies applying the POD to free shear flows ([17,18,16,15]). Glauser *et al.* concluded that a large portion of the overall energy of the system could be represented with only a small number of POD eigenfunctions. This work combined with the continued efforts of Citriniti and George [10] concluded that azimuthal modes 0, 3, 4, 5 and 6 can rebuild an accurate representation of the coherent structures dynamics, for the axisymmetric jet. Citriniti and George also found that sreamwise vortex pairs generated as a result of the potential core collapse are response for the intensity of the generated sound.

1.1 Flow Control Methods for Jet Noise Reduction

Previous studies have shown that the key to reducing jet noise lies in understanding the physics of the structures created in the region of the potential core collapse (Tinney *et al.* [53, 55]; Tam *et al.* [51]; Low *et al.* [32]). A deep understanding of how these noise producing events propagate to the far-field is paramount. To date, the strategy for reducing jet noise has been primarily focused on flow control. Flow control is a method of modifying flow

conditions based on a control objective, and is broken up into passive and active flow control. Active flow control consists of both open-loop and closed-loop methods.

Passive flow control is a form of flow control which involves a geometrical modification to a system to achieve the control objective. Passive flow control is an attractive flow control strategy with respect to jet noise, since it does not require any energy input to the system. Up to this point, the community has seen various passive flow control methods for jet noise suppression, typically in the form of chevrons (Brown and Bridges *et al.* [6,7]; Bridges and Brown *et al.* [5]; Callender *et al.* [9]; Mengle [35]). These triangular serrations around the jet exit greatly enhance mixing and shorten the potential core length, which has been shown to reduce far-field noise (Bargsten and Gibson [3]).

Chevrons have been shown to reduce noise in the low frequency band however they increase noise in the high frequency band. Moreover they are permanent and therefore are inefficient for military applications where flight conditions are continuously changing. In recent years, the focus has shifted to active flow control, which serves to modify the flow field using energy input to the system. The advantage of active control is that it is not permanent and can be turned on and off depending on the flow conditions. Open-loop flow control methods for jet noise reduction involve some sort of actuator or fluidic injection at the nozzle lip. These methods act to enhance mixing, as with chevrons, however they can be adapted for different flow parameters. Fluid injection has been studied extensively by Alkislar *et al.* [1], Arakeri *et al.* [2], Henderson *et al.* [24,25,26] and Laurendeau *et al.* [29,28], among others. These microjets have been shown to reduce the noise by the same amount as chevrons but over a broader frequency range. There has also been a large interest in plasma actuators as studied primarily by the group at Ohio State (Fischer and Samimy [13]; Gaitonde and Samimy [14]; Samimy *et al.* [37,40,39,42,41,38]). These actuators allow for high frequency forcing and have been shown to reduce the far-field noise at 30° with respect to the jet axis, when actuating at frequencies on the order of Strouhal number between 1.5 and 2.0.

While open-loop control has its benefits, many researchers in the community believe that closed-loop control will provide the most promising results, drawing on intelligence from the system. By feeding back information from sensors in the flow field in real-time, the actuation system can then adjust the output based on the flow conditions. Closed-loop control applied to jet noise has recently been explored and compared to passive and open-loop methods. (Samimy *et al.* [41]; Laurendeau *et al.* [30]; Low *et al.* [33]; Sinha *et al.* [46, 47]). At Syracuse University, an actuation glove consisting of eight synthetic jet actuators (based on the designs of Glezer & Amitay [19] and Smith & Glezer [49]), is placed on the jet nozzle in order to provide a shear layer excitation. Both open and closed-loop flow control will be investigated throughout the course of this paper.

1.2 Motivation for Large-Window PIV

The motivation for this work stems from a large time-resolved particle image velocimetry (TRPIV) data set collected in 2011 at Syracuse University (Low *et al.* [31]). During this set of experiments, 10 kHz time-resolved PIV measurements were collected simultaneously with near and far-field pressure on the uncontrolled jet at various Mach numbers. The two-component streamwise windows for these experiments were approximately 1.5 jet diameters (D) in each direction. Low-dimensional modeling in the form of (POD) was implemented to extract “loud” modes in the flow by correlating the time-dependent POD coefficients with the far-field acoustics. Windowing effects from the TRPIV experiments led to the interest

in a larger view of the flow-field and thus a large window PIV data set was collected. The effects of control were also of interest and thus a six diameter PIV window was obtained with open and closed-loop flow control for a Mach 0.6 jet. The focus was kept on Mach 0.6 for these studies due to the control authority of the actuation system.

2 Experimental Setup

Experiments were conducted in the Syracuse University anechoic chamber on the Skytop campus. The facility is constructed from 12 inch thick reinforced single poured concrete. The anechoic chamber housing the jet facility is 206 m^3 and is lined with fiberglass wedges having a cutoff frequency of 150 Hz. The chamber houses an axisymmetric matched 5^{th} order polynomial nozzle with a diameter of 2 inches (50.8 mm) as described by Tinney *et al.* [54]. The anechoic chamber can be seen in Figure 1.

Fig. 1 Syracuse University Anechoic Chamber

2.1 Near-field pressure

For hydrodynamic pressure measurements in the near-field, two azimuthal arrays of high temperature *Kulite* pressure transducers are used (XCE-093-5G), each consisting of five sensors located at x/D = 6 and 8. These transducers operate in gauge mode and the reference tube is open to the ambient chamber pressure. The *Kulites* have a range of 0 to 5 psi with a full scale output of 100 mV. They also have a flat frequency response out to 20 kHz. The diaphragm is 2.36 mm corresponding to a maximum frequency resolution of approximately 70 kHz. All sensors are placed 1 cm outside of the expanding shear layer to measure the hydrodynamic pressure. The placement of the two arrays is motivated by the desire to sample the pressure at different points during collapse of the potential core. The azimuthal array of sensors at x/D = 6 are used for feedback in the closed-loop control, which will be elaborated upon in later sections.

2.2 Far-field acoustics

For far-field acoustic sensing, twelve $\frac{1}{4}$ inch pre-polarized free-field condenser G.R.A.S. microphones (Type 40BE) are used in two arrays. The microphones have a flat frequency

response out to 5 kHz for 0° incidence. The first six microphones are in the plane of the jet and the second array is offset by 15° out of plane with respect to the jet. For each array, the microphones are spaced evenly from 15° to 90° (in 15° increments) with respect to the jet axis, in the polar direction. All microphones are located 75D away from the nozzle lip. This configuration for the near and far-field pressure arrays can be seen in Figure 2.

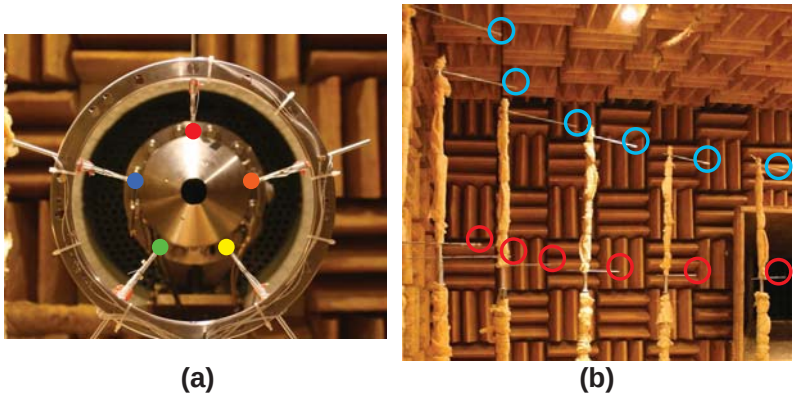

Fig. 2 (a) Near-Field Pressure Sensors and (b) Far-Field Microphones

2.3 Particle Image Velocimetry System

A Dantec Dynamics PIV system was used to take ensemble averaged velocity field measurements along the center plane of the jet. The PIV system consisted of three 12-bit, 1.2 megapixel HiSense cameras, a New Wave Gemini Nd:YAG laser with a peak output of 200 mJ/pulse, and a Laskin nozzle with olive oil as the working fluid for flow seeding. The large window PIV (LWPIV) system had a maximum acquisition rate of 4 Hz, and two-component measurements were taken in the streamwise plane with the three cameras arranged with slightly overlapping viewing fields to obtain a larger sample region along the center plane of the jet. The large window velocity field data presented in what follows are assembled from the three simultaneously sampled inspection regions. Images were processed using an adaptive, multi-pass processing configuration. The combined inspection region had a height of approximately 1.6 diameters in the r direction (centered along the jet axis) and spanned from x/D of approximately 3.2 to 9.0. The PIV setup can be seen in Figure 3.

A PIVTEC twelve Laskin nozzle seeder was used to seed the bulk flow of the jet. The device uses olive oil as the medium to aerosolize particles with a diameter on the order of 1 μm. The particle size has been shown by Melling [11] to be optimal for laser-based measurements at these flow conditions. For the co-flow seeding, a glycol-based commercial show-fogging machine was used to provide a uniform distribution of particles from the entrainment to the bulk flow of the jet.

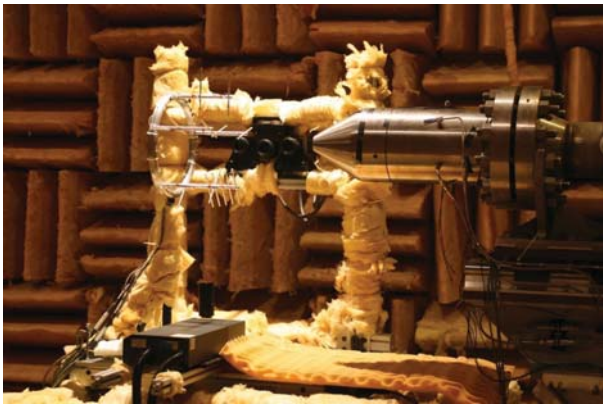

Fig. 3 Large Window PIV Setup

3 Active Flow Control System

For active flow control, an actuation glove comprised of a circular array of eight synthetic jet actuators has been designed and optimized. Synthetic jet actuators operate on the principle of unsteady ingestion and expulsion of a working fluid in the jet's cavity. In this particular configuration, a piezoelectrically driven membrane acts as a zero-net mass-flux actuator driven by a sinusoidal input function. Synthetic jets are an appealing form of actuation because no external air supply is needed. Moreover, their high frequency response (up to 2 kHz) makes them more versatile than steady blowing or suction forms of actuation. More information on the investigation of synthetic jet actuators can be found in the work of Low *et al.* [31].

For shear layer excitation, the actuation glove was placed directly on the nozzle and has been optimized to output azimuthally unsteady velocity fluctuations. Hot-wire measurements have been taken at the exit of the synthetic jet orifice and have shown the actuators are capable of producing velocities on the order of 30-80 m/s. These velocities are sufficient to disturb the developing shear layer, changing the potential core length in open and closed-loop configurations. With the actuation glove being placed directly on the nozzle, the eight individual slots are located 0.6 mm from the lip of the nozzle. The actuators are evenly distributed azimuthally such that a uniform actuation is provided at the nozzle exit. The actuation glove was designed such that the synthetic jets inject flow into the bulk flow at a 45° angle. The current design is a 3^{rd} generation model which allows for each actuator to be controlled independently for high model forcing. The actuation glove can be seen in Figure 4, and further information regarding the actuation system is outline in Low *et al.* [31].

3.1 Actuation Strategies

In the current investigation, each near-field pressure array contains five sensors and thus only spatial Fourier modes 0, 1 and 2 can be sampled to avoid spatial aliasing. For the studies presented here, the focus will be on modes 0 and 1. Four different control schemes, two open-loop and two-closed loop, are implemented to see the effects of the control on

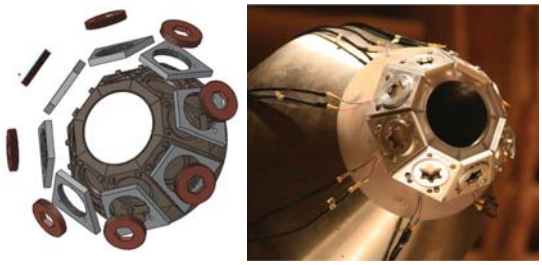

Fig. 4 Actuation Glove for Flow Control

the flow-field with a large window, as well as to see how control affects the far-field noise. There are two different types of physical forcing implemented for both open and closed-loop control. The first type of forcing is mode 0 in which all actuators are driven in phase to mimic the first spatial Fourier mode (column mode). The second type of forcing is mode 1 in which half of the actuators are driven 180° out of phase to mimic the second spatial Fourier mode (flapping mode). In this case, the actuators are broken up into two sets of four, half on the top and half on the bottom. This mode 1 forcing acts to create a flapping mode about the x-axis since the PIV planes are in the streamwise direction.

For feedback in the closed-loop control tests, spatially Fourier-filtered modes from the near-field azimuthal pressure array at x/D = 6 are used for amplitude modulation of the original signal, which is a 1200 Hz sine wave. This frequency is used because it is the preferred frequency of the synthetic jet actuators. For the first closed-loop scenario, Fourier-filtered mode 1 of the near-field pressure is fed back to drive a physically forced mode 0 (this will be known as M1 $\rightarrow$ M0). The second scenario used Fourier-filtered mode 0 of the near-field pressure to drive a physically forced mode 1 (this will be known as M0 $\rightarrow$ M1).

The reasons for choosing the two different closed-loop control strategies are inspired by the work of Hall *et al.* [23,22,21], who showed that the first two spatial Fourier modes of the near-field azimuthal pressure can almost completely rebuild the original unfiltered signal. Moreover, Hall *et al.* showed that Fourier mode 0 of the pressure correlates highly with the far-field, but Fourier mode 1 (and subsequently higher order modes) have a very weak correlation with the far-field. Therefore, the M1 $\rightarrow$ M0 closed-loop strategy seeks to break up the axisymmetric events, accounting for strong far-field correlations. Conversely, the M0 $\rightarrow$ M1 closed-loop strategy seeks to amplify the mode 1 structures. The idea here is to either excite the quiet mode or break up the loud mode in a feedback manner using information from the near-field pressure. The azimuthal array at x/D = 6 is chosen as this the region where the potential core collapses, accounting for the generation of many noise sources. More information on the low-dimensional nature of the near-field pressure can be found in Low *et al.* [31].

4 Reduced-Order Modeling

Reduced-order models are incredibly important in the fluid mechanics community especially when one is interested in extracting large scale, dominant flow structures of a complex flow field. When looking at the jet noise problem specifically, reduced-order modeling is essential due to increasingly large data sets and complex flow physics. In order to develop a

low-dimensional model of the flow field, POD is implemented. This technique seeks a set of basis functions maximizing the kinetic energy of the system using a spatial two-point correlation tensor in an integral eigenvalue problem. The problem is formulated via a constrained optimization problem, which organizes the resulting modes in terms of energy.

$$\begin{cases} max_{\psi} \frac{\langle |(u,\psi)|^2 \rangle}{(\psi,\psi)} = \frac{\langle |(u,\phi)|^2 \rangle}{(\phi,\phi)} \\ (\phi,\phi)^2 = 1 \end{cases} \tag{1}$$

where $\langle . \rangle$ denotes an averaging operation and $|,|$ denotes the L^2 norm.

Later, Sirovich [48] proposed a simplification to the POD problem, which occurs when the number of grid points is greater than the number of snapshots. Computational time is a concern with PIV data sets in which the eigenvalue problem can be quite large and computationally expensive. In this modified snapshot POD approach, the problem becomes a temporal formulation instead of spatial and thus becomes more computationally manageable. Using the snapshot POD approach, the kernel used for solving the constrained optimization problem becomes a temporal formulation. There the problem reduces to the solution of the Fredholm integral eigenvalue problem:

$$\int_T C(t,t')a_n(t')dt' = \lambda^{(n)} a_n(t) \tag{2}$$

where T is the integration time, $a_n(t)$ is the temporal eigenfunction and $C(t,t')$ is the two-time correlation tensor which is defined by:

$$C(t,t') = \frac{1}{T} \int_{\mathscr{D}} \sum_{i=1}^{3} u_i(\mathbf{x},t) u_i(\mathbf{x},t') d\mathbf{x} \tag{3}$$

where $\mathscr{D}$ is the entire spatial domain. Snapshot POD yields similar properties to that of the classical formulation. The time-dependent POD coefficients must be scaled such that the norm is equal to that of its corresponding eigenvalue.

$$\langle a_m(t), a_n(t) \rangle = \lambda^{(m)} \delta_{mn} \tag{4}$$

where $\langle f,g \rangle = \frac{1}{T} \int_0^T f(t)g(t)dt$ denotes the inner product for functions of time. The spatial eigenfunctions $\phi_i^{(n)}(\mathbf{x})$ are therefore defined by:

$$\phi_i^{(n)}(\mathbf{x}) = \frac{1}{T\lambda^n} \int_T a_n(t) u_i(\mathbf{x},t) dt \tag{5}$$

With the spatial and temporal components of the flow known, the original random field can be fully reconstructed using Equation 6

$$u_i(\mathbf{x},t) = \sum_{n=1}^{N} a_n(t) \phi_i^{(n)}(\mathbf{x}) \tag{6}$$

The summation over all of the eigenvalues, $\lambda^{(n)}$, accounts for the total turbulent kinetic energy (TKE) of the system. Therefore, when reconstructing the flow field, it is common practice to select a number modes that contain a certain amount of overall energy in the system. When building up low-dimensional models, the goal is to use as few modes as possible to retain as much energy as possible. Moreover, for control purposes, it also of

interest to study the individual energy contributions from each POD mode. The individual contribution of each POD mode to the overall TKE is defined by:

$$\Lambda^{(n)} = \frac{\lambda^{(n)}}{K} X100 \tag{7}$$

where K is the fluctuation level (twice the TKE), defined in the following equation:

$$K = \sum_{n=1}^{N_{POD}} \lambda^{(n)} \tag{8}$$

The first two spatial eigenfunctions will be examined in subsequent sections to see the effects of control on the dominant, large scale structures in the flow field, as the jet develops downstream.

5 Results

The following section will be broken up into four main parts: the large window PIV results, the near-field pressure spectra, a POD analysis, and finally the overall sound pressure levels (OASPL) in the far-field. Unless otherwise specified, whenever open and closed-loop results are discussed in this section, it will refer to a mode 1 physical forcing. Therefore for the closed-loop case, this means M0 $\rightarrow$ M1. The mode 1 forcing is chosen for the analysis since the effects of the control can easily be seen in the PIV window. For the last part of the section, pertaining to the OASPL, all control cases are compared to the baseline (uncontrolled) jet.

5.1 Large Window PIV

For the PIV acquisition, three cameras were placed side by side to acquire three independent windows, each spanning approximately two diameters in the streamwise direction. In order to create one large window from these three separate images, the windows needed to be stitched together during post-processing using algorithms generated at Syracuse University. The stitching process was performed in three main steps: *1.)* the identification of the optimal offset locations for the inspection regions, *2.)* determination of adjusted scale factors, and *3.)* merging of the data sets using a weighted average in the region of the overlap. The stitching is performed by interpolating the images onto a large grid using a weighted average scheme. This method is described in further detail by Shea *et al.* [45]. An example of the resulting large window PIV image for the baseline case can be seen in Figure 5. The blanked regions at six and eight diameters in the window are shadows from the azimuthal array of *Kulites*. These sensors are out of the PIV plane but show up in the images and are therefore blanked out for purposes of the POD analysis.

5.1.1 Mean Velocity Flow Field

In order to see the effects of the control on the flow-field, the mean flow for the different cases is observed in Figure 6. The plots show the mean streamwise velocity contours for the baseline and two control cases. In the uncontrolled jet, the potential core collapses just before 8D, whereas for the open-loop and closed-loop cases, the potential core is shortened to about 6D and 6.5D, respectively.

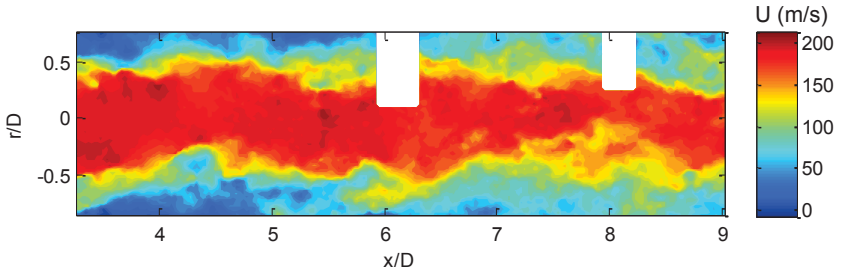

Fig. 5 Large Window PIV Baseline Snapshot

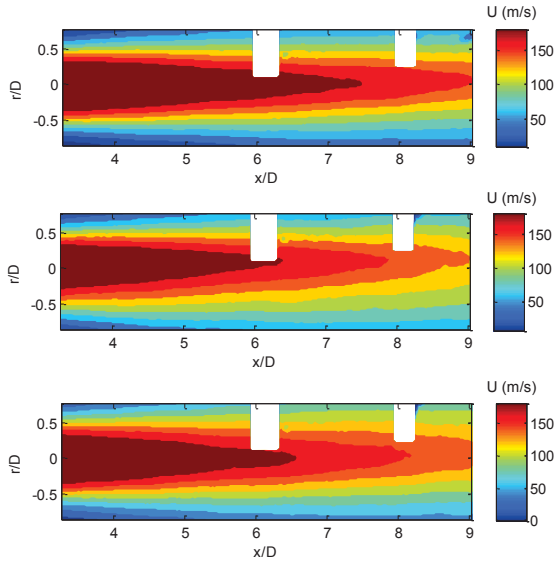

Fig. 6 Streamwise Velocity Contours of Mean Flow: Baseline (top), Open-Loop (center), Closed-Loop (bottom)

The effects of the control can also be seen by taking velocity profiles at multiple downstream locations for the different cases. As can be seen in Figure 7, the streamwise velocity is reduced in the potential core region indicating a shift in the potential core length. In addition at x/D = 7, it can be seen that the shear layer expands as a result of the control, as seen by the increased velocity in the shear layers.

This shows that with the current control schemes, the potential core length has been significantly reduced. Though the two control cases seen here seem to have a similar effect on the flow field, a control strategy which requires less energy input to the system is desired. By looking at the RMS of the actuation input signals, the closed-loop control requires less energy input to the system, having an RMS value of 2.75 volts as compared to 3.08 volts for the open-loop. Moreover, the closed-loop control draws on intelligence from the system, continuously sampling the near-field pressure in real-time and feeding back this information.

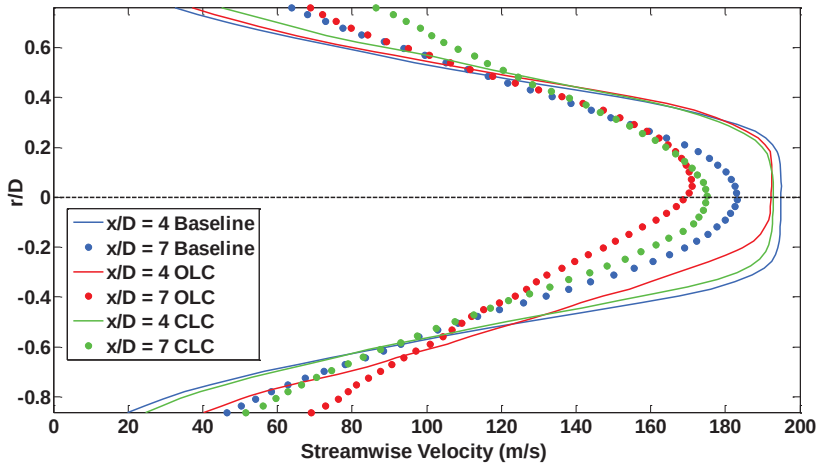

Fig. 7 Streamwise Velocity Profiles for Two Downstream Locations

Therefore closed-loop control is a more desirable form of flow control than open-loop in this particular case.

In the open-loop case, one might notice a slight vectoring of the jet in the upwards direction (see Figure 7). The reason for this vectoring is still being investigated however one explanation is that the driving of the actuators induces an initial condition which causes a slight vectoring of the jet in the open-loop case. It is possible that this wouldn't be seen in the closed-loop case since the feedback allows for the control system to turn on and off. Once again, these concepts are being investigated but at this point the actuation input is thought to be the cause of vectoring in the open-loop case.

5.2 Near-Field Pressure Spectra

The collapse of the potential core at approximately six and eight diameters for the control and baseline, respectively, motivates the investigation of the near-field pressure at these locations. For comparisons, the near-field pressure spectra at x/D = 8 for the baseline and x/D = 6 for the closed-loop control are shown in Figure 8. The arrangement of the *Kulites* with respect to the jet can be seen in Figure 2(a), corresponding to the colors in Figure 8. Similar trends are observed for the two cases and the sensors all collapse quite well indicating that the jet is axisymmetric both with and without control. For the baseline case, the array is just beyond the collapse and therefore there is a slight amplitude shift in some of the sensors. For the closed-loop case, the dominant frequency is preserved however there is a noticeable increase in overall energy. This is not only attributed to the fact that these sensors are closer to the jet exit, but also the control has increased the spreading rate of the jet, accounting for the additional energy increase seen by the sensors. Despite the fact that a mode 1 physical forcing is applied, the feedback of Fourier mode 0 keeps the flow relatively axisymmetric across the entire frequency band.

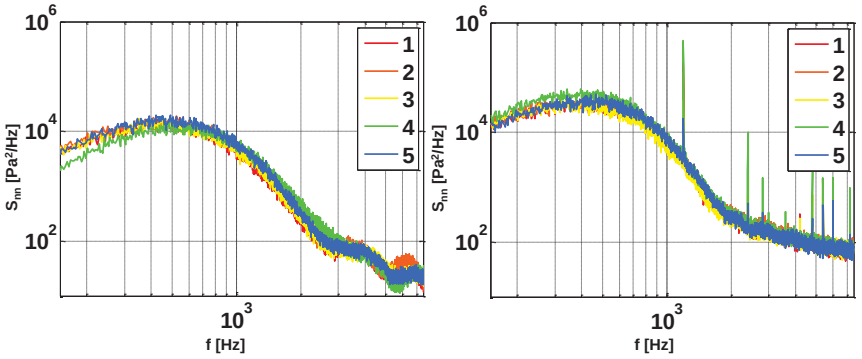

Fig. 8 Near-Field Azimuthal Pressure Spectra: Baseline, x/D = 8 (Left), Closed-Loop, x/D = 6 (Right)

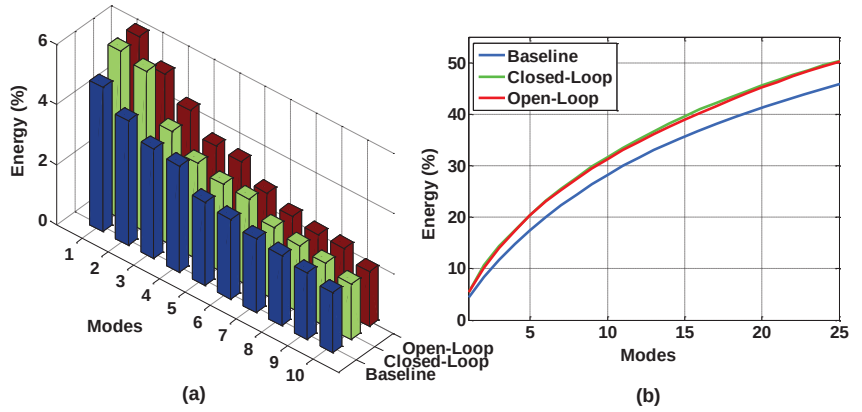

Fig. 9 (a) Energy distribution of the POD Modes and (b) Cumulative energy over expansion order for baseline, open-loop and closed-loop control

5.3 POD Analysis

Performing the POD analysis on this data set provides information about the low-dimensional, highly energetic structures in a large region of the flow field where the flow physics change dramatically. From the POD, it is found that there is a favorable convergence rate of the eignenvalues, as approximately 50% of the total kinetic energy is recovered with 25 modes (out of a total 300 modes for the control cases and 500 modes for the baseline). In addition, the analysis shows that none of the individual modes contain more than 6% of the total kinetic energy. The distribution of the energy in first 10 modes as well as the total kinetic energy contribution from the first 25 modes is shown in Figure 9.

The first two spatial eigenfunctions in the streamwise direction, $\phi_u^{(n)}(\mathbf{x})$, for the baseline and closed-loop control cases are shown in Figure 10. These two modes are the highest in energy and are the fundamental building blocks of the flow field. For the baseline flow, the development of large scale vortices can be seen along the shear layer beginning near the collapse of the potential core. In the closed-loop configuration, small scale vortices can be

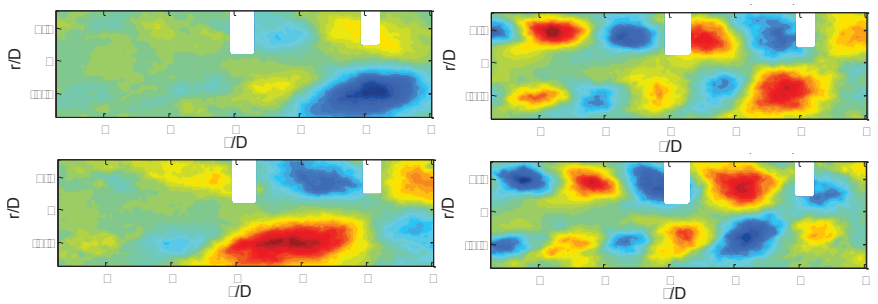

Fig. 10 Spatial POD Modes: Mode 1 (top), Mode 2 (bottom); Baseline (left), Closed-Loop (right)

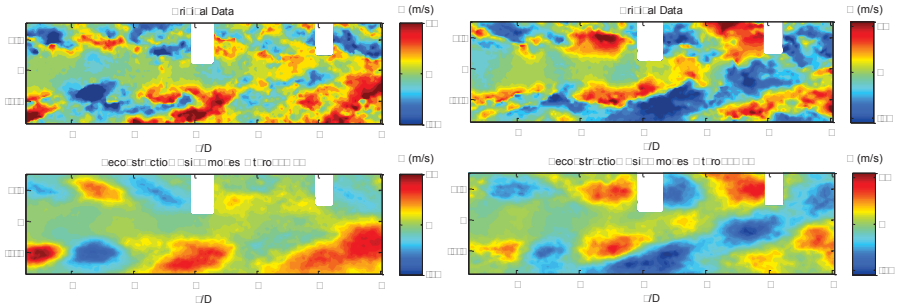

Fig. 11 Fluctuating Velocity Reconstructions: Baseline (Left), Closed-Loop (Right); ordinate: r/D

seen along the shear layer across the entire PIV window. In addition, the mode 1 forcing can be observed by the opposite phase of the structures seen in the top and bottom shear layers. Beyond the collapse of the potential core the structures grow and become less organized due to the interaction of the vortices caused by the collapse. Interestingly enough, the mode 1 forcing with feedback from Fourier mode 0, keeps the flow organized and greatly enhances the overall mixing in the shear layer.

Using a select number of POD modes, the velocity field can be reconstructed as shown in Figure 11. The baseline is shown on the left and the closed-loop on the right. The top plot shows the fluctuating velocity contours in the streamwise direction. The bottom plot shows the 25 mode reconstruction, which accounts for approximately 50% of the total kinetic energy. As can be seen in both the baseline and closed-loop cases, the large scale structures are represented accurately with the reconstruction. From these plots, it can be seen that the closed-loop control keeps the flow organized before the collapse, as observed in the reconstructions. The mode 1 forcing causes the potential core to collapse sooner, evident in even a single snapshot. The advantage to the large window PIV is that it allows one to examine the flow structures before and after the collapse of the potential core, while reducing the windowing effects (which can be problematic in standard-sized PIV windows).

5.4 Far-Field Sound Pressure Levels

In order to quantify differences in sound pressure level for the various control cases, a directivity plot of the far-field microphones is presented. This plot shows the change in overall sound pressure level at each of the far-field microphones with respect to the baseline (uncontrolled) jet. The sound pressure level (SPL) in the far-field is given by:

$$SPL = 10log_{10}\left(\frac{S_{ff}(f)}{(20*10^{-6})^2}\right) \tag{9}$$

where $S_{ff}(f)$ is the auto-spectra of each of the far-field microphones as defined in Bendat and Piersol [4]. The value in the denominator of equation 9 is the reference pressure measured in Pascals. The uncertainty of the overall sound pressure level is approximately $\pm$ 1 dB with a repeatability of $\pm$ 0.2 dB based on the measurements, consistent with the work of Laurendeau *et al.* [30]. Presented here are the directivity plots for both arrays of far-field microphones. Figure 12 shows that there is an increase in the OASPL for all control cases. However this also indicates that control authority over the jet has been achieved. Moreover, the different control cases seem to exhibit a directivity effect which is to be expected, as different forcing and feedback mechanisms are provided for the control input. The increased streamwise vorticity created as a result on the actuation increases the high frequency noise, seen at the steep polar angles. The various types of forcing applied tend to enhance mixing and therefore change the structures being propagated to the far-field due to a shift in the potential core length and growth of the shear layer.

Focusing on the microphone at 15 degrees where the sound pressure level is largest, it can be seen that the closed-loop control case in which Fourier mode 0 is fed back to physically force mode 1, is the closest to the baseline. At this microphone, the closed-loop control resulted in a 1.5 % increase in the OASPL. In addition, an open-loop forcing of mode 1 seems to be the loudest control case at this particular microphone, resulting in a 2.2 % increase in the OASPL. As was observed from the mean velocity field and POD analysis, with active flow control (both open and closed-loop), the potential core length has been significantly shortened and a slight increase in the shear layer expansion is also observed. Subtle changes between the open and closed-loop control can be accounted for by the feedback mechanism present in the closed-loop case. These subtle changes clearly result in slight differences in the overall sound pressure levels in the far-field and requires further investigation.

6 Conclusions

Previous investigations into the jet flow field using standard PIV techniques have shown limited analysis capabilities due to the small window sizes. Therefore, a PIV window stitching algorithm has been developed and implemented at Syracuse University. Here, the large PIV window comprised of approximately six jet diameters in the streamwise direction has been presented and analyzed to help gain insight into the flow structures being created as a result of the potential core collapse. In addition, simultaneous near and far-field pressure measurements were acquired with both open and closed-loop flow control. Mean velocity contour profiles indicate that the potential core of the jet has been significantly shortened using active flow control. Moreover, since the closed-loop control uses less input energy and draws on intelligence from the flow field, this becomes a more desirable control option than

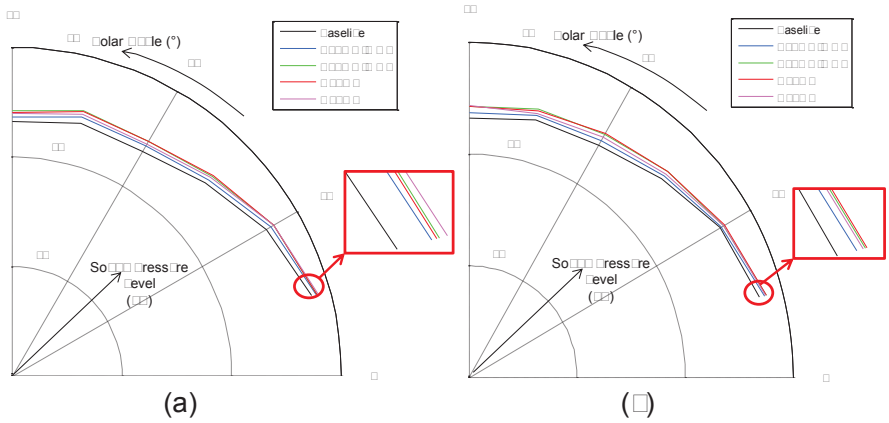

Fig. 12 Sound Pressure Level Directivity for (a) In-plane and (b) Out-of-plane Microphones

open-loop, for jet noise applications. This is further validated by the fact that the closed-loop control case has a lower overall sound pressure level in the far-field across all of the microphones, as compared to the open-loop case. The POD analysis shows that a large amount of the total energy of the system can be recovered with a small number of modes. Looking at the first two POD modes indicates that the closed-loop control keeps the flow organized until the collapse of the potential core. The result of the mode 1 forcing, as a shear layer excitation, can clearly be observed as the small streamwise vortices propagate downstream eventually resulting in the potential core collapse.

The results presented indicate that control authority has been achieved for the Mach 0.6 jet using active flow control in the form of synthetic jet actuators. This actuation system has been shown to shorten the potential core length by enhancing the mixing in the shear layers of the jet. This is seen in both mean flow and POD contours in the PIV window. The actuation induces an increased amount of streamwise vorticity which eventually leads to complex vortex interactions during the collapse of the potential core. This leads to a small increase in far-field noise at shallow polar angles and a slightly higher increase at steep polar angles. Moreover, the near-field pressure at six and eight diameters reveals that the jet remains relatively axisymmetric as a result of the flow control.

The open-loop flow control shortens the potential core length more than the closed-loop flow control. As the potential core length decreases, the OASPL increases across all far-field microphones. Therefore, it is possible that by organizing the flow to delay the collapse of the potential core, this may in turn reduce the far-field noise. The key is to gain a deeper understanding of the mechanisms responsible for the far-field noise and using this information in conjunction with closed-loop flow control. More advanced control algorithms coupled with novel reduced-order modeling techniques provide a viable framework for jet noise reduction strategies moving forward. With all of the toolkits described thus far for analyzing the flow field, a more mathematically rigorous method for defining low-dimensional flow structures that account for the far-field noise is desirable. A reduced-order modeling technique known as observable inferred decomposition (OID) has been used on previous data sets to identify "loud" modes in the flow field which greatly contribute to the far-field noise. The details of the OID can be found in the works of Jordan *et al.* [27] and Schlegel *et al.* [43]. The

technique forms a linear mapping between the low-dimensional velocity and pressure fields to identify the most acoustically observable modes in the flow field.

This reduced-order modeling technique along with the observations from the control presented here, should provide the necessary tools for designing a more effective controller for far-field jet noise reduction. Since control authority over the flow field has been demonstrated and "loud" modes in the flow have been identified (Low *et al.* [31]), the key is to now gain a deeper understanding of the flow physics related to the noise producing events in the flow.

Acknowledgements

The authors would like to acknowledge Spectral Energies, LLC. Phase II SBIR, with AFRL, Dr. Barry V. Kiel as project monitor, for the ongoing support and interactions throughout these research endeavors. The authors also acknowledge Dr. Jacques Lewalle, Pingqing Kan and Christopher Ruscher (Syracuse University) for many insightful discussions throughout the experiments and analysis. The authors acknowledge the funding and excellent working conditions of the Chair of Excellence 'Closed-loop control of turbulent shear flows using reduced-order models' (TUCOROM) supported by the French Agence Nationale de la Recherche (ANR) and hosted by Institute PPRIME.

References

1. Alkislar, M., Krothapalli, A., Butler, G.W.: The effect of streamwise vortices on the aeroacoustics of a mach 0.9 jet. Journal of Fluid Mechanics **578**, 139–169 (2007)
2. Arakeri V. H. amd Krothapalli, A., Siddavaram, V., Alkislar, M.B., Lourenco, L.: On the use of microjets to suppress turbulence in a mach 0.9 axisymmetric jet. Journal of Fluid Mechanics **490**, 75–98 (2003)
3. Bargsten, C., Gibson, M.T.: Nasa innovation in aeronautics: Select technologies that have shaped modern aviation (the chevron nozzle: A novel approach to reducing jet noise). NASA/TM (216987) (2011)
4. Bendat, J.S., Pierson, A.G.: Engineering applications of correlation and spectral analysis (1980)
5. Bridges, J., Brown, C.A.: Parametric testing of chevrons on single flow hot jets. NASA/TMŮ213107 (2004)
6. Brown, C., Bridges, J.: An analysis of model scale data transformation to full scale flight using chevron nozzles. NASA/TM (212732) (2003)
7. Brown, C.A., Bridges, J.: Acoustic efficiency of azimuthal modes in jet noise using chevron nozzles. 12th AIAA/CEAS Aeroacoustics Conference (27th AIAA Aeroacoustics Conference) (2645) (2006)
8. Brown, G.L., Roshko, A.: On density effects and large structure in turbulent mixing layers. Journal of Fluid Mechanics **64**(04), 775–816 (1974)
9. Callender, B., Gutmark, E., Martens, S.: Far-field acoustic investigation into chevron nozzle mechanisms and trends. American Institute of Aeronautics and Astronautics Journal **43**(01), 87–Ű95 (2005)
10. Citriniti, J.H., George, W.K.: Reconstruction of the global velocity field in the axisymmetric mixing layer utilizing the proper orthogonal decomposition. Journal of Fluid Mechanics **418**(01), 137–Ű166 (2000)
11. College, M.: Tracer particles and seeding for particle image velocimetry. Measurement Science and Technology **8**(12) (1997)
12. Crow, S.C., Champagne, F.H.: Orderly structure in jet turbulence. Journal of Fluid Mechanics **48**(03), 547–591 (1971)
13. Fischer, M.K., Samimy, M.: Noise control of a high reynolds number mach 1.3 heated jet using plasma actuators. 48th AIAA Aerospace Sciences Meeting Including the New Horizons Forum and Aerospace Exposition (0013) (2010)
14. Gaitonde, D.V., Samimy, M.: Effect of plasma-based azimuthal mode excitation on supersonic jet flow. 5th Flow Control Conference (4416) (2010)

15. Glauser, M., George, W.: An orthogonal decomposition of the axisymmetric jet mixing layer utilizing cross-wire velocity measurements. Proceedings Sixth Symposium on Turbulent Shear Flows, Toulouse, France pp. 10.1.1–10.1.6. (1987)
16. Glauser, M., George, W.: Orthogonal decomposition of the axisymmetric jet mixing layer including azimuthal dependence. Advances in Turbulence, Spring-Verlag (Editors: G. Comte-Bellot and J. Mathieu) pp. 357–366 (1987c)
17. Glauser, M., Leib, S., George, W.: Coherent structures in the axisymmetric turbulent jet mixing layer. Turbulent Shear Flows 5, Springer-Verlag pp. 134–145 (1987a)
18. Glauser, M.N.: Coherent structures in the axisymmetric turbulent jet mixing layer. Ph.D. dissertation, Syracuse University (1987b)
19. Glezer, A., Amitay, M.: Synthetic jets. Annual Review of Fluid Mechanics **34** (2002)
20. Hall, A.M., Glauser, M.N.: An experimental analysis of the modal characteristics intrinsic to both the heated and cold jet. 47th AIAA Aerospace Sciences Meeting and Exhibit, Orlando, FL (2009-1238), 1–11 (2009)
21. Hall, J., Hall, A., Pinier, J., Glauser, M.: A cross-spectral analysis of the pressure in a mach 0.85 turbulent jet. AIAA Journal **47**(1) (2009)
22. Hall, J., Pinier, J., Hall, A., Glauser, M.: A spatio-temporal decomposition of the acoustic source in a mach 0.85 jet. 45th AIAA Aerospace Sciences Meeting and Exhibit (2007-442) (2007)
23. Hall, J.W., Pinier, J.T., Hall, A.M., Glauser, M.N.: Two-point correlations of the near and far-field pressure in a transonic jet. ASME Joint U.S. European Fluids Engineering Summer Meeting, Miami, FL (2006-98458), 1–7 (2006)
24. Henderson, B., Kinzie, K., Whitmire, J., Abeysinghe, A.: The impact of fluidic chevrons on jet noise. 11th AIAA/CEAS Aeroacoustics Conference (2888) (2005)
25. Henderson, B., Kinzie, K., Whitmire, J., Abeysinghe, A.: Aeroacoustic improvements to fluidic chevron nozzles. 12th AIAA/CEAS Aeroacoustics Conference (27th AIAA Aeroacoustics Conference) (2706) (2006)
26. Henderson, B., Norum, T.: Impact of azimuthally controlled fluidic chevrons on jet noise. 14th AIAA/CEAS Aeroacoustics Conference (29th AIAA Aeroacoustics Conference) (3062) (2008)
27. Jordan, P., Schlegel, M., Stalnov, O., Noack, B.R., Tinney, C.E.: Identifying noisy and quiet modes in a jet. 13th AIAA/CEAS Aeroacoustics Conference (28th AIAA Aeroacoustics Conference) (3602) (2007)
28. Laurendeau, E., Bonnet, J.P., Jordan, P., Delville, J.: Impact of fluidic chevrons on the turbulence structure of a subsonic jet. 3rd AIAA Flow Control Conference (3510) (2006)
29. Laurendeau, E., Jordan, P., Bonnet, J.P., Delville, J.: Turbulent jet noise control by fluid chevrons. Turbulence and Shear Flow Phenomena IV (2005)
30. Laurendeau, E., Jordan, P., Bonnet, J.P., Delville, J., Parnaudeau, P., Lamballais, E.: Subsonic jet noise reduction by fluidic control: The interaction region and the global effect. Physics of Fluids **20**(101519), 1–15 (2008)
31. Low, K., Berger, Z., Kostka, S., El Hadidi, B., Gogineni, S., Glauser, M.: A low-dimensional approach to closed-loop control of a mach 0.6 jet. Experiments in Fluids pp. 1–17 (2013)
32. Low, K.R., Berger, Z.P., Lewalle, J., El-Hadidi, B., N., G.M.: Correlations and wavelet based analysis of near-field and far-field pressure of a controlled high-speed jet. 41st AIAA Fluid Dynamics Conference and Exhibit (4020) (2011)
33. Low, K.R., El-Hadidi, B., Glauser, M.N., Andino, M.Y., Berdanier, R.: Investigation of different active flow control strategies for high speed jets using synthetic jet actuators. 40th Fluid Dynamics Conference and Exhibit (4267) (2010)
34. Lumley, J.L.: The structure of inhomogeneous turbulent flows. Atm. Turb. and Radio Wave Prop. ed. by A.M. Yaglom and V. I. Tatarsky, (Nauka, Moscow) pp. 166–178 (1967)
35. Mengle, V.G.: Jet noise characteristics of chevrons in internally mixed nozzles. 11th AIAA/CEAS Aeroacoustics Conference (2934) (2005)
36. Mollo-Christensen, E., Kolpin, M.A., Martuccelli, J.R.: Experiments on jet flows and jet noise far-field spectra and directivity patterns. Journal of Fluid Mechanics **18**(285), 285–301 (1964)
37. Samimy, M., Adamovich, I., Webb, B., Kastner, J., Hileman, J., Keshav, S., Palm, P.: Development and characterization of plasma actuators for high speed jet control. Experiments in Fluids **37**(04), 577–588 (2004)
38. Samimy, M., Fischer, M.K., Kim, J.H., Sinha, A.: High speed and high reynolds number jet control using arc filament plasma actuators for noise mitigation and for flow and noise diagnostics. 49th AIAA Aerospace Sciences Meeting including the New Horizons Forum and Aerospace Exposition (0022) (2011)
39. Samimy, M., Kim, J.H., Adamovich, I., Utkin, Y., Kastner, J.: Active control of high speed and high reynolds number free jet using plasma actuators. 44th AIAA Aerospace Sciences Meeting and Exhibit (0711) (2006)

40. Samimy, M., Kim, J.H., Adamovich, I., Utkin, Y., Keshav, S.: High speed jet control using plasma actuators. 4th International Symposium on Turbulence and Shear Flow Phenomena (2005)
41. Samimy, M., Kim, J.H., Fischer, M.K., Sinha, A.: Acoustic and flow fields of an excited high reynolds number axisymmetric supersonic jet. Journal of Fluid Mechanics **656**, 507–Ű529 (2010)
42. Samimy, M., Kim, J.H., Kastner, J., Adamovich, I., Utkin, Y.: Active control of a mach 0.9 jet for noise mitigation using plasma actuators. AIAA Journal **45**(04) (2007)
43. Schlegel, M., Noack, B.R., Jordan, P., Dillmann, A., Groschel, E., Schröder, W., Wei, M., Freund, J.B., Lehmann, O., Tadmor, G.: On least-order flow representations for aerodynamics and aeroacoustics. Journal of Fluid Mechanics **679**, 367–398 (2012)
44. Seiner, J.M.: A new rational approach to jet noise reduction. Theoretical and Computational Fluid Dynamics **10**(1-4), 373–383 (1998)
45. Shea P.R., B.Z.B.M.G.S.G.M.: Low-dimensional modeling of a mach 0.6 axisymmetric jet. 52^{nd} AIAA Aerospace Sciences Meeting (2014)
46. Sinha, A., Kim, K., Kim, J.H., Serrani, A., Samimy, M.: Extremizing feedback control of a high-speed and high reynolds number jet. AIAA Journal **48**(02) (2010)
47. Sinha, A., Serrani, A., Samimy, M.: Development of empirical estimators for feedback control of high-speed axisymmetric jets. AIAA Journal **49**(09) (2011)
48. Sirovich, L.: Turbulence and the dynamics of coherent structures, part i,ii, and iii. Quarterly Applied Mathematics **45** (1987)
49. Smith, B.L., Glezer, A.: The formation and evolution of synthetic jets. Physics of Fluids **10**, 2281–Ű2297 (1998)
50. Tam, C.K.W., Chen, P.: Turbulent mixing noise from supersonic jets. AIAA Journal **32**, 1774–1780 (1994)
51. Tam C.K., V.K.A.K.P.J.: Journal of Fluid Mechanics (, Numpages = , Pages = 253-292, Title = The Sources of Jet Noise: Experimental Evidence, Volume = 615, URL = , Year = 2008, doi =)
52. Tinney, C.E.: Low-dimensional techniques for sound source identification in high speed jets. Ph.D. dissertation, Syracuse University (2005)
53. Tinney, C.E., Glauser, M.N., Ukeiley, L.S.: Low-dimensional characteristics of a transonic jet. part 1. proper orthogonal decomposition. Journal of Fluid Mechanics **612**, 107–141 (2008a)
54. Tinney, C.E., Hall, A.M., Glauser M. N.and Ukeiley, L.S., Coughlin, T.: Designing an anechoic chamber for the experimental study of high speed heated jets. 42nd AIAA Aerospace Sciences Meeting and Exhibit (0010) (2004)
55. Tinney, C.E., Ukeiley, L.S., Glauser, M.N.: Low-dimensional characteristics of a transonic jet. part 2. estimate and far-field prediction. Journal of Fluid Mechanics **615**, 53–92 (2008b)
56. Viswanathan, K., Pilon, A.: Year in review 2011: Aeroacoustics. Aerospace America (2011)
57. Winant, C.D., Browand, F.K.: Vortex pairing: The mechanism of turbulent mixing-layer growth at moderate reynolds number. Journal of Fluid Mechanics **63**, 237–255 (1974)

Bibliography

[1] Fiscal years 2013-2033. *Federal Aviation Administration: FAA Aerospace Forecast*, 2013.

[2] Acquisition safety - noise control aboard navy ships. *Naval Safety Center*, 2014. http://www.public.navy.mil/navsafecen/Pages/acquisition/noise_control.aspx.

[3] How loud is too loud? *Hearing Speech & Deafness Center: Noise-Induced Hearing Loss - Protect Your Hearing!*, 2014. http://www.hsdc.org/noise-induced-hearing-loss.

[4] R. J. Adrian. On the role of conditional averages in turbulence theory. *Proceedings of the Fourth Biennial Symposium on Turbulence in liquids*, pages 323–332, September 22-24 1977.

[5] R. J. Adrian. Scattering particle characteristics and their effect on pulsed laser measurements of fluid flow: speckle velocimetry vs. particle image velocimetry. *Applications in Optics*, 23:1690–1691, 1984.

[6] RJ Adrian and CS Yao. Power spectra of fluid velocities measured by laser doppler velocimetry. *Experiments in Fluids*, 5(1):17–28, 1986.

[7] K.K. Ahuja. Noise studies of cold and heated model jets at supersonic and high subsonic speeds with particular reference to noise reduction. *PhD Dissertation, Syracuse University*, 1976.

[8] K.K. Ahuja and K.W. Bushell. An experimental study of subsonic jet noise and comparison with theory. *Journal of Sound and Vibration*, 30(03):317–341, 1973.

[9] M.B. Alkislar, A. Krothapalli, and G .W. Butler. The effect of streamwise vortices on the aeroacoustics of a mach 0.9 jet. *Journal of Fluid Mechanics*, 578:139–169, 2007.

[10] M. Andino, J. Pinier, R. Schmit, R. Wallace, C. Camphouse, J. Myatt, and M. Glauser. Flow control over a cylindrical turret using synthetic jets. *46th AIAA Aerospace Sciences Meeting and Exhibit*, (0736), January 7-10 2008.

[11] M. Andino, R. Wallace, M. N. Glauser, R. Schmit, J. Myatt, and R. C. Camphouse. Flow and aero-optics around a turret. part 1: Open loop flow control. *39th AIAA Plasmadynamics and Lasers Conference*, (4216), June 23-26 2008.

[12] M. Y. Andino and M. N. Glauser. Flow control effects on the length scales over a turret. *48th AIAA Aerospace Sciences Meeting*, (0087), January 4-7 2010.

[13] M. Y. Andino, R. D. Wallace, M. N. Glauser, R. F. Schmit, and J. H. Myatt. Boundary feedback flow control: Proportional control with potential application to aero-optics. *AIAA Journal*, 49(01):32–40, 2011.

[14] A. Arakeri, V. H. amd Krothapalli, V. Siddavaram, M. B. Alkislar, and L. Lourenco. On the use of microjets to suppress turbulence in a mach 0.9 axisymmetric jet. *Journal of Fluid Mechanics*, 490:75–98, 2003.

[15] J Atvars, LK Schubert, E Grande, and HS Ribner. *Refraction of sound by jet flow or jet temperature*. Institute for Aerospace Studies, University of Toronto, 1965.

[16] J. Ausseur and J. Pinier. Towards closed-loop feedback control of the flow over naca-4412 airfoil. *43rd AIAA Aerospace Sciences Meeting and Exhibit*, (343), January 10-13 2005.

[17] J. Ausseur, J. Pinier, M. Andino, C. Braud, M. Glauser, and H. Higuchi. Closed-loop feedback control of the flow over a naca 4412- airfoil. *Proceedings 1st European Forum on Flow Control*, pages 75–77, October 11-14 2004.

[18] J. Ausseur, J. Pinier, and M. Glauser. Flow separation control using a convection based pod approach. *3rd AIAA Flow Control Conference*, (3017), June 5-8 2006.

[19] J. Ausseur, J. Pinier, M. Glauser, and H. Higuchi. Experimental development of a reduced order model for flow separation control. *44th AIAA Aerospace Sciences Meeting and Exhibit*, (1251), January 9-12 2006.

[20] J. Ausseur, J. Pinier, M. Glauser, H. Higuchi, and H. Carlson. Controller development for closed-loop feedback control of flows. *35th AIAA Fluid Dynamics Conference and Exhibit*, (3017), June 6-9 2005.

[21] J. M. Ausseur. Application of low dimensional techniques for closed-loop control of turbulen flows. *Ph.D. dissertation, Syracuse University*, December 2007.

[22] J. Banke. Shhhh! keep it down, please. *NASA Aeronautics Research Mission Directorate*, 2009. http://www.nasa.gov/topics/aeronautics/features/aircraft_noise.html#.UwNq__ldXa4.

[23] C. Bargsten and M. T. Gibson. Nasa innovation in aeronautics: Select technologies that have shaped modern aviation (the chevron nozzle: A novel approach to reducing jet noise). *NASA/TM*, (216987), 2011.

[24] D. B. Barker and M. E. Fourney. Measuring fluid velocities with speckle patterns. *Optics Letters*, 1(4):135–137, 1977.

[25] G. K. Batchelor. Energy decay and self-preserving correlation functions in isotropic turbulence. *Quarterly of Applied Mathematics*, 6:97–116, 1948.

[26] G. K. Batchelor. The theory of homogeneous turbulence. *Cambridge University Press, Cambridge*, 1953.

[27] J. S. Bendat and A. G. Pierson. Random data: Analysis and measurement procedures. 1971.

[28] J. S. Bendat and A. G. Pierson. Engineering applications of correlation and spectral analysis. 1980.

[29] Z.P. Berger, M.G. Berry, P.R. Shea, M.N. Glauser, N. Jiang, B.R. Noack, S. Gogineni, E. Kaiser, and A. Spohn. Analysis of high speed jet flow physics with time-resolved piv. *52nd AIAA Aerospace Sciences Meeting*, (1226), 2014.

[30] Z.P. Berger, K.R. Low, M.G. Berry, M.N. Glauser, S. Kostka, S. Gogineni, L. Cordier, and B.R. Noack. Reduced order models for a high speed jet with time-resolved piv. *51st AIAA Aerospace Sciences Meeting*, (0011), 2013.

[31] Z.P. Berger, K.R. Low, S. Kostka, S. Gogineni, and M.N. Glauser. Investigation of an axisymmetric transonic jet with high resolution time-resolved piv. *48th AIAA Joint Propulsion Conference*, (3822), 2012.

[32] Z.P. Berger, P.R. Shea, M.G. Berry, B.R. Noack, S. Gogineni, and M.N. Glauser. Active flow control for high speed jets with large window piv. *Journal of Flow Turbulence and Control (In Review)*, 2014.

[33] G. Berkooz, P. Holmes, and J. L. Lumley. The proper orthogonal decomposition in the analysis of turbulent flows. *Annu. Rev. Fluid Mech.*, 25, 1993.

[34] Christophe Bogey and Christophe Bailly. Investigation of downstream and sideline subsonic jet noise using large eddy simulation. *Theoretical and Computational Fluid Dynamics*, 20(1):23–40, 2006.

[35] JP Bonnet, DR Cole, J Delville, MN Glauser, and LS Ukeiley. Stochastic estimation and proper orthogonal decomposition: complementary techniques for identifying structure. *Experiments in fluids*, 17(5):307–314, 1994.

[36] J. Bridges and C. A. Brown. Parametric testing of chevrons on single flow hot jets. *NASA/TMŮ213107*, 2004.

[37] C. Brown and J. Bridges. An analysis of model scale data transformation to full scale flight using chevron nozzles. *NASA/TM*, (212732), 2003.

[38] C. A. Brown and J. Bridges. Acoustic efficiency of azimuthal modes in jet noise using chevron nozzles. *12th AIAA/CEAS Aeroacoustics Conference (27th AIAA Aeroacoustics Conference)*, (2645), May 8-10 2006.

[39] G. L. Brown and A. Roshko. On density effects and large structure in turbulent mixing layers. *Journal of Fluid Mechanics*, 64(04):775–816, January 1974.

[40] HH Bruun. Hot wire anemometry: Principles and signal analysis, 1995.

[41] Preben Buchhave, William K. Jr. George, and John L. Lumley. The measurement of turbulence with the laser-doppler anemometer. *Annu Rev of Fluid Mech*, 11:443–503, 1979.

[42] R. Bui-Thanh, M. Damodaran, and K. Wilcox. Aerodynamic data reconstruction and inverse design using proper orthogonal decomposition. *AIAA Journal*, 42(8):1505–1516, 2004.

[43] B. Callender, E. Gutmark, and S. Martens. Far-field acoustic investigation into chevron nozzle mechanisms and trends. *American Institute of Aeronautics and Astronautics Journal*, 43(01):87–95, 2005.

[44] Brian J Cantwell. Organized motion in turbulent flow. *Annual Review of Fluid Mechanics*, 13(1):457–515, 1981.

[45] J. H. Citriniti and W. K. George. Reconstruction of the global velocity field in the axisymmetric mixing layer utilizing the proper orthogonal decomposition. *Journal of Fluid Mechanics*, 418(01):137–166, 2000.

[46] D. J. Coe, M. G. Allen, B. L. Smith, and A. Glezer. Addressable micromachined jet arrays. *Technical Digest: TRANSDUCERS*, 1995.

[47] D. J. Coe, M. G. Allen, M. A. Trautman, and A. Glezer. Micromachined jets for manipulation of macroflows. *Solid-State Sensor and Actuator Workshop*, 1994.

[48] F. Coiffet, P. Jordan, J. Delville, Y. Gervais, and F. Ricaud. Coherent structures in subsonic jets: a quasi-irrotational source mechanism? *Intl J. Aeroacoust*, 05(01):67–89, 2006.

[49] Daniel R Cole and Mark N Glauser. Applications of stochastic estimation in the axisymmetric sudden expansion. *Physics of Fluids (1994-present)*, 10(11):2941–2949, 1998.

[50] Daniel R Cole, Mark N Glauser, and Yann G Guezennec. An application of the stochastic estimation to the jet mixing layer. *Physics of Fluids A: Fluid Dynamics (1989-1993)*, 4(1):192–194, 1992.

[51] Media College. Tracer particles and seeding for particle image velocimetry. *Measurement Science and Technology*, 8(12), 1997.

[52] Geneviéve Comte-Bellot. Hot-wire anemometry. *Annu Rev of Fluid Mech*, 8:209–231, 1976.

[53] S. Corrsin. An experimental verification of local isotropy. *Journal of the Aeronautical Sciences*, 16:757–758, 1949.

[54] A. Crook, A. M. Sadri, and N. J. Wood. The development and implementation of synthetic jets for control of separated flow. *Appl. Aerodyn. Conf.*, 10(99-3176), 1999.

[55] S. C. Crow and F. H. Champagne. Orderly structure in jet turbulence. *Journal of Fluid Mechanics*, 48(03):547–591, 1971.

[56] GT Csanady. The effect of mean velocity variations on jet noise. *Journal of Fluid Mechanics*, 26(01):183–197, 1966.

[57] Daniel Cuppoletti, Ephraim Gutmark, Haukur Hafsteinsson, Lars-Erik Eriksson, and Erik Prisell. Analysis of supersonic jet thrust with fluidic injection. *52nd Aerospace Sciences Meeting: AIAA SciTech*, 2014.

[58] J. W. Deardorff. A numerical study of three-dimensional turbulent channel flow at large reynolds numbers. *Journal of Fluid Mechanics*, 41(04):453–480, 1970.

[59] A. F. Deming. Propeller rotation noise due to torque and thrust. *Journal of the Acoustical Society of America*, 12(01):173–182, 1940.

[60] D. S. Dosanjh, K. K. Ahuja, M. R. Bassiouni, and P. K. Bhutiani. Some recent developments in supersonic jet noise reduction. *American Institute of Aeronautics and Astronautics, 2nd Aero-Acoustics Conference*, (75-502), 1975.

[61] D. S. Dosanjh, M. R. Bassiouni, P. K. Bhutiani, and K. K. Ahuja. Potential of coaxial multi-nozzle configurations for reduction of noise from high velocity jets. *Proceedings of the Second Symposium of University Research in Transportation Noise*, June 1974.

[62] A. P. Dowling, J. E. Ffowcs Williams, and M. E. Goldstein. Sound production in a moving stream. *Philosophical Transactions of the Royal Society of London. Series A, Mathematical and Physical Sciences*, 288(1353):321–349, 1978.

[63] T. D. Dudderar and P. G. Simpkins. Laser speckle photography in a fluid medium. *Nature*, 270:45–47, 1977.

[64] PA Durbin. High frequency green function for aerodynamic noise in moving media, part i: General theory. *Journal of Sound and Vibration*, 91(4):519–525, 1983.

[65] PA Durbin. High frequency green function for aerodynamic noise in moving media, part ii: Noise from a spreading jet. *Journal of Sound and Vibration*, 91(4):527–538, 1983.

[66] F Durst, J Jovanovic, and J Sender. Lda measurements in the near-wall region of a turbulent pipe flow. *Journal of Fluid Mechanics*, 295:305–335, 1995.

[67] Daniel Ewing, HJ Hussein, and WK George. Spatial resolution of parallel hot-wire probes for derivative measurements. *Experimental thermal and fluid science*, 11(2):155–173, 1995.

[68] J. E. Ffowcs Williams. The noise from turbulence convected at high speed. *Philosophical Transactions of the Royal Society of London. Series A, Mathematical and Physical Sciences*, 255(1061):469–503, 1963.

[69] J. E. Ffowcs Williams. Aeroacoustics. *Annual Review of Fluid Mechanics*, 9(8110):477–468, 1977.

[70] J. E. Ffowcs Williams and L. H. Hall. Aerodynamic sound generation by turbulent flow in the vicinity of a scattering half plane. *Journal of Fluid Mechanics*, 40(04):657–670, 1970.

[71] J. E. Ffowcs Williams and D. L. Hawkings. Sound generation by turbulence and surfaces in arbitrary motion. *Philosophical Transactions of the Royal Society of London. Series A, Mathematical and Physical Sciences*, 264(1151), 1969.

[72] J.E. Ffowcs Williams and A.J. Kempton. The noise from the large-scale structure of a jet. *Journal of Fluid Mechanics*, 84(4), 1978.

[73] HE Fiedler. Coherent structures in turbulent flows. *Progress in Aerospace Sciences*, 25(3), 1988.

[74] HE Fiedler. Control of free turbulent shear flows. In *Flow Control*, volume 25. 1998.

[75] M. K. Fischer and M. Samimy. Noise control of a high reynolds number mach 1.3 heated jet using plasma actuators. *48th AIAA Aerospace Sciences Meeting Including the New Horizons Forum and Aerospace Exposition*, (0013), January 4-7 2010.

[76] D. V. Gaitonde and M. Samimy. Effect of plasma-based azimuthal mode excitation on supersonic jet flow. *5th Flow Control Conference*, (4416), June 28-1 2010.

[77] T. B. Gatski, M. Y. Hussaini, and J. L. Lumley. Simulation and modelling of turbulent flows: Icase/larc series in computational science and engineering. *Oxford University Press*, 1996.

[78] William K George and John L Lumley. The laser-doppler velocimeter and its application to the measurement of turbulence. *Journal of Fluid Mechanics*, 60(2):321–362, 1973.

[79] M. N. Glauser. Coherent structures in the axisymmetric turbulent jet mixing layer. *Ph.D. dissertation, University of Buffalo*, 1987.

[80] M. N. Glauser, E. Eaton, J. Taylor, D. Cole, L. Ukeiley, J. Citriniti, W. K. George, and S. Stokes. Low-dimensional descriptions of turbulent flows: Experiment and

modeling. *30th AIAA Fluid Dynamics Conference*, (3699):1–15, 28 June Ű 1 July 1999.

[81] M.N. Glauser and W.K. George. Orthogonal decomposition of the axisymmetric jet mixing layer including azimuthal dependence. *Advances in Turbulence, Spring-Verlag (Editors: G. Comte-Bellot and J. Mathieu)*, pages 357–366, 1987.

[82] M.N. Glauser and W.K. George. An orthogonal decomposition of the axisymmetric jet mixing layer utilizing cross-wire velocity measurements. *Proceedings Sixth Symposium on Turbulent Shear Flows, Toulouse, France*, pages 10.1.1–10.1.6., September 7-9 1987.

[83] M.N. Glauser, S.J. Leib, and W.K. George. Coherent structures in the axisymmetric turbulent jet mixing layer. *Turbulent Shear Flows 5, Springer-Verlag*, pages 134–145, 1987.

[84] A. Glezer and M. Amitay. Synthetic jets. *Annual Review of Fluid Mechanics*, 34, 2002.

[85] M. E. Goldstein. Aeroacoustics. *McGraw-Hill International Book Co.*, 1976.

[86] M. E. Goldstein. Aeroacoustics of turbulent shear flows. *Annual Review of Fluid Mechanics*, 16(1):263–285, 1984.

[87] Brenton Greska, Anjaneyulu Krothapalli, John M Seiner, Bernard Jansen, and Lawrence Ukeiley. The effects of microjet injection on an f404 jet engine. *11^{th} AIAA/CEAS Aeroacoustics Conference*, 3047, 2005.

[88] R. Grousson and S. Mallick. Study of flow pattern in a fluid by scattered laser light. *Applications in Optics*, 16:2334–2336, 1977.

[89] L. Gutin. On the sound field of a rotating propeller. *National Advisory Committee for Aeronautics Technical Memorandum*, (1195), 1936.

[90] A. M. Hall. An experimental investigation of low-dimensional techniques for large scale noise source characterization in a heated jet. *Ph.D. dissertation, Syracuse University*, December 2008.

[91] A. M. Hall and M. N. Glauser. An experimental analysis of the modal characteristics intrinsic to both the heated and cold jet. *47th AIAA Aerospace Sciences Meeting and Exhibit, Orlando, FL*, (2009-1238):1–11, January 2009.

[92] A. M. Hall, J. T. Pinier, J. W. Hall, and M. N. Glauser. Identifying the most energetic modes of the pressure near- field region of a mach 0.85 axisymmetric jet. *44th AIAA Aerospace Sciences Meeting and Exhibit, Reno, NV*, (2006-314):1–9, January 2006.

[93] J. W. Hall, J. T. Pinier, A. M. Hall, and M. N. Glauser. Two-point correlations of the near and far-field pressure in a transonic jet. *ASME Joint U.S. European Fluids Engineering Summer Meeting, Miami, FL*, (2006-98458):1–7, July 2006.

[94] J.W. Hall, A.M. Hall, J.T. Pinier, and M.N. Glauser. A cross-spectral analysis of the pressure in a mach 0.85 turbulent jet. *AIAA Journal*, 47(1), 2009.

[95] J.W. Hall, J. Pinier, A. Hall, and M.N. Glauser. A spatio-temporal decomposition of the acoustic source in a mach 0.85 jet. *45th AIAA Aerospace Sciences Meeting and Exhibit*, (2007-442), January 8-11 2007.

[96] F. H. Harlow. Transport of anisotropic or low-intensity turbulence. *Los Alamos Scientific Laboratory report LA-3947*, July 1968.

[97] F. H. Harlow and C. W. Hirt. Generalized transport theory of anisotropic turbulence. *Los Alamos Scientific Laboratory report LA-4086*, May 1969.

[98] F. H. Harlow and P. I. Nakayama. Simulating fluid turbulence. *Scientific Journal*, 3(9):74, 1967.

[99] F. H. Harlow and P. I. Nakayama. Turbulence transport equations. *Physics of Fluids*, 10:2323, 1967.

[100] F. H. Harlow and P. I. Nakayama. Transport of turbulence energy decay rate. *Los Alamos Scientific Laboratory report LA-3854*, February 1968.

[101] F. H. Harlow and N. C. Romero. Turbulence distortion in a non-uniform tunnel. *Los Alamos Scientific Laboratory report LA-4247*, October 1968.

[102] MAZ Hasan and AKMF Hussain. The self-excited axisymmetric jet. *Journal of Fluid Mechanics*, 115(1):59–89, 1982.

[103] W. Heisenberg. On the theory of statistical and isotropic turbulence. *Proceedings of the Royal Society of London. Series A, Mathematical and Physical Sciences*, 195:402–406, 1948.

[104] B. Henderson. Fluidic injection for jet noise reduction. *Ohio State University 880 Seminar*, November 2009.

[105] B. Henderson, K. Kinzie, J. Whitmire, and A. Abeysinghe. The impact of fluidic chevrons on jet noise. *11th AIAA/CEAS Aeroacoustics Conference*, (2888), May 23-25 2005.

[106] B. Henderson, K. Kinzie, J. Whitmire, and A. Abeysinghe. Aeroacoustic improvements to fluidic chevron nozzles. *12th AIAA/CEAS Aeroacoustics Conference (27th AIAA Aeroacoustics Conference)*, (2706), May 8-10 2006.

[107] B. Henderson and T. Norum. Impact of azimuthally controlled fluidic chevrons on jet noise. *14th AIAA/CEAS Aeroacoustics Conference (29th AIAA Aeroacoustics Conference)*, (3062), May 5-7 2008.

[108] Brenda Henderson. Fifty years of fluidic injection for jet noise reduction. *International Journal of Aeroacoustics*, 9(1):91–122, 2010.

[109] C. W. Hicks and H. H. Hubbard. Comparison of sound emission from two-blade, four-blade, and seven-blade propellers. *National Advisory Committee for Aeronautics Technical Memorandum*, (1354), 1947.

[110] Philip Holmes, John L Lumley, and Gal Berkooz. *Turbulence, coherent structures, dynamical systems and symmetry*. 1998.

[111] H. Hotelling. Analisys of a complex of statistical variables into principal components. *Journal of Educational Psychology*, 24(06):417–441, 1933.

[112] M. S. Howe. Contributions to the theory of aerodynamic sound, with application to excess jet noise and the theory of the flute. *Journal of Fluid Mechanics*, 71(04):625–673, 1975.

[113] AKM Fazle Hussain. Coherent structures – reality and myth. *Physics of Fluids*, 26:2816–2850, 1983.

[114] P. Jordan, M. Schlegel, O. Stalnov, B. R. Noack, and C. E. Tinney. Identifying noisy and quiet modes in a jet. *13th AIAA/CEAS Aeroacoustics Conference (28th AIAA Aeroacoustics Conference)*, (3602), 2007.

[115] P. Kan. Near-field diagonstics contributing to far-field noise. private communication, 2014.

[116] P. Kan, J. Lewalle, and G. Daviller. Comparison of near-field events and their far-field acoustic signatures in experimental and numerical high speed jets. *International Symposium on Turbulence and Shear Flow Phenomena (TSFP-8)*, 2013.

[117] P. Kan, J. Lewalle, and S. Gogineni. Mach-number dependence of acoustic source properties in high speed jets – part ii: event based description. *52nd AIAA Aerospace Sciences Meeting*, (1229), 2014.

[118] Pinqing Kan and Jacques Lewalle. Comparison and properties of near-field and far-field events of high speed jet. *Bulletin of the American Physical Society*, 58, 2013.

[119] K. Karhunen. Zur spektraltheorie stochastischer prozesse. *Annales Academiae Scientiarum Fennicae. Series A. I, Mathematica*, 7, 1946.

[120] Jeff Kastner, Nick Heeb, Ephraim Gutmark, Junhui Liu, and Kailas Kailasanath. Using chevrons and fluidic injection to reduce supersonic jet nnoise. In *INTER-NOISE and NOISE-CON Congress and Conference Proceedings*, number 9, pages 2184–2194, 2012.

[121] JC Klewicki and RE Falco. On accurately measuring statistics associated with small-scale structure in turbulent boundary layers using hot-wire probes. *J. Fluid Mech*, 219:119–142, 1990.

[122] A. N. Kolmogorov. Dissipation of energy in the locally isotropic turbulence. *Proceedings of the Royal Society of London. Series A. Mathematical and Physical Sciences*, 434(1890):15–17, July 1991.

[123] A. N. Kolmogorov. The local structure of turbulence in incompressible viscous fluid for very large reynolds numbers. *Proceedings of the Royal Society of London. Series A. Mathematical and Physical Sciences*, 434(1890):9–13, July 1991.

[124] Gopi Krishnan and Kamran Mohseni. An experimental study of a radial wall jet formed by the normal impingement of a round synthetic jet. *European Journal of Mechanics-B/Fluids*, 29(4):269–277, 2010.

[125] A. Krothapalli, L. Venkatakrishnan, L. Lourenco, R. Greska, and R. Elavarasan. Turbulence and noise suppression of a high-speed jet by water injection. *Journal of Fluid Mechanics*, 491:131–159, 2003.

[126] Max C Kurbjun. *Limited investigation of noise suppression by injection of water into exhaust of afterburning jet engine*. National Advisory Committee for Aeronautics, 1958.

[127] MT Landahl and E Mollo-Christensen. *Turbulence and random processes in fluid mechanics*. 1992.

[128] L. D. Landau and E. M. Lifshitz. Fluid mechanics, (translated by j. b. sykes and w. h. reid from original russian published in 1944). *Pergamon Press, Oxford*, 1959.

[129] J.C. Lau. The vortex-street structure of turbulent jets. part 2. *Proceedings of the Royal Society of London. A. Mathematical and Physical Sciences*, 368(1735):547–571, 1979.

[130] J.C. Lau and M.J. Fisher. The vortex-sheet structure of turbulent jets. part 1. *Journal of Fluid Mechanics*, 67:299–337, 1975.

[131] JC Lau, MJ Fisher, and HV Fuchs. The intrinsic structure of turbulent jets. *Journal of Sound and Vibration*, 22(4):379–406, 1972.

[132] E. Laurendeau, J. P. Bonnet, P. Jordan, and J. Delville. Impact of fluidic chevrons on the turbulence structure of a subsonic jet. *3rd AIAA Flow Control Conference*, (3510), June 5-8 2006.

[133] E. Laurendeau, P. Jordan, J. P. Bonnet, and J. Delville. Turbulent jet noise control by fluid chevrons. *Turbulence and Shear Flow Phenomena IV*, 2005.

[134] E. Laurendeau, P. Jordan, J. P. Bonnet, J. Delville, P. Parnaudeau, and E. Lamballais. Subsonic jet noise reduction by fluidic control: The interaction region and the global effect. *Physics of Fluids*, 20(101519):1–15, 2008.

[135] J. Lewalle. Jet noise: Jet near-field events. *Jacques Lewalle website: Research Specialty*, 2014. http://lcs3.syr.edu/faculty/lewalle/.

[136] J. Lewalle, J. Delville, and J. Bonnet. Decomposition of mixing layer turbulence into coherent structures and background fluctuations. *Flow, Turbulence and Combustion*, 64:301–328, July 2000.

[137] J. Lewalle, P. Kan, and S. Gogineni. Mach-number dependence of acoustic source properties in high speed jets – part i: ensemble statistics of acoustically active regions. *52nd AIAA Aerospace Sciences Meeting*, (1228), 2014.

[138] Jacques Lewalle and Pinqing Kan. Sequencing of acoustic events in the near field of subsonic jets. *Bulletin of the American Physical Society*, 58, 2013.

[139] M. J. Lighthill. On sound generated aerodynamically. i. general theory. *Proceedings of the Royal Society of London. Series A. Mathematical and Physical Sciences*, 211(1107):564–587, 1952.

[140] M. J. Lighthill. On sound generated aerodynamically. ii. turbulence as a source of sound. *Proceedings of the Royal Society of London. Series A. Mathematical and Physical Sciences*, 222(1148):1–32, 1954.

[141] G. M. Lilley. On the noise from jets: Noise mechanisms. *AGARD Conference Proceedings*, (131):13–1, 1974.

[142] G.M. Lilley. Apparatus for reducing noise, 1961. US Patent 2,987,136.

[143] M. Loeve. Functions aleatoire de second ordre. *Comptes Rendus de l'Académie des Sciences*, page 220, 1945.

[144] K. R. Low, M. Y. Andino, R. D. Wallace, A. M. Hall, and M. N. Glauser. Closed-loop control of a turbulent compressible mach 0.6 jet. *47th AIAA Aerospace Sciences Meeting*, (0854), January 5-9 2009.

[145] K. R. Low, Z. P. Berger, J. Lewalle, B. El-Hadidi, and Glauser M. N. Correlations and wavelet based analysis of near-field and far-field pressure of a controlled high-speed jet. *41st AIAA Fluid Dynamics Conference and Exhibit*, (4020), June 27-30 2011.

[146] K. R. Low, B. El-Hadidi, M. N. Glauser, M. Y. Andino, and R. Berdanier. Investigation of different active flow control strategies for high speed jets using synthetic jet actuators. *40th Fluid Dynamics Conference and Exhibit*, (4267), June 28-1 2010.

[147] K. R. Low, R. D. Wallace, M. Y. Andino, and M. N. Glauser. Characteristics of closed-loop control in an axisymmetric jet at mach 0.6. *Proceedings of the 6th International Symposium on Turbulence and Shear Flow Phenomena*, June 22-24 2009.

[148] K.R. Low. Towards closed-loop control of a high-speed jet for noise reduction. *Ph.D. dissertation, Syracuse University*, May 2012.

[149] K.R. Low, Z.P. Berger, S. Kostka, B. El Hadidi, S. Gogineni, and M. Glauser. A low-dimensional approach to closed-loop control of a mach 0.6 jet. *Experiments in Fluids*, pages 1–17, 2013.

[150] J. L. Lumley. The structure of inhomogeneous turbulent flows. *Atm. Turb. and Radio Wave Prop. ed. by A.M. Yaglom and V. I. Tatarsky, (Nauka, Moscow)*, pages 166–178, 1967.

[151] R. Maury, P. Jordan, A. Cavalieri, J. Delville, and J.P. Bonnet. A study of the response of a round jet to pulsed fluidic actuation. *17th AIAA/CEAS Aeroacoustics Conference (32nd AIAA Aeroacoustics Conference*, (2750), June 2011.

[152] V. G. Mengle. Jet noise characteristics of chevrons in internally mixed nozzles. *11th AIAA/CEAS Aeroacoustics Conference*, (2934), May 23-25 2005.

[153] V. G. Mengle, R. Elkoby, L. Brusniak, and R. H. Thomas. Reducing propulsion airframe aeroacoustic interactions with uniquely tailored chevrons: 1. isolated nozzles. *12th AIAA/CEAS Aeroacoustics Conference*, (2467), May 8-10 2006.

[154] R. Meynart. Equal velocity fringes in a rayleighŰbenard flow by a speckle method. *Applied Optics*, 19(9):1385–1386, 1980.

[155] R. Meynart. Convective flow field measurement by speckle velocimetry. *Applied Physics Reviews*, 17(11):301–305, 1982.

[156] R. Meynart. Digital image processing for speckle flow velocimetry. *Review of Scientific Instruments*, 53(1):110–111, 1982.

[157] R. Meynart. Instantaneous velocity field measurement in unsteady gas flow by speckle velocimetry. *Applications in Optics*, 22(4):535–540, 1983.

[158] R. Meynart. Speckle velocimetry study of vortex pairing in a low-re unexcited jet. *Physics of Fluids*, 26(8):2074–2079, 1983.

[159] R. Meynart. Speckle velocimetry: an application of image analysis techniques to the measurement of instantaneous velocity fields in unsteady flow. *Proceedings*

of the international congress on instrumentation in aerospace simulation facilities, 1983:30–36, 1983c.

[160] W. Mohring. On vortex sound at low mach number. *Journal of Fluid Mechanics*, 85(04):685–691, 1978.

[161] E. Mollo-Christensen, M. A. Kolpin, and J. R. Martuccelli. Experiments on jet flows and jet noise far-field spectra and directivity patterns. *Journal of Fluid Mechanics*, 18(285):285–301, 1964.

[162] CJ Moore. The role of shear-layer instability waves in jet exhaust noise. *Journal of Fluid Mechanics*, 80(02):321–367, 1977.

[163] Philip J Morris, Dennis K McLaughlin, and Ching-Wen Kuo. Noise reduction in supersonic jets by nozzle fluidic inserts. *Journal of Sound and Vibration*, 332(17):3992–4003, 2013.

[164] PJ Morris, W Richarz, and HS Ribner. Reduction of peak jet noise using jet refraction. *Journal of Sound and Vibration*, 29(4):443–455, 1973.

[165] M. O. Muller, L. P. Bernal, P. K. Miska, P. D. Washabaugh, T. K. A. Chou, B. A. Parviz, C. Zhang, and K. Najafi. Flow structure and performance of axisymmetric synthetic jets. *AIAA 39th Aerospace Sciences Meeting and Exhibit*, (1008), 2001.

[166] N. Murray, G. Lyons, C.E. Tinney, B. Donald, W. Baars, B. Thurow, H. Haynes, and P. Panickar. A laboratory framework for synchronous near/far-field acoustics and mhz piv in high-temperature, shock-containing, jets. *InterNoise 2012 ASME NCAD Meeting*, August 19-22 2012.

[167] N. Murray and L. Ukeiley. Modified quadratic stochastic estimation of resonating subsonic cavity flow. *Journal of Turbulence*, 8(53), 2007.

[168] Nathan. E. Murray and Lawrence. S. Ukeiley. An application of gappy pod for subsonic cavity flow piv data. *Experiments in Fluids*, 42:79–91, 2007.

[169] A.M. Naguib, C.E. Wark, and O. Juckenhofer. Stochastic estimation and flow sources associated with surface pressure events in a turbulent boundary layer. *Physics of Fluids*, 13(9), June 2001.

[170] D.K. Nance and K.K. Ahuja. Experimentally separating jet noise contribution of large-scale turbulence from that of small-scale turbulence. *15th AIAA/CEAS Aeroacoustics Conference*, (3213), May 11-13 2009.

[171] Thomas D Norum. Reductions in multi-component jet noise by water injection. *AIAA Paper*, 2976, 2004.

[172] S. A. Orszag and G. S. Patterson. Numerical simulation of turbulence: statistical models and turbulence. *Lecture Notes in Physics*, 12:127–147, 1972.

[173] R. K. Otnes and L. Enochson. Applied time series analysis. 1, 1978.

[174] A. P. Pao. A generalized theory on the noise generation from supersonic shear layers. *Journal of Sound and Vibration*, 19(4):401–410, 1971.

[175] D. Papamoschou, P. Morris, and D. McLaughlin. Beamformed flow-acoustic correlations in high-speed jets. *15th AIAA/CEAS Aeroacoustics Conference*, (3212), May 11-13 2009.

[176] K. Pearson. On lines and planes of closest fit to systems of points in space. *Philosophical Magazine*, 2:559–572, 1901.

[177] B. Petitjean, K. Viswanathan, D. McLaughlin, and P. Morris. Space-time correlation measurements in subsonic and supersonic jets using optical deflectometry. *13th AIAA/CEAS Aeroacoustics Conference*, (3613), May 21-23 2007.

[178] O. M. Phillips. On the generation of sound by supersonic turbulent shear layers. *Journal of Fluid Mechanics*, 9(01), 1960.

[179] C. Picard and J. Delville. Presure velocity coupling in a subsonic round jet. *International Journal of Heat and Fluid Flow*, 21(3):359–364, June 2000.

[180] C. J. D. Pickering and N. Halliwell. Lsp and piv: photographic film noise. *Applications in Optics*, 23:2961–2969, 1984.

[181] Anthony R Pilon, Russell W Powers, Dennis K McLaughlin, and Philip J Morris. Design and analysis of a supersonic jet noise reduction concept. *52nd AIAA Aerospace Sciences Meeting: AIAA SciTech*, 2014.

[182] J. T. Pinier. Low-dimensional techniques for active control of high- speed jet aeroacoustics. *Ph.D. dissertation, Syracuse University*, December 2007.

[183] J. T. Pinier, J. M. Ausseur, M. N. Glauser, and H. Higuchi. Proportional closed-loop feedback control of flow separation. *AIAA Journal*, 45(01):181–190, 2007.

[184] J. T. Pinier and M. N. Glauser. Dual-time piv investigation of the sound producing region of the controlled and uncontrolled high-speed jet. *Advances in Turbulence XI: Proceeding of the 11^{th} EUROMECH European Turbulence Conference*, 117:392–394, June 25-28 2007.

[185] J. T. Pinier and M. N. Glauser. An empirical reduced order model of the mach 0.6 turbulent axisymmetric jet. *49^{th} AIAA Aerospace Sciences Meeting*, (282), Jan. 4-7 2011.

[186] L. Prandtl. Bericht uber untersuchungen zur ausgebildeten turbulenz. *Zs. agnew. Math. Mech.*, 5:136–139, 1925.

[187] Markus Raffel, Christian E Willert, and Jürgen Kompenhans. *Particle Image Velocimetry: A Practical Guide; with 24 Tables*. Springer, 1998.

[188] O. Reynolds. An experimental investigation of the circumstances which determine whether the motion of water shall be direct or sinuous, and of the law of resistance in parallel channels. *Philosophical Transactions of the Royal Society of London*, 35(1883a):84–99, 1883.

[189] O. Reynolds. An experimental investigation of the circumstances which determine whether the motion of water shall be direct or sinuous, and of the law of resistance

in parallel channels. *Philosophical Transactions of the Royal Society of London*, 174(1883b):935–982, 1883.

[190] O. Reynolds. Iv. on the dynamical theory of incompressible viscous fluids and the determination of the criterion. *Philosophical Transactions of the Royal Society of London A.*, 186(1895):123–164, March 1895.

[191] H. S. Ribner. The generation of sound by turbulent jets. *Advances in Applied Mechanics, Academic Press*, 03:103–182, 1964.

[192] GP Romano, RA Antonia, and T Zhou. Evaluation of lda temporal and spatial velocity structure functions in a low reynolds number turbulent channel flow. *Experiments in fluids*, 27(4):368–377, 1999.

[193] Christopher J. Ruscher, John F. Dannenhoffer, and Mark N. Gluaser. Application of snapshot pod on a varying grid. In *51st AIAA ASM*, Grapevine, Texas, 7-10 January 2013. AIAA-2013-0256.

[194] C.J. Ruscher. Application of data fusion to fluid dynamic data. *Ph.D. dissertation, Syracuse University*, May 2014.

[195] M. Samimy. Plasma actuators for high-speed flow control. *The Ohio State University: Non-Equilibrium Thermodynamics Laboratory*, 2014. https://www.mecheng.osu.edu/netl/plasma-actuators-high-speed-flow-control.

[196] M. Samimy, I. Adamovich, B. Webb, J. Kastner, J. Hileman, S. Keshav, and P. Palm. Development and characterization of plasma actuators for high speed jet control. *Experiments in Fluids*, 37(04):577–588, 2004.

[197] M. Samimy, M. K. Fischer, J.-H. Kim, and A. Sinha. High speed and high reynolds number jet control using arc filament plasma actuators for noise mitigation and for flow and noise diagnostics. *49th AIAA Aerospace Sciences Meeting including the New Horizons Forum and Aerospace Exposition*, (0022), January 4-7 2011.

[198] M. Samimy, J.-H. Kim, I. Adamovich, Y. Utkin, and J. Kastner. Active control of high speed and high reynolds number free jet using plasma actuators. *44th AIAA Aerospace Sciences Meeting and Exhibit*, (0711), January 9-12 2006.

[199] M. Samimy, J.-H. Kim, I. Adamovich, Y. Utkin, and S. Keshav. High speed jet control using plasma actuators. *4th International Symposium on Turbulence and Shear Flow Phenomena*, 2005.

[200] M. Samimy, J.-H. Kim, M. K. Fischer, and A. Sinha. Acoustic and flow fields of an excited high reynolds number axisymmetric supersonic jet. *Journal of Fluid Mechanics*, 656:507–529, 2010.

[201] M. Samimy, J.-H. Kim, J. Kastner, I. Adamovich, and Y. Utkin. Active control of a mach 0.9 jet for noise mitigation using plasma actuators. *AIAA Journal*, 45(04), April 2007.

[202] M. Schlegel, B. R. Noack, P. Comte, D. Kolominskiy, K. Schneider, M. Farge, J. Scouten, D. M. Luchtenburg, and G. Tadmor. Reduced-order modelling of turbulent jets for noise control. *In Numerical Simulation of Turbulent Flows and Noise Generation (ed. C. Brun, D. Juve, M. Manhart and C.-D. Munz). Notes on Numerical Fluid Mechanics and Multidisciplinary Design*, 104:3–27, 2009.

[203] M. Schlegel, B. R. Noack, P. Jordan, A. Dillmann, E. Groschel, W. Schröder, M. Wei, J. B. Freund, O. Lehmann, and G. Tadmor. On least-order flow representations for aerodynamics and aeroacoustics. *Journal of Fluid Mechanics*, 679:367–398, 2012.

[204] J. M. Seiner. A new rational approach to jet noise reduction. *Theoretical and Computational Fluid Dynamics*, 10(1-4):373–383, 1998.

[205] John M Seiner, Laurence S Ukeiley, and Bernard J Jansen. Aero-performance efficient noise reduction for the f404-400 engine. *AIAA Paper*, 3048, 2005.

[206] P.R. Shea. Experimental investigation of an actively controlled three-dimensional turret wake. *Ph.D. dissertation, Syracuse University*, May 2012.

[207] P.R. Shea, Z.P. Berger, M.G. Berry, S. Gogineni, and M.N. Glauser. Low-dimensional modeling of a mach 0.6 axisymmetric jet. *52nd AIAA Aerospace Sciences Meeting*, (0245), 2014.

[208] P.R. Shea and M.N. Glauser. Experimental investigation of an actively controlled three-dimensional turret wake. *50th AIAA Aerospace Sciences Meeting*, (0745), January 9-12 2012.

[209] P.R. Shea and M.N. Glauser. Closed-loop active flow control of a three-dimensional turret wake. *51st AIAA Aerospace Sciences Meeting*, (0394), 2013.

[210] P.R. Shea, M.N. Glauser, H.A. Carlson, R. Verberg, and R.F. Schmidt. Active flow control of a pitching turret flow field using closed-loop feedback control. *50th AIAA Aerospace Sciences Meeting*, (2804), January 9-12 2012.

[211] M. Sheplak and E. F. Spina. Control of high-speed impinging-jet resonance. *AIAA Journal*, 32(8):1583–1588, July 1994.

[212] A. Sinha, K. Kim, J.-H. Kim, A. Serrani, and M. Samimy. Extremizing feedback control of a high-speed and high reynolds number jet. *AIAA Journal*, 48(02), 2010.

[213] A. Sinha, A. Serrani, and M. Samimy. Development of empirical estimators for feedback control of high-speed axisymmetric jets. *AIAA Journal*, 49(09), September 2011.

[214] L. Sirovich. Turbulence and the dynamics of coherent structures, part i,ii, and iii. *Quarterly Applied Mathematics*, 45, 1987.

[215] B. L. Smith and A. Glezer. Vectoring and small-scale motions effected in free shear flows using synthetic jet actuators. *AIAA 35th Aerospace Sciences Meeting*, (97–213), January 1997.

[216] B. L. Smith and A. Glezer. The formation and evolution of synthetic jets. *Physics of Fluids*, 10:2281–2297, 1998.

[217] C. K. W. Tam. Jet noise: Since 1952. *Theoretical and Computational Fluid Dynamics*, 10(1-4):393–405, 1998.

[218] C. K. W. Tam and P. Chen. Turbulent mixing noise from supersonic jets. *AIAA Journal*, 32:1774–1780, 1994.

[219] Christopher KW Tam and Laurent Auriault. Mean flow refraction effects on sound radiated from localized sources in a jet. *Journal of Fluid Mechanics*, 370(2):149–174, 1998.

[220] Christopher KW Tam and Laurent Auriault. Jet mixing noise from fine-scale turbulence. *AIAA Journal*, 37(2):145–153, 1999.

[221] C.K. Tam, K. Viswanathan, K. Ahuja, and J. Panda. The sources of jet noise: Experimental evidence. *Journal of Fluid Mechanics*, 615:253–292, 2008.

[222] G. I. Taylor. Statistical theory of turbulence. *Proceedings of the Royal Society of London. Series A. Mathematical and Physical Sciences*, 151:421–478, 1935.

[223] J.A. Taylor and M.N. Glauser. Towards practical flow sensing and control via pod and lse based low-dimensional tools. *Journal of Fluids Engineering*, 126(3):337–345, 2004.

[224] H. Tennekes and J. L. Lumley. A first course in turbulence. *MIT Press*, 1972.

[225] T. Theodorsen and A. A. Regier. The problem of noise reduction with reference to light airplanes. *National Advisory Committee for Aeronautics Technical Memorandum*, (1145), 1946.

[226] C. Tinney, P. Jordan, A. Guitton, J. Delville, and F. Coiffet. A study in the near pressure field of co-axial subsonic jets. *12th AIAA/CEAS Aeroacoustics Conference (27th AIAA Aeroacoustics Conference)*, (2589), May 8-10 2006.

[227] C. E. Tinney. Low-dimensional techniques for sound source identification in high speed jets. *Ph.D. dissertation, Syracuse University*, May 2005.

[228] C. E. Tinney, M. N. Glauser, and L. S. Ukeiley. Low-dimensional characteristics of a transonic jet. part 1. proper orthogonal decomposition. *Journal of Fluid Mechanics*, 612:107–141, June 2008.

[229] C. E. Tinney, A. M. Hall, L. S. Glauser, M. N.and Ukeiley, and T. Coughlin. Designing an anechoic chamber for the experimental study of high speed heated jets. *42nd AIAA Aerospace Sciences Meeting and Exhibit*, (0010), January 5-8 2004.

[230] C. E. Tinney, L. S. Ukeiley, and M. N. Glauser. Low-dimensional characteristics of a transonic jet. part 2. estimate and far-field prediction. *Journal of Fluid Mechanics*, 615:53–92, July 2008.

[231] CE Tinney, F Coiffet, J Delville, AM Hall, P Jordan, and MN Glauser. On spectral linear stochastic estimation. *Experiments in fluids*, 41(5):763–775, 2006.

[232] A. A. Townsend. The measurement of double and triple correlation derivatives in isotropic turbulence. *Proceedings of the Cambridge Philosophical Society*, 43(04):560–570, 1947.

[233] A. A. Townsend. The structure of turbulent shear flow. *Cambridge University Press*, 1955.

[234] L. Ukeiley, C. E. Tinney, Mann R., and M. Glauser. Spatial correlations in a transonic jet. *AIAA Journal*, 45(06):1357–1369, June 2007.

[235] LS Ukeiley, DR Cole, and MN Glauser. An examination of the axisymmetric jet mixing layer using coherent structure detection techniques. In *Eddy Structure Identification in Free Turbulent Shear Flows*, pages 325–336. Springer, 1993.

[236] T. Vaithianathan, H. Carlson, R.D. Wallace, P. Shea, and M.N. Glauser. Feedback flow control for a pitching turret (part 1). *48th AIAA Aerospace Sciences Meeting*, (0360), January 4-7 2010.

[237] T. Vaithianathan, H.A. Carlson, R. D. Wallace, P.R. Shea, and M. N. Glauser. Model-based feedback flow control development and simulation for a pitching turret. *AIAA Journal*, 50(9), September 2012.

[238] Alexander Vendl and Heike Faßbender. Proper orthogonal decomposition for steady aerodynamic applications. *PAMM*, 10(1):635–636, 2010.

[239] K. Viswanathan and A. Pilon. Year in review 2011: Aeroacoustics. *Aerospace America*, December 2011.

[240] T. von Karman. On the statistical theory of turbulence. *Proceedings of the National Academy of Sciences, Washington*, 23(2):98–105, 1937.

[241] T. von Karman. Some remarks on the statistical theory of turbulence. *Proceedings of the 5th International Congress for Applied Mechanics*, 1938.

[242] T. von Karman. Progress in the statistical theory of turbulence. *Proceedings of the National Academy of Sciences, Washington*, 34(11):530–539, 1948.

[243] T. von Karman and L. Howarth. On the statistical theory of isotropic turbulence. *Proceedings of the Royal Society of London. Series A. Mathematical and Physical Sciences*, 164(917):192–215, January 1938.

[244] R. D. Wallace, M. Y. Andino, M.N. Glauser, R. C. Camphouse, R. Schmit, and J. Myatt. Flow characteristics of active control around a 3d turret. *47th AIAA Aerospace Sciences Meeting*, (0537), January 5-9 2009.

[245] R. D. Wallace, P. Shea, M. N. Glauser, T. Vaithianathan, and H. Carlson. Closed-loop flow control for an articulating turret. *5th Flow Control Conference*, (4966), June 28-1 2010.

[246] R. D. Wallace, P. Shea, M. N. Glauser, T. Vaithianathan, and H. Carlson. Feedback flow control for a pitching turret (part 2). *48th AIAA Aerospace Sciences Meeting*, (0361), January 4-7 2010.

[247] R. D. Wallace, P. Shea, M. N. Glauser, T. Vaithianathan, H. Carlson, and R. Schmit. Suction flow control at high reynolds number. *41st AIAA Fluid Dynamics Conference and Exhibit*, (3716), June 27-30 2011.

[248] R. D. Wallace, P.R. Shea, M. N. Glauser, T. Vaithianathan, and H.A. Carlson. Simulation-guided, model-based feedback flow control for a pitching turret. *AIAA Journal*, 50(8), August 2012.

[249] R.D. Wallace, M.Y. Andino, M.N. Glauser, R.C. Camphouse, R. Schmit, and J. Myatt. Flow and aero-optics around a turret. part 2: Surface pressure based closed-loop control. *39th AIAA Plasmadynamics and Lasers Conference*, (4217), June 23-26 2008.

[250] G. Wang. Experimental investigation of the active flow ccontrol on a two-dimensional wind turbine airfoil. *Ph.D. dissertation, Syracuse University*, August 2013.

[251] G. Wang, J. Lewalle, M. Glauser, and J. Walczak. Investigation of the benefits of unsteady blowing actuation on a 2d wind turbine blade. *Journal of Turbulence*, 14(1):165–189, March 2013.

[252] Mark P Wernet. Time-resolved piv for space-time correlations in hot jets. In *Instrumentation in Aerospace Simulation Facilities, 2007. ICIASF 2007. 22nd International Congress on*, pages 1–11. IEEE, 2007.

[253] Karen Wilcox. Unsteady flow sensing and estimation via the gappy proper orthogonal decomposition. *Computers & fluids*, 35(2):208–226, 2006.

[254] C. D. Winant and F. K. Browand. Vortex pairing: The mechanism of turbulent mixing-layer growth at moderate reynolds number. *Journal of Fluid Mechanics*, 63:237–255, 1974.

[255] JC Wyngaard. Measurement of small-scale turbulence structure with hot wires. *Journal of Physics E: Scientific Instruments*, 1(11):1105, 1968.

[256] A. M. Yaglom. Homogeneous and isotropic turbulence in a viscous compressible fluid. *Izv. Akad. Nauk. SSSR Ser. Geogr. i Geofiz.*, 12:501–522, 1948.

[257] Y. Yeh and H. Cummins. Localized fluid flows measurements with a he-ne laser spectrometer. *Applied Physics Letters*, 4:176–178, 1964.

[258] AJ Yule. Large-scale structure in the mixing layer of a round jet. *Journal of Fluid Mechanics*, 89(3):413–432, 1978.

[259] Y Zhu and RA Antonia. The spatial resolution of hot-wire arrays for the measurement of small-scale turbulence. *Measurement Science and Technology*, 7(10):1349, 1996.

Zachary P. Berger

Office:	263 Link Hall Syracuse, NY 13244 315-443-2960	**Home:**	233 Robert Drive Syracuse, NY 13210 203-641-0417
Email:	zpberger@syr.edu	**Citizenship:**	United States of America
Date of CV:	20 January 2014	**Date of Birth:**	15 May 1987

Research Interests: High-speed jet flows, free shear flows, flow control, bluff body aerodynamics, and aeroacoustics

Education

2014	Ph.D.	*In Progress (Anticipated Graduation: May 2014)* Syracuse University; Syracuse, NY Mechanical and Aerospace Engineering *Advisor:* Mark N. Glauser PhD GPA: 4.0/4.0 *Oral Qualifying Examination:* Aug. 13, 2013
2011	M.S.	Syracuse University; Syracuse, NY Mechanical and Aerospace Engineering *Advisor:* Mark N. Glauser Master's GPA: 3.87/4.0 *Capstone Defense:* April 28, 2011
2009	B.S.	Syracuse University; Syracuse, NY Aerospace Engineering *Advisor:* Mark N. Glauser
	B.A.	Syracuse University; Syracuse, NY Mathematics *Advisor:* Dan Zacharia Undergraduate GPA: 3.947/4.0

Work Experience

6/2010 – Present **Graduate Research Assistant**
Syracuse University; Syracuse, NY

- Applied advance filtering and low-dimensional modeling techniques such as POD and wavelets to various jet noise data sets.
- Explored Mach 0.6 heated jet data set, looking at relationships between near field hydrodynamic pressure and far-field acoustics. .
- Applying reduced order modeling techniques to a time-resolved jet data set for flow control.
- Investigate cross-correlations and cross-spectra between near and far field pressure regions and as well as low-dimensional velocity field.

- Currently working on using the techniques discussed above to develop closed loop control methods for far-field jet noise reduction.

6/2009-6/2010 **Graduate Research Assistant**
Syracuse University; Syracuse, NY

- Helped design a disk to incorporate synthetic jet actuators and pressure transducers in order to conduct closed loop control tests for flow separation analysis.
- Perform Proper Orthogonal Decomposition (POD) on a previous time resolved, open loop data set involving the near wake region of a disk in a water flow.
- Analyze mathematical reduced order modeling techniques in order perform closed loop control of the disk problem using an observer-based controller.
- Compiled and presented preliminary results at 2009 APS Fluid Dynamics Conference in Minneapolis, MN.

6/2008-8/2008 **Undergraduate Research Assistant**
Syracuse University; Syracuse, NY

- Worked in the turbulence research laboratory with graduate and undergraduate students to help solve a flow control problem related to turbulence.
- Designed a pitching and yawing mechanism for a turret model to be used for communications in aerospace applications.
- Collaborated with a team of students to solve issues of boundary layer separation via pressure valves to be readily placed on the turret model.
- Helped to order parts, arrange the building of the final mechanism and make sure it was ready to begin wind tunnel testing in the fall semester.

Honors and Awards

2007-2009	Annual Student Awards and Recognition by the Department of Mechanical and Aerospace Engineering, Syracuse University
2009	William Peil Inventors Award
2008	Award for Excellence by an Aerospace Engineering Junior
2007	Award for Excellence by an Aerospace Engineering Sophomore
2006	Kin-Nee Tong Outstanding Academic Achievement Award

Teaching Experience

Fall 2009-Fall 2011	**Mechanical and Aerospace Engineering Laboratory** (MAE 315) Teaching Assistant: *Syracuse University*
Spring 2011	**Aerodynamics** (AEE 342) Teaching Assistant: *Syracuse University*
Fall 2010	**Aircraft Performance and Flight Dynamics** (AEE 472) Teaching Assistant: *Syracuse University*
Spring 2010	**Statics** (ECS 221) Teaching Assistant: *Syracuse University* **Thermodynamics** (MAE 251) Teaching Assistant: *Syracuse University*

Professional Activities

2008 – Present	Student Member, American Institute of Aeronautics and Astronautics
2009 – Present	Student Member, American Physical Society
2010 – Present	Student Member, American Society of Mechanical Engineers
2014	Peer Reviewer, Journal of Flow Turbulence and Combustion Peer Reviewer, Journal of Fluid Mechanics Rapids
2013	Peer Reviewer, Journal of Hydro-Environmental Research
2012	Session Chair, AIAA Region 1-NE Student Conference, 4-6 April 2012, Syracuse University, Syracuse, NY.

Publications

[1] Low, K.R., Berger, Z.P., Kostka, S., El Hadidi, B., Gogineni, S., Glauser, M.N., "A Low-Dimensional Approach to Closed-Loop Control of a Mach 0.6 Jet". *Experiments in Fluids,*Vol. 54, No. 4, 2013, pp. 1-17.

In review:

[1] Bai, Z., Wimalajeewa, T., Berger, Z.P., Wang, G., Glauser, M.N., Varshney, P., "A Low Dimensional Approach for Reconstruction of Airfoil Data via Compressive Sensing", *AIAA Journal*.

[2] Berger, Z.P., Berry, M.G., Shea, P.R., Noack, B.R., Gogineni, S., Glauser, M.N., "Active Flow Control for High Speed Jets Using Advanced Modeling Coupled with PIV", *Journal of Flow Turbulence and Combustion.*

To be submitted:

[1] Ruscher, C.J., Berger, Z.P., Shea, P.R., Glauser, M.N., Gogineni, S., Kiel, B.V., "Comparisons of High Speed Optical Measurements in a Jet Flow", *Experiments in Fluids.*

Invited Talks

[1] Shea, P.R., Glauser, M.N., Berger, Z.P., Berry, M.G., Kiel, B.V., Gogineni, S., Noack, B.R., "Validation of Estimation Methods via Time-Resolved PIV in High Speed Compressible Jet", 52nd AIAA Aerospace Sciences Meeting, 13-17 January 2014, National Harbor, MD.

[2] *Invited Researcher:* Turbulence Control Team PPRIME, Poitiers, France, August 19-30 2013. Topic: Cluster-based reduced-order modeling (CROM) applied to high speed jet data.

[3] Glauser, M.N., Varshney, P., Wimalajeewa, T., Bai, Z., Berger, Z.P., Wang, G., "Application of Compressive Sensing to NACA 4412 PIV Data", 51st AIAA Aerospace Sciences Meeting, 7-10 January 2013, Dallas, TX, AIAA-2013-0772.

[4] Berger, Z.P., Low, K.R., Kostka, S., Cordier, L., Gogineni, S., Noack, B.R., Glauser, M.N., "Exploring High Subsonic Jet Noise with Time-Resolved PIV and Reduced-Order Modeling", *32nd Israeli Conference on Mechanical Engineering (ICME)*, Tel Aviv, Israel, Oct. 17-18, 2012.

Conference Proceedings (Peer Reviewed)

[1] Berry, M.G., Magstadt, A., Berger, Z.P., Shea, P.R., Gogineni, S., Kiel, B.V., Glauser, M.N., "Loud Mode Filtering for a High Speed Jet Using Reduced Order Modeling", 50th AIAA Joint Propulsion Conference, 28-30 July, 2014, Cleveland, OH, *To be submitted.*

[2] Shea, P.R., Berger, Z.P., Berry, M.G., Glauser, M.N., Kiel, B.V., Gogineni, S., "Low-Dimensional Modeling of a Mach 0.6 Axisymmetric Jet", 52nd AIAA Aerospace Sciences Meeting 13-17 January 2014, National Harbor, MD, AIAA-2014-0245.

[3] Berger, Z.P., Berry, M.G., Shea, P.R., Glauser, M.N., Jiang, N., Gogineni, S., Kiel, B.V., Kasier, E., Noack, B.R., Spohn, A., "Analysis of High Speed Jet Flow Physics with Time-Resolved PIV", 52nd AIAA Aerospace Sciences Meeting 13-17 January 2014, National Harbor, MD, AIAA-2014-1226.

[4] Berger, Z.P., Berry, M.G., Shea, P.R., Noack, B.R., Gogineni, S., Glauser, M.N., "Active Flow Control for High Speed Jets Using Advanced Modeling Coupled with PIV", 8th International Symposium on Turbulence and Shear Flow Phenomena (TSFP-8), 28-30 August 2013, Poitiers, France.

[5] Berger, Z.P., Low, K.R., Berry, M.G., Kostka, S., Cordier, L., Noack, B.R., Gogineni, S., Glauser, M.N., "Reduced-Order Models for a High Speed Jet with Time-Resolved PIV", 51st AIAA Aerospace Sciences Meeting, 7-10 January 2013, Dallas, TX, AIAA-2013-0011.

[6] Berger, Z.P., Low, K.R., Kostka, S., Lewalle, J., Cordier, L., Noack, B.R., Gogineni, S., Glauser, M.N., "High Subsonic Jet Flow Physics and Noise", 2012 ASME InterNoise Conference, 19-22 August 2012, New York City, NY, IN12-346.

[7] Berger, Z.P., Low, K.R., Kostka, S., Gogineni, S., Glauser, M.N., "Investigation of an Axisymmetric Transonic Jet with High Resolution Time-Resolved PIV", 48th AIAA Joint Propulsion Conference, 30 July- 1 August, 2012, Atlanta, GA, AIAA-2012-3822.

[8] Low, K.R., Berger, Z.P., Kostka, S., Gogineni, S., Glauser, M.N., "Application of Low-Dimensional Modeling Techniques to an Axisymmetric Jet with Time-Resolved PIV", 42nd AIAA Fluid Dynamics Conference, 25-28 June 2012, New Orleans, LA, AIAA-2012-3079.

[9] Lewalle, J., Low, K.R., Glauser, M.N., Berger, Z.P., "Correlations of Near and Far-Field Acoustic Data in a High Speed Jet", 7th International Symposium on Turbulence and Shear Flow Phenomena (TSFP-7), 28-31 July, 2011, Ottawa, Canada.

[10] Low, K.R., Berger, Z.P., Lewalle, J., El Hadidi, B., Glauser, M.N., "Correlations and Wavelet Based Analysis of Near-Field and Far-Field Pressure of a Controlled High Speed Jet", 41st AIAA Fluid Dynamics Conference, 27-30 June 2011, Honolulu, HI, AIAA-2011-4020.

[11] Berger, Z.P., Bigger, R., Fardad, M., Higuchi, H., Glauser, M.N., Angeli, M., "Investigation of POD Bases for Flow Control on Disk Wakes", ASME 2010 3rd Joint US-European Fluids Engineering Summer Meeting, 1-5 August 2010, Quebec, Canada, FEDSM-ICNMM2010-31071.

Conference Presentations (Non-Refereed)

[1] Rossetti, J., Berger, Z.P., Berry, M.G., Glauser, M.N., "Heater Applications for High Speed Jets", 66th APS Division of Fluid Dynamics Meeting, 24-26 November 2013, Pittsburgh, PA.

[2] Zelenyak, A.R., Berger, Z.P., Berry, M.G., Shea, P.R., Glauser, M.N., "Characterization of synthetic jet actuators used for jet noise reduction by flow control", 66th APS Division of Fluid Dynamics Meeting, 24-26 November 2013, Pittsburgh, PA.

[3] Berry, M.G., Kiel, B.V., Berger, Z.P., Jiang, N., Gogineni, S., Glauser, M.N., "Analysis and comparison of non-axisymmetric and circular nozzle configurations of a high speed jet", 66th APS Division of Fluid Dynamics Meeting, 24-26 November 2013, Pittsburgh, PA.

[4] Berger, Z.P., Berry, M.G., Shea, P.R., Kiel, B.V., Jiang, N., Noack, B.R., Gogineni, S., Glauser, M.N., "Towards High Speed Jet Noise Reduction Using Time-Resolved PIV", 66th APS Division of Fluid Dynamics Meeting, 24-26 November 2013, Pittsburg, PA.

[5] Berger, Z.P., Berry, M.G., Shea, P.R., Glauser, M.N., "Active Control of High Speed Jets with Large-Window PIV", 1000 Islands Fluid Dynamics Meeting, 26-28 April, 2013, Gananoque, Ontario, Canada.

[6] Berry, M.G., Berger, Z.P., Low, K.R., Zelenyak, A.R., Gogineni, S., Glauser, M.N., "Flow Control Characterization of PIV Flow Field Using POD", 65th APS Division of Fluid Dynamics Meeting, 18-20 November 2012, San Diego, CA.

[7] Bai, Z., Wimalajeewa, T., Berger, Z.P., Glauser, M.N., Varshney, P., "Physics Based Compressive Sensing Approach Applied to Airfoil Data Collection and Analysis", 65th APS Division of Fluid Dynamics Meeting, 18-20 November 2012, San Diego, CA.

[8] Berger, Z.P., Berry, M.G., Low, K.R., Cordier, L., Noack, B.R., Gogineni, S., Glauser, M.N., "Active Control of Jet Noise Using Observable Inferred Decomposition and Large Window PIV", 65th APS Division of Fluid Dynamics Meeting, 18-20 November 2012, San Diego, CA.

[9] Berger, Z.P., Low, K.R., Kostka, S., Gogineni, S., Glauser, M.N., "Low-Dimensional Modeling of a Mach 1.0 Jet Flow Field Using Time-Resolved PIV", 1000 Islands Fluid Dynamics Meeting, 27-29 April 2012, Gananoque, Ontario, Canada.

[10] Berger, Z.P., Kostka, S., Low, K.R., Berry, M.G., Gogineni, S., Glauser, M.N., "Active Control of Jet Noise Using High Resolution TRPIV Part 1: POD Analysis", 64th APS Division of Fluid Dynamics Meeting, 20-22 November 2011, Baltimore, MD.

[11] Low, K.R., Kostka, S., Berger, Z.P., Berry, M.G., Gogineni, S., Glauser, M.N., "Active Control of Jet Noise Using High Resolution TRPIV Part 2: Velocity-Pressure-Acoustic Correlations", 64th APS Division of Fluid Dynamics Meeting, 20-22 November 2011, Baltimore, MD.

[12] Berger, Z.P., Hall, A., Low, K.R., Glauser, M.N., "Low-Dimensional Modeling Techniques (sLSE/POD) Applied to a Moderately Heated Mach 0.6 Turbulent Jet Flow Field", 1000 Islands Fluid Dynamics Meeting, 15-17 April 2011, Gananoque, Ontario, Canada.

[13] Low, K., El Hadidi, B., Berger, Z.P., Glauser, M.N., "Shear Layer Excitation of a High Speed Turbulent Jet", 63rd APS Division of Fluid Dynamics Meeting, 21-23 November 2010, Long Beach, CA.

[14] Lewalle, J., Berger, Z.P., Low, K.R., Glauser, M.N., "High Speed Jet Noise Source Identification by Wavelet Filtering", 63rd APS Division of Fluid Dynamics Meeting 21-23 November 2010, Long Beach, CA.

[15] Berger, Z.P., Bigger, R., Fardad, M., Higuchi, H., Glauser, M.N., Orbaker, A.J., "Investigation of POD Bases for Flow Control on Disk Wakes", 1000 Islands Fluid Dynamics Meeting, 23-25 April 2010, Gananoque, Ontario, Canada.

[16] Berger, Z.P., Bigger, R., Fardad, M., Higuchi, H., Glauser, M.N., Orbaker, A.J., "Application of Proper Orthogonal Decomposition to Disk Wakes", 62nd APS Division of Fluid Dynamics Meeting, 22-24 November 2009, Minneapolis, MN.

Laboratory Experience

2010 – Present	High Reynolds Number Compressible Turbulent Jet (Fully Anechoic Chamber – Syracuse University)
2008 – Present	Flight Simulator
2007 – Present	Subsonic Wind Tunnel
2008	Supersonic Wind Tunnel
	Shock Tube

Computer Skills

Operating Systems	Windows-based systems up to and included Windows 7 Microsoft packages, i.e. Word, Excel, PowerPoint
Engineering Software	Pro Engineer Wildfire, SolidWorks, Gambit, Fluent, EES (Engineering Equation Solver)
Data Acquisition/Processing	Matlab, Maple, LaTex, LabView, Dantec Dynamic (Dynamic Studio and Flow Manager), LaVision, National Instruments Data Acquisition Systems

Team Projects

Spring 2009 Senior Design Project
- Worked in teams of three to build an aircraft
- The aircraft had to carry payload from one side of the Carrier Dome to the other
- Had to carry as much payload as possible with one charge of a battery pack.

Spring 2006 CAD Model Clock Project
- Use Pro Engineer Wildfire CAD program to design and build a clock
- Work in groups to put together a project containing parts, mechanical drawings, and assemblies consistent with design specifications.
- Build a finalized CAD model clock that if manufactured could be fully operational.

Fall 2005 Mars Rover Design Project
- Design, build, program and test a fully operational Mars Rover model.
- Work in groups with peers in order to design a successful rover.
- Build a rover that can successfully capture and releases specified payloads.

Leadership Experience

2010 – Present	Global Graduate Ambassadors
8/2008 – 5/2009	Syracuse University Resident Advisor
8/2007 – 5/2008	Syracuse University Resident Advisor
8/2006 – 5/2007	Syracuse University Resident Advisor